Ultrafast, broadband and multi-pulse transmissions for ultrasonic imaging

Mehdi Yanis Benane

N°d'ordre NNT : 2018LYSE1268

THESE de DOCTORAT DE L'UNIVERSITE DE LYON
opérée au sein de
l'Université Claude Bernard Lyon 1

Ecole Doctorale N° 162
MECANIQUE, ENERGETIQUE, GENIE CIVIL, ACOUSTIQUE

Spécialité de doctorat : ACOUSTIQUE ET TRAITEMENT DE SIGNAL
Discipline : Imagerie ultrasonore

Soutenue publiquement le 10/12/2018, par :
Yanis Mehdi BENANE

Ultrafast, broadband and multi-pulse transmissions for ultrasonic imaging

---

Devant le jury composé de :

Président du jury :
Mireille Garreau, Professeur des Universités, Université Rennes 1

Rapporteur :
Denis Kouamé, Professeur des Universités, Université de Toulouse
Caroline Petitjean, Maître de conférences, Université de Rouen Normandie

Examinateurs :
Roberto Lavarello, Professeur des Universités, Pontificia Universidad Católica del Perú
Mireille Garreau, Professeur des Universités, Université Rennes 1
Jean Christophe Béra, Professeur des Universités, Université Claude Bernard Lyon 1

Co-directeur de thèse :
Olivier Basset, Professeur des Universités, Université Claude Bernard Lyon 1
Christian Cachard, Professeur des Universités, Université Claude Bernard Lyon 1

Yanis Mehdi Benane

UNIVERSITE CLAUDE BERNARD - LYON 1

Président de l'Université	**M. le Professeur Frédéric FLEURY**
Président du Conseil Académique	M. le Professeur Hamda BEN HADID
Vice-président du Conseil d'Administration	M. le Professeur Didier REVEL
Vice-président du Conseil Formation et Vie Universitaire	M. le Professeur Philippe CHEVALIER
Vice-président de la Commission Recherche	M. Fabrice VALLÉE
Directeur Général des Services	M. Alain HELLEU

COMPOSANTES SANTE

Faculté de Médecine Lyon Est – Claude Bernard	Directeur : M. le Professeur J. ETIENNE
Faculté de Médecine et de Maïeutique Lyon Sud – Charles Mérieux	Directeur : Mme la Professeure C. BURILLON
Faculté d'Odontologie	Directeur : M. le Professeur D. BOURGEOIS
Institut des Sciences Pharmaceutiques et Biologiques	Directeur : Mme la Professeure C. VINCIGUERRA
Institut des Sciences et Techniques de la Réadaptation	Directeur : M. le Professeur Y. MATILLON
Département de formation et Centre de Recherche en Biologie Humaine	Directeur : Mme la Professeure A-M. SCHOTT

COMPOSANTES ET DEPARTEMENTS DE SCIENCES ET TECHNOLOGIE

Faculté des Sciences et Technologies	Directeur : M. F. DE MARCHI
Département Biologie	Directeur : M. le Professeur F. THEVENARD
Département Chimie Biochimie	Directeur : Mme C. FELIX
Département GEP	Directeur : M. Hassan HAMMOURI
Département Informatique	Directeur : M. le Professeur S. AKKOUCHE
Département Mathématiques	Directeur : M. le Professeur G. TOMANOV
Département Mécanique	Directeur : M. le Professeur H. BEN HADID
Département Physique	Directeur : M. le Professeur J-C PLENET
UFR Sciences et Techniques des Activités Physiques et Sportives	Directeur : M. Y.VANPOULLE
Observatoire des Sciences de l'Univers de Lyon	Directeur : M. B. GUIDERDONI
Polytech Lyon	Directeur : M. le Professeur E.PERRIN
Ecole Supérieure de Chimie Physique Electronique	Directeur : M. G. PIGNAULT
Institut Universitaire de Technologie de Lyon 1	Directeur : M. le Professeur C. VITON
Ecole Supérieure du Professorat et de l'Education	Directeur : M. le Professeur A. MOUGNIOTTE
Institut de Science Financière et d'Assurances	Directeur : M. N. LEBOISNE

ACKNOWLEDGMENT

- First of all, I would like to thank my two thesis supervisors Prof Christian Cachard and Prof Olivier Basset who believed in me and gave me my chance three years ago. Without your trust, this dream would certainly never have come true. THANK YOU!
- A big “thank you” also to Prof Roberto Lavarello for the very fruitful close collaboration that we have maintained during these three years.
- I would like to thank all the people from the CREATIS laboratory with whom I collaborated. A special mention for the "Ultrasound team" and even more special for Denis Bujoreanu, Emilia Badescu, Vincent Perrot and Maxime Polichetti.
- I would like to acknowledge all the collaborators and friends at the "Laboratorio d'Imagenes Medicas" for their sense of welcome and support during my 6 month stay in Peru.
- A special thank also for Jean-Michel Escoffre and Anthony Novell from the laboratory “Imagerie et Cerveau” in Tours and Emilie Franceschini from the LMA laboratory in Marseille.

To my friends: Pininou, Tarik, Lazhar and Farouk;

To my brother-in-law: Anass;

To my sisters: Belynda, Lylia and Aziadée.

Three more people to thank:

DAD and MUM, all the words of the world are not enough to describe my gratitude and my respect towards you and all what you have done for me.

LYNDA, you are MY ALL.

ABSTRACT

Ultrasound imaging is a diagnostic tool widely used thanks to such virtues as real-time data acquisition / processing, ease of use and safety for the patient / practitioner during examination. However, when compared to other imaging methods such as X-ray tomography and Magnetic Resonance Imaging, the echography has the disadvantage to provide relatively low image quality. In this thesis, a method that is able to increase the ultrasound image quality, thus paving the way towards improved diagnostics based on echography and novel ultrasound applications, is studied. In order to increase the echo signal to noise ratio of the received signals, linear frequency modulated signals (also called chirps) are proposed. To avoid the negative effect of the bandlimited acquisition probe, a pre-enhancement step is applied on the probe excitation signals, in order to boost the signal energy in the frequency bands where the probe is less efficient. Wiener filters that allow obtaining a good trade-off between the spatial resolution and noise stability are used to compress the echo energy. The previously detailed pipeline (also called REC: Resolution Enhancement Technique) is applied on ultrafast imaging schemes. Promising results in simulation and in-vitro, ex-vivo, in-vivo acquisitions are shown. Furthermore, REC was adapted in such way that the frequency dependent tissue attenuation effect is compensated for. This improvement is validated in simulation and phantom experiments. REC was also adapted to the nonlinear propagation of ultrasound waves, by proposing a pulse inversion technique that uses REC to provide a better image resolution and contrast to noise ratio. Then, the generality of the REC method was demonstrated by applying it to different acquisition schemes such as diverging wave compounding and Multi Line Transmit (MLT). We also show that the image quality can be increased more by taking into account the spatial impulse response of the ultrasound probe when REC and MLT are combined. The last contribution of this thesis consists on combining orthogonal binary codes with REC pre-enhanced chirps in order to boost further the eSNR provided by REC while keeping its good performance in axial resolution. The method is applied to diverging wave compounding. Pairs of diverging waves are transmitted/received/reconstructed simultaneously thanks to the orthogonality property of the Golay codes. The results show that the proposed method is able to obtain a better image quality than conventional pulse imaging.

CONTENTS

LIST OF SYMBOLS AND ABBREVIATIONS

Latin letter

$a(t)$	Excitation signal (pre-enhanced chirp in the REC case)
$a(t)$	Linear chirp used to enhance the designed (fictive) impulse response
B/A	Nonlinear parameter
c	Celerity of the ultrasound wave in the tissue ($m.s^{-1}$)
c_0	Equilibrium celerity of the ultrasound wave in the tissue ($m.s^{-1}$)
$cp(t)$	Conventional pulse excitation
f	Frequency (Hz)
$h_1(t)$	Real impulse response
$h_2(t)$	Designed impulse response
$h_{att}(t,d)$	Attenuation impulse response
J_n	Bessel function
$k = \omega / c$	Wave number
$p(\vec{r},t)$	Pressure (Pa) of the ultrasound wave at the point (x,y,z) and at the time t
p_0	Equilibrium pressure (Pa) amplitude
$\tilde{r}$	Reflection coefficient (from medium 1 to medium 2)
$\tilde{t}$	Transmission coefficient (from medium 1 to medium 2)
R	Intensity reflection coefficient
T	Intensity transmission coefficient
$\vec{v}$	Particle velocity ($m.s^{-1}$)
$Z = \rho c$	Acoustic impedance of the medium ($kg.m^{-2}.s^{-1}$)
x	Lateral dimension (m)
y	Elevation dimension (m)
z	Axial dimension (m)

Greek letter

∇	Nabla operator
Δ	Laplace operator
α	Attenuation coefficient
β	Nonlinear coefficient
β_{REC}	Proposed Wiener filter
ζ	Laplace coefficient
γ	Smoothing parameter that controls the tradeoff between bandwidth and eSNR
λ	Wave length of the pressure wave (m)

ρ	Density of the tissue ($kg.m^{-3}$)
ρ_0	Equilibrium density of the tissue ($kg.m^{-3}$)
τ_b	Bulk delay
τ_m	Minimum-phase delay factor
ω	Angular frequency ($rad.s^{-1}$)

Abbreviations

AACL	Axial autocorrelation length
CDWC	Coherent diverging wave compounding
CMUT	Capacitive Micromachined Ultrasonic Transducers
CNR	Contrast-to-noise ratio
CU	Conventional ultrasound
CP	Conventional pulse
CPWC	Coherent plane wave compounding
DAS	Delay and sum
DW	Diverging wave
eSNR	echo signal-to-noise ratio
FR	Frame rate
FWHM	Full width at half maximum
LACL	Lateral autocorrelation length
MLT	Multi-line transmit
MTF	Modulation transfer function
PC	Pulse compression
PI	Pulse inversion
PRF	Pulse Repetition Frequency
PSF	Point spread function
PW	Plane wave
REC	Resolution enhancement compression
REC-opt	Resolution enhancement compression optimised
RF	Radio frequency
SLT	Single-line transmit
SNR	Signal-to-noise ratio
TBP	Time bandwidth product
TRF	Tissue reflectivity function
US	Ultrasound

INTRODUCTION

Chapter I

INTRODUCTION

Contents

1.1 Medical ultrasound imaging

Ultrasound has become one of the predominant medical imaging modalities and is currently the first diagnostic examination tool for most organs except for brain and lungs. This is related to the many benefits of ultrasound imaging, such as the relatively low cost of an ultrasound scanner (compared to the price of other modalities such as the X-ray tomography, Positron Emission Tomography and Magnetic Resonance Imaging), the small size and portability of the equipment, the safety of the ultrasound examination (no radiation) for the patient and for the practitioner, the fact that the ultrasound is non-invasive and the excellent temporal resolution. This makes ultrasound imaging the only non-invasive imaging modality capable to acquire images in real time and therefore to provide the ability of visualizing and evaluating static and also moving tissues.

Ultrasound imaging relies on the interaction between an acoustic wave and the medium in which it propagates. The main forms of interactions with the medium are refraction, reflection and absorption, which can be either specular or diffuse. When the wave reaches an interface between two media with different acoustic properties, a part of it is reflected back to the source. In addition, the ultrasonic wave transfers energy to the insonified medium, which is then converted into heat. It is thus obvious that, by transmitting an ultrasonic pulse in the imaged tissue, the obtained echoes contain important information on both the acoustic properties of the insonified media and on the spatial position of the interfaces separating them.

The ultrasound imaging process can be split in three main phases: a transmission, a reception and an image reconstruction phase. First, an acoustic wave is generated by a piezoelectric transducer excited by an electrical signal. The wave propagates inside the medium and the presence of heterogeneities in the medium density field leads to the formation of echoes which propagates in all directions and thus in the direction of the ultrasound probe. Same transmission probe is used to collect the backscattered echoes and transform them in electrical signal. This signal contains information on the geometry of the medium and is called radiofrequency (RF) signal. Therefore, these signals can be filtered (to reduce the noise) and beamformed in order to reconstruct the final image of the tissue.

Despite the many advantages it presents, ultrasound imaging has some disadvantages, including the provided image quality that cannot compete with those of most other imaging modalities (X-ray tomography and Magnetic Resonance Imaging). Thus, ultrasound imaging is not able to furnish the details of biological structures with the same level of precision.

The image quality can be quantified using different metrics. One of the most important being the spatial resolution, usually expressed in millimeters. Many approaches can be used to evaluate this fundamental metric but the general idea is to consider that the resolution of an imaging system is its ability to clearly distinguish the thinner details of an image. To improve the spatial resolution in ultrasound imaging, it is necessary to drive the ultrasound probe with shorter excitations. However, shorter signals carry more high frequencies which are inevitably accompanied by a limitation of the penetration depth due to the attenuation effect. This phenomenon limits heavily the application field of high frequency ultrasound imaging to surface tissues such as the superficial layers of the epidermis and subcutaneous tissues.

1.2 Thesis objective

The main goal of this thesis is to provide an ultrasound imaging method that improves the image quality while keeping a good penetration depth in the tissue and a high frame acquisition rate.

The second objective is to implement the proposed method on different ultrasound research scanners, using different probe technologies.

The third goal is to study the nonlinear propagation of the ultrasound wave inside the imaged medium by applying the proposed method to second harmonic imaging based on ultrasound multi-pulse techniques.

1.3 Thesis organization

The manuscript is divided in the following five parts:

- Introduction part: Chapter I leads the readers into the topic of this thesis through a general introduction of medical ultrasound, thesis objective and its layout.
- Part I: This part corresponds to the state of the art and is divided in two chapters. Chapter II introduces the principles of the linear propagation of ultrasound waves, the objective being to provide the background necessary to understand ultrasound imaging. In this chapter is also detailed the nonlinear propagation of the ultrasound waves and an imaging technique (Pulse Inversion) that rely on this property of the medium called second harmonic imaging. In Chapter III, the existing transmission/reception schemes together with their corresponding beamforming methods are presented. In this chapter, are described also the different metrics used to evaluate the provided image quality. Finally, classical pulse compression is reminded as a method that allows increasing the image quality provided by the conventional ultrasound imaging.
- Part II: This part details the first contribution of the thesis following three chapters. Chapter IV presents the background of the proposed approach that increases the image quality of an ultra-fast acquisition scheme (plane wave imaging). The detailed process of generating the excitation signals (that allow boosting the bandwidth of the ultrasound transducer) and the corresponding compression filters is presented. Simulation results that overcome the performance of classical acquisition schemes are shown and discussed. Furthermore, the proposed imaging method is implemented on an ultrasound research scanner where it can be seen, through in-vitro / ex-vivo / in-vivo experiments, that the proposed approach outperforms the classical imaging methods. Experimental results obtained with two different probe technologies (piezoelectric and CMUT) are illustrated and discussed at the end of this chapter. In Chapter V, the impact of frequency dependent tissue attenuation effect on the method proposed in Chapter IV is addressed. An optimized technique that overcomes the previously stated effect is thereby proposed. Simulation and experimental results that prove the advantage of compensating the attenuation effects are displayed. Chapter VI presents how second harmonic imaging can be improved through the application of the optimized pulse compression technique presented in Chapter V to the pulse inversion technique. In-vitro results show the image quality enhancement when the proposed approach is used in comparison to classical pulse inversion.
- Part III: Here, the second contribution of the thesis is developed. In Chapter VII an implementation of the excitation signals / compression filters generated in Chapter V to a Multi-Line Transmit imaging technique is proposed. In addition, the compression filters are furthermore adapted in order to compensate the spatial impulse response of the employed ultrasound probe in Chapter VIII. Simulation and in-vitro/ex-vivo experimental results are displayed and show the impact of the proposed amelioration on the image quality. Chapter IX proposes to combine the advantages of enhanced chirp signals with the orthogonality properties of the Golay sequences. Furthermore, we apply thereby designed signals to a diverging wave compounding imaging technique and evaluate its performances by comparing the obtained image quality metrics to the classical way of acquiring diverging waves.

- Conclusion and perspectives part: Chapter X discusses and concludes the contributions of the thesis and gives some perspectives of the work.

PART I: STATE OF THE ART

Chapter II

ULTRASOUND GENERALITIES

Contents

2.1 Linear ultrasound

Ultrasound imaging is based on the propagation of ultrasound waves in a studied medium which is generally a biological tissue in medical imaging. The multiple density inhomogeneities of the medium cause the retro-diffusion of the incident waves towards the source, which makes it possible to characterize the internal structure of the insonified tissues.

2.1.1 The ultrasound wave

The physical phenomenon on which ultrasound imaging relies is the propagation of an ultrasonic acoustic wave [**Szabo (2004)**]. The difference between ultrasound and the classical audible sound comes from their higher frequencies $1\,MHz \leq f \leq 20\,MHz$ (in comparison to $20\,Hz \leq f \leq 20\,kHz$ for the audible sound). The velocity c of the acoustic wave, in the soft biological tissues of the human body composed mainly of water, is usually fixed at $c = 1540\,m.s^{-1}$. The wavelength λ reflects the spatial periodicity of the signal and is given by:

$$\lambda = \frac{c}{f}. \tag{1}$$

In medical ultrasound imaging, the value of the wavelength λ is therefore generally between 0.077 and $1.54\,mm$. The wavenumber k (expressed in m^{-1}) is related to the wavelength and is proportional to the number of oscillations. It is expressed by:

$$k = \frac{2\pi}{\lambda} = \frac{\omega}{c}, \tag{2}$$

where $\omega = 2\pi f$ is the wave pulsation expressed in $rad.s^{-1}$.

2.1.2 Propagation phenomenon

Ultrasounds are mechanical waves that propagate in a physical environment via the displacement of an acoustic pressure field P induced by the vibration of the particles of the medium, unlike electromagnetic waves (such as light), which can propagate in the void. The propagation of the ultrasonic wave is carried out step by step via a local mechanical compression of the medium, resulting in a local pressure variation. Three different propagations can be distinguished (Fig.1):

- Longitudinal waves (or compression waves), which oscillate in a parallel direction to the one of the propagation (Fig.1a);
- Transverse waves (or shear waves), which oscillate perpendicularly to the direction of propagation and are very quickly attenuated in soft biological tissues (Fig.1b);
- Surface waves, which propagate only at the interface of the medium and are also very quickly attenuated in soft biological tissues (Fig.1c).

In this work, only the compression waves are considered.

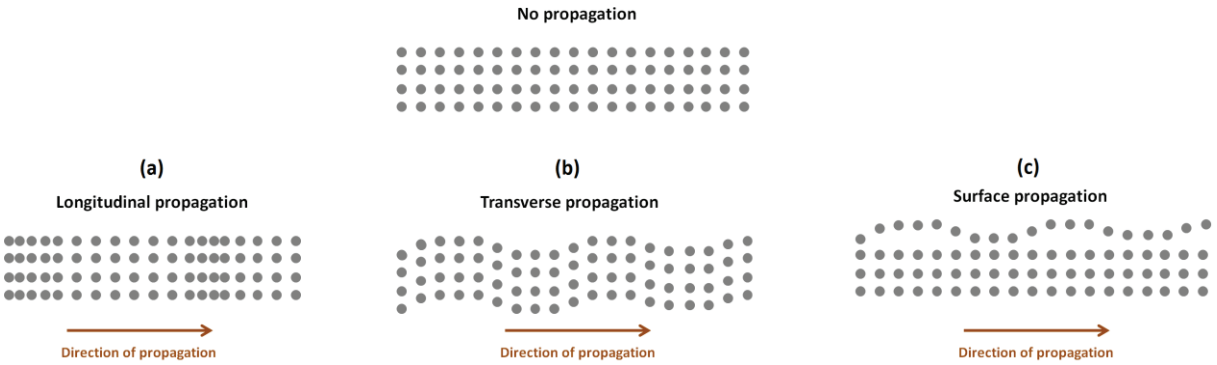

Fig.1: The different propagation modes, (a) longitudinal waves, (b) transverse waves, (c) surface waves.

2.1.3 Linear propagation

To fully understand where the ultrasound wave propagation equation comes from and how to find it, some variables as well as assumptions must be defined. If an object moves slowly in a fluid, the fluid flows around it. If the object moves rapidly, it produces a local displacement of the fluid, which leads to a local density variation. The change in density also corresponds to a change in pressure. Let us consider the example of a speaker diaphragm whose displacement produces a compression of the adjacent air layer (Fig.2)**.** In this situation, the surrounding air, having a pressure P_0 (atmospheric pressure) and a density $\rho_{0,}$ is subject to an acoustic disturbance. This experience generates a local pressure P and a local density ρ. To derive the linear wave equation the following three laws have to be considered:

- The conservation of the mass equation;
- The fluid equation of state;
- The Euler's equation.

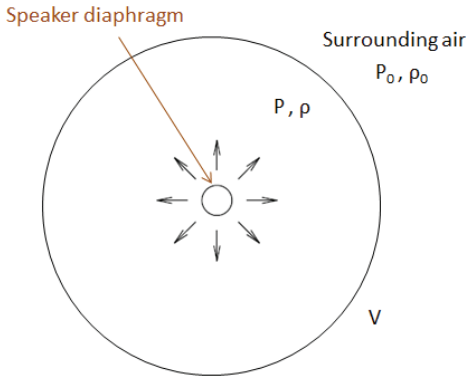

Fig.2: The volume of air (V) subject to an acoustic disturbance (due to a speaker diaphragm) generates the pressure P and density ρ. The ambient pressure of the surrounding air is denoted P_0 and its density ρ_0.

- **Conservation of the mass**

Let us consider a volume of fluid whose position in space is fixed. The mass flow across the surface encompassing this volume is given by:

$$\iint \rho\left(\vec{r},t\right)\vec{v}\left(\vec{r},t\right)\vec{n}\,dS \tag{3}$$

$\vec{n}$ denotes the vector normal to the surface at the point $\vec{r}$. In the absence of a source, the conservation of the mass imposes that this flux is equal to the mass variation in this same volume ($-\frac{\partial}{\partial t}\iiint_{V}\rho\left(\vec{r},t\right)d\tau$):

$$\iiint_{V}\left(\vec{\nabla}\cdot\left(\rho\vec{v}\right)+\frac{\partial\rho}{\partial t}\right)d\tau=0 \tag{4}$$

This leads to the local expression of mass conservation:

$$\vec{\nabla}\cdot\left[\rho\left(\vec{r},t\right)\vec{v}\left(\vec{r},t\right)\right]+\frac{\partial\rho\left(\vec{r},t\right)}{\partial t}=0 \tag{5}$$

In the presence of a source, a term $K\left(\vec{r},t\right)$ must be added in the right side of equation (5) (instead of 0). This term is homogeneous at a density per unit of time.

- **Fluid equation of state**

The equation of state describes the relationship between the pressure *P* and the density ρ. In the case of a perfect gas, the equation of state is written as:

$$P\left(\frac{1}{\rho}\right)^{\zeta}=constant \tag{6}$$

where ζ is the Laplace coefficient defined as the ratio of specific heats to constant pressure and volume respectively.

In the case of other fluids, one can use the Taylor expansion around the ambient density ρ_0. The following expression of the pressure P is then obtained:

$$P=P_0+\left(\rho-\rho_0\right)\left.\frac{\partial P}{\partial\rho}\right|_{s,\rho_0}+\left(\rho-\rho_0\right)^2\left.\frac{\partial P}{\partial\rho}\right|_{s,\rho_0}+\ldots \tag{7}$$

The indices *s* and ρ_0 indicate that the partial derivatives are computed with constant entropy in ρ_0.

- **The Euler's equation**

In general, a part of the acoustic energy is dissipated during the propagation. To write the equation of state, the thermal conduction that contributes to this dissipation should be neglected. The viscous losses associated to the relative motion of two adjacent portions of fluid are also neglected. Concretely, this results in supposing that the characteristic relaxation times of these two phenomena are much smaller than the acoustic period.

Let us apply the fundamental law of dynamics to a fluid particle that we follow in its motion. Its volume $dV=dx\,dy\,dz$ contains a mass $dm=\rho dV$. The force equation states that the force df acting on the fluid volume is equal to the acceleration *a* times the mass of the volume dm .

$$df=a\,dm \tag{8}$$

The component along the x-axis of the pressure forces acting on the fluid particle can be written as:

$$df_x = \left(P - \left[P + \frac{\partial P}{\partial x} dx \right] \right) dydz = -\frac{\partial P}{\partial x} dV \tag{9}$$

By writing the two other components (along *y* and *z*) of the force vector *df* in analogy with equation (9)**,** the net forces acting on the fluid can be generalized by:

$$df = -\nabla P dV \tag{10}$$

To determine the acceleration of one particle, it must be taken into account that its velocity depends on both the time and the position in the fluid. Thus, the acceleration is calculated as the particle derivative $D\vec{v} / Dt$ of the velocity with respect to time:

$$\vec{a} = \frac{D\vec{v}}{Dt} = \frac{\vec{v}(x+dx, y+dy, z+dz, t+dt) - \vec{v}(x,y,z,t)}{dt} \tag{11}$$

Knowing that: $\vec{v}(x+dx, y+dy, z+dz, t+dt) - \vec{v}(x,y,z,t) = \frac{\partial \vec{v}}{\partial x} dx + \frac{\partial \vec{v}}{\partial y} dy + \frac{\partial \vec{v}}{\partial z} dz + \frac{\partial \vec{v}}{\partial t} dt$ with $dx = v_x dt$, $dy = v_y dt$ and $dz = v_z dt$, the acceleration becomes:

$$\begin{aligned} \vec{a} &= \frac{D\vec{v}}{Dt} \\ \vec{a} &= \frac{\partial \vec{v}}{\partial t} + \left[\frac{\partial \vec{v}}{\partial x} v_x + \frac{\partial \vec{v}}{\partial y} v_y + \frac{\partial \vec{v}}{\partial z} v_z \right] \\ \vec{a} &= \frac{\partial \vec{v}}{\partial t} + \left[\vec{v} \cdot \vec{\nabla} \right] \vec{v} \end{aligned} \tag{12}$$

The term $\frac{\partial \vec{v}}{\partial t}$ defines local acceleration and $\left[\vec{v} \cdot \vec{\nabla} \right] \vec{v}$ convective acceleration. The equation of conservation of the momentum is thus written finally:

$$\rho \frac{\partial \vec{v}}{\partial t} + \rho \left(\vec{v} \cdot \vec{\nabla} \right) \vec{v} = -\vec{\nabla} P \tag{13}$$

- **The wave equation**

Here, the following assumption is made: the passage of the acoustic wave creates small differences of pressure, density and speed with respect to the equilibrium values. Therefore, only the terms of order 1 in the three previous equations are kept.

- Noting $\rho_a = \rho - \rho_0$ the excess of density, the conservation equation of mass can be written as **[Hamilton (1988)]**:

$$\rho_0 \vec{\nabla} \cdot \left[\vec{v}\left(\vec{r}, t \right) \right] + \frac{\partial \rho_a \left(\vec{r}, t \right)}{\partial t} = 0 \tag{14}$$

- The first-order state equation is given by $p = c^2 \rho_a$. So the conservation equation of the mass is deduced as follows:

$$\rho_0 \vec{\nabla} \cdot \left[\vec{v}\left(\vec{r},t\right) \right] + \frac{1}{c^2} \frac{\partial p\left(\vec{r},t\right)}{\partial t} = 0 \tag{15}$$

- Finally, the linearized Euler equation becomes **[Hamilton (1988)]**:

$$\rho_0 \frac{\partial \vec{v}}{\partial t} + \vec{\nabla} p = 0 \tag{16}$$

All the elements are gathered now to derive the linear wave equation. To obtain it, the temporal derivative of the conservation equation of the mass must be subtracted from the divergence of the Euler equation. The result of this operation gives:

$$\Delta p\left(\vec{r},t\right) - \frac{1}{c^2} \frac{\partial^2 p\left(\vec{r},t\right)}{\partial t^2} = 0 \tag{17}$$

- **Solution of the wave equation**

The general spherical wave solution to the previous equation is:

$$p\left(\vec{r},t\right) = \frac{1}{r} g\left(t - \frac{r}{c} \right) + \frac{1}{r} h\left(t - \frac{r}{c} \right) \tag{18}$$

where *r* is the distance (radial) between the origin point and the considered point. *g* and *h* are arbitrary functions. By developing (18), one can have access to the pressure field expression in each point $\vec{r}$:

$$p(\vec{r},t) = P_0 e^{j(\omega t - \vec{k}\vec{r})} + P_0^{'} e^{j(\omega t + \vec{k}\vec{r})} \tag{19}$$

where P_0 is the amplitude of the propagating wave in the direction z and $P^{'}_0$ the amplitude of the returning wave (in the direction - z). Let us say that the phase term can also be expressed as (20), in which appears a fraction representing the travel time at the speed of the ultrasound wave

$$\omega t - \vec{k}\vec{r} = \omega\left(t - \frac{r}{c} \right) \tag{20}$$

In practice, it is common to model the pressure as the real part (note Re ()) of the progressive wave:

$$p(\vec{r},t) = P_0 \times \mathrm{Re}\left(e^{j(\omega t - \vec{k}\vec{r})} \right) = P_0 \cos(\omega t - \vec{k}\vec{r}) \tag{21}$$

2.1.4 Transmission and reflection of an ultrasound wave

Each medium is characterized by its acoustic impedance Z (expressed in $kg^{-2}.s^{-1}$) which is a function of the wave propagation speed *c* and of the medium density ρ:

$$Z = \rho c \tag{22}$$

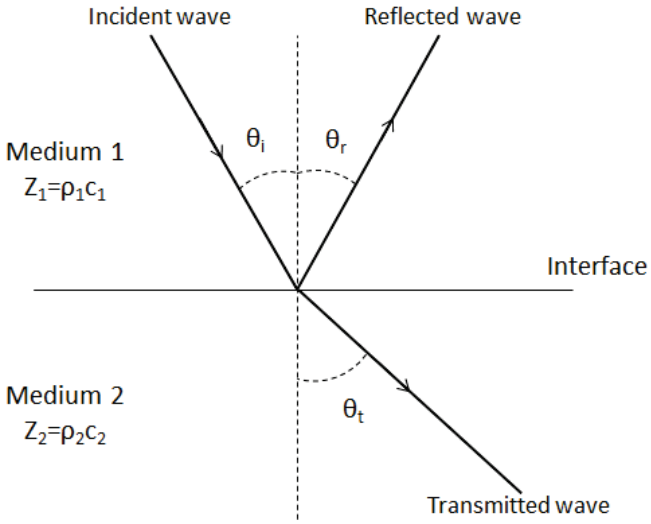

Fig. 3: Illustration of the incident reflected and transmitted pressure wave between two different medium.

When an ultrasound wave arrives at the interface between two different media, characterized by two different acoustic impedances Z_1 and Z_2, it generates a reflected and a transmitted wave (Fig.3). The relationship between the angles of incidence, reflection, and transmission is given by the law of Snell Descartes:

$$\theta_r = \theta_i , \tag{23}$$

$$Z_1 \sin(\theta_i) = Z_2 \sin(\theta_t) . \tag{24}$$

Following (21), let us express the pressure before the interface which takes into account the incident and the reflected wave.

$$p_1(\vec{r},t) = P_0 e^{j(\omega t - \vec{k_1}\vec{r})} + \tilde{r} P_0 e^{j(\omega t - \vec{k_1}\vec{r})} , \tag{25}$$

where $\tilde{r}$ is the reflection coefficient being the ratio between $P_0/P_0^{'}$ from equation (19). The pressure of the transmitted wave after the interface is given by:

$$p_1(\vec{r},t) = \tilde{t} P_0 e^{j(\omega t - \vec{k_2}\vec{r})} , \tag{26}$$

where $\tilde{t}$ is the transmission coefficient in the second medium. The conditions of continuity of the pressure and of the particle velocity at the interface result in:

$$\left[p_1(\vec{r},t) \right]_{r=0} = \left[p_2(\vec{r},t) \right]_{r=0} \quad \Rightarrow \quad 1 + \tilde{r} = \tilde{t} \tag{27}$$

where $p_2(\vec{r},t)$ is supposed to be the pressure after the interface which takes into account only the transmitted wave.

$$\left[\frac{1}{\rho_1} \frac{\partial p_1(\vec{r},t)}{\partial r} \right]_{r=0} = \left[\frac{1}{\rho_2} \frac{\partial p_2(\vec{r},t)}{\partial r} \right]_{r=0} \quad \Rightarrow \quad 1 - \tilde{r} = \frac{Z_1 \cos(\theta_t)}{Z_2 \cos(\theta_i)} \tilde{t} \tag{28}$$

By combining these two continuity conditions, the reflection and the transmission coefficients can be deduced:

$$\tilde{r} = \frac{Z_2 \cos(\theta_i) - Z_1 \cos(\theta_t)}{Z_2 \cos(\theta_i) + Z_1 \cos(\theta_t)} \quad ; \quad \tilde{t} = \frac{2Z_2 \cos(\theta_i)}{Z_2 \cos(\theta_i) + Z_1 \cos(\theta_t)}. \tag{29}$$

When the incidence is normal to the interface, $\theta_i = \theta_r = \theta_t = 0$. (29) becomes:

$$\tilde{r} = \frac{Z_2 - Z_1}{Z_2 + Z_1} \quad ; \quad \tilde{t} = \frac{2Z_2}{Z_2 + Z_1}. \tag{30}$$

The intensity coefficients of reflection R and of transmission T are defined, in this particular case, by **[Ziomek (1995)]**:

$$\begin{aligned} R &= \tilde{r}^2 = \left(\frac{Z_2 - Z_1}{Z_2 + Z_1} \right)^2, \\ T &= 1 - R = \frac{4Z_1 Z_2}{(Z_2 + Z_1)^2} \end{aligned} \tag{31}$$

By analyzing (31), one can notice that three particular cases can be separated:

- When $Z_1 \gg Z_2$, we have T ≈ 0 and R ≈ 1, implying that all the pressure wave is reflected in the initial medium;
- When $Z_1 \approx Z_2$, we have T ≈ 1 and R ≈ 0, meaning that the entire pressure wave is transmitted (refracted) in the second medium;
- For all other values of Z_1 and Z_2, both a refracted and a reflected wave are generated.

The energy transmitted through an interface between two media having two very different acoustic impedance coefficients is very low. Fortunately, since biological tissues and blood are mainly composed of water and have limited impedance variations, the interface between these two environments do not alter a lot the transmitted energy of the ultrasound wave. In addition, in the context of medical ultrasound, an aqueous gel is applied to the probe in order to avoid air interface and adapt the impedance between the piezoelectric material of the probe and the images tissue. This impedance adaptation allows the ultrasound waves to penetrate the tissue without being reflected by the air in contact with the skin.

2.1.5 Ultrasound wave scattering

In the case of medical ultrasound imaging, biological tissues are not perfect homogeneous media. Indeed, they are composed of multiple inhomogeneities, smaller than the ultrasonic wavelength, randomly distributed [**Meunier (1995)**]. Each of these small inhomogeneities, when insonified by the incident acoustic wave, becomes a point source that reemit a spherical wave in all directions of space (Fig.4). A part of the echoes generated by the set of reflectors are thus retro-diffused towards the ultrasound probe, and their analysis allows the characterization of the internal tissues structure. The amplitude of the received signal is determined by the echogenicity of the imaged medium.

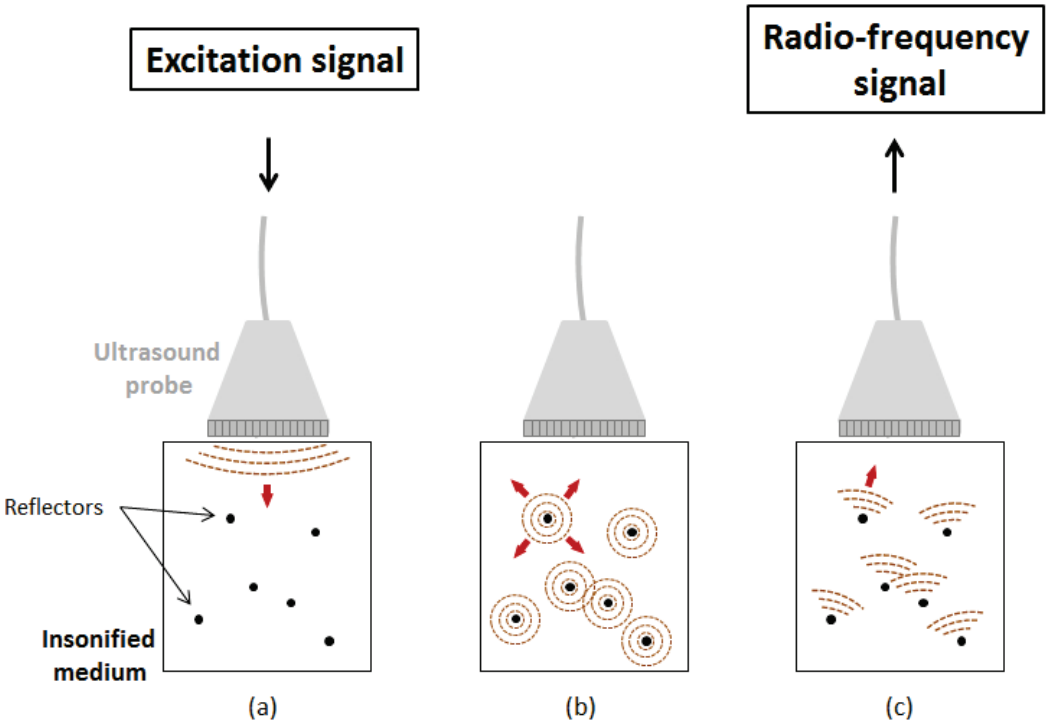

Fig.4: Transmission and diffuse reflection of the ultrasonic wave. (a) A pulsed electrical signal excites the ultrasonic probe and causes the creation of an incident wave propagating in the medium. (b) In contact with the incident wave, the multiple reflectors backscatter a spherical wave. (c) The backscattered echoes are received by the probe and converted into an electrical signal known as radiofrequency.

The imaged tissues can be seen as homogenous media of mean density ρ_0 that contain small density variations ($\Delta\rho(\vec{r})$) randomly distributed as a function of the position $\vec{r}$. Since the propagation speed of sound inside soft tissues ($c(\vec{r})$) depends directly on the density of the medium ($\rho_0(\vec{r})$), $c(\vec{r})$ is also spatially variable following the evolution of $\rho_0(\vec{r})$. In such conditions one can write the following relations:

$$\begin{aligned}\rho_0(\vec{r}) &= \rho_0 + \Delta\rho_0(\vec{r}) \\ c_0(\vec{r}) &= c_0 + \Delta c_0(\vec{r})\end{aligned} \tag{32}$$

The presence of such small impurities in the density field of the medium generates what is called the acoustic scattering. This phenomenon can be modeled by adding to the acoustic wave propagation equation (17) the scattering operator [**Jensen (1991)**]. Therefore, (17) becomes:

$$\Delta p\left(\vec{r},t\right) - \frac{1}{{c_0}^2}\frac{\partial^2 p\left(\vec{r},t\right)}{\partial t^2} = -\frac{2\Delta c_0(\vec{r})}{{c_0}^3}\frac{\partial^2 p\left(\vec{r},t\right)}{\partial t^2} + \frac{1}{\rho_m}\nabla[\Delta\rho_0(\vec{r})]\cdot\nabla p_1(\vec{r},t) \tag{33}$$

Where ∇ represents the gradient operator. Indeed, in the previous relation one can see that if the medium is perfectly homogeneous ($\Delta c_0(\vec{r}) = 0$ and $\Delta\rho(\vec{r}) = 0$), this relation becomes equivalent to (17).

Suppose now that the acoustic wave is transmitted by a piezoelectric transducer of surface S_e and that the scattered echoes are measured by a transducer of surface S_r. As it was shown in [**Jensen (1991); Jensen (1992)**], the expression of the received electrical signal by S_r (that verifies the propagation equation (33)) when S_e is excited using an excitation $a(t)$ can be written as follows:

$$y(t) = h_e(t) *_t a(t) *_t h_r(t) *_t TRF(\vec{r}) *_{\vec{r}} h_{er}(\vec{r},t) \tag{34}$$

Where $h_e(t)$ and $h_r(t)$ are the electro-acoustical impulse responses of the transducers S_e and S_r respectively. In (34), the $TRF(\vec{r})$ stands for the Tissue Reflectivity Function of the medium and represents the distribution of the scatterer amplitude as a function of the position $(\vec{r})$. $h_{er}(\vec{r},t)$ is the pulse echo spatial impulse response of the two transducers at a point r and is defined as follows[**Jensen (1991); Jensen (1992)**]:

$$h_{er}(\vec{r},t) = h_e(\vec{r},t) *_t h_r(\vec{r},t) \qquad \text{with}: \begin{cases} h_e(\vec{r},t) = \int_{S_e} \dfrac{\delta\left(t - t_e - \dfrac{\left\|\vec{r} - \overrightarrow{r_{S_e}} - \overrightarrow{r^0_{S_e}}\right\|_2}{c_0}\right)}{2\pi\left\|\vec{r} - \overrightarrow{r_{S_e}} - \overrightarrow{r^0_{S_e}}\right\|_2} d^2\overrightarrow{r_{S_e}} \\ h_r(\vec{r},t) = \int_{S_r} \dfrac{\delta\left(t - \dfrac{\left\|\vec{r} - \overrightarrow{r_{S_r}} - \overrightarrow{r^0_{S_r}}\right\|_2}{c_0}\right)}{2\pi\left\|\vec{r} - \overrightarrow{r_{S_r}} - \overrightarrow{r^0_{S_r}}\right\|_2} d^2\overrightarrow{r_{S_r}} \end{cases} \tag{35}$$

where $\overrightarrow{r^0_{S_e}}$ and $\overrightarrow{r^0_{S_r}}$ are the vector positions of the surfaces S_e and S_r origins respectively. t_e is the transmission delay of the source. In (35), $h_e(\vec{r},t)$ and $h_r(\vec{r},t)$ can be referred to as the spatial impulse responses of the respective transducers in transmission and reception respectively.

2.2 Nonlinear ultrasound

The linear propagation of an ultrasound wave in a given medium is an approximation of the reality. Indeed, the ultrasound propagation is a nonlinear process and the conservation of the momentum in (13) has to be considered (instead of (16) in the linear case). The difference is that (13) introduces the convective acceleration term $\left(\vec{v}\cdot\vec{\nabla}\right)\vec{v}$, which represent the nonlinear effect of the medium.

2.2.1 Nonlinear parameters

In order to express the evolution of the pressure wave as a function of the density, the pressure is expanded using the Taylor series **[Beyer (1960)]**:

$$p - p_0 = \left(\frac{\partial p}{\partial \rho}\right)_s (\rho - \rho_0) + \frac{1}{2!}\left(\frac{\partial^2 p}{\partial \rho^2}\right)_s (\rho - \rho_0)^2 + \frac{1}{3!}\left(\frac{\partial^3 p}{\partial \rho^2}\right)_s (\rho - \rho_0)^3 + \ldots \quad (36)$$

By using the five following notations in (37):

$$\begin{cases} p' = p - p_0 \\ \rho' = \rho - \rho_0 \end{cases} \quad \text{and} \quad \begin{cases} A = \rho_0 \left(\frac{\partial p}{\partial \rho}\right)_s \equiv \rho_0 c_0 \\ B = \rho_0^2 \left(\frac{\partial^2 p}{\partial \rho^2}\right)_s \\ C = \rho_0^3 \left(\frac{\partial^3 p}{\partial \rho^3}\right)_s \end{cases} \quad (37)$$

where c_0 is the equilibrium celerity of the ultrasound wave in the tissue (expressed in $m.s^{-1}$). Thus, (36) can be written as:

$$p' = A\left(\frac{\rho'}{\rho}\right) + \frac{B}{2!}\left(\frac{\rho'}{\rho}\right)^2 + \frac{C}{3!}\left(\frac{\rho'}{\rho}\right)^3 + \ldots \quad (38)$$

By analyzing (38), one can notice that if only the parameter A is kept, the development is equivalent to the linear propagation theory. Since parameter B is assumed to be not equal to zero, the relationship between the pressure and the density is nonlinear. The nonlinear parameter is defined as the ratio between the coefficients B and A. Its expression depends on the celerity, the density and the pressure:

$$\frac{B}{A} = \frac{\rho_0}{c_0^2}\left(\frac{\partial^2 p}{\partial \rho^2}\right)_s \quad (39)$$

The nonlinear parameter is directly linked to the velocity of the pressure wave through the following expression:

$$c = c_0 \left(1 + \frac{B}{2A}\frac{v}{c_0}\right)^{\frac{2A}{B}+1} \quad (40)$$

By assuming that v / c_0 is very small in comparison to 1, the velocity is usually simplified, using a Taylor series on (40), as:

$$c = c_0 + \left(1 + \frac{B}{2A}\right)v \quad (41)$$

The nonlinear coefficient of the medium, noted β, is then defined as:

$$\beta = 1 + \frac{B}{2A} \quad (42)$$

This nonlinear coefficient is linearly linked to the nonlinear parameter B / A. One can also deduce the expression that links the velocity to the nonlinear coefficient of the medium:

$$c = c_0 + \beta v \quad (43)$$

2.2.2 Interpretation of the nonlinear effect

Equation (41) demonstrates that the nonlinearity has an effect on the velocity of the pressure wave. Using the definition of the particle velocity $v = P/(\rho_0 c_0)$, the celerity variation Δc can be written as:

$$\begin{aligned} c = c_0 + \beta \frac{P}{\rho_0 c_0} \quad &\Rightarrow \quad c - c_0 = +\beta \frac{P}{\rho_0 c_0} \\ &\Rightarrow \quad \Delta c = +\beta \frac{P}{\rho_0 c_0} \end{aligned} \tag{44}$$

Thus it can be deduced that the celerity varies during the propagation and its ripples are proportional to the local pressure and to the nonlinearity of the considered medium.

During the propagation of the wave, two different phenomena appear. A compression effect that is obtained for a positive pressure variation and a dilatation effect that is obtained for a negative pressure variation. The corresponding celerities of these two effects, noted respectively c^+ and c^-, are expressed as:

$$c^{\pm} = c_0 \pm \frac{\beta}{\rho_0 c_0} P \tag{45}$$

The analysis of equation (45) demonstrates that the high pressure part of the wave (compression part) travels faster than the low pressure wave (dilatation part) (Fig.5a). Fig.5b shows, in simulation, the distortion of the ultrasound wave after its propagation in a nonlinear medium. Their corresponding Fourier spectra confirm the deformation of the ultrasound wave. Indeed, the spectrum of the initial ultrasound signal presents only a fundamental component (Fig.5c), while the spectrum of the deformed wave generates both a fundamental and a harmonic components (Fig.5d).

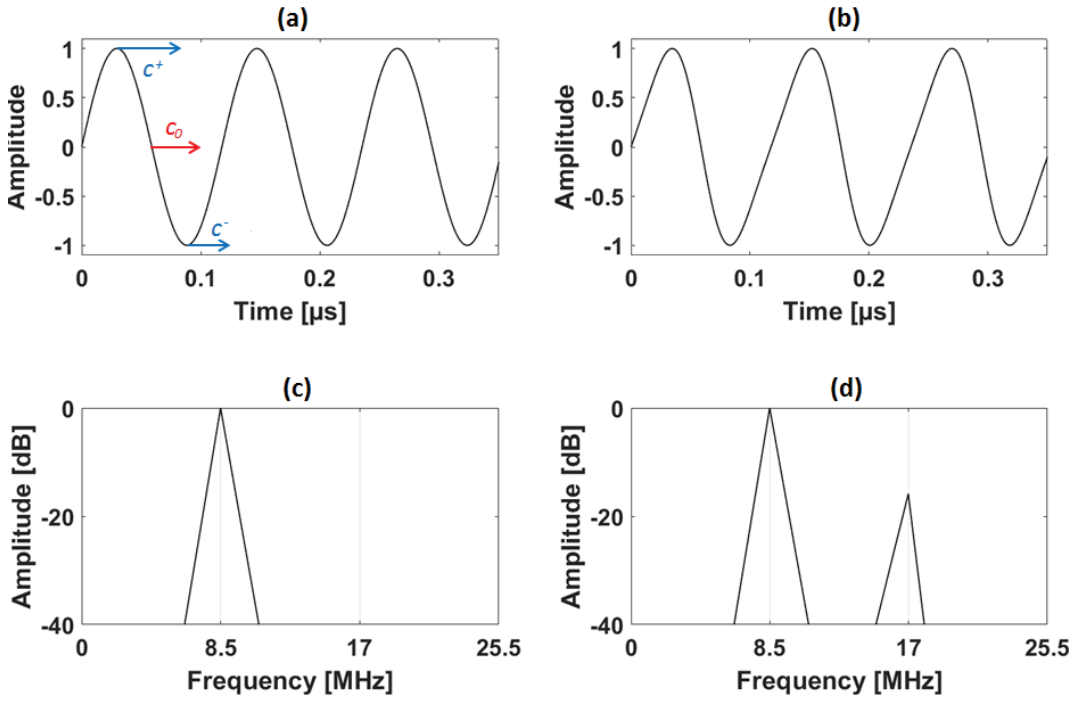

Fig.5: (a) A signal that contains three sinusoid cycles at 8.5 MHz. (b) the same sinusoidal signal created in (a) after its distortion due to nonlinear effects. (c) Fourier spectrum of the signal in (a) which present only a

fundamental component. (d) Fourier spectrum of the signal in (b) which present both fundamental and second harmonic components.

2.2.3 Burgers equation

After determining the expression of the celerity as a function of the nonlinear coefficient, the work can be focused now on the resolution of the propagation equation in the presence of a nonlinear effect.

- Lossless Burgers equation

In a lossless medium without viscosity, the propagation of a plane wave pressure is defined by the lossless Burgers equation [**Beyer (1974)**]:

$$\frac{\partial p}{\partial z} = \frac{\beta p}{\rho_0 c_0^3}\frac{\partial p}{\partial \tau} \tag{46}$$

where z is the propagation direction and τ (expressed as: $\tau = t - \left(z / c_0\right)$) is the delayed time. [**Fubini (1935)**] proposed the following solution of this equation:

$$p\left(z,\tau\right) = p_0 \sum_{n=1}^{\infty} \frac{2}{n\phi} J_n\left(n\phi\right)\sin\left(n\omega_0\tau\right) \tag{47}$$

where n is the number of the considered harmonic, ω_0 is the central angular frequency of the transmitted signal, J_n is the Bessel function of n^{th} order and ϕ is a dimensionless distance that is related to the medium parameters as follows:

$$\phi = \frac{\omega_0 \beta p_0}{\rho_0 c_0^3} z\,. \tag{48}$$

- Complete Burgers equation

The equation presented previously is an approximation of the reality, because of the non-dissipative hypothesis assumption made on the considered waves. When ultrasound waves propagate inside a medium, they are exposed naturally to the absorption phenomenon. This effect converts ultrasound energy into heat because of the thermos-viscous dissipation. The previous Burgers equation can then be extended as follow [**Beyer (1974)**]:

$$\frac{\partial p}{\partial z} = \frac{\psi}{2c_0^3}\frac{\partial^2 p}{\partial \tau^2} + \frac{\beta p}{\rho_0 c_0^3}\frac{\partial p}{\partial \tau} \tag{49}$$

where ψ is the diffusivity of sound and is a combination of different thermo-viscous dissipation effects. The complete Burgers equation is the simplest model describing the combined effects of the nonlinearity and losses on the ultrasound wave propagation.

2.2.4 KZK equation

The proposed propagation equation described previously does not take into account the finite size of the transducer generating the ultrasound wave. By taking into account the finite size of the transmitter, the diffraction of the transducer is naturally considered during the propagation. The previous Bergers

equation is then replaced by the KZK equation, expressed as [**Kuznetsov (1970); Zabolotskaya (1969)**]:

$$\frac{\partial p}{\partial z} = \Delta_{\perp} p + \frac{\psi}{2c_0^3}\frac{\partial^2 p}{\partial \tau^2} + \frac{\beta p}{\rho_0 c_0^3}\frac{\partial p}{\partial \tau} \tag{50}$$

where $\Delta_{\perp} p$ is the diffraction's effect of the transducer. Because $\Delta_{\perp} p$ defines the focalization pattern due to the shape of the probe, its expression depends intrinsically on the geometric parameters of the ultrasound probe.

- For a circular piston source with a circular elements having a r_{el} radius:

$$\Delta_{\perp} p = \int_{-\infty}^{\tau} \left(\frac{\partial^2 p}{\partial r_{el}^2} + \frac{1}{r_{el}}\frac{\partial^2 p}{\partial r_{el}^2} \right) \partial \tau' \tag{51}$$

- For a linear piston source where (x, y) are the lateral and the elevation dimension of the probe:

$$\Delta_{\perp} p = \int_{-\infty}^{\tau} \left(\frac{\partial^2 p}{\partial x^2} + \frac{\partial^2 p}{\partial y^2} \right) \partial \tau' \tag{52}$$

2.2.5 Multi-pulse techniques

As previously showed, when an ultrasound wave propagates inside a nonlinear medium, the wave is subject to a gradual deformation and thus generates harmonics. Harmonic imaging can then be applied to nonlinear tissues. This imaging technique has several advantages in comparison to conventional imaging, including improvement of the axial resolution and reduction of artefacts.

However, in conventional harmonic imaging if a short pulse (that has a broadband frequency spectrum) is transmitted, there is an inevitable spectral overlap between the fundamental and harmonic components. To better detect harmonic echoes, a multiple-cycle pulse (that has a narrowband frequency spectrum) should be transmitted, which unfortunately causes the deterioration of the imaging resolution **[Frinking (2000); Chiao (2003)].**

To overcome the trade-off between contrast detectability and imaging resolution in conventional harmonic imaging, many multi-pulse techniques have been developed. Most of them modulate the transmission/reception frequency, pulse amplitude, pulse phase, pulse duration, number of pulses, Pulse Repetition Frequency (PRF).

Assuming the transmitted acoustic wave is:

$$p_{tr}(t) = P_{TR}\, e^{j\omega_0 t + \varphi_0} \tag{53}$$

where P_{TR} and φ_0 represent the amplitude of the wave and the phase respectively. The received wave $p_{re}(t)$ is expressed using polynomial expansion of a basis waveform for the nonlinear components, noted q_0 [**Haider (2001)**]:

$$p_{re}(t) = a_1 q_0(t) + a_2 q_0^2(t) + \ldots + a_N q_0^N(t) = \sum_{n=1}^{N} a_n q_0^n(t) \tag{54}$$

where a_n is the weight of the n^{th} order nonlinear component and N is the presumed model order. a_n is a complex term depending on the tissue, on the frequency and on the amplitude of the transmitted wave. The waveform q_0 also depends on the transmitted wave p_{tr}. In a linear system, only a_1 is kept in (54).

In the frequency domain, the time domain multiplication $q_0^N(t)$ that appears in (54) becomes *n*-times auto-convolution of the spectrum of the linear term q_0 centred in ω_0 (Fig.6).

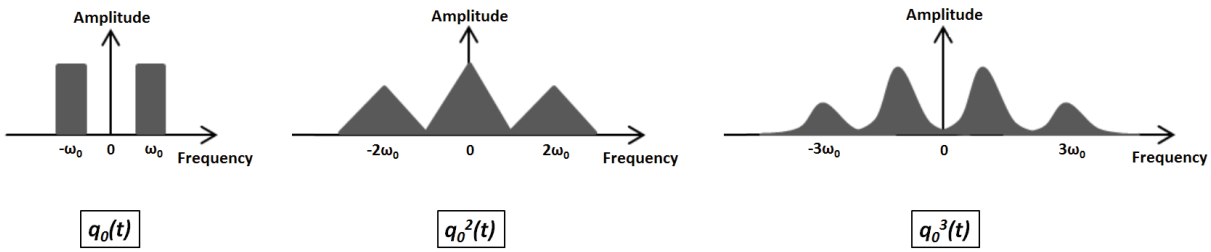

Fig.6: Illustration of n-times auto-convolution of the spectrum of q_0.

These successive convolutions result in both spectra components of the frequency band centred in $n\omega_0$ and of the lower frequency band. This means that the final signal level of the n^{th} frequency band is given by the n^{th} -order nonlinear component and by the higher order nonlinear components. In (54), odd nonlinear components create spectrum at odd multiples of ω_0 components, and non-linear components of the same order create spectral components at even multiples of ω_0 [**Haider (2001); Eckersley (2005)**]. This property shows the possibility to increase or decrease the specific nonlinear component in one frequency band using multi-pulse transmission techniques. Let us suppose a total number of L pulse transmissions which propagates inside a given medium. The l^{th} transmitted pulse p_{tr}^l and the basic waveform p_{tr} are related by the term b_l through the following expression:

$$p_{tr}^l(t) = b_l P_{TR}\, e^{j\omega_0 t + \varphi_0}$$
$$\text{where: } b_l = |b_l| e^{j\varphi_l} \quad \text{with, } \begin{cases} \varphi_l \in [0, 2\pi] \\ l = 1, 2, \ldots, L \end{cases} \tag{55}$$

After the propagation, the received echoes are multiplied by a weighted vector c_l and summed. The general expression for L pulse transmissions is given by:

$$p_{sum}(t) = \sum_{l=1}^{L} c_l \left(\sum_{n=1}^{N} a_n b_l^n q_0^n(t) \right) \tag{56}$$

The coefficients b and c given in (57) control the fact of being able to improve or decrease (to even cancel) certain nonlinear components.

$$\begin{cases} b = (b_1, \ldots, b_L) \\ c = (c_1, \ldots, c_L) \end{cases} \tag{57}$$

To make this dependency (on the coefficients b and c) more evident, one can rewrite (56) as follows:

$$p_{sum}(t) = \sum_{n=1}^{N}\left(\sum_{l=1}^{L} c_l b_l^n\right) a_n q_0^n(t) \tag{58}$$

where $\sum_{l=1}^{L} c_l b_l^n$ is the weight of the n^{th} nonlinear component in the final summed signal.

2.2.5.1 Pulse Inversion (PI)

In pulse inversion (PI), a sequence of two phase inverted pulses is transmitted **[Hwang (1999); Simpson (1999)]**. For a linear system, the response to the second pulse is an inverted copy of the response to the first one and the sum of the two responses is zero. For a non-linear system, the sum is not zero. PI uses the entire bandwidth of the received echo signal and achieves better image resolution. In PI, $\varphi_{PI} = \pi$ is the phase shift between the two transmitted pulses. The obtained values of b and c in this case are **[Lin (2015)]**:

$$\begin{cases} b = (1, e^{j\varphi_{PI}}) = (1, e^{j\pi}) \\ c = (1,1) \end{cases} \tag{59}$$

The summation of the two received signals can be written as:

$$p_{sum}(t) = \sum_{n=1}^{N}\left(1 + e^{jn\pi}\right) a_n q_0^n(t) \tag{60}$$

By analyzing (60), one can notice that when n is odd $e^{jn\pi} = -1$ and when n is even $e^{jn\pi} = 1$. This means that every odd nonlinear component is canceled and every even nonlinear component is doubled.

Chapter III

MATERIALS AND METHODS

Contents

3.1 Echographic material

- Ultrasound scanner

Medical ultrasound images are acquired using an ultrasound system. It is generally composed of a probe for transmitting and receiving the acoustic waves, a console for selecting the parameters, a computer system for constructing the images, an acquisition card for performing the analog-to-digital conversion signals, and a screen for visualizing images and parameters (Fig.7).

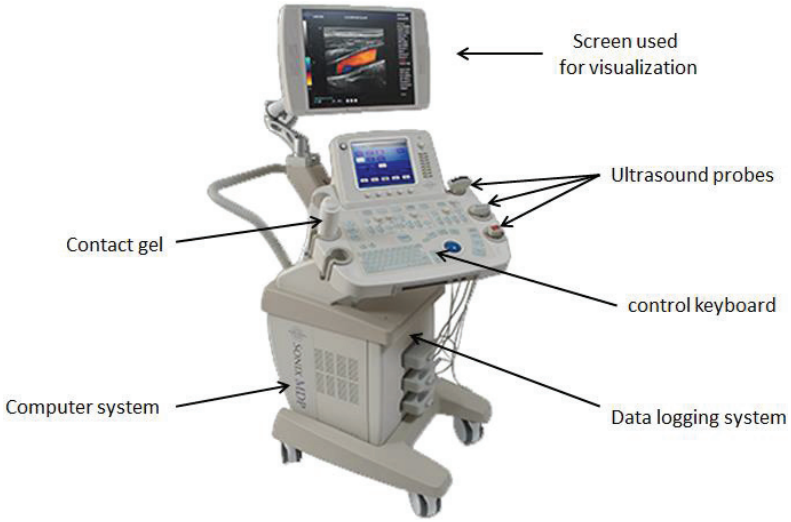

Fig.7: Ultrasound scanner, SonixMDP (Ultrasonix Medical Corporation).

- Ultrasound probe

There are several categories of probes with different geometries and characteristics. This work focuses on the linear probe, well adapted to major types of clinical examinations. This probe consists of a single row of small sensors, aligned longitudinally (Fig.8). The length of a linear probe is of the order of 5 cm, and the number N of elementary sensors is generally between 64 and 256.

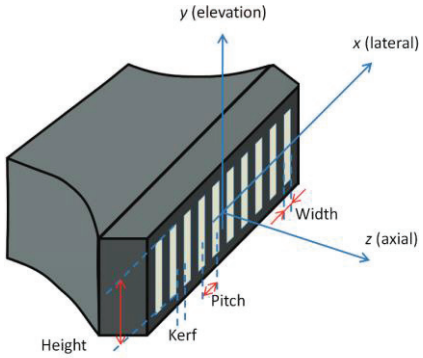

Fig.8: Geometrical description of a linear array probe.

The geometry of the probe, shown in Fig.8, is characterized by the width and the height of each sensor element. It is also characterized by the space separating two neighboring elements (called kerf, usually between 20 and 40 µm) as well as the center-to-center space between two neighboring sensors (called pitch, usually between 250 and 500 µm). Due to the rectilinear arrangement of the elements of the linear probe, the acquired image corresponds to a bi-dimensional section along the radial and longitudinal directions of the space. The height of the elements in the azimuthal direction (around 3

mm) is small compared to the other two dimensions of the reconstructed image (approximately 30 mm), and makes it possible to consider that the thickness is negligible in this direction . This is why, in our context, a bi-dimensional representation (along the radial and longitudinal directions) is used to describe ultrasound imaging. Depending on the principle of manufacturing, different probe technologies are distinguishable:

- Piezoelectric probes:

Each elementary sensor of the probe is a ceramic crystal having the property of converting an electrical signal into a mechanical deformation, and vice versa, according to the piezoelectric principle. A picture of a linear piezoelectric probe (model LA523E) is shown in Fig.9a.
The transmission of an acoustic wave exploits the inverse piezoelectric effect, by exciting the elements of the probe with an electric pulse at a given frequency, generating the mechanical resonance of the elements and the propagation of a vibration inside the scanned medium. Unlike the transmission, the reception of an acoustic wave uses the direct piezoelectric effect, collecting the raw electrical signal generated by the element exposed to the pressure wave backscattered by the medium.

- CMUT (Capacitive Micromachined Ultrasonic Transducers) probes:

The basic element of a CMUT probe (Fig.9b) is a capacitor cell with a fixed electrode (backplate) and a free electrode (membrane). The principle of operation is the well-known electrostatic transduction mechanism. If an alternating voltage is applied between the membrane and the backplate, the modulation of the electrostatic force results in membrane vibration with generation of ultrasounds. Conversely, when the membrane is subjected to an incident ultrasonic wave, the capacitance change can be detected as a current or voltage signal. A DC bias voltage must be used in reception for signal detection, and it is required in transmission for linear operation. In addition, both the transmit and the receive sensitivities increase with increasing the bias voltage.
The main advantages of CMUTs compared to piezoelectrics are the better acoustic matching to the propagation medium, resulting in wider immersion bandwidth and improved image resolution, the ease of fabrication, the ability to be integrated with electronic circuits on the same wafer, and the expected reduction of production costs.

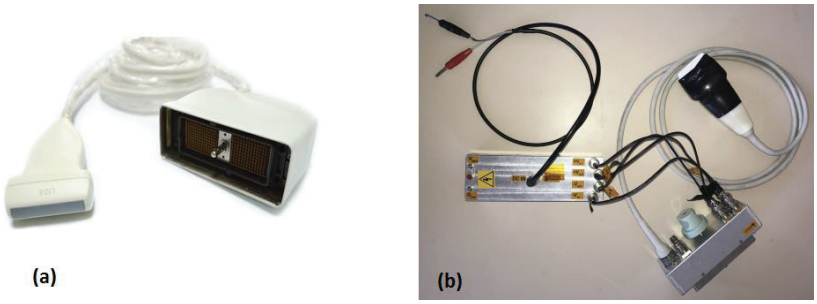

Fig. 9: Linear piezoelectric (a) and linear prototype CMUT (b) probe.

3.2 Image formation

In ultrasound imaging, the echoes propagation is based on the model described in Chapter 2. From the initial transmitted ultrasound wave, the different scatterers of the scanned medium backscatter echoes to the ultrasound probe. By using the ultrasound probe in reception mode, (which means that

the probe records the pressure that hits its surface and converts it in an electrical signal) an image is created. Indeed, all the scatterers reemit waves that arrive at different times to the probe surface according to scatterrer position. The sum of these different echoes gives this noisy aspect visible in the resulting image (also called "speckle").

The conventional (Focused) ultrasound image is obtained by applying the following steps. First, a sub-part of the ultrasound probe is selected and only this part of the transducer transmits the ultrasound wave in the medium. From the global pressure waves backscattered by the medium, each active transducer of the probe records the echoes and creates what is called a RF signal. By juxtaposing these signals together, the pre-beamformed RF image is obtained. Using a beamforming strategy in reception, the elementary RF image is combined into one signal called: post-beamformed RF line. Then, by changing the sub-part of the used probe, different post-beamformed RF lines are created and correspond to different part of the medium. The final post-beamformed RF image is obtained using all these lines together.

However, the RF image, despite the quantity of information it contains, is difficult to visualize because of the backscattered echoes are sinusoidal oscillations at the transmitted frequency (Fig.10a). To visualize the image, it is necessary to demodulate the signal around a lower frequency that contains less information compared to the RF signal. This demodulation generally is conducted in two steps, first a multiplication with a sinusoid centred at the frequency of the emitted wave, is conducted. Then a low pass filter is applied on the intermediate result. The absolute value of an Hilbert transform can also be used. The resulting image, called the B-mode image, proposes an interpretable image (Fig.10b). To reduce the dynamic of the image and to highlight the different regions, a log-compression is used. In the resulting image, where the amplitude is expressed in *dB*, all the structures are finally visible and the user has the possibility to choose the dynamic for the display (Fig10.c).

To compensate the attenuation effect present in the tissues, a Time Gain Compensation (TGC) function is used. The TGC increases synthetically the amplitude of the backscattered echoes as a function of the depth in order to compensate the loss due to the attenuation. For instance, a TGC of *1 dB.cm*$^{-1}$ increases the dynamic by *1 dB* each centimeter.

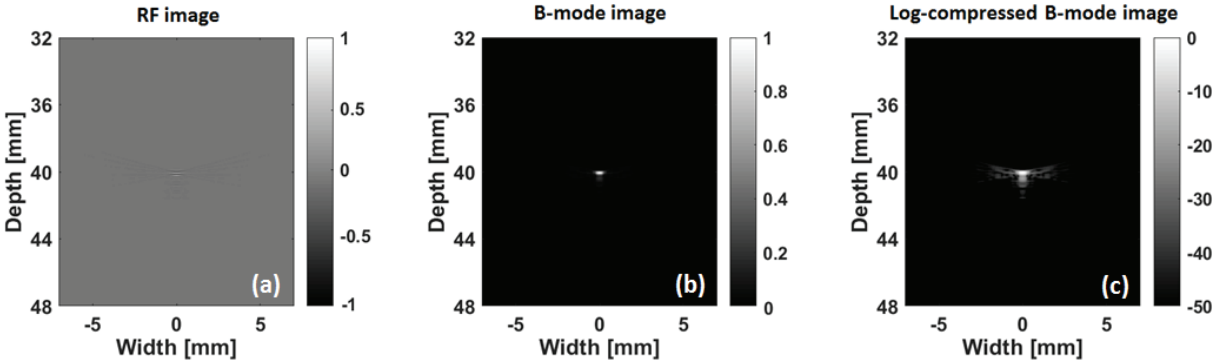

Fig.10: Illustration of the different simulated ultrasound images obtained from a point target: (a) the post beamformed RF image, (b) the B-mode image before log-compression and (c) the log-compressed B-mode image.

In Fig.11 are displayed the typical obtained images of a medium containing a high density of scatters. In this case, the imaged medium has *110 scatt./mm*$^{-2}$ and contains a hypoechoic cyst of radius *8 mm* placed at *40 mm* depth. In Fig11.c is shown the regions of interest used for the calculation of the image signal to-noise-ratio and the contrast to-noise-ratio (defined in part 3.3).

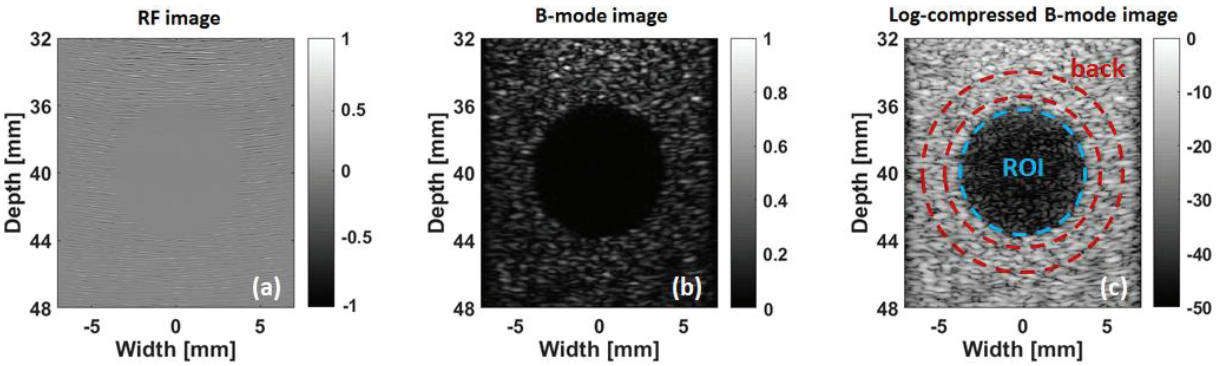

Fig.11: Illustration of the different simulated ultrasound images obtained for a hypoechoic cyst: (a) the post beamformed RF image, (b) the B-mode image before log-compression and (c) the log-compressed B-mode image, which shows clearly the different structures in the medium.

3.3 Evaluation of the image quality

To evaluate the image quality, several metrics exist. In this thesis, the spatial resolution, the spatial autocorrelation length, the echo Signal to-Noise-Ratio (*eSNR*), the image Signal to-Noise-Ratio (*SNR*) and the Contrast to-Noise-Ratio (*CNR*) are used.

3.3.1 Spatial resolution

The spatial resolution provided by an image can be evaluated in both directions of the image **[Van Wijk (2002)]**. Therefore, axial / lateral resolution is defined as the ability of the system to discern two scaterrers in the parallel / perpendicular direction of the ultrasound beam. The axial resolution is strongly linked to the length (number of cycles, for sinusoidal signals) of the transmitted signal. Shorter is the pulse length, better is the axial resolution. The lateral resolution is also linked to the transmitted signal but also to the aperture and the geometry of the probe. The axial / lateral resolution is defined as the full width at half maximum (at *-6 dB* on a log-scale) of an axial / lateral line in the B-mode image (Fig.10c). A smaller width at *-6 dB* corresponds to a better axial (lateral) resolution of the imaging system.

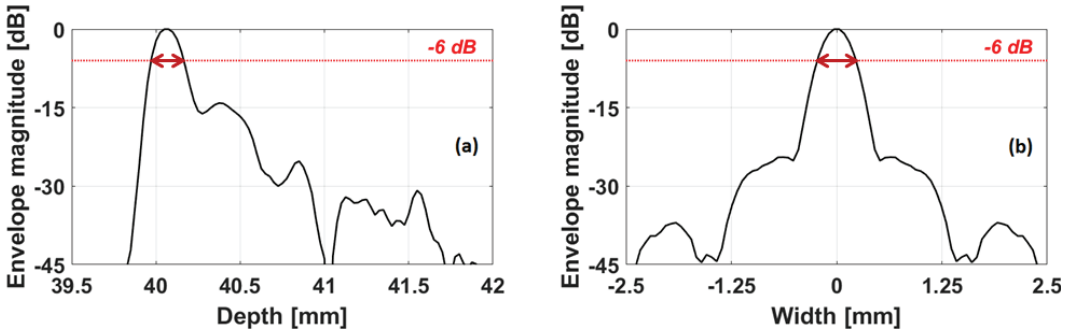

Fig.12: Axial (a) and lateral (b) profiles of the PSF presented in Fig.10c. The dashed lines are traced for an amplitude of -6dB, where the axial and lateral resolutions are measured.

3.3.2 Modulation Transfer Function (MTF)

To measure the axial resolution of an imaging system, the MTF can be also used. The MTF is superior to bandwidth in representing the resolution of a system. A chirp can have longer duration than

a short pulse, but it could have the same −6 dB bandwidth. The MTF is defined as $MTF(k)=|H(k)|/|H(0)|$, where $k=2\pi f/c$, $c=1540 m.s^{-1}$ and $H(k)$ is the spatial Fourier transform of the received signal envelope. For shorter emitted signals the MTF decreases slower than for longer emitted pulses. This property makes MTF a good estimator of the axial resolution of an imaging system, which can be obtained from the MTF **[Beutel (2000)]** using $res_{ax}=1/2\times(2\pi/k_0)$, where k_0 is the value of k at which the MTF falls to 0.1, which corresponds to -20 dB on a logarithmic scale.

3.3.3 Bandwidth

The bandwidth is one of the most important metrics that can determine the ability system to provide improvements in terms of axial resolution. For instance, in quantitative ultrasound imaging, larger bandwidths result in more precise estimation of the scatterer size **[Chaturvedi (1996)]**. Thus, this parameter represents an important metric to quantify the ability to provide improvements in axial resolution. In the following study, the bandwidths at −6 dB are considered.

3.3.4 Spatial autocorrelation length

The size of the speckle depends on the scatterer density inside the considered medium and also on the capacity of the imaging system to separate closely placed scatterers (spatial resolution). To quantify the speckle dimension on a log-compressed B-mode image, the spatial autocorrelation length is used **[Rouyer (2015); Benane (2018a)]**. The Axial / Lateral Auto-Correlation (A/L AC) of the radio-frequency image is defined as:

$$AAC[m,p]=\sum_{i=-\infty}^{+\infty} M[i+m,p]M[i,p] \quad ; \quad LAC[o,s]=\sum_{i=-\infty}^{+\infty} M[o,s+i]M[o,i] \tag{61}$$

where M is the image containing speckle before envelope and log compression (for instance image represented in Fig. 11a), p and s are respectively the indexes of the axial and lateral beamformed image line (before envelope extraction). AACL and LACL are calculated as the full widths at half maximum of AAC and LAC respectively. These two metrics quantify the coherence of the speckle in the axial and lateral direction of the image. Smaller A/L ACL imply smaller speckle in the image.

Fig.13a and Fig13b show respectively the plots of ACL and LAC respectively. The AACL and LACL are measured on the red lines present at *-6 dB*.

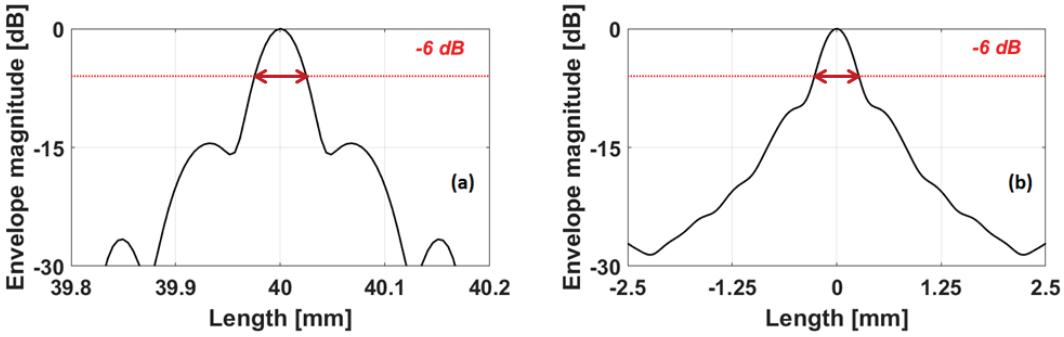

Fig.13: Plots of the axial (a) and lateral (b) autocorrelations on the RF image displayed in Fig.11a. AAC was performed on the axial line $x=6mm$ and LAC was performed on a lateral line at $z=45mm$. The dashed lines are traced for an amplitude of -6dB, where the axial and lateral resolutions are measured.

3.3.5 Contrast to-Noise-Ratio (CNR)

This image quality allows to assess the system ability to distinguish the different parts present in the tissue depending on their level of brightness. For instance, the lesion detectability is calculated through the CNR, defined as [**Thijssen (2003); Stentson (1997); Jensen A.C (2012)**]:

$$CNR = 10\log_{10}\left(\frac{|\mu_{ROI} - \mu_{back}|}{\sqrt{\sigma_{ROI}^2 + \sigma_{back}^2}}\right) \tag{62}$$

where μ_{ROI} (μ_{back}) and σ_{ROI} (σ_{back}) represent the average and the variance intensity inside (outside) the region of interest (ROI) respectively. The targets ROI (Region Of Interest) and back are usually the center of a cyst and its surrounding background respectively (Fig.11c) (nonetheless, as one can observe in (62), if the regions are inversed, the result remains the same). To calculate the CNR, the log-compressed B-mode images with the dynamic range mentioned in each figure are used. Higher is the CNR, better is the contrast in the image.

3.3.6 Signal to-Noise-Ratio (SNR)

In ultrasound log compressed B-mode images, the speckle can be interpreted in two points different ways. First way, consists in seeing the speckle as a noise that degrades the quality of the ultrasound image [**Wagner (1983)**]. In the second interpretation, the speckle can be seen as a source of information that can be used for tissue characterization or movement measurement [**Thijssen (2003); Wagner (1983)**]. The speckle noise is quantified by the SNR defined as:

$$SNR = 10\log_{10}\left(\frac{\mu_{ROI}}{\sigma_{ROI}}\right) \tag{63}$$

In homogeneous anechoic ROIs of the ultrasound image, the SNR could give a very good synopsis of the imaging system response to noise, since in such ROIs $\mu_{ROI} \approx \mu_{Noise}$ and $\sigma_{ROI} \approx \sigma_{Noise}$. Therefore, in this thesis, the SNR will be a good indicator to quantify the relative proportion between the beamformed signal and the noise (including acquisition noise and artefacts: reverberation, cross-talk …) in the obtained B-mode images. As previously mentioned for the CNR measurement, the log-compressed B-mode images with the dynamic range mentioned in each figure were used to calculate SNR.

3.3.7 Echo Signal to-Noise-Ratio (eSNR)

The $eSNR$ represents the ratio between the power of the backscattered echoes and the power of the acquisition noise. The definition of $eSNR$ is given by **[Liu (2005)]**:

$$eSNR = 10\log_{10}\left(\frac{E\left\{|y(t)|^2\right\}}{E\left\{|b(t)|^2\right\}}\right) \tag{64}$$

where $y(t)$ is the received signal defined in (34) and $b(t)$ the acquisition noise. In (64), $E\left\{|\,.\,|^2\right\}$ represents the energy of the considered signal. The $eSNR$ is directly linked to the voltage waveforms

used to excite the probe. It is also related to the emission scheme (detailed in paragraph 3.4) used for imaging a given tissue but is not impacted by the image reconstruction algorithms since is computed before the beamforming step.

3.3.8 Frame rate

One of the important characteristic of the ultrasound imaging is its ability to provide images of the medium in real-time. In conventional ultrasound imaging, the acquisition time can be increased or decreased depending on the number of focused emission / reception events performed in order to obtain the final image and also on the exploration depth inside the imaged tissue. Thus, for conventional ultrasound imaging, the total acquisition time is computed using several parameters as the maximum considered depth $(z_{\max})$, the steering angle of each transmission (θ_k), the number of angles (N_{angles}), the number of scan lines for each angle (N_{line}) and the sound velocity inside the tissue (c_0).

$$t_{acq} = \sum_{i=1}^{N_\theta} \frac{N_{line}}{\cos(\theta_i)} \frac{2z_{max}}{c_0} \tag{65}$$

The Frame Rate (FR) can be deduced from the acquisition time as follows **[Tanter (2014)]**:

$$FR = \frac{1}{t_{acq}} \tag{66}$$

3.4 Imaging methods

The transmission / reception of acoustic waves that propagate inside the tissue are performed by the ultrasound probe, allowing the reciprocal conversion of the ultrasonic waves into electrical signals. As shown in equation (34), for one pair of transmission / reception transducers the received signal contains information of the scanned medium through its Tissue Reflectivity Function (TRF). This means that for several hundred transducers in transmission / reception (that the ultrasound probe contains) not only more information on the TRF is acquired (due to the multiple receivers) but also this information is less noisy (due to the multiple transmitters). The fact that each ultrasound probe has multiple elements in transmission / reception also allows generating different transmission / reception beamforming strategies that provide a wide range of image qualities and frame acquisition rates. These techniques are: Conventional Ultrasound Imaging (called also focused imaging), Multi Line Transmit, Plane Wave Imaging, Diverging Wave Imaging. In this section, these imaging methods were reviewed by succinctly detailing the process of image formation. In order to better understand the specificity of each approach, the process of ultrasound image formation is split into three main blocks:

- Transmission: the transmitted signals are generated and the corresponding transmission delays for each element of the probe are calculated in order to perform the transmission beamforming;
- Reception: the backscattered echoes of the medium are received;
- Post-processing: depending on the imaging method, different beamforming approaches are applied in order to reconstruct an estimation of the TRF.

Before presenting the different imaging approaches, one needs to consider the far field approximation on which rely all of the transmission / reception beamforming schemes. Consider the

case of the two transducers modelled by the equations (34) and (35). In far field conditions $\left\|\vec{r_{S_e}}\right\|_2 \ll \left\|\vec{r_{S_e}^0}\right\|_2$ and $\left\|\vec{r_{S_r}}\right\|_2 \ll \left\|\vec{r_{S_r}^0}\right\|_2$ thus (35) becomes:

$$h_{er}(\vec{r},t) \approx \frac{\delta\left(t - t_e - \frac{\left\|\vec{r} - \vec{r_{S_e}^0}\right\|_2 + \left\|\vec{r} - \vec{r_{S_r}^0}\right\|_2}{c_0}\right)}{4\pi^2 \left\|\vec{r} - \vec{r_{S_e}^0}\right\|_2 \left\|\vec{r} - \vec{r_{S_r}^0}\right\|_2} \tag{67}$$

Under such conditions, (34) becomes:

$$y(t) = h_e(t) *_t a(t) *_t h_r(t) *_t \int TRF(\vec{r}) \frac{\delta\left(t - t_e - \frac{\left\|\vec{r} - \vec{r_{S_e}^0}\right\|_2 + \left\|\vec{r} - \vec{r_{S_r}^0}\right\|_2}{c_0}\right)}{4\pi^2 \left\|\vec{r} - \vec{r_{S_e}^0}\right\|_2 \left\|\vec{r} - \vec{r_{S_r}^0}\right\|_2} d\vec{r} \tag{68}$$

It can be seen in the previous relation that the received signal is a superposition of echoes (with a typical waveform $h_e(t) *_t a(t) *_t h_r(t)$) that come at different arrival times (set by the sum of the transmission delays and propagation time $t_e - \frac{\left\|\vec{r} - \vec{r_{S_e}^0}\right\|_2 + \left\|\vec{r} - \vec{r_{S_r}^0}\right\|_2}{c_0}$) and with an amplitude that depends on the reflectivity function in the point where the echo was generated ($TRF(\vec{r})$) and on the geometrical spreading ($4\pi^2 \left\|\vec{r} - \vec{r_{S_e}^0}\right\|_2 \left\|\vec{r} - \vec{r_{S_r}^0}\right\|_2$).

For a finite number of scatterers (N_s) inside the imaged medium, (68) becomes:

$$y(t) = h_e(t) *_t a(t) *_t h_r(t) *_t \sum_{l=1}^{N_s} TRF_l \frac{\delta\left(t - t_e - \frac{\left\|\vec{r_l} - \vec{r_{S_e}^0}\right\|_2 + \left\|\vec{r_l} - \vec{r_{S_r}^0}\right\|_2}{c_0}\right)}{4\pi^2 \left\|\vec{r_l} - \vec{r_{S_e}^0}\right\|_2 \left\|\vec{r_l} - \vec{r_{S_r}^0}\right\|_2} \tag{69}$$

(69) can also be written as:

$$y(t) = e(t) *_t \delta(t - t_e) *_t g_{S_eS_r}(t) \quad \text{with:} \begin{cases} e(t) = h_e(t) *_t a(t) *_t h_r(t) = h_I(t) * a(\mathrm{t}) \\ g_{S_eS_r}(t) = \sum_{l=1}^{N_s} TRF_l \frac{\delta\left(t - \frac{\left\|\vec{r_l} - \vec{r_{S_e}^0}\right\|_2 + \left\|\vec{r_l} - \vec{r_{S_r}^0}\right\|_2}{c_0}\right)}{4\pi^2 \left\|\vec{r_l} - \vec{r_{S_e}^0}\right\|_2 \left\|\vec{r_l} - \vec{r_{S_r}^0}\right\|_2} \end{cases} \tag{70}$$

where TRF_l is the reflectivity of the lth scatterer and $\vec{r_l}$ is its position. In (70), it can be seen that the received signal can be written as a convolution between a typical waveform $e(t)$, a transmission delay

$\delta(t-t_e)$ and a function $g_{S_eS_r}(t)$ that represents the pulse echo impulse response of the medium seen by the receiver S_r when S_e transmits.

Moreover, for the rest of this section, it is supposed that for an ultrasound probe, the acousto electrical impulse response in transmission and reception are equal for each element, thus: $h_1(t) = h_e(t) * h_r(t)$.

3.4.1 Conventional ultrasound imaging

The principle of Conventional Ultrasound (CU) imaging is presented in Fig.14. Here, it can be seen that a full ultrasound image of the medium is achieved after N_f transmission / reception / beamforming events. As it can be seen in Fig.11, after each transmission / reception / beamforming event an image line or several are beamformed **[Shattuck (1984)]**. N_f is the exact number of transmission / reception / beamforming events needed to reconstruct a full image of the medium.

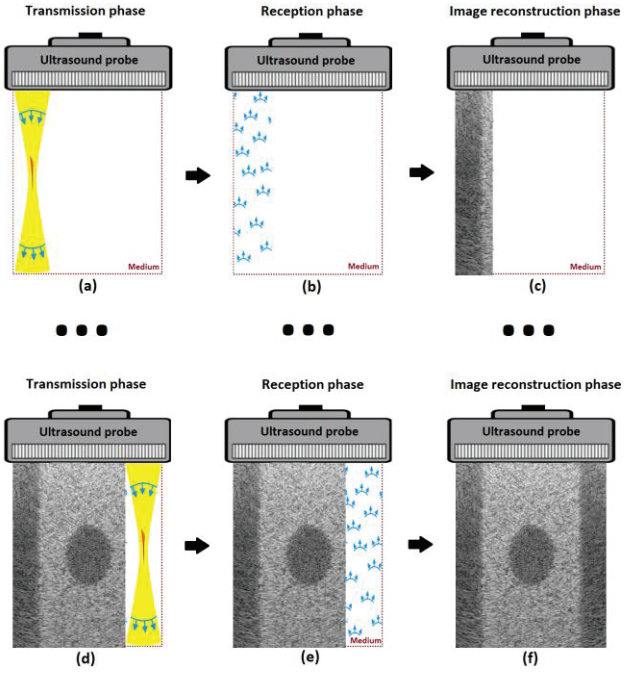

Fig.14: Principle of CU imaging. (a) Transmission of the focused beam, (b) reception of the backscattered echoes, (c) reconstruction of the first line of the image. (d), (e) and (f) are respectively the transmission, the reception and the reconstruction phase for the last line of the image.

- The transmission phase

In order to focus the ultrasound beam at the medium point $r_j^0 = (x_f, 0, z_f)$, each element j of the transducer needs to be excited with the following excitation signal:

$$a_j(t) = w_j a(t) * \delta(t - t_j) \tag{71}$$

where $a(t)$ is the waveform carried by the ultrasound beam, $\delta(t-t_j)$ is a time shifted Dirac function and w_j is a spatial tapering factor applied on each element of the transducer j during transmission. In

(71), $(*)$ represents the temporal convolution and t_j are the transmission delays that trigger a beam focalization at the medium point $r_f = (x_f, 0, z_f)$.

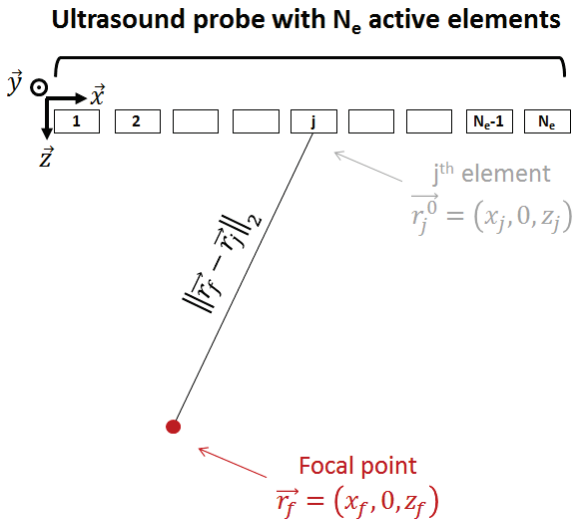

Fig.15: Geometrical draft of the ultrasound probe used for the computation of the delay during the transmission phase.

Based on the geometrical representation of the probe displayed in Fig.15, one can calculate the transmission delays as:

$$\left\| \overrightarrow{r_f} - \overrightarrow{r_j} \right\|_2 = c_0 (t_{max} - t_j)$$

$$\Leftrightarrow t_j = t_{max} - \frac{\left\| \overrightarrow{r_f} - \overrightarrow{r_j} \right\|_2}{c_0} = \max_{j \in [1..N_e]} \left(\frac{\sqrt{(x_f - x_j)^2 + (z_f - z_j)^2}}{c_0} \right) - \frac{\sqrt{(x_f - x_j)^2 + (z_f - z_j)^2}}{c_0} \quad (72)$$

In (72), t_{max} stands for the maximum forward propagation delay between an element of the ultrasound probe and the focal point. Thus, one can understand from (72) that by compensating, for each element of the probe the difference between the maximal propagation distance and the distance for each element, all the transmitted spherical wave (by each element of the probe) arrives at the same time in the focal point.

- <u>The reception phase</u>

Assuming that the propagation of the wave transmitted by each element of the transducer is linear and using the far field approximations shown in the relations (68) and (72), the received signal by the i^{th} element can be written as:

$$y_i(t) = w_i \sum_{j=1}^{N_e} w_j a_j(t) * h_1(t) * g_{ji}(t) + b(t) \quad (73)$$

where $g_{ji}(t)$ is computed using the model described in (69). In (73), $b(t)$ represents the acquisition noise and usually is supposed to be an Additive White Gaussian Noise (AWGN). Using (70), (73) can be further simplified to:

$$y_i(t) = e(t) * g_i(t) + b(t) \quad \text{with} : \begin{cases} g_i(t) = w_i \sum_{j=1}^{N_e} w_j \, \delta(t - t_j) * g_{ji}(t) \\ e(t) = a(t) * h_1(t) \end{cases} \tag{74}$$

Since $g_i(t)$ depends on the excitation delays t_j and the signals $g_{ji}(t)$, it can be seen as the pulse echo impulse response of the medium when insonified with an ultrasound beam focused in the point r_f seen by the element i [**Bujoreanu (2017a)**].

- The post-processing phase

Numerous beamforming strategies exist both in the temporal and in the frequency domains. However the most common one that is widely used even in nowadays commercial ultrasound scanners is called Delay And Sum (DAS). The DAS algorithm uses the total number of N_l received signals $y_i(t)$ in order to reconstruct one vertical line of the ultrasound image A through the following equation:

$$A(x_f, z) = \sum_{i=1}^{N_l} y_i(\tau_i(x_f, z))$$
$$\text{with} : \tau_i(x_f, z) = \min_{j \in [1..N_e]} \left(t_j + \frac{\sqrt{(x_f - x_j)^2 + (z - z_j)^2}}{c} \right) + \frac{\sqrt{(x_f - x_i)^2 + (z - z_i)^2}}{c} \tag{75}$$

Since the transmitted beam is focused along the $x_f = const$ (with a focal point in z_f), the echo signal to noise ratio provided by CU is very high, thus the resulted image quality of A is optimal. However, in order to obtain an image with a sufficient lateral field of view, one needs to repeat the transmission / reception / beamforming events usually around one hundred times. Suppose now that $N_l = 128$ and that the depth of the imaged medium is $d = 6\,cm$. The total reconstruction time for one full CU image (by neglecting the post-processing beamforming time) can be roughly approximated as: $T_f = (2\,d\,N_l)/c_0 \approx 0.01\,s$. This means that the maximal acquisition rate of such an image can reach around 100 Hz. Such low frame acquisitions can be sufficient to acquire images of non-moving tissues however for the good imaging of the fast transient events in the human body (such as shear wave propagation, heart movement, blood flow imaging) faster acquisition rates **[Tanter (2014)]** are required.

3.4.2 Multi Line Transmit imaging

The MLT acquisition scheme represents a variation of focused transmission that increases the frame acquisition rate by employing simultaneous transmission of focused ultrasound beams inside the scanned medium. The principle of MLT is displayed in Fig.16. As N_{MLT} beams are transmitted simultaneously (thus N_{MLT} image lines can be reconstructed simultaneously), the frame rate is increased by a factor of N_{MLT} (in Fig.16, $N_{MLT} = 2$).

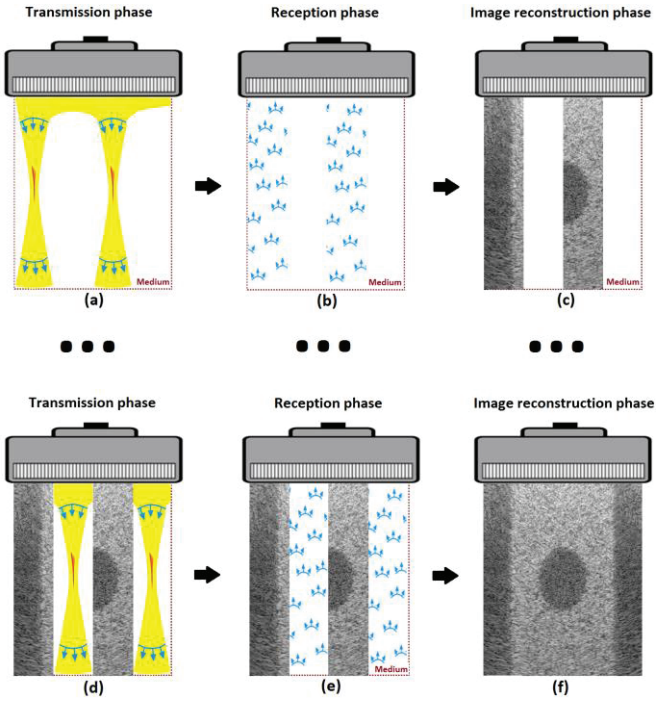

Fig.16: Principle of MLT imaging. (a) Transmission of the focused beams, (b) reception of the backscattered echoes, (c) simultaneous reconstruction of two lines of the image. (d), (e) and (f) are respectively the transmission, the reception and the reconstruction phase for the two last lines of the image.

- The transmission phase

In Fig.16, it can be seen, that for each transmission event, N_{MLT} focused beams are transmitted simultaneously in the imaged medium. This effect is achieved by, first, separately creating the excitation signals for each focused beam (using the same principle described for CU). Then, for each element of the ultrasound probe, the N_{MLT} excitation signals are coherently added. The expression of obtained excitation signal for each probe element is:

$$a_j^{MLT}(t) = w_j \sum_{k=1}^{N_{MLT}} a^k(t) * \delta(t - t_j^k) \tag{76}$$

where $a^k(t)$ is the waveform carried by each of the focused beam k. The transmission delays t_j^k are computed by applying (66) to the coordinates of each focal point (x_f^k, z_f^k). The depth z_f of the focal point in MLT, as in CU, is defined by the application. However $x^f(k)$, depends on the geometry of the probe, and needs to be set in such way so the crosstalk between the N_{MLT} beams transmitted simultaneously is limited. A way to compute the focal positions is:

$$x_f^k = x_0 + k\frac{N_e pitch}{N_{MLT}} \tag{77}$$

where x_0 is the x position of the first element of the transducer and p is the pitch of the transducer.

Finally, in order to have N_{MLT} focused beams that propagate inside the ultrasound medium, one needs to assume that the medium is linear to the superposition of acoustic beams. This assumption however, is already made when one focused beam is generated (in CU), where in order to have a focalization at the point $r_f = (x_f, 0, z_f)$, N_e acoustic waves are superposed.

- The reception phase

By applying the principle of linear propagation to (74), one can use (76) in order to write the MLT received signals at each element i of the transducer:

$$y_i^{MLT}(t) = w_i \sum_{k=1}^{N_{MLT}} e^k(t) * g_i^k(t) + b(t) \tag{78}$$

where $g_i^k(t) = \sum_{j=1}^{N_e} w_j \delta(t - t_j^k) * g_{ji}(t)$ is the pulse echo impulse response of the medium when insonified with the focused ultrasound beam k, seen by the element i (computed using the relation (74)). In (78), $e^k(t) = a^k(t) * h_1(t)$ represents the typical waveform generated by an arbitrary scatterer in the medium. Since each focused beam carries the same excitation signal $(a(t) = a^k(t), \forall k)$, then (78) becomes:

$$y_i^{MLT}(t) = e(t) w_i * \sum_{k=1}^{N_{MLT}} g_i^k(t) + b(t) \tag{79}$$

- The post-processing phase

Each line k of the final image A^{MLT}, corresponding to a simultaneously transmitted focused beam, is reconstructed using DAS:

$$A^{MLT}(x_f^k, z) = \sum_{i=1}^{N_l} y_i^{MLT}(\tau_i(x_f^k, z)) \tag{80}$$

where the delays $\tau_i(x_f^k, z)$ are computed as showed in (75).

Since the N_{MLT} beams are transmitted simultaneously, an inherent noise inside the $y_i^{MLT}(t)$ acquisition signals is present. For each beam k, this noise, called crosstalk, represents the echoes (received in the same time by the probe) generated by the other $N_{MLT} - 1$ focused beams. Nonetheless, (79) and (80) are performing well (minimize the crosstalk between the beams) when the pulse echo impulse responses $g_i^k(t)$ are very low correlated. This can be achieved by spatially separating the focal points (x_f^k, z_f^k) as much as possible. Spatial separation is easily achievable for low values of N_{MLT} (for which the spacing $x_f^{k+1} - x_f^k = \frac{N_e p}{N_{MLT}}$ becomes bigger in (77)). However in the quest for higher acquisition rates, N_{MLT} increases and the space between the consecutive focal points (x_f^k, z_f^k)

and (x_f^{k+1}, z_f^{k+1}) decreases. This results in high amounts of crosstalk between the focused beams and finally, in the degradation of the image quality of A^{MLT} [**Tong (2014)**]. Thus, by providing a frame rate gain of N_{MLT} compared to CU, MLT reduces the image quality due to the crosstalk. At this point one can observe the inherent trade-off, present in ultrasound imaging, between the image acquisition and the frame rate.

3.4.3 Plane Wave imaging

As shown in Fig.17, in plane wave imaging, the entire medium is insonified using a single plane wave. After each transmission event, all the backscattered echoes are received and beamformed using a variation of the DAS algorithm detailed further in this section **[Sandrin &Fink (1999)]**. The lack of beam focussing in transmission, implies that the backscattered echoes have a lower echo signal to noise ratio, thus the beamformed radiofrequency image that DAS outputs, is of a very low quality compared to CU and even to MLT. In order to overcome this drawback, **[Montaldo (2009)]** proposed an approach that relies on the coherent summation of low quality images obtained from insonification of the medium with plane waves tilted in different directions. This technique is called Coherent Plane Wave Compounding (CPWC).

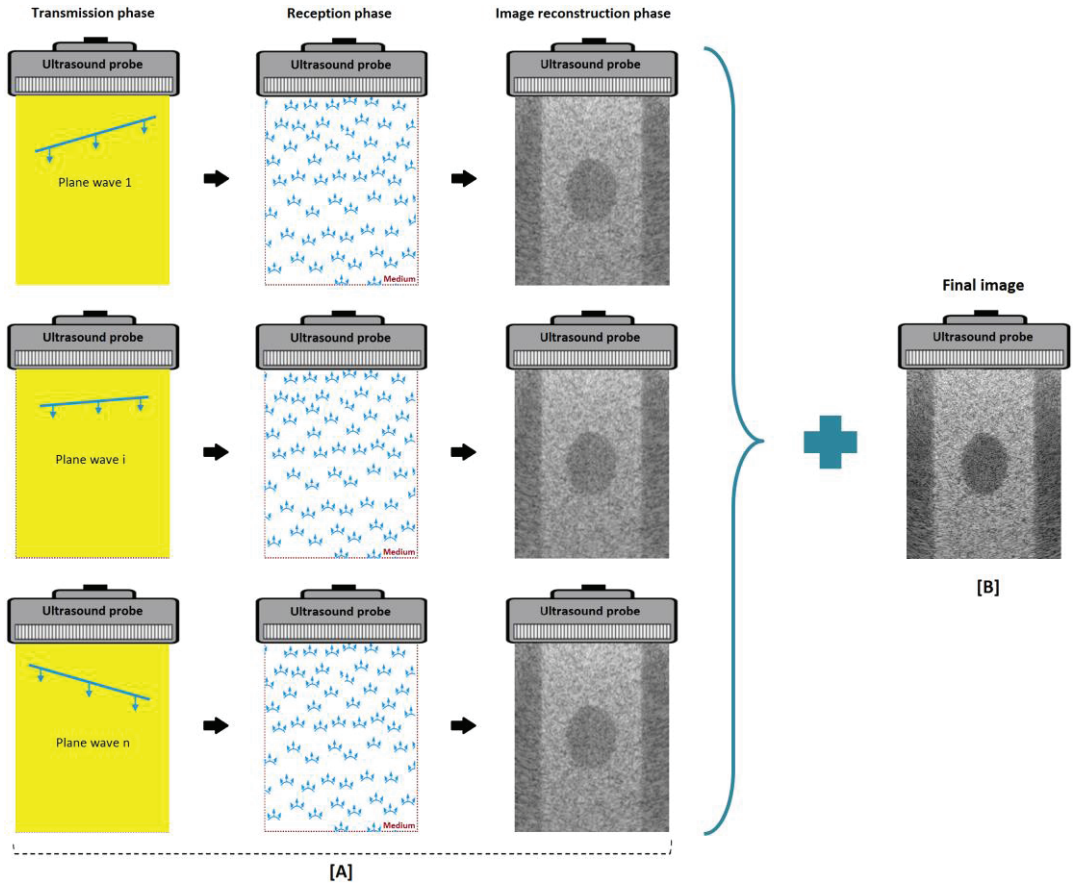

Fig.17: Principle of PW imaging. [A]: (Left) Transmission of the different plane waves, (middle) reception of the different backscattered echoes, (right) reconstruction of the different low quality images. [B]: Final image obtained after the coherent compounding of the different low quality images.

- The transmission phase

In **[Montaldo (2009)]** was shown, that in order to achieve the same quality at the depth z_f as provided by CU, N_{pw} plane wave insonifications must be employed in CPWC. N_{pw} is given by:

$$N_{pw} = \frac{N_e\, pitch}{\lambda F^{\#}} \tag{81}$$

where $N_e\, pitch$ is the total width covered by the active transmission elements usually referred to as the lateral aperture size, λ is the transmitted pulse wavelength, and $F^{\#}$ is the F-number defined as:

$$F^{\#} = \frac{z_f}{N_e pitch} \tag{82}$$

The transmission direction for plane wave k can be computed using the following relation:

$$\theta_k = \arcsin\left(\frac{k\lambda}{N_e pitch}\right) \tag{83}$$

with $k = -(N_{pw} - 1)/2, \ldots, +(N_{pw} - 1)/2$

Under these conditions, for the k^{th} plane wave transmission, the transmission delays for each element of the probe can be obtained by using the geometrical model displayed in Fig.18. Thus:

$$t_j^k = \frac{(j-1)\cdot pitch \cdot \tan(\theta_k)}{c_0} \tag{84}$$

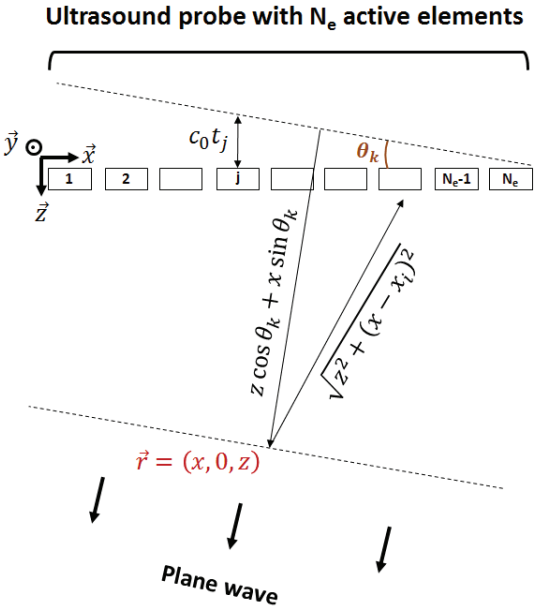

Fig.18: Geometrical draft of the ultrasound probe used for the computation of the delay during the transmission phase. Direction θ_k.

Using the excitation delays, the excitation signals at each element of the probe can be written as:

$$a_j^k(t) = w_j \sum_{k=1}^{N_{MLT}} a^k(t) * \delta(t - t_j^k) \tag{85}$$

To be noted that, since each element of the probe transmits a spherical wave with a delay t_j^k, PW transmission relies on the approximation that the superposition of N_e spherical waves (transmitted with a accordingly computed delay) generates a plane wave inside the medium.

- The reception phase

As shown in CU, MLT and as previously explained for plane waves, the focused / plane wavefront is achieved thanks to the superposition of N_e spherical waves. This means that the received signal at each element of the probe can be written as:

$$y_i^{PW}(t) = w_i e^k(t) * {}^{PW}g_i^k(t) + b(t) \tag{86}$$

where ${}^{PW}g_i^k(t) = \sum_{j=1}^{N_e} w_j \delta(t - t_j^k) * g_{ji}(t)$ represents the pulse echo impulse response of the medium when the plane wave k is transmitted and the echoes are received by the i^{th} element of the probe. In (86), $e^k(t) = a^k(t) * h_1(t)$ represents the typical waveform generated by an arbitrary scatterer in the medium. $g_{ji}(t)$ is computed using (70).

- The post-processing phase

After the simultaneous reception of all N_e $y_i^{PW}(t)$ radiofrequency signals a low quality image is obtained using the following DAS equation:

$$A^{PW}(x,z) = \sum_{i=1}^{N_e} y_i^{MLT}(\tau_i(x\ ,z)) \tag{87}$$

where $\tau_i(x\ ,z)$ represents the time of flight needed for the plane wave / echo to propagate between the transmission / scattering in the point $(x\ ,z)$ / reception at the element i of the probe. $\tau_i(x\ ,z)$ can be computed using the following relation:

$$\tau_i(x,z) = \frac{z\cos(\theta_k) + x\sin(\theta_k)}{c_0} + \frac{\sqrt{z^2 + (x - x_i)^2}}{c_0} \tag{88}$$

Once all the N_{pw} low quality images A^{PW} are reconstructed, following the principle of CPWC, the final image is obtained using:

$$A^{CPWC} = \sum_{k=1}^{N_{pw}} A^{PW} \tag{89}$$

Let us suppose a case where an ultrasound probe with $N_e = 128$ elements and a pitch of $0.245\mu m$ is used for CPWC imaging. It would appear, from (81), that for a depth of $z_f = 0.04\mu m$, $N_{pw} = 137 (\approx N_e)$ plane wave insonifications would be needed in order to obtain the same image quality as CU. In such a case the actual frame rate provided by CPWC would be comparable to CU since, in order to provide the same image quality as CU, 137 transmission / reception events are needed and since in CU, for a full image with 128 lines, 128 transmission / reception events are required. However, recent studies **[Toulemonde (2015)]** showed that for CPWC, the image quality improves very little if the number of compounded plane wave exceeds 9, which means that plane wave imaging is able to provide a gain in frame acquisition rate of at least 15 fold (≈ 128/9) when compared to CU.

3.4.4 Diverging wave imaging

The principle of Diverging Wave (DW) imaging is represented in Fig.17. Similar to plane wave imaging, DW relies on broad beam insonification of the medium in order to reconstruct full ultrasound images from one transmission / reception event. However, as in PW, the lack of beam focusing in transmission decreases the provided image quality. Thus, spatial compounding is also applied to DW in order to improve the final image.

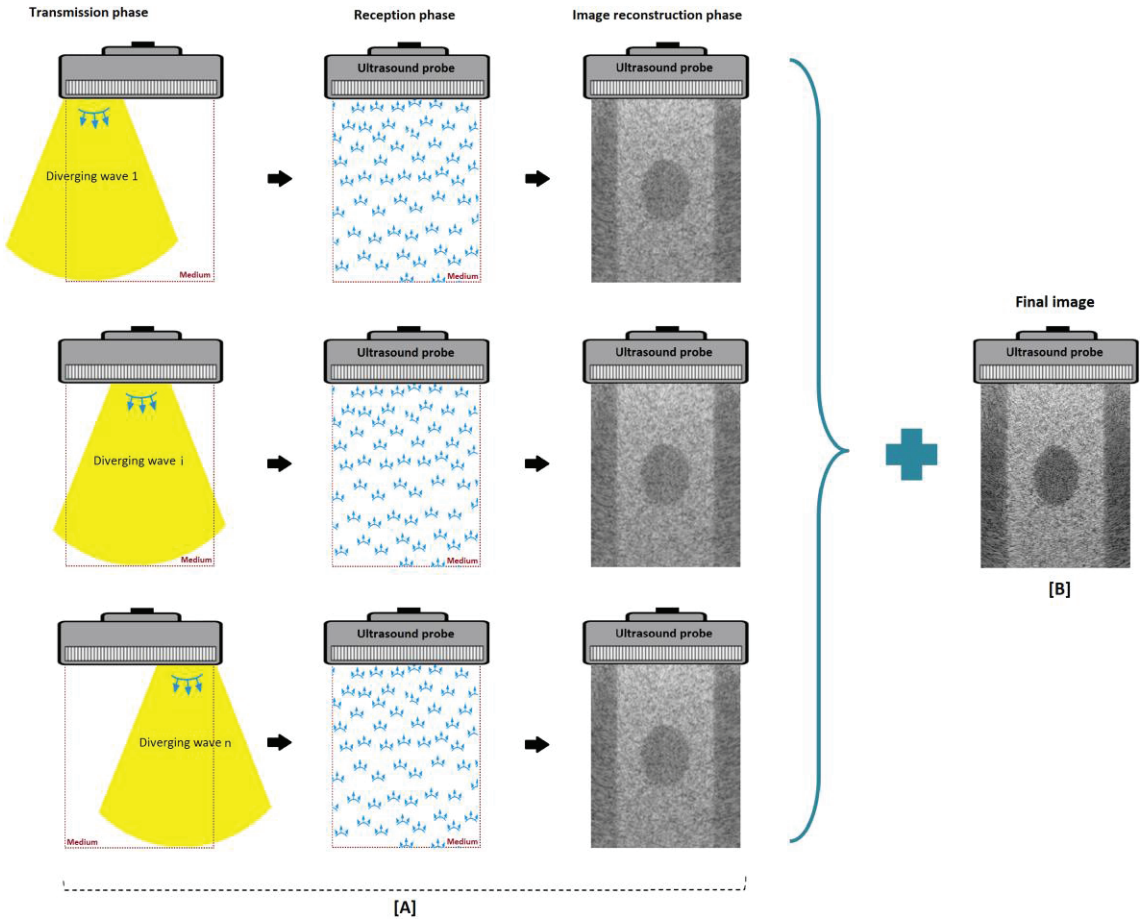

Fig.19: Principle of DW imaging. [A]: (Left) Transmission of the different diverging waves, (middle) reception of the different backscattered echoes, (right) reconstruction of the different low quality images. [B]: Final image obtained after the coherent compounding of the different low quality images.

- The transmission phase

As shown in Fig.19, in order to transmit a diverging wave using a linear ultrasound probe, one should consider a punctual virtual source located at the point $\vec{r}_v = (x_v, 0, z_v)$ with $z_v = 0$. Depending on the region of interest in the medium, which imposes a certain angular aperture θ, n elements of the probe are excited with the same excitation $a(t)$ slightly delayed depending on the position of each active element (Fig.20). The number of active elements n and the transmission delay t_j are determined by:

$$n = \frac{2\,|z_v|\,tan\left(\frac{\theta}{2}\right)}{pitch} \tag{90}$$

$$t_j^k = \frac{1}{c_0}\left[\sqrt{z_v^2 + \left(\frac{j.pitch}{2}\right)^2} - z_v\right] \tag{91}$$

where $j \in \{-n/2, ..., n/2-1\}$. Thus, the excitation signals for the diverging k, at each element j of the probe can be written as:

$$a_j^k(t) = a^k(t) * \delta(t - t_j^k) \tag{92}$$

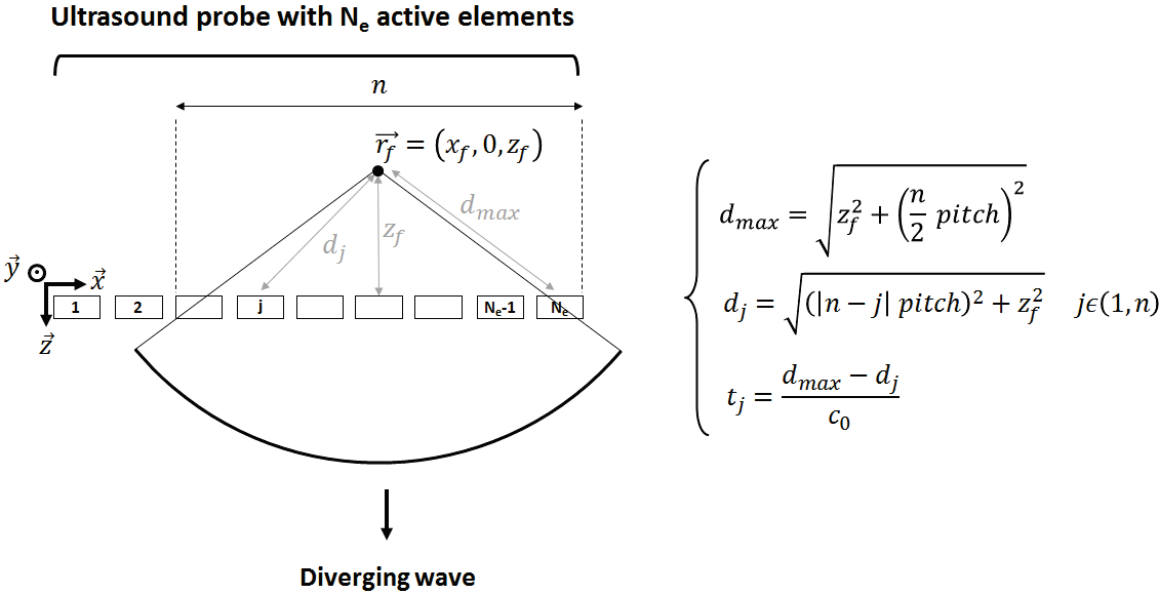

Fig.20: Geometrical draft of the ultrasound probe used for the computation of the delay during the transmission phase.

- The reception phase

As in the rest of the imaging methods that employ simultaneous transmission of spherical acoustic waves with a large number of probe elements, the received electrical signal at each element of the probe can be seen as a linear superposition of each transmission element contribution. Thus the received signal for the i^{th} element can be written as:

$$y_i^{DW}(t) = w_i e^k(t) * {}^{DW}g_i^k(t) + b(t) \tag{93}$$

where ${}^{DW}g_i^k(t) = \sum_{j=1}^{N_e} w_j \delta(t - t_j^k) * g_{ji}(t)$ represents the pulse echo impulse response of the medium when the diverging wave k is transmitted. $g_{ji}(t)$ is computed using (70). In (93), $e^k(t) = a^k(t) * h_1(t)$ represents the typical waveform generated by an arbitrary scatterer in the medium. As it can be seen in (93), various reception (w_i) and transmission (w_j) apodization windows can be applied to the electrical signal in order to adjust the image quality.

- The post-processing phase

After the simultaneous reception of all N_e $y_i^{DW}(t)$ radiofrequency signals, a low quality image is obtained using the following DAS equation:

$$A^{DW}(x,z) = \sum_{i=1}^{N_e} y_i^{DW}(\tau_i(x\ ,z)) \tag{94}$$

$$\text{with : } \tau_i(x\ ,z) = \min_{j\in[1..N_e]} \left(t_j + \frac{\sqrt{(x\ - x_j)^2 + (z\ - z_j)^2}}{c_0} \right) + \frac{\sqrt{(x\ - x_i)^2 + (z\ - z_i)^2}}{c_0} \tag{95}$$

As one can see, the reconstruction of a low quality DW image in (88) is performed using the DAS algorithm. However, the time of flights $\tau_i(x\ ,z)$ are slightly different when compared to the PW ones. Briefly, this delays are computed using the same principle as the ones for MLT and CU, in other words they represent the sum between the forward propagation time, approximated by the fastest spherical wave transmitted by an element j to reach the point $(x\ ,z)$, added to the backward propagation delays which can be computed as seen in Fig.20.

Finally, similar to plane wave imaging, DW has the disadvantage that after one transmission / reception / reconstruction event the provided image is of a poor quality. Thus, spatial coherent compounding is also performed in DW. Therefore the final image can be approximated as:

$$A^{CDWC} = \sum_{k=1}^{N_{dw}} A^{DW} \tag{96}$$

where N_{dw} is the number of diverging wave transmitted successively inside the medium. Similar to CPWC, in order for CDWC to reach the same image quality as provided by CU, around one hundred images need to be compounded in (96). This implies that no frame rate increase is provided. However the work [**Zhang (2016)**] showed that after compounding of 15 DW images the final image quality improves slightly, thus as CPWC, CDWC has the potential to improve the frame rate.

3.5 Chirp compression technique

By transmitting short pulses in medical ultrasound imaging, high resolution can be achieved at the expense of poor penetration depth. In order to improve the penetration depth, the energy of the excitation signal should be boosted by increasing either the transmitted pulse duration or the amplitude. However, extending the pulse duration implies a decrease in the axial resolution of the

image and increasing the pulse amplitude (or peak pressure level) can potentially cause bio-effects. Thus, the Food and Drug Administration (FDA) has set a limitation on Mechanical Index (MI) and Thermal Index (TI), where large values of MI and TI can cause inertial cavitation and therefore tissue damage **[Szabo (2004)**]. A big challenge therefore arises in ultrasound imaging, which is to achieve good penetration depth without exceeding the safety limits.

Chirp compression techniques were initially introduced in radar **[Cook & Bernfeld (1967); Skolnik (1981)]** and were successfully adapted to ultrasound imaging systems few years later **[Chiao (2005); Misaridis (2000); O'Donnell (1992)]**. Their main use, until recent years, was to increase the *eSNR* and the penetration depth by increasing the total transmitted energy while maintaining the same peak intensity level using longer pulse durations **[O'Donnell (1992)]**. Nowadays, such signals are also used to increase the frame acquisition rate of the ultrasound systems relying on the orthogonality properties of the linear frequency modulated signals [**Lashkari (2016); Bujoreanu (2017); Benane (2018b); Benane (2018c)**].

Although chirp excitations have numerous advantages over short sinusoid pulses, it is not easy to employ and design a chirp signal. Firstly, it is not easy to design the right excitation signals, choosing the adapted bandwidths, excitation lengths etc. being a very laborious task. Secondly, the backscattered echoes that carry the chirp, need to be filtered consequently. The filtering step is performed in post processing by applying a pulse compression technique. This step allows to gather all the energy carried by the chirp in a very short impulsion, thus providing a good axial resolution while keeping a good *eSNR*. The bandwidth of the excitation chirp is the key for achieving a substantial compression, for bandwidths comparable to the bandpass of the employed ultrasound probe, the achieved axial resolution being comparable to the one provided by the conventional pulse systems. However, if the chirp excitation and the pulse compression are not well designed, the high sidelobe levels thus generated can strongly decrease image resolution, contrast to noise ratio and other metrics that quantify its quality **[Borsboom (2005)]**.

3.5.1 Chirp excitation definition

The analytical formulation of a chirp signal signal is:

$$a(t) = C(t)e^{j2\pi\phi(t)} \tag{97}$$

where $C(t)$ and $\phi(t)$ are respectively the amplitude and the phase modulation functions. $\phi(t)$ is defined as:

$$\phi(t) = \left(f_c + \frac{B}{2T} t \right) t \quad \text{with: } -\frac{T}{2} \le t \le \frac{T}{2} \tag{98}$$

where f_c is the center frequency, B is the sweeping bandwidth, T is the duration of the signal and $f_c - (B/2)$ is the starting frequency. The instantaneous frequency is given by:

$$f_i(t) = \frac{d\phi(t)}{dt} = \frac{d\left[\left(f_c + \frac{B}{2T} t \right) t \right]}{dt} = f_c + \frac{B}{T} t \tag{99}$$

As seen in (99), the instantaneous frequency of the chirp is a linear function of time thus its name as linear frequency modulated signal. Although, a contradiction can exist between the notion of instantaneous frequency and the Fourier theory (which considers that a signal must be infinite in time

to be limited in band), in practice, the term f_i indicates the spectral band in which the signal energy is concentrated at the time instant t. The parameter $\kappa = B/T$ is the frequency modulation rate. Thus, the signal sweeps linearly the frequencies in the interval $[f_c - \frac{B}{2}, f_c + \frac{B}{2}]$.

For digital generation of the linear frequency signal, an alternative expression with no negative times has the following form:

$$a(t) = C(t)e^{\left(j2\pi\left[\left(f_c-\frac{B}{2}\right)t+\frac{B}{2T}t^2\right]\right)}, \quad 0 \le t \le T \tag{100}$$

An example of linear frequency modulated chirp is shown in Fig.21. The waveform parameters given in Table 1 and a 20% Tukey window are used to design the envelope of the signal $C(t)$.

Table 1: Chirp excitation parameters

Parameter	Value
Sampling frequency	100 MHz
Center frequency	8.5 MHz
Fractional bandwidth	100 %
Duration	10 µs

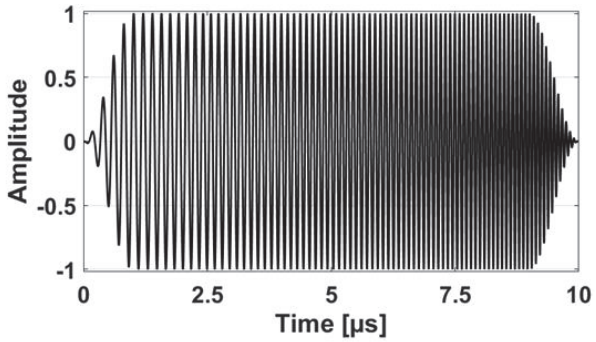

Fig.21: Illustration of a tapered linear chirp.

The instantaneous frequency of a linear chirp can increase or decrease. The callings of "chirp up" and "chirp down" are respectively used to describe these two different situations.

3.5.2 Spectrum of the linear chirp

The Fourier transform of a linear chirp signal with a rectangular envelope $(C(t) = 1)$ is given by:

$$A(f) = \int_{-T/2}^{T/2} e^{j2\pi\left(f_c t+\frac{\kappa}{2}t^2\right)} e^{-j2\pi ft} dt = \int_{-T/2}^{T/2} e^{j2\pi\left((f_c-f)t+\frac{\kappa}{2}t^2\right)} dt \tag{101}$$

knowing that:

$$(f_c - f)t + \frac{\kappa}{2}t^2 = \frac{\kappa}{2}\left(t - \frac{f-f_c}{\kappa}\right)^2 - \frac{(f-f_c)^2}{2\kappa} \tag{102}$$

The integral in (101) becomes:

$$A(f) = e^{\left(-j\frac{\pi}{\kappa}(f-f_c)^2\right)} \int_{-T/2}^{T/2} e^{j\frac{\pi}{2}2\kappa\left(t-\frac{f-f_c}{\kappa}\right)^2} dt \tag{103}$$

Let us introduce the variable $u = \sqrt{2\kappa}\left(t - \frac{(f-f_c)}{\kappa}\right)$. The expression of $A(f)$ becomes:

$$A(f)=\frac{1}{\sqrt{2\kappa}}e^{-j\frac{\pi}{\kappa}(f-f_c)^2}\left[\int_{-U_1}^{U_2}\cos\left(\frac{\pi}{2}u^2\right)du+j\int_{-U_1}^{U_2}\sin\left(\frac{\pi}{2}u^2\right)du\right] \tag{104}$$

The new limits of the integral are:

$$U_1=\sqrt{2\kappa}\left(\frac{T}{2}+\frac{f-f_c}{\kappa}\right)\quad,\quad U_2=\sqrt{2\kappa}\left(\frac{T}{2}-\frac{f-f_c}{\kappa}\right) \tag{105}$$

These limits can be written using the time-bandwidth product noted $TBP=B\times T$:

$$U_1=\sqrt{\frac{TBP}{2}}\left(1+2\frac{f-f_c}{B}\right)\quad,\quad U_2=\sqrt{\frac{TBP}{2}}\left(1-2\frac{f-f_c}{B}\right) \tag{106}$$

Both integrals in (104) can be written as sum of the Fresnel integrals as follow:

$$L(E)=\int_0^E\cos\left(\frac{\pi}{2}u^2\right)du\quad,\quad Q(E)=\int_0^E\sin\left(\frac{\pi}{2}u^2\right)du \tag{107}$$

The final form of the frequency spectrum of the linear chirp is:

$$A(f)=\frac{1}{\sqrt{2\kappa}}e^{-j\frac{\pi}{\kappa}(f-f_c)^2}\left[L(U_1)+L(U_2)+j[Q(U_1)+Q(U_2)]\right] \tag{108}$$

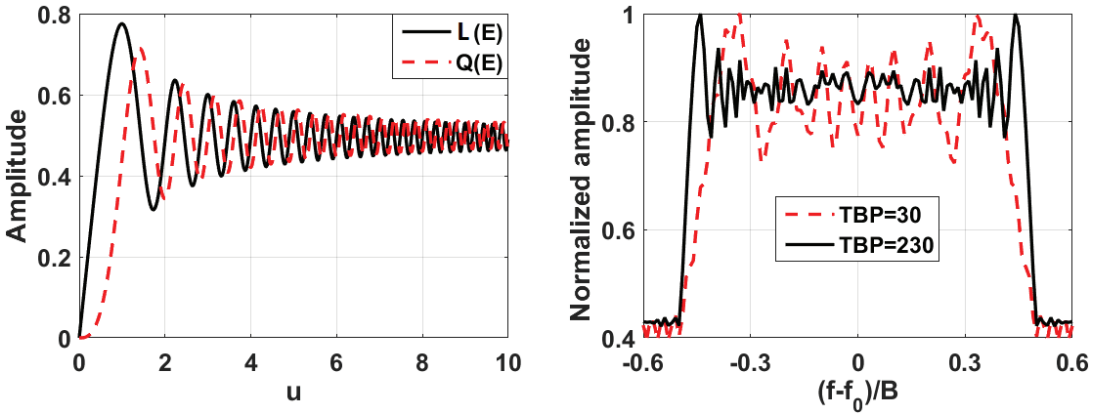

Fig.22: (a) Plots of the Fresnel integrals presented in (107), (b) spectra of two linear chirps having two different TBP.

The Fresnel integrals defined in (107) are shown in Fig.22a where it can be observed that both integrals approach 0.5 when the argument is much higher than 1. In Fig.22b is displayed the spectrum of the linear frequency modulated signal. Since the arguments of the Fresnel integrals depend on the TBP, the spectrum approaches a rectangular form for high values of TBP. Concerning the phase of the frequency spectrum defined in (108), it can be written as a sum of two terms $\vartheta_1(f)$ and $\vartheta_2(f)$:

$$\begin{cases}\vartheta_1(f)=-\dfrac{\pi}{\kappa}(f-f_c)^2=-\pi\,TBP\left(\dfrac{f-f_c}{B}\right)^2\\ \vartheta_2(f)=\tan^{-1}\left[\dfrac{Q(U_1)+Q(U_2)}{L(U_1)+L(U_2)}\right]\end{cases} \tag{109}$$

In Fig.23 is displayed the second term $\vartheta_2(f)$, where it can be noticed that it is constant and equal to $\pi/4$ within the signal bandwidth. The approximation to a constant value is better for high values of TBP . Therefore, for high value of TBP the phase of the signal is given by the quadratic function of frequency represented by $\vartheta_1(f)$ plus the constant $\pi/4$.

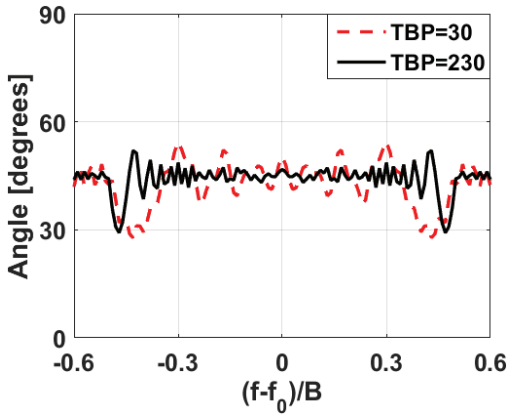

Fig.23: The phase distortion term $\vartheta_1(f)$ of the spectrum of two linear chirps having different TBP values.

3.5.3 Pulse compression

After transmitting a linear chirp inside a medium, the received echoes must be compressed to restore a good resolution in the final image. This filtering step (also called pulse compression) is achieved by correlating the received signals with the transmitted chirp. Several pulse compression techniques with different advantages/disadvantage exist, and the most used of them are described in the following parts.

3.5.3.1 Inverse filter

As it was previously shown in (69), (86) and (93), in a noiseless acquisition, the received backscattered echoes at an element I of the probe can be written as follows:

$$y_i(t) = a(t) * h_I(t) * g_i(t) \tag{110}$$

where $g_i(t)$ represents the impulse response of the medium to the corresponding insonification seen by the ith element. Thus, $g_i(t)$ represents the signal that one would obtain if the excitation used was a perfect Dirac delta function. In such conditions, the signals $g_i(t)$ become very suitable data for the image reconstruction. Thus, at this point one needs to obtain from the received data $y_i(t)$ the signals $g_i(t)$. By writing (110) in frequency domain one can obtain:

$$Y_i(f) = A(f).H_1(f).G_i(f) \tag{111}$$

where the capital letters stand for the Fourier transforms of the corresponding temporal signals. From (111), it can be seen that by multiplying the right and the left term of the equation by $1/A(f)$ one can obtain the following relation:

$$H_1(f)\cdot G_i(f)=\frac{Y_i(f)}{A(f)}=H_{INVERSE}(f)\cdot Y_i(f) \tag{112}$$

where $H_{INVERSE}(f)=1/A(f)$. As it can be seen in (112), the filter $H_{INVERSE}(f)$ allows reconstructing exactly the signals $h_1(t)*g_i(t)$ thus providing the best achievable image resolution (that corresponds to the resolution that one would achieve if the transmitted signal was a very short impulsion (Dirac delta function)) **[Cook (1993); Misaridis (1999)]**. However this filter is unstable in presence of noise (because of the spectra division in (112) that can amplify the noise in the frequency bands where the spectrum of $A(f)$ is close to zero).

3.5.3.2 Matched filter

As previously seen, the inverse filter performs poorly in presence of noise, thus a more stable filter is needed. The theory of matched filter was developed in the 1950s to optimize target detection in radar systems. The matched filter is a linear time-invariant filter that works by correlating a known signal with an unknown signal to detect the presence of the known signal. A matched filter optimizes the probability of the detection by maximizing the $eSNR$ in the presence of white Gaussian noise. Its impulse response is equal to the time reversal of the transmitted signal with a time shift τ_d. For the real signal $a(t)$, defined in (97), the impulse response of the matched filter is given by **[Cook (1993); Misaridis (1999)]**:

$$h_{matched}=a(\tau_d-t) \tag{113}$$

The transfer function of the matched filter is the complex conjugate of the signal spectrum. It can be written as:

$$H_{MATCHED}(f)=e^{-j2\pi f\tau_d}\ A^*(f) \tag{114}$$

The matched filter can be generalized taking into account the non-white noise in the imaging system. Let us call $N(f)$ the power density of this noise which depends on frequency. In this case, the expression of the transfer function becomes:

$$H_{MATCHED}(f)=e^{-j2\pi f\tau_d}\ \frac{A^*(f)}{N(f)} \tag{115}$$

3.5.3.3 Wiener filter

The matched filter offers a good stability with respect to the acquisition noise, however it provides a much lower temporal resolution than the inverse filter. Thus, a need for a filter that provides a trade-off between the achievable temporal resolution and noise stability, arises. A filter that is able to provide such a trade-off is the Wiener filter **[Gordon (1987); Oppenheim (1989); Benane (2018a)]**:

$$H_{WIENER}(f)=\frac{A^*(f)}{|A(f)|^2+SNR(f)^{-1}} \tag{116}$$

As it can be seen in (116), if the signal to noise ratio of the received signals $y_i(t)$ is very high, we have:

$$H_{WIENER}(f) \approx \frac{1}{A(f)} \quad \left(\text{for: } SNR(f)^{-1} \ll A(f)^2\right) \tag{117}$$

One can conclude that, for high values of $SNR(f)$, the Wiener filter becomes an inverse filter. In the presence of high acquisition noise, the $SNR(f)$ value becomes smaller and in this case (116) can be written as:

$$H_{WIENER}(f) \approx \frac{A^*(f)}{SNR(f)^{-1}} \quad \left(\text{for: } SNR(f)^{-1} \gg A(f)^2\right) \tag{118}$$

Comparing (115) and (118), it can be deduced that, for high levels of acquisition noise, the optimal pulse compression filter is a matched filter.

3.5.3.4 Compression filter performance assessment

In order to compare the performance of the three previously detailed filters, two cases must be analyzed. The first one without noise and the second one in presence of noise, which is more close to the reality.

Suppose the noiseless received signal showed in Fig. 24a. This signal was obtained after a chirp transmission using a plane wave transmission scheme. The result obtained after the compression using the inverse filter is represented as a dashed green line in Fig. 24b. As one can observe the provided resolution of the main lobe is not a Dirac impulsion as expected. Indeed, the obtained result represents the convolution between the acousto-electrical impulse response of the probe in emission and reception. The result of the matched filter (dashed red line in Fig.24b and Fig.24c) applied to the noiseless received data shows that the provided resolution is lower than the one obtained by the inverse filter. Finally the Wiener filter results (solid black line in Fig.24b and Fig.24c) shows that the wiener filter allows to achieve resolution comparable to the one provided by the inverse filter.

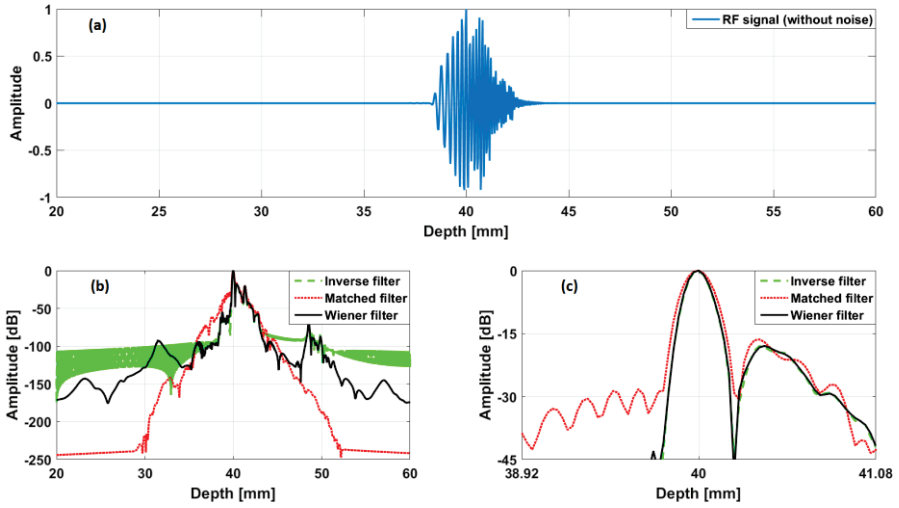

Fig.24: (a) RF signal without noise, (b) the obtained envelope after compression with the three filters described previously, (c) zoom on the envelope shown in (b).

However the performance of the same three filters applied to a noisy (eSNR=20dB) acquisition data (Fig.25a) helps to assess the limits of the inverse filter. In fact, one can observe that while the level of noise after compression for the matched and Wiener filters are still acceptable for ultrasound domain (around -50 dB), the result provided by the inverse filter is completely overwhelmed by noise. This behavior of the inverse filter is the result of the noise amplification that happens during the division of the spectrum of the received signal (that is noisy thus contains large number of non-null frequency channels) by the spectrum of the transmitted signal (that is finite thus has null frequency channels). The Wiener filter compensates this effect by adding a non-null value in the frequency channels where the transmitted signal is very low, thus stabilizing the result with respect to noise. However the payoff for this improvement is a slight loss in resolution (Fig.24c). Finally, the matched filter is the filter that is the most stable with respect to noise as it can be observed in Fig.25b (the red dashed line goes way below the Wiener and inverse filter curves). This result however comes together with a significant loss in provided main lobe resolution (Fig.25c) with respect to the Wiener filter. Thus, it can be concluded that in a noisy environment, the most reliable way to proceed in order to compress the received data is by designing a Wiener filter that is stable to the specific amount of noise present in the acquisition. In such way, the result will provide both a good spatial resolution and a noise stability.

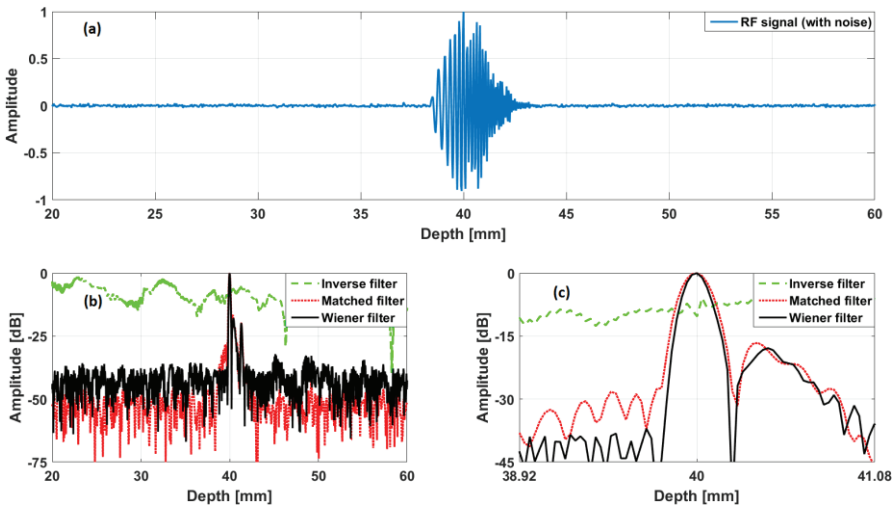

Fig.25: (a) RF signal with a 20 dB additive noise, (b) the obtained envelope after compression with the three filters described previously, (c) zoom on the envelope shown in (b).

3.5.4 Resolution Enhancement Compression (REC)

REC is a coded excitation and pulse compression technique that enhances the bandwidth of an ultrasonic imaging system and improves the axial resolution of the image. It is based on the following convolution equivalence:

$$a(t) * h_1(t,x) = \tilde{a}(t) * h_2(t,x) \tag{119}$$

where, as shown in Fig.26, $h_1(t,x)$ is the pulse-echo impulse response of the ultrasound probe element. $h_2(t,x)$ is the desired pulse-echo impulse response of an array element that has a larger bandwidth than $h_1(t,x)$. x is the lateral position of the element and t represents time dependence.

$\tilde{a}(t)$ is a linear frequency modulated chirp that excites the bandwidth of the desired impulse response ($h_2(t,x)$) and $a(t)$ is the pre-enhanced chirp used to excite the elements of the probe. At this point, one can make the hypothesis that all the elements of the probe have approximately the same pulse-echo impulse response, which means that x can be removed from (119), which gives $h_i(t) = h_i(t,x),\ \forall x, i \in \{1,2\}$. Under such assumptions relation (119) becomes:

$$a(t) * h_1(t) = \tilde{a}(t) * h_2(t) \tag{120}$$

By solving (120) in the frequency domain, the temporal convolution becomes a point-wise spectrum multiplication and the pre-enhanced chirp can be calculated by the following equation:

$$A(f) = \tilde{A}(f) \times \psi(f) \quad \left(\text{with: } \psi(f) = \frac{H_2(f)}{H_1(f)} \right) \tag{121}$$

In order to obtain a good approximation of $A(f)$, [**Oelze (2007)**] proposed to replace $\psi(f)$ in (121) with the following filter:

$$\psi(f) = \frac{H_1^*(f) H_2(f)}{|H_1(f)|^2 + |H_1(f)|^{-2}} \tag{122}$$

where the $(\,)^*$ symbol denotes the complex conjugate. Multiplying the pre-enhanced chirp $A(f)$ with a Tukey-cosine window with a 20% taper was also proposed in order to reduce side-lobe levels [**Chiao (2005)**].

Once $a(t)$ is transmitted, the compression of the reflected echoes from the medium is achieved by multiplying the frequency spectra of the received signals with a Wiener filter defined as:

$$\beta_{REC}(f) = \frac{\tilde{A}'^*(f)}{\left|\tilde{A}'(f)\right|^2 + \gamma \overline{eSNR}(f)^{-1}}, \tag{123}$$

where $\overline{eSNR}(f)$ is the average signal-to-noise ratio per frequency channel of the received signals. γ is a smoothing parameter that controls the trade-off between the bandwidth enhancement (better axial resolution), the $eSNR$ gain and the sidelobe level. Low γ values for which $\beta_{rec}(f)$ becomes an inverse filter improve axial resolution but increase the sidelobe level which results in a decreased $eSNR$ whereas high γ values, for which $\beta_{rec}(f)$ becomes a matched filter, have the opposite effect. In (123), $\tilde{A}'(f)$ is slightly different from $\tilde{A}(f)$ ($\tilde{A}'(f) \neq \tilde{A}(f)$) that was used to generate the pre-enhanced FM chirp in (121). This discrepancy is due to the tapering of the pre-enhanced FM chirp that cancels the perfect match of the convolution product. In order to preserve the convolution equivalence, it is necessary to recalculate the modified linear FM chirp generated from the pre-enhanced one using the following equation:

$$\tilde{A}'(f) = A(f) \times \frac{H_1(f)}{H_2(f)} \tag{124}$$

The advantage of using $\tilde{A}'(f)$ over $\tilde{A}(f)$ is that the compression using this new linear FM chirp yields a better image quality, in particular by lowering the sidelobe level.

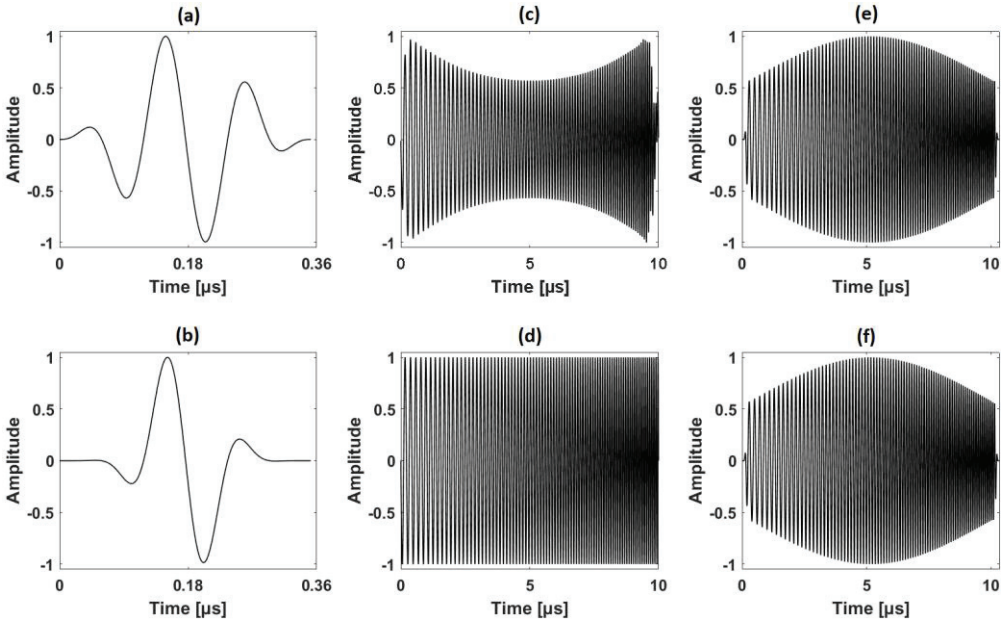

Fig. 26. Pulse/echo impulse responses, chirps and the resulting convolution products involved in the REC scheme. (a) is a pulse with 100% −6 dB pulse/echo bandwidth. (b) is a pulse with approximately 200% -6 dB pulse/echo bandwidth. (c), modified chirp used to excite h_1. (d), linear chirp used to excite h_2. (e) and (f) Convolution of the pulses with their respective chirp sequences.

In Fig.27a, are displayed the spectra of both impulse responses used for the REC computations and also the spectrum of the pre-enhanced chirp used as the excitation. As one can notice, the shape of the pre-enhanced chirp spectrum is different than the one of a normal linear chirp. This effect of increasing the amplitude of the chirp frequency channels, that correspond to non-efficient frequency bands in the probe bandpass, represents the core principle of REC. As it can be seen in Fig.27b, this pre-enhancement results in echo waveforms (solid black line) that have a significantly larger bandwidth and thus that have the potential to provide better image resolution. In the same time, in Fig.27b it can be seen that if no pre-enhancement is done, the bandwidth of the received echoes (black line containing round points) would follow exactly the bandwidth of the probe $H_1(f)$ (dashed black line).

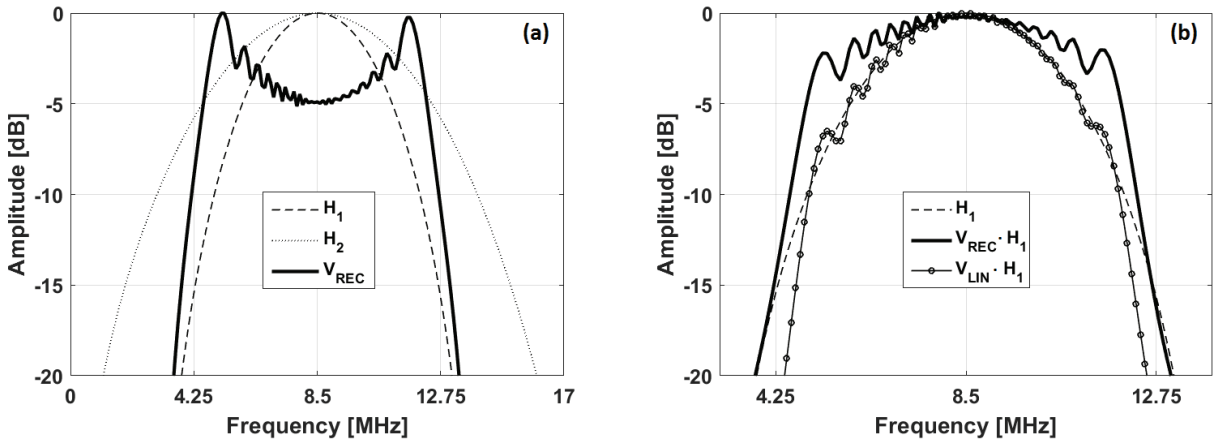

Fig.27. (a) - Spectra of the real impulse response, the fictive impulse response and the pre-enhanced chirp signal, (b) – Spectrum of the probe impulse response $H_1(f)$, spectrum of the echoes generated by the pre-enhanced excitation signals and by the excitation signals without any enhancement.

PART II: CONTRIBUTION 1

Chapter IV

RESOLUTION ENHANCEMENT COMPRESSION USING COHERENT PLANE WAVE COMPOUNDING

Contents

4.1 Introduction

As it was demonstrated in the previous chapters, in ultrasound, the transmission / reception schemes that enhance the frame acquisition rate come together with an inherent trade-off for the echo signal to noise ratio, which is due to the lack of emission focalisation. Plane wave imaging is such an emission scheme that, as previously mentioned, employs broad insonifications of the medium in order to reconstruct full B-mode images at once. Pulse compression techniques, can be applied to plane wave imaging to increase the echo signal to noise ratio, however as demonstrated in [**Lashkari (2016, Nowicki (2007)**] the provided image resolution is capped by the pulse-echo acousto-electrical impulse response of the probe. As shown at the end of Chapter III, REC allows overcoming the drawbacks generated by the bandwidth of the ultrasound probe by transmitting an amplitude modulated chirp with increased energy at the frequencies where the ultrasound probe is less efficient. Thus, this study aims to combine REC technique with coherent plane wave compounding (CPWC) in order to merge the advantages of both of these techniques. Namely, REC would allow CPWC to gain in terms of axial resolution, SNR and CNR at very high frame acquisition rates. To summarize, the proposed solution consist in the following steps: first, using the probe's pulse echo impulse response, the pre-enhanced excitation signals are generated. Second, these signals are emitted using the CPWC emission scheme. Then, once all the echoes are received they are compressed using the corresponding Wiener filter. Finally the results are beamformed using a delay and sum algorithm, and the images obtained after each plane wave insonification are coherently added in order to obtain a final, improved image.

4.2 Theoretical background

As it was shown in Section 3.4.3, the received backscattered echoes from a full insonification of the medium using a plane wave k can be written as:

$$y_i^{PW}(t) = w_i e^k(t) * \sum_{j=1}^{N_e} w_j \sum_{l=1}^{N_s} TRF_l \frac{\delta\left(t - t_j^k - \frac{\left\| \vec{r_l} - \vec{r_{S_j}^0} \right\|_2 + \left\| \vec{r_l} - \vec{r_{S_i}^0} \right\|_2}{c_0} \right)}{4\pi^2 \left\| \vec{r_l} - \vec{r_{S_j}^0} \right\|_2 \left\| \vec{r_l} - \vec{r_{S_i}^0} \right\|_2} \tag{125}$$

where N_s represents the number of scatterers inside the medium, $\vec{r_{S_j}^0}$ and $\vec{r_{S_i}^0}$ are the position of the element j and i respectively. Suppose now an echo generated by a single scatterer l, the corresponding received signal can be written as:

$$y_i^{PW}(t) = w_i \sum_{j=1}^{N_e} w_j TRF_l \frac{e^k\left(t - t_j^k - \frac{\left\| \vec{r_l} - \vec{r_{S_j}^0} \right\|_2 + \left\| \vec{r_l} - \vec{r_{S_i}^0} \right\|_2}{c_0} \right)}{4\pi^2 \left\| \vec{r_l} - \vec{r_{S_j}^0} \right\|_2 \left\| \vec{r_l} - \vec{r_{S_i}^0} \right\|_2} \tag{126}$$

It can be seen in (126), that the received signal is a weighted (by w_j, w_i, $1/4\pi^2 \left\| \vec{r_l} - \vec{r_{S_j}^0} \right\|_2 \left\| \vec{r_l} - \vec{r_{S_i}^0} \right\|_2$) superposition of slightly delayed (by $t_j^k - \left[\left\| \vec{r_l} - \vec{r_{S_j}^0} \right\|_2 + \left\| \vec{r_l} - \vec{r_{S_i}^0} \right\|_2 \right] / c_0$) versions of the transmitted

waveform $e^k(t) = a^k(t) * h_1(t)$. Thus it can be seen that, if a compression filter (matched or Wiener) adapted only to the excitation waveform $a^k(t)$ is applied to the signal $y_i^{PW}(t)$, the obtained resolution is the one set by the pulse echo impulse response of the probe $h_1(t)$. In other words, for ultrasound probes with lower bandwidths, the provided image resolution is degraded.

Now, let us consider an ideal hypothetical case, where a transducer of acousto-electrical pulse echo impulse response $h_2(t)$ (Fig.28d), of bandwidth larger than the one of $h_1(t)$ (Fig.28a), and no frequency dependent tissue attenuation effect is present into the medium. In these conditions, the relation (126) becomes:

$$\tilde{y}_i^{PW}(t) = w_i \sum_{j=1}^{N_e} w_j TRF_l \frac{\tilde{e}^k\left(t - t_j^k - \frac{\left\| \vec{r_l} - \vec{r_{S_j}^0} \right\|_2 + \left\| \vec{r_l} - \vec{r_{S_i}^0} \right\|_2}{c_0} \right)}{4\pi^2 \left\| \vec{r_l} - \vec{r_{S_j}^0} \right\|_2 \left\| \vec{r_l} - \vec{r_{S_i}^0} \right\|_2} \tag{127}$$

with $\tilde{e}^k(t) = \tilde{a}^k(t) * h_2(t)$ (Fig.28f). In the previous relation, $\tilde{a}^k(t)$ (Fig.28e) is a chirp that covers all the bandwidth of $h_2(t)$. Inarguably the potential resolution provided by $\tilde{e}^k(t)$ is better than the one of $e^k(t)$ since $h_2(t)$ has a larger bandwidth than $h_1(t)$ and since no attenuation effect is present.

The core principle of our method relies on the equivalence between $e^k(t)$ and $\tilde{e}^k(t)$ which implies:

$$a^k(t) * h_1(t) = \tilde{a}^k(t) * h_2(t) \tag{128}$$

(127) represents an equivalent of the REC expression described in Section 2.5.4, thus it allows to compute the excitation signal of the real transducer $a^k(t)$ (Fig.28b) that needs to be used in order to obtain the same resolution as the fictive transducer, of wider bandwidth, excited with $a^k(t)$. Applying the same reasoning as in (120) and (122), it can be deduced that the excitation signal $a^k(t)$ can be generated using:

$$A^k(f) = \tilde{A}^k(f) \frac{H_1^*(f) H_2(f)}{|H_1(f)|^2 + |H_1(f)|^{-2}} \tag{129}$$

Finally, using (123) the Wiener filter needed to compress the echoes $e^k(t)$ can be written as:

$$\beta_{REC}(f) = \frac{(\tilde{A}'^k)^*(f)}{\left|\tilde{A}'^k(f)\right|^2 + \gamma \overline{eSNR}(f)^{-1}}, \tag{130}$$

with $\tilde{A}'^k(f) = \frac{\tilde{A}^k(f) H_1(f)}{H_2(f)}$.

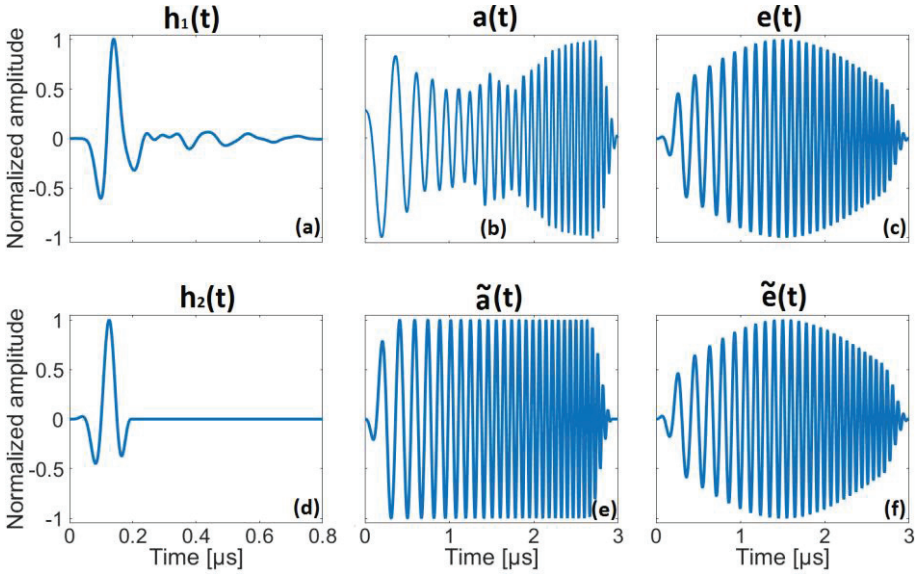

Fig.28. Pulse/echo impulse responses, chirps and the resulting convolution products involved in the REC scheme. (a) is a pulse with approximately 92% −6 dB pulse/echo bandwidth. (d) is a pulse with approximately 125% -6 dB pulse/echo bandwidth. (b) is a modified chirp used to excite (a). (e) is a linear chirp used to excite (d). (c) and (f) are the convolution products of the pulses with their respective chirp sequences.

4.3 Simulation results

4.3.1 Simulation setup

In order to validate the theory described previously, simulations were performed using CPWC. The pulse-echo impulse response $h_1(t)$ was measured experimentally from a reflexion on a planar surface immersed in water after transmission and reception with the central element of the LA523E probe (Esaote, Florence, Italy). Two different excitations were used: $cp(t)$ composed of a half sinusoid and the pre-enhanced chirp $a(t)$ compressed by the modified Wiener filter. $cp(t)$ and $a(t)$ signals are centred at 8.5 MHz (the center frequency of the pulse/echo impulse response of the probe $h_1(t)$) with a fractional bandwidth of 92 % and 142 % at -6 dB, respectively. The simulations were conducted using Field II **[Jensen (1992); Jensen (1996)]**. For the CPWC, an angular aperture of 16° was divided into nine different directions equally spaced by 2°. On the ultrasound probe, only the 64 central elements were used for both transmit and receive. The simulation parameters are detailed in Table II.

Two different simulations were performed:

1- A wire phantom in water (without attenuation), the purpose being to validate the theoretical performance of the CPWC-REC approach.

2- Thirteen scatterers closely placed in an arrangement that allows evaluating the ability of the imaging system to resolve very close scatterers. In this case, the attenuation coefficient was set to 0.5 dB/MHz/cm which is a typical value for human liver.

A white Gaussian noise (AWGN, eSNR ≈ 20 dB) was added to the RF data (for both simulations) prior to beamforming (**[Tanter (2014); Garcia (2013)]**) in order to evaluate the performance of the Wiener filter used for compression in presence of observation noise.

Table II. Parameters used in the simulation and experimental setups

Parameter	Value
Linear piezoelectric array	
Kerf	30 µm
Pitch	245 µm
Central frequency	8.5 MHz
Total number of elements	192
Number of active elements	64
Effective aperture	15.68 mm
Plane Wave i	
Steering angle θ_i	2x(i-4) °, i ∈ {0 ; 8}
Aperture angle	16°
Sampling frequency	50MHz
Transmission	
Transmitted signal	cp(t) / a(t) (Fig. 28)
Length	0.06 µs / 3 µs

4.3.2 Simulation 1 (without attenuation)

The obtained B-mode images for both excitations are shown in Fig. 29.

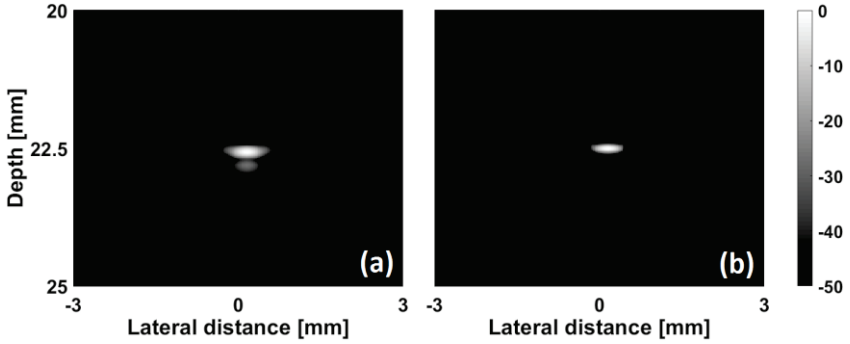

Fig.29. B-mode images obtained with CPWC-CP (a) and CPWC-REC (b).

The B-mode images show that CPWC-REC was capable of properly compressing the RF data. The envelope profile of the scatterer is displayed in Fig.30a and Fig.30b. It can be qualitatively observed that REC allowed obtaining a better spatial resolution. As shown in Fig.27c, this improvement was quantified through the calculation of the MTF derived from the envelope data. In particular, the wave numbers k_0 at which the MTFs decreased by -20 dB were 16.1 mm^{-1} and 23.9 mm^{-1} for CP and REC, respectively. These results yield a resolution enhancement from CPWC-CP to CPWC-REC of 48.5%.

The power spectra of the scatterer in Fig.29 using both CPWC-CP and CPWC-REC approaches are shown in Fig.30d. In accordance with the improvements in the MTF, the -6 dB bandwidths were 3.9 MHz and 6.0 MHz, respectively, corresponding to a 53.5% bandwidth boost.

The resulting eSNR for CPWC-CP and CPWC-REC was 28.3 dB and 35.9 dB respectively, which correspond to a 7.6 dB improvement. Theoretically this gain is given by the TBP of the linear chirp which is equal to 36.3. This TBP yields an enhancement of 15.6 dB over the classical pulsing

technique. The difference (8 dB) between the theoretical value and the one given by CPWC-REC is due to the γ parameter of the Wiener filter that is tuned to enhance the resolution.

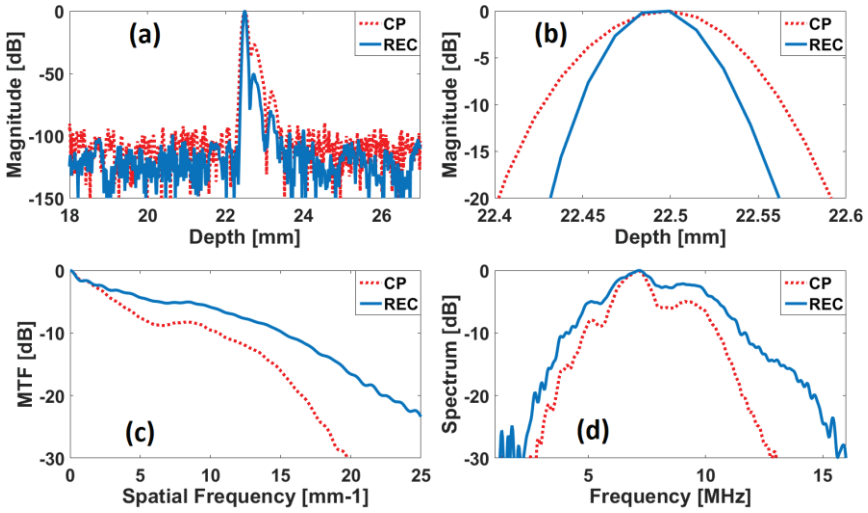

Fig.30. Comparison of performance between CPWC-REC (solid line) and CPWC-CP (dashed line). (a) Envelope of the radiofrequency data of the scatterer. (b) Zoom of the envelope shown in (a). (c) MTF derived from the envelope. (d) Normalized spectrum derived from the radiofrequency data.

4.3.3 Simulation 2 (with attenuation)

The obtained B-mode images are shown in Fig. 31.

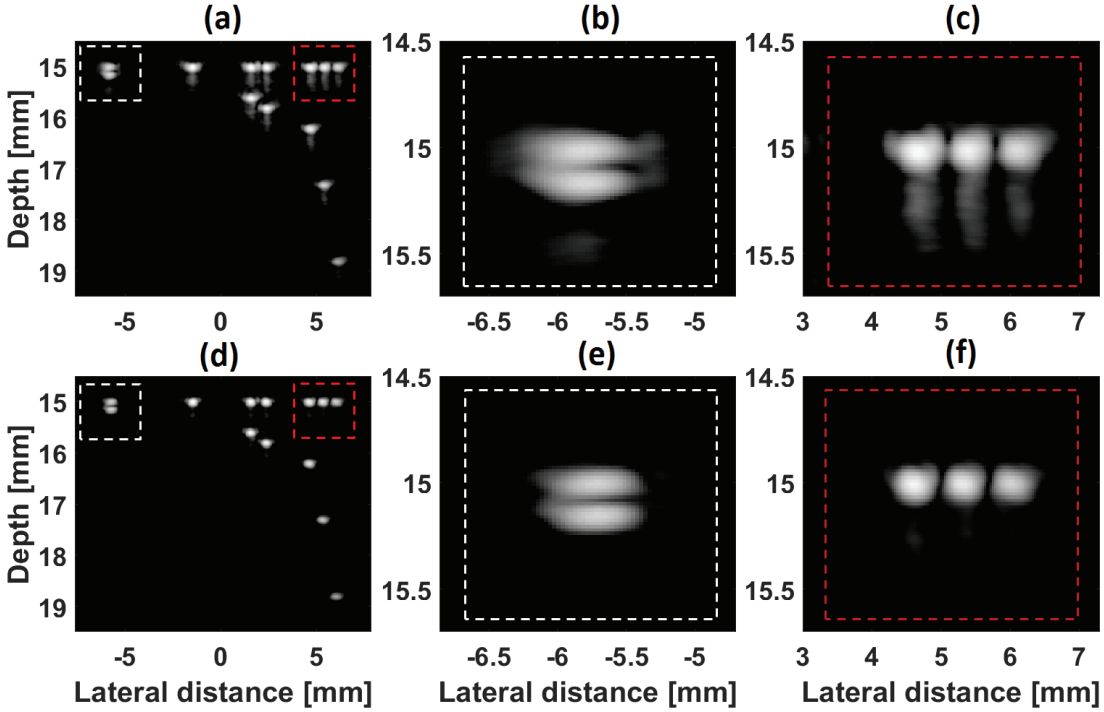

Fig.31. B-mode images obtained with CPWC-CP ((a), (b), (c)) and CPWC-REC ((d), (e), (f)). (b) and (e) are a zoom on two points very close axially on the left side of the images. (c) and (f) are a zoom on three points very close laterally on the right side of the images. All images have a dynamic range of 50 dB.

The envelope of the scatterer placed at 15 mm depth and -1 mm lateral position is displayed in Fig. 32a and Fig.32b. One can observe that CPWC-REC allowed obtaining a better spatial resolution despite the presence of attenuation effect. As shown in Fig.32c, the MTF in the CPWC-REC image was enhanced from 15.8 mm^{-1} to 18.8 mm^{-1} in comparison with CPWC-CP image. These results yield a resolution enhancement of 19.0%.

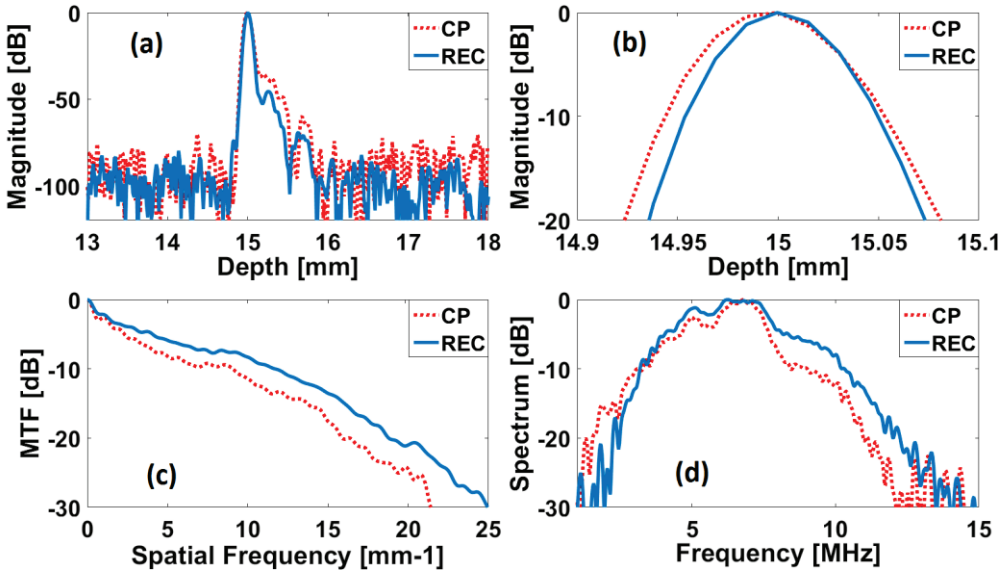

Fig.32. Comparison of performance between CPWC-REC (solid line) and CPWC-CP (dashed line). (a) Envelope of the radiofrequency data of the scatterer placed at 15 mm depth and -1 mm lateral position. (b) Zoom of the envelope shown in (a). (c) MTF derived from the envelope. (d) Normalized spectrum derived from the radiofrequency data.

Fig.32d shows the improvements in the power spectra of the beamformed received signals. The -6 dB bandwidths were 3.7 MHz and 5.2 MHz, respectively, corresponding to a 40.5% bandwidth boost.

CPWC-CP and CPWC-REC yields an eSNR of 23.7 dB and 26.9 dB respectively. The proposed approach improves therefore the eSNR by 3.2 dB.

The lateral resolutions of the images obtained using both CP and REC were also compared. In order to have a smoother visualization of the lateral envelope, a linear interpolation by a factor of 8 was chosen to increase the number of vertical lines in the image ($64 \rightarrow 512$). As it can be observed in Fig.33, CPWC-REC improves the lateral resolution by 11% in comparison to CPWC-CP (452.3 µm and 502.1 µm for CPWC-REC and CPWC-CP, respectively).

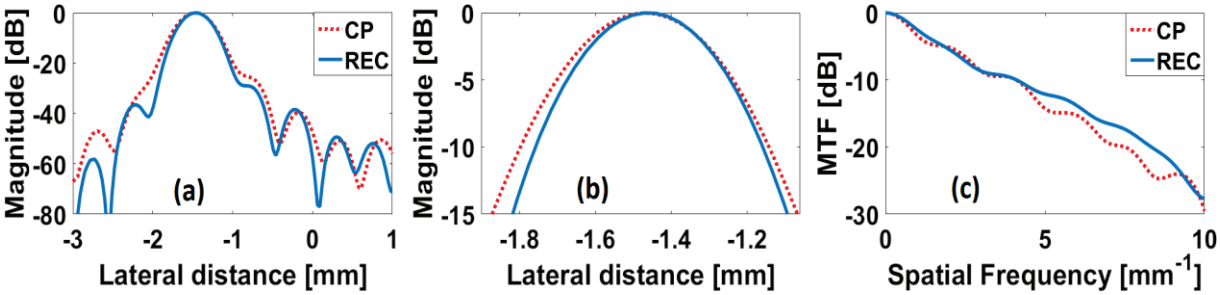

Fig.33. (a) Lateral envelope of the point spread function (PSF) of the same scatterer studied in Fig.6. (b) Zoom of the envelope shown in (a). (c) MTF derived from the envelope shown in (a).

The enhancement in the axial resolution is still obvious for the other scatterers. The axial and lateral envelopes of the scatterers closely distributed axially (Fig.31b-e) and laterally (Fig.31c-f) are reported in Fig.33. From the envelope obtained using CPWC-REC, one can note that the locations of the scatterers are correctly found after compression. Moreover, the envelope plots reveal that all the scatterers are better resolved axially (Fig.34a) and laterally (Fig.34b), using CPWC-REC technique than using CPWC-CP. The sidelobe levels were detected to be below the noise floor (SNR of ~35 dB in the compressed waveform).

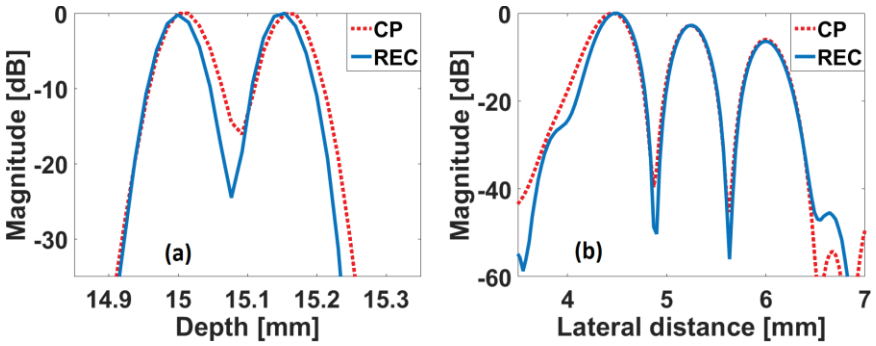

Fig.34. (a) Resolution of two axially close scatterers. (b) resolution of three laterally close scatterers.

4.4 Experimental results

For experimental implementation, the open ultrasound platform UlaOp-64 (Microelectronics System Design Lab, Florence, Italy) equipped with a LA523E linear array probe was used. UlaOp-64 can transmit arbitrary waveforms defined by customized transmission and reception strategies **[Tortoli (2009)]**. The LA523E specifications and the acquisition parameters are presented in Table II. The same pulse-echo impulse response $h_I(t)$ as in simulations was used in order to generate the pre-enhanced chirp. The excitation signals for the UlaOp-64 were generated with a sampling frequency of 600MHz while the received signals were sampled at 50MHz. Thus, the received signals were up-sampled to 600MHz in order to compress them at the same sampling frequency. The excitation signals are shown in Fig.35. The same bandwidths as in simulation setups were used.

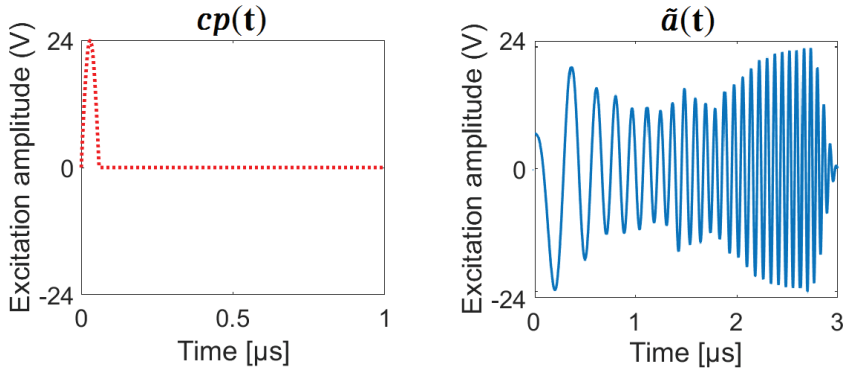

Fig.35. CPWC-CP (left) and CPWC-REC (right) excitation signals used for experimental acquisitions.

4.4.1 Acquisition on a single scatterer media

The first set of measurements contained the backscattered signals recorded from a single nylon wire with, 50 µm diameter, located at 22 mm depth. The obtained B-mode images are shown in Fig.36.

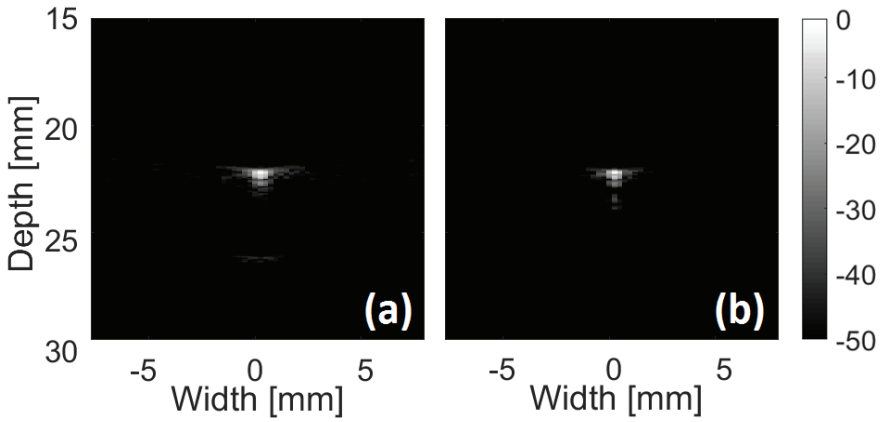

Fig.36. Log-compressed images of nylon wire obtained using the UlaOp-64 scanner: CPWC-CP (a) and CPWC-REC (b).

A graph of the wire PSF profile (axial), obtained with the conventional pulsing technique and with the CPWC-REC technique, is displayed in Fig.37a and 37b.

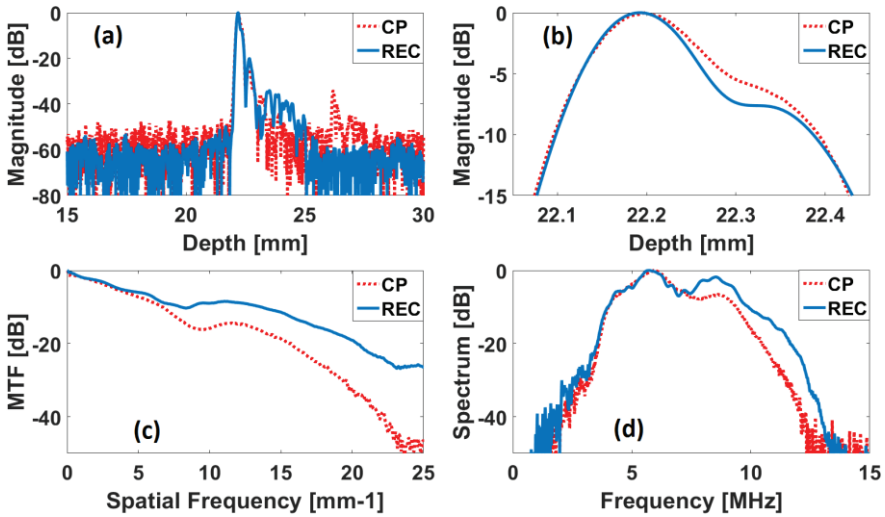

Fig.37. Comparison of performance between CPWC-REC (solid line) and CPWC-CP (dashed line). (a) Envelope of the radiofrequency data. (b) Zoom of the envelope shown in (a). (c) MTF derived from the envelope. (d) Normalized spectrum derived from the radiofrequency data.

The CPWC-REC approach successfully shows RF data compression and a lower background noise compared to CP (around 7 dB difference, see Fig.37a). The sidelobes created, from 0 dB until -40 dB, are slightly lower than the ones of CP (Fig.37a). In addition, the axial resolution derived from the MTF was improved using the CPWC-REC technique by 29%. The corresponding values are 201.7 µm / 156.3 µm for CPWC-(CP / REC) (Fig.37c).

Power spectra of the compressed waveforms using the REC technique and conventional pulsing are shown in Fig.37d. Examination of CPWC-REC power spectra reveals that more energy is carried by higher frequencies. This can be explained by the fact that, since frequencies on the bandwidth edges are excited with greater energy, the compressed waveform has a broadened bandwidth. The −6 dB pulse/echo bandwidth of the transducer impulse response ($h_1(t)$) is 7.82 MHz (92% of the central frequency). On the other hand the enhanced bandwidth of the transducer ($h_2(t)$) is 12.07 MHz (142% of the central frequency). Fig.37d shows that CPWC-REC approach boosts the -6 dB bandwidth by 49%. The measured bandwidths at -6 dB were respectively 4.65 MHz for CPWC-REC and 3.13 MHz

for CP. To be noticed, the difference between the bandwidth of the transmitted signals and the received signals is due to the propagation phenomena and the beamforming used to reconstruct the image.

The resulting eSNR for CPWC-CP and CPWC-REC was 26.6 dB and 32.1 dB respectively, which correspond to a 5.5 dB improvement.

The lateral resolution of the images obtained using both CPWC-CP and CPWC-REC was also compared. The same interpolation as in Section III-B was made ($64 \rightarrow 512$). As it can be observed in Fig.38a and 38b, REC improves the lateral resolution by 19% in comparison to CP (i.e., 644.2 µm vs. 768.6 µm).

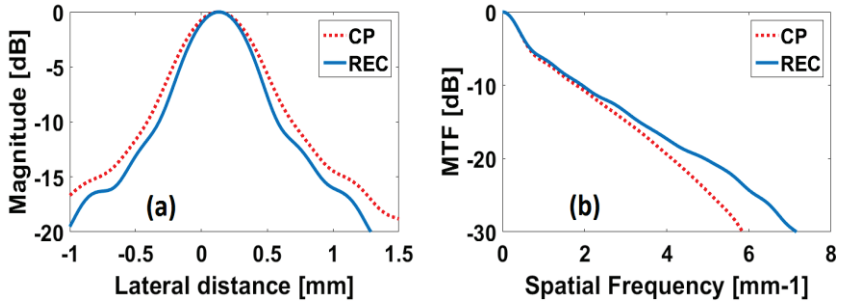

Fig.38. (a) Lateral envelope of the wire target. (b) MTF derived from the envelope shown in (a).

4.4.2 Acquisition on a cyst phantom

The proposed method was also evaluated experimentally by imaging hypoechoic cysts using an ultrasound quality assurance phantom model 410SCG HE 0.5 (Gammex Sun nuclear, Neu-Isenburg, Germany). The phantom is characterized by an attenuation coefficient of 0.5 dB/MHz/cm.

As displayed in Fig.36, the results show a significant improvement of the image quality with the CPWC-REC approach when compared to CPWC-CP. Indeed, the B-mode image obtained using CPWC-REC shows a better overall contrast than the one obtained by CPWC-CP, especially for the second cyst which appears deeper in the medium (cf Fig.39a and Fig.39b).

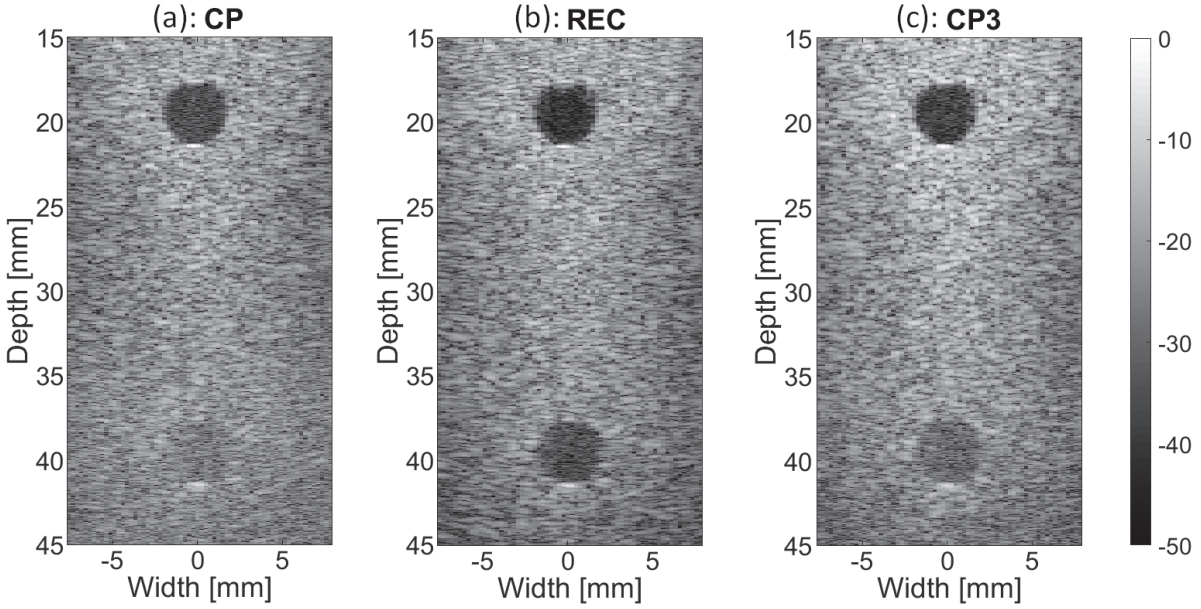

Fig.39. Log-compressed images of hypoechoic cyst obtained with nine plane waves using the UlaOp-64 scanner: (a) CPWC-CP, (b) CPWC-REC and (c) CPWC-CP3.

Once adjusted, as discussed previously, the γ parameter of the Wiener filter used for compression in the CPWC-REC approach allowed considerably extending (in post processing) the axial resolution/SNR trade-off compared to CPWC-CP. Due to the low level of energy contained in the conventional pulse ($cp(t)$), a comparison in terms of SNR and CNR was also performed with a $cp_3(t)$ weighted in the time domain with a Hanning window.

The B-mode images show that CPWC-REC combines two improvements:

- A high axial resolution, better than CPWC-CP (as previously demonstrated in part 4.4.1);
- A comparable or even better SNR and CNR (especially deeper in the medium) than CPWC-CP3, and thus better than CPWC-CP.

In order to quantify all these observations, a study of the SNR and CNR as a function of the number of transmitted plane waves is carried out in Fig. 40. The three imaging techniques yield better image quality in terms of CNR and SNR as the number of plane waves increases. For all nine compounded plane waves, CPWC-REC improves the CNR by 3.6 dB (and by 9.3 dB) for the upper (lower) cyst compared to CPWC-CP. A 1.3 dB (3dB) enhancement of the SNR for the upper (lower) cyst is also provided by the REC approach.

Moreover, for the upper cyst, CPWC-REC and CPWC-CP3 are comparable in terms of CNR (11.8 dB and 11.7 dB respectively) and SNR (17.2 dB and 16.9 dB respectively) since both transmitted signals carry more energy than CPWC-CP. The discrepancy between these two approaches increases with the depth since 4.1 dB and 1.2 dB improvement on the CNR and SNR respectively can be noticed for the lower cyst.

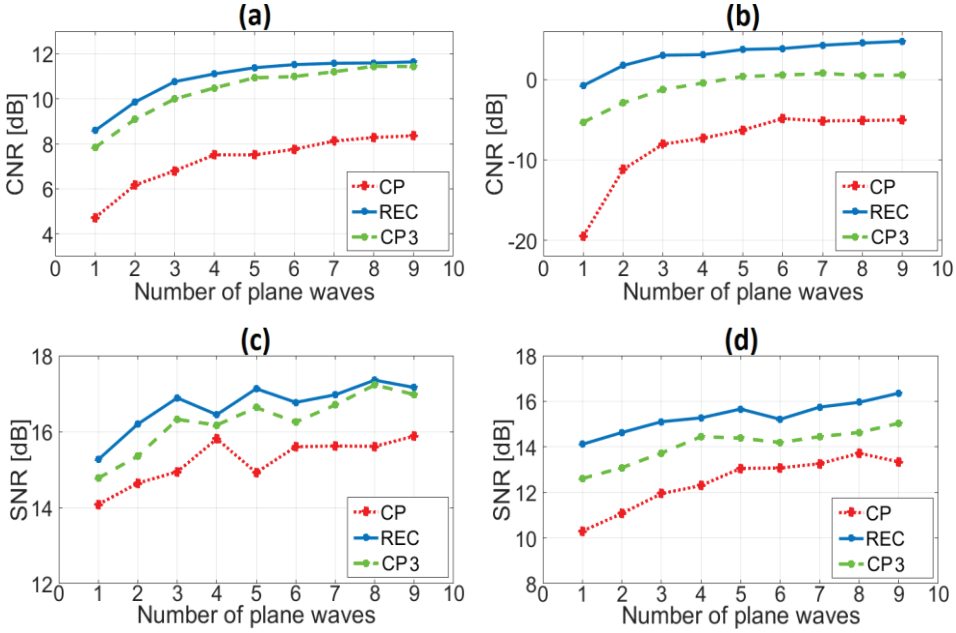

Fig.40. CNR in the upper (a) and lower (b) cyst. SNR in the upper (c) and lower (d) cyst.

Whatever the number of plane waves involved in the resulting images, Fig.40c and Fig.40d suggest that the SNR is better in the CPWC-REC case. This can be explained by the fact that more energy was transmitted and the CPWC-REC property to keep the acquisition noise from being amplified (by optimizing γ). CNR and SNR indicators decrease from the upper cyst (Fig.40a and Fig.40c) to the

lower cyst (Fig.40b and Fig.40d). This result can be explained by the fact that the backscattered echoes at higher depths have lower amplitude.
On the other hand, as it can be observed in Fig.39, CPWC-REC yields a slightly thinner speckle than CP. This is confirmed by the autocorrelation length on the axial and lateral directions as shown in Fig.41.

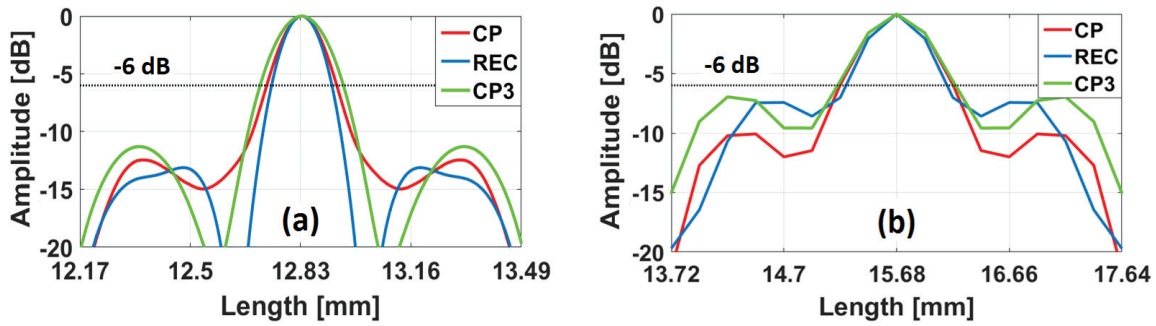

Fig. 41. Autocorrelation length in the axial (a) and lateral (b) directions around 2.5 cm depth.

Fig.41a shows an improvement of 16.3% (39.2%) for the axial autocorrelation peak at -6 dB with the CPWC-REC technique compared to the CPWC-CP (CPWC-CP3) methods. The same behaviour is observed for the lateral autocorrelation length at -6 dB, Fig.41b, where again CPWC-REC gives 12.2% (16.5%) improvement regarding to CPWC-CP (CPWC-CP3).
Finally, one can observe on the CPWC-REC image (Fig.39b) that the speckle size increases with the depth. An explanation to this effect could be the tissue attenuation of the highest frequency content of the transmitted signal. Since in CPWC-REC the wave that propagates into the medium carries a broader band signal, its highest frequencies are more attenuated than the lowest (effect also present in CPWC-CP and CPWC-CP3). In such cases, at reception, the Wiener filter $\beta_{REC}(f)$, is less adapted. Thus, the compression is not optimal, which means that CPWC-REC gives better results at shallower depths (where the filter is better adapted because the effects of attenuation are less significant).

4.4.3 Pre-clinical study

All procedures were performed according to ethical guidelines and were approved by the Animal Care and Regional Commitee for Ethics in Animal Experiments, Centre-Val de Loire (N. 2016020116011353-3872). New Zealand white rabbits were purchased from Charles Rivers laboratories (Bois des Oncins, France). They were maintained at constant room temperature with 12 hours light cycle in ventilated isolation cages.The rabbits were nine weeks old at the beginning of the experiment weighing 2.3-2.7 kg.

4.4.3.1 Ex-vivo acquisitions

To validate the simulation and experimental phantom results, a set of *ex-vivo* experimental measurements were conducted on rabbit liver. This first experimental setup was chosen in order to validate the CPWC-REC performance on biological tissues, without the presence of skin, subcutaneous fat and muscles, which have a higher attenuation than the internal organs **[Pan (1998)]** and cause significant phase aberration **[Hinkelman (1998)]**.

As depicted in Fig.42, the CPWC-REC technique yields better results than CP. The contrast between the anechoic part of the medium (water in which the liver was submerged) and the adjacent echogenic

area (the liver) is higher for CPWC-REC. The corresponding CNR and SNR improvements are 4.4 dB and 0.45 dB respectively.

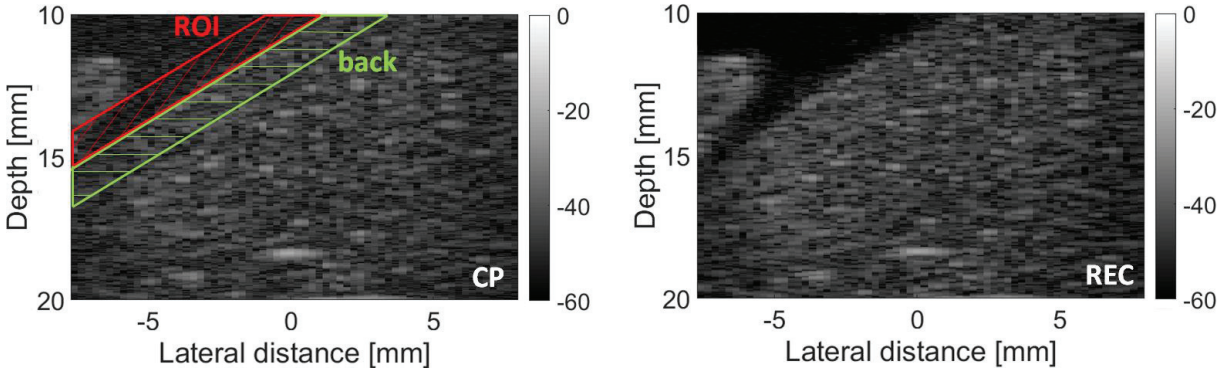

Fig.42. Log-compressed images of a part of a rabbit liver obtained using the UlaOp-64 scanner: CPWC-CP (left) and CPWC-REC (right).

These results are also visible on the CNR curve presented in Fig.43a. The CNR obtained with CPWC-REC with only one transmitted plane wave is higher than the CNR obtained with CPWC-CP using nine transmitted plane wave (Fig.43a). Therefore, this result suggests CPWC-REC is capable of achieving a better CNR at a higher frame acquisition rate than CPWC-CP. Qualitatively speaking, the anechoic part of the medium presented in the two images (Fig.42) is less noisy in the CPWC-REC image. This result is demonstrated by the evolution of the SNR shown in Fig.43b, where the SNR achieved by CPWC-REC with about two plane wave emissions is approximately equivalent to the SNR obtained with CPWC-CP with nine plane wave emissions.

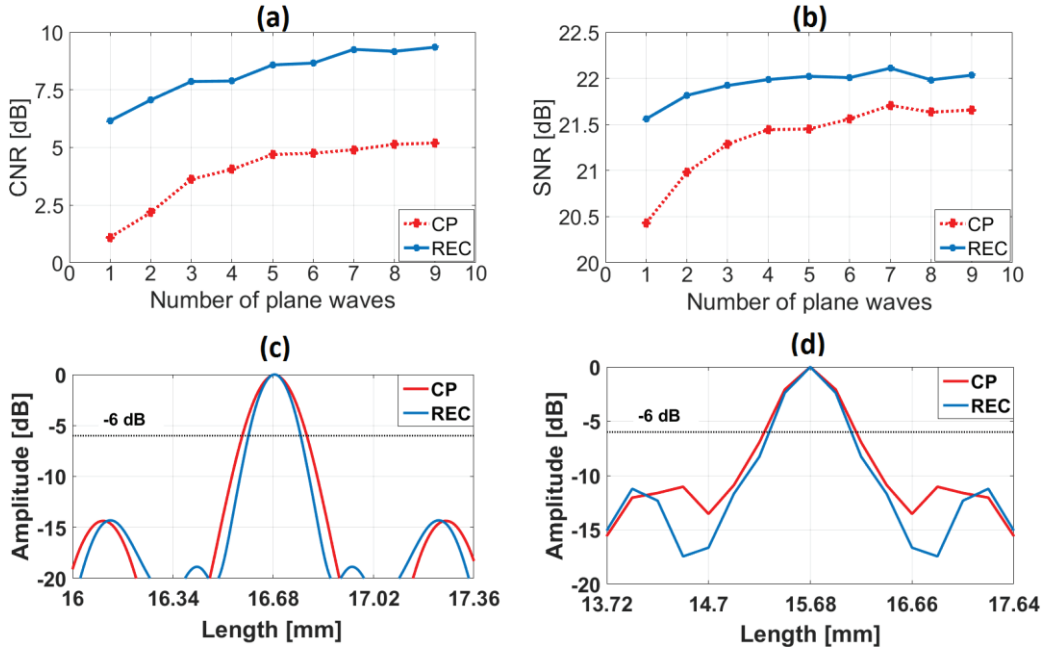

Fig.43. Evolution of (a) CNR and (b) SNR with CPWC-REC and CPWC-CP in rabbit liver images as a function of the number of plane waves. Autocorrelation length in the axial (c) and lateral (d) directions for CPWC-REC and CPWC-CP.

In addition, one can observe that CPWC-REC exhibits a thinner speckle than CPWC-CP specially in the axial direction as confirmed by the autocorrelation length graphs calculated in the axial (Fig.43c) and lateral (Fig.43d) directions. An improvement of 23% (11%) is measured at -6 dB axially (laterally). It can be noticed that the refinement of speckle size by CPWC-REC axially is more important in this case than previously for the cyst phantom. This is certainly due to the fact that, in this case, only the two first centimeters of the liver were imaged because of the experimental protocol, which limites the effects of attenuation in comparison with the previous case of the phantom. Once again, these observations leads to the conclusion that REC achieves higher image quality than CP at higher frame acquisition rate.

4.4.3.2 In-vivo acquisitions

A final experiment was conducted *in-vivo* on a rabbit that was under gaseous anaesthesia (Aerrane, Baxter, Deerfield, IL). CPWC-CP and CPWC-REC images were acquired on the animal's gallbladder. In this case, the intervening animal tissues (i.e., skin, subcutaneous fat, and muscles) were not removed, so the attenuation properties of these tissues and the presence of aberration artefacts directly affected the acquisitions results.

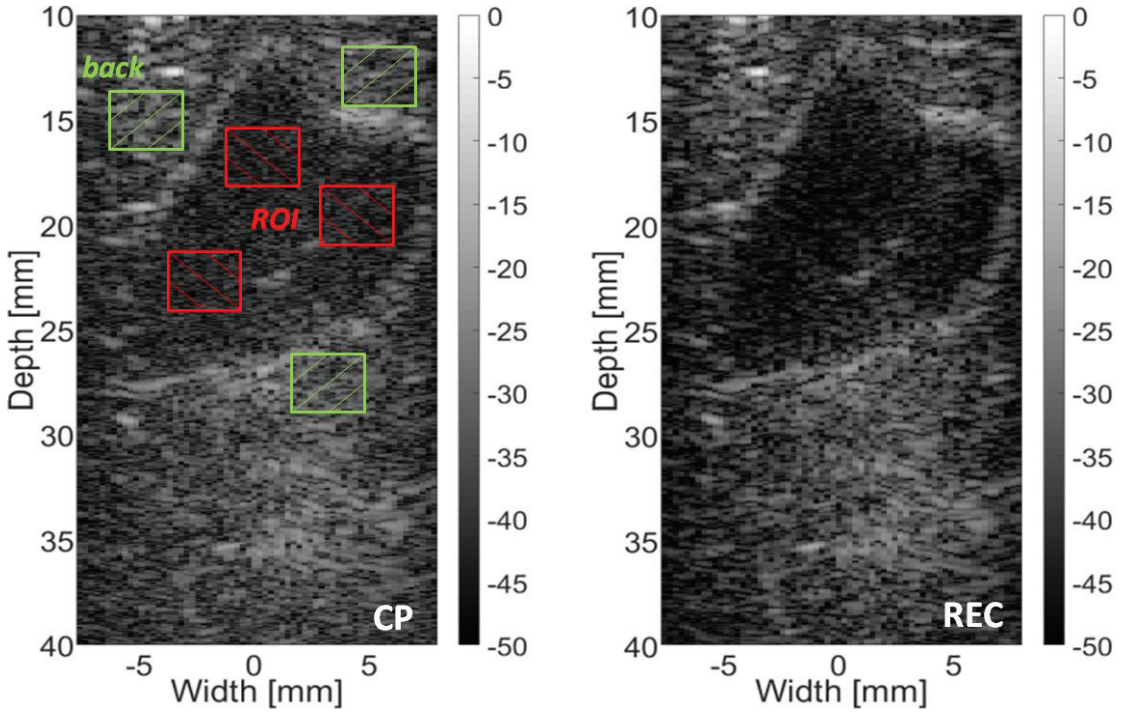

Fig.44. Log-compressed images of the gallbladder of a rabbit obtained using the UlaOp-64 scanner: CPWC-CP (left) and CPWC-REC (right). ROI and back are the area used to calculate the SNR and CNR.

The images obtained with CPWC-CP and CPWC-REC are reported in Fig.44, where again it can be observed that CPWC-REC offers better overall image quality according to the obtained metrics showed in Fig.45. An improvement of 2.2 dB for the CNR and 0.6 for the SNR are achieved, as well as an improvement in the autocorrelation length measurement at -6 dB of 9.5% and 7.0% respectively in the axial and lateral directions (Fig.45c and Fig.45d)). The evolution of CNR as a function of the number of compounded plane waves (Fig.45a) confirms that the contrast between the inner part of the gallbladder body (anechoic) and the liver, outside part of the gallbladder (echogenic) is better in the image obtained using CPWC-REC than in the image obtained using CPWC-CP.

It can be noticed that the CNR obtained using a single plane wave with CPWC-REC is higher than the best CNR obtained with CP, even with nine plane waves. The SNR curves presented in Fig.45b verify the visual observation that the anechoic zones in CPWC-REC image are darker than the ones in CPWC-CP image. Equivalent SNR is obtained with CPWC-REC when a few plane waves are involved in the image construction than with CPWC-CP using several plane waves.

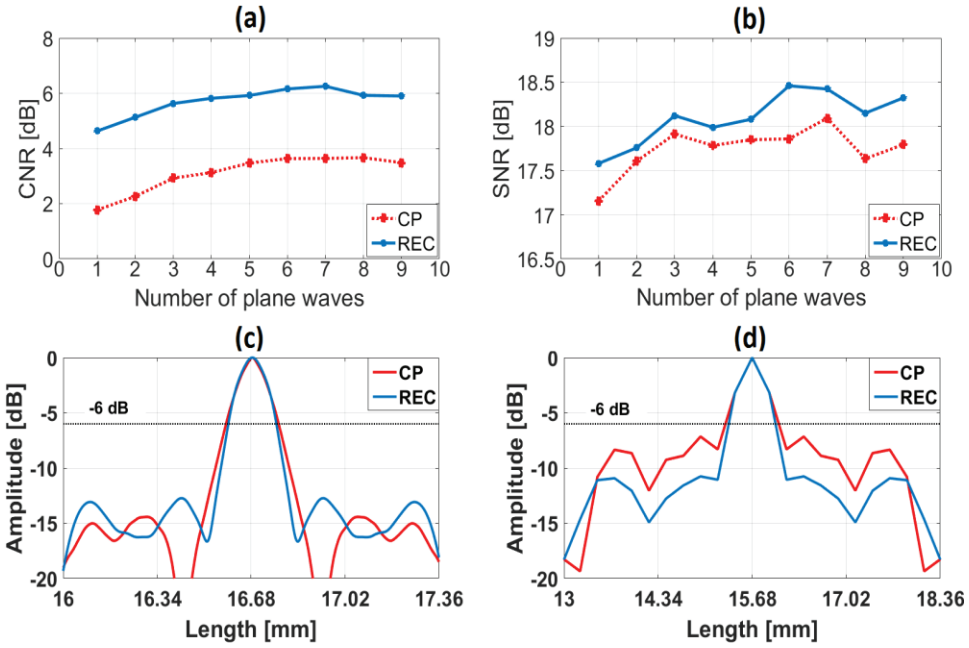

Fig.45. Evolution of (a) CNR and (b) SNR with CPWC-REC and CPWC-CP as a function of the number of plane waves. Autocorrelation length in the axial (c) and lateral (d) directions CPWC-REC and CPWC-CP.

4.5 Discussion

A pulse compression technique (REC) combined with the CPWC approach was implemented on an array based ultrasonic imaging system to enhance its bandwidth (that implies an improvement of the axial resolution in the image) while providing a significant boost in the eSNR, SNR and CNR. The technique combines an amplitude modulated chirp signal in emission (to increase the energy at the frequencies where the probe is less efficient) and a modified Wiener filter in reception (to adjust the trade-off between the image resolution and noise level). Simulation and experimental results were used to assess the performance of the CPWC-REC technique in enhancing the image quality in terms of axial resolution, bandwidth, eSNR, SNR and CNR. The excitation signals used in both simulation and experimental setups were generated in order to provide a theoretical boost of 54 % of the bandwidth of the received backscattered echoes.

The results obtained with both simulations (Fig.30d and Fig.32d) and experiments (Fig.37d) demonstrated bandwidth improvements (i.e., 53%, 40% and 49%, respectively) of CPWC-REC in comparison to CPWC-CP, consistent with the intended bandwidth boost of 54%. The difference between the expected bandwidth boost and the results obtained from the lossy medium can be explained by the effect of attenuation that alters the simulated received echoes, thus the compression filter performs inefficiently since it is no longer adapted. This effect is less significant in the experimental results, since the bandwidth measurements were made on a wire immersed in water. The somewhat reduced bandwidth enhancement obtained in the case of the wire phantom can be due to the multiple reflections which occur inside the wire. They can be observed in the axial profile in Fig.37a

and Fig.37b caused by the large reflection coefficient of nylon in water. The improvement in the axial resolution of the wire profiles (i.e., 48.5%, 19.0 % and 29.0% for simulation, simulation with attenuation and experiment, respectively, as quantified with the k_{-20} dB value derived from the MTF curves) was also consistent with the intended bandwidth improvements.
Initially, the REC technique was not designed to improve the lateral resolution (Fig.33 and Fig.34). However, the combination between REC and coherent plane wave compounding yields an 11.0% / 19.0% enhancement (in simulations / experiments) compared to CPWC-CP. The coherent compounding of the slightly steered point spread functions (due to the transmission angle of the plane wave) gives a final point spread function with a better lateral resolution when each low quality image has a better axial resolution.

The proposed approach (CPWC-REC) was also capable to improve the CNR by 9.0 dB and SNR by 4.0 dB in the final compounded images (Fig.40), compared to CPWC-CP. On the evolution curve of these two metrics as a function of the number of plane waves (Fig.40, Fig.43 and Fig.45), it can also be observed that only two CPWC-REC plane waves provide a better CNR and SNR values than nine CPWC-CP plane waves. In other words, the frame rate can be increased 4.5 time using CPWC-REC.
In pulse compression techniques using chirps, the enhancement of eSNR after compression can be determined by computing the chirp TBP. However, in the presented study the SNR was evaluated on the final beamformed B-mode images. It is therefore not appropriate to associate the improvement in the measured SNR to the TBP. Nonetheless, one can evaluate the impact of the TBP by measuring the eSNR before the beamforming for CPWC-CP and CPWC-REC (after compression). By comparing the values of eSNR a gain of 5.5 dB was achieved by the proposed method. The TBP of the linear chirp used in the compression filter corresponds to a predicted gain in eSNR of 15.6 dB. The difference between achieved and predicted gain in eSNR is due to the Wiener filter used in the CPWC-REC technique. When the eSNR is small, the Wiener filter (used for compression) acts like a matched filter. A matched filter decreases the axial resolution of the system while providing the largest gain in eSNR. By increasing the bandwidth of the imaging system through the CPWC-REC technique, the trade-off between gain in eSNR and axial resolution is extended over elementary pulse compression techniques. Therefore, significant improvements in eSNR are achieved, although less than the theoretical value, with corresponding enhancements in axial resolution.
Also for the cyst phantoms a thinner speckle was observed, as shown by the AACL and the LACL (Fig.41, Fig.43 and Fig.45), which is a direct result of the fact that CPWC-REC improves the axial resolution.

The computational cost of the REC-CPWC technique is slightly increased than the one of CPWC-CP. Indeed CPWC-REC uses a compression filter in post-processing. This step includes a Fourier transform of the raw data, a frequency multiplication of these transformed data with the Wiener filter (β_{rec}) and an inverse Fourier transform of the result of the multiplication. Note that the computation time required for the compression step increases as the quantity of raw data recorded increases.

Because this method was implemented on a real ultrasound system, a short chirp transmission has been defined in order to avoid a potential heating of the probe and of the insonified tissue. A chirp duration of 3 µs seems to be a satisfying trade-off between the energy sent into the medium and the acoustic intensity Ispta (Spatial-peak temporal average Intensity). The compression technique leads to large enough signal whereas Ispta remains lower than 60 mW/cm^2 (the FDA advises not to pass the threshold of 720 mW/cm^2).

4.6 Conclusion

In the presented study, the first implementation of resolution enhancement compression (REC) technique with coherent plane wave compounding (CPWC) imaging is presented. In comparison with conventional plane wave imaging, the results show improvements in terms of image quality as quantified by CNR, SNR, and axial and lateral resolution. The experimental results suggest that REC and plane wave imaging can be integrated and provide advantages for ultrasound imaging when implemented in array systems: enhanced resolution, boosted bandwidth and faster frame rate. Nonetheless, a discrepancy between the expected theoretical improvements and the results obtained both in simulations using attenuation and in experimental setups is observed. This is the effect of the frequency dependent tissue attenuation and a solution to overcome its negative impact on the proposed pulse compression technique is developed in Chapter V.

Chapter V

AN ATTENUATION ADAPTED PULSE COMPRESSION TECHNIQUE TO ENHANCE THE BANDWIDTH AND THE RESOLUTION USING ULTRAFAST ULTRASOUND IMAGING

Contenu

5.1 Introduction

In the previous chapter, it was concluded that the frequency dependent tissue attenuation effect impairs the performance of CPWC-REC technique. Here this effect is studied and the method is optimized (REC-Opt) in order to compensate this effect.

5.2 Theoretical background

As it was shown in [**Gurumurthy (1982)**] the effect of attenuation can be modelled by its impulse response $h_{att}(t,d)$. This impulse response models the ultrasound wave evolution during the propagation between two medium points separated by a distance d. In [**Gurumurthy (1982)**] the following expression was proven to be a good approximation for the Fourier transform of $h_{att}(t,d)$:

$$H_{att}(f,d) = e^{-\alpha d|f|}\; e^{-j2\pi f\tau d}\; e^{j\frac{2f\alpha d}{\pi}ln(2\pi f)} \tag{131}$$

$$\text{with, } \tau = \tau_b + \frac{\alpha}{\pi^2}\tau_m$$

where α is the attenuation coefficient slope, supposed to be known, τ_b is the bulk delay, and τ_m is the minimum-phase delay factor. In [**Gurumurhy (1982)**], the authors proposed to use $\tau_m = 20$ and $\tau_b = 6.67\mu m/s$ in order to fit the dispersion in the soft tissues. In (131):

- $e^{-\alpha d|f|}$ corresponds to the evolution of the magnitude of each frequency in the spectrum of the waveform that propagates inside the medium.
- $e^{-j2\pi f\tau d}$ represents the phase response of the tissue with the assumption that the phase velocity is constant.
- $e^{j\frac{2f\alpha d}{\pi}ln(2\pi f)}$ represents a Hilbert dispersive term that makes $h_{att}(t,d)$ causal.

In Fig.46 is shown how an echo generated by a scatterer, when only one element of the probe emits a short impulsion, evolves as a function of depth (distance between the element and scatterer).

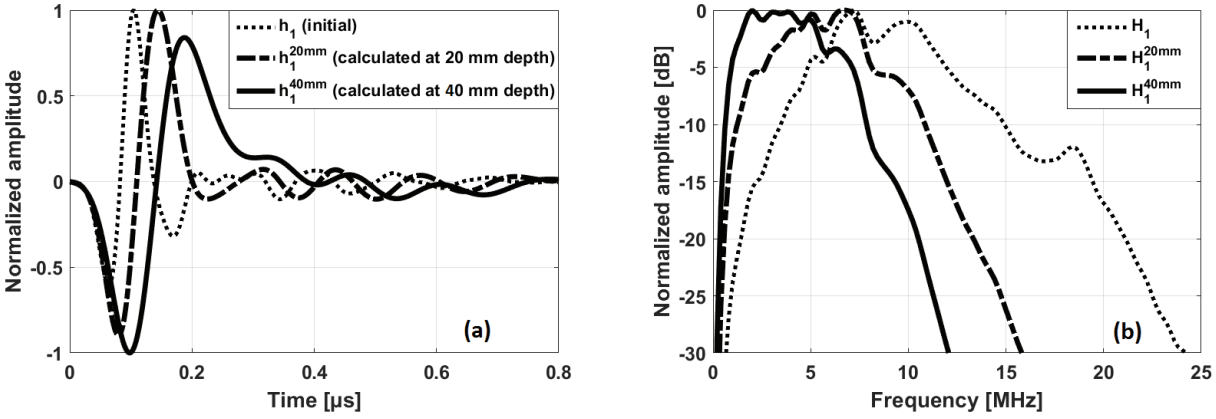

Fig.46. Evolution of an echo generated by a scatterer placed at different depths (20 mm and 40 mm) when only one element of the probe emits a short impulsion (Dirac pulse). (a) – temporal representation, (b) – frequency representation. The dotted line represents the received echo if no attenuation was present, the dashed line represents the echo generated at 20 mm depth and the solid line represents the echo generated at 40 mm.

Indeed, if no frequency dependent attenuation effect was present inside the medium, the received echoes would be a slightly weighted version of the acousto-electrical pulse echo impulse response of the probe (126).
However, the presence of the attenuation reduces the magnitude of the high frequency content of the transmitted signal as a function of the propagation distance, resulting into a received signal with a narrower bandwidth. This can be seen in Fig.46b, where between an echo generated at 20 mm and another generated at 40 mm it can be seen that a fractional bandwidth reduction of 10% was generated.

Under such conditions, the expression of the received signals for an insonification using a plane wave k (125) becomes:

$$y_i^{PW}(t) = w_i \sum_{j=1}^{N_e} w_j \sum_{l=1}^{N_s} TRF_l \frac{e^k\left(t - t_j^k - \frac{d_{lS_j} + d_{lS_i}}{c_0}\right)}{4\pi^2 d_{lS_j} d_{lS_i}} * h_{att}\left(t - t_j^k - \frac{d_{lS_j} + d_{lS_i}}{c_0}, d_{lS_j} + d_{lS_i}\right) \quad (132)$$

where $d_{lS_j} = \left\| \vec{r_l} - \vec{r_{S_j}^0} \right\|_2$ and $d_{lS_i} = \left\| \vec{r_l} - \vec{r_{S_i}^0} \right\|_2$. It can be seen in (132) that the received signal, in presence of attenuation, is similar to the one obtained in (126) only the attenuation impulse response being added. At this point one can rewrite (132) as follows:

$$y_i^{PW}(t) = w_i \sum_{j=1}^{N_e} w_j \sum_{l=1}^{N_s} TRF_l \frac{e_{att}^k\left(t - t_j^k - \frac{d_{lS_j} + d_{lS_i}}{c_0}, d_{lS_j} + d_{lS_i}\right)}{4\pi^2 d_{lS_j} d_{lS_i}} \quad (133)$$

$$\text{with: } e_{att}^k\left(t - t_j^k - \frac{d_{lS_j} + d_{lS_i}}{c_0}, d_{lS_j} + d_{lS_i}\right) = e^k\left(t - t_j^k - \frac{d_{lS_j} + d_{lS_i}}{c_0}\right) * h_{att}\left(t - t_j^k - \frac{d_{lS_j} + d_{lS_i}}{c_0}, d_{lS_j} + d_{lS_i}\right)$$

(133) can be interpreted as follows: the tissue attenuation effect modifies the echoes in such way that a reflexion generated by a scatterer l will have a waveform $e_{att}^k\left(t - t_j^k - \frac{d_{lS_j} + d_{lS_i}}{c_0}, d_{lS_j} + d_{lS_i}\right)$ that is different for scatterers placed at different positions.

Now applying the core equivalence of REC yields:

$$\begin{aligned} & e_{att}^k(t,d) = \tilde{e}^k(t) \\ \Leftrightarrow \quad & a^k(t) * h_1(t) * h_{att}(t,d) = \tilde{a}^k(t) * \mathrm{h}_2(t) \end{aligned} \quad (134)$$

(134) shows that in order to receive echoes $\tilde{e}^k(t)$ when transmitting with the probe (of impulse response $h_1(t)$) one should adapt the transmission signal for each scattering point (since the attenuation effect depends on the wave propagation distance). This requirement could be feasible if one wanted to adapt the transmission only for one point in the medium. However, in order to take into account all the scattering points (in a medium with dense distribution of scatterers), we propose to perform the compensation of the attenuation effect only in reception. Thus the next processing pipeline must be followed:

1- generate the excitation signal $a^k(t)$ as if there was no frequency dependent tissue attenuation effect present inside the image medium (thus using (129))

2- emit the plane wave and receive the backscattered echoes $y_i^{PW}(t)$

3- for each time sample τ_i of the signal $y_i^{PW}(t)$

- compute the impulse response of the attenuation using the following relation:

$$H_{att}\left(f,\tau_i c_0\right)=e^{-\alpha\tau_i c_0|f|}\ e^{-j2\pi f\tau\tau_i c_0}\ e^{j\frac{2f\alpha\tau_i c_0}{\pi}ln(2\pi f)} \tag{135}$$

- compute the compression filter $\beta_{REC}(f,\tau_i)$ by using (135) and by solving (133) in the frequency domain

$$\beta_{REC}\left(f,\tau_i\right)=\frac{(\tilde{A}'^k)^*\left(f,\tau_i\right)}{\left|\tilde{A}'^k(f,\tau_i)\right|^2+\gamma\overline{eSNR}(f)^{-1}} \tag{136}$$

where $(\tilde{A}'^k)^*\left(f,\tau_i\right)=A^k(f,\tau_i)H_1(f)H_{att}(f,\tau_i)/H_2(f)$

- apply the compression filter for the sample τ_i

4- Repeat the step 3 for the received signals of all the elements $i\in[1..N_{el}]$ of the probe.

5.3 Simulation results

In order to validate the theory described in Section 2, simulations were performed using CPWC. Two different excitations were used: $cp(t)$ with a half period of a sinusoid at the center frequency of the impulse response of the probe (8.5 MHz), and a pre-enhanced chirp (Fig.28b). In the second case, the received signals were compressed using $\beta_{REC}(f)$ for REC and using $\beta_{REC}(f,d)$ for the proposed method (that will be called REC-Opt). The simulation was conducted using Field II **[Jensen (1992); Jensen (1996)]**. An angular aperture of 18° was divided in 9 directions equally spaced by 2° (in accordance with Section 2.1). On the ultrasound probe, only the 64 central elements were used for both transmit and receive. The medium contained six scatterers arranged on two horizontal lines at depths of 4 cm and 5 cm. The simulated medium had an attenuation coefficient slope of 0.5dB/MHz/cm, which is comparable to the value in the human liver. Additive white Gaussian noise (AWGN, eSNR ≈ 20 dB) was added to the RF data prior to beamforming (for CP) and prior to compression (for REC and REC-Opt) in order to evaluate the approach in presence of observation noise. The obtained B-mode images for the different techniques are shown in Fig.47.

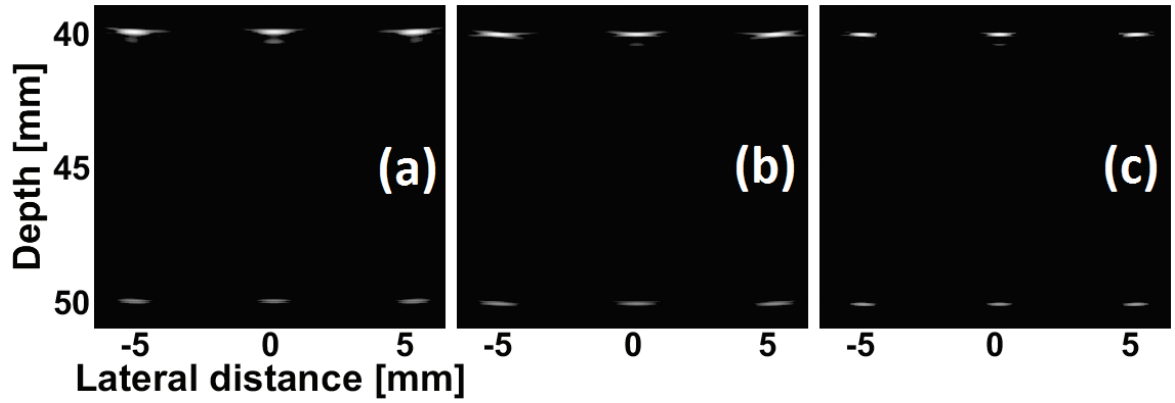

Fig.47. Log-compressed B-mode images of a simulated wire phantom obtained with CP (a), REC (b) and REC-Opt (c) using 9 plane waves. All images have a dynamic range of 55 dB.

It can be visually observed that REC-Opt allowed obtaining a better spatial resolution than REC and CP. The choice of γ (γ = 50) for REC and REC-Opt was made with the aim of obtaining the best axial resolution possible while preserving a noise level below the one of CP. A difference of about 15 dB can be observed between noise level of CP regarding to REC and REC-Opt (Fig.48a). As shown in Fig.48b, the improvement concerning the axial resolution was quantified through the calculation of the modulation transfer function (MTF) derived from the envelope data. In particular, the wave numbers k_{-20dB} at which the MTFs dropped below -20 dB were 35, 37.1 and 45.2 mm^{-1} for CP, REC and REC-Opt, respectively. The power spectra of the reflection from the wire at a depth of 4 cm are shown in Fig.48c. In accordance with the improvements in the MTF, the -6 dB bandwidths were 3.9, 4.1 and 5.5 MHz, respectively. These results correspond to enhancements in axial resolution and bandwidth between REC-Opt and CP of 30 % and 40.5%, respectively.

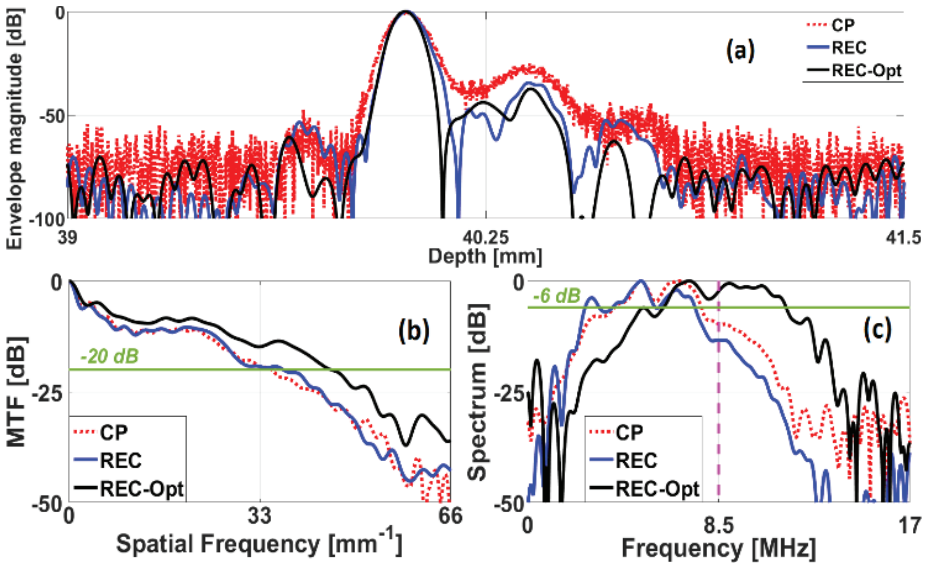

Fig.48. Comparison of performance between REC-Opt (solid black line), REC (solid blue line) and CP (dashed red line). (a) Envelope of the radiofrequency data of the scatterer placed at 4 cm depth in the center of the image. (b) MTF derived from (a). (c) Normalized spectrum derived from the radiofrequency data of the same scaterrer.

5.4 Experimental results

For the data acquisition, the open ultrasound platform UlaOp-64 (Microelectronics System Design Lab, Florence, Italy) equipped with a LA523E linear array probe (Esaote, Genova, Italy) was used. The UlaOp-64 can transmit arbitrary waveforms defined by customized transmission and reception strategies **[Tortoli (2009)]**. The probe has 192 elements (pitch = 0.245 mm) and is centered at 8.5 MHz. The experimental acquisitions were conducted with the same parameters as in simulation. The phantom studied (model 410SCG HE 0.5 Gammex Sun nuclear, Neu-Isenburg, Germany) has an attenuation coefficient slope of 0.5 dB/MHz/cm.

5.4.1 Wire phantom acquisitions

The first experiment consists on imaging a phantom that contains two wires of 100 µm thickness, placed at 2.25 cm and 3.25 cm depth. The obtained B-mode images using the three different techniques are shown in Fig.49.

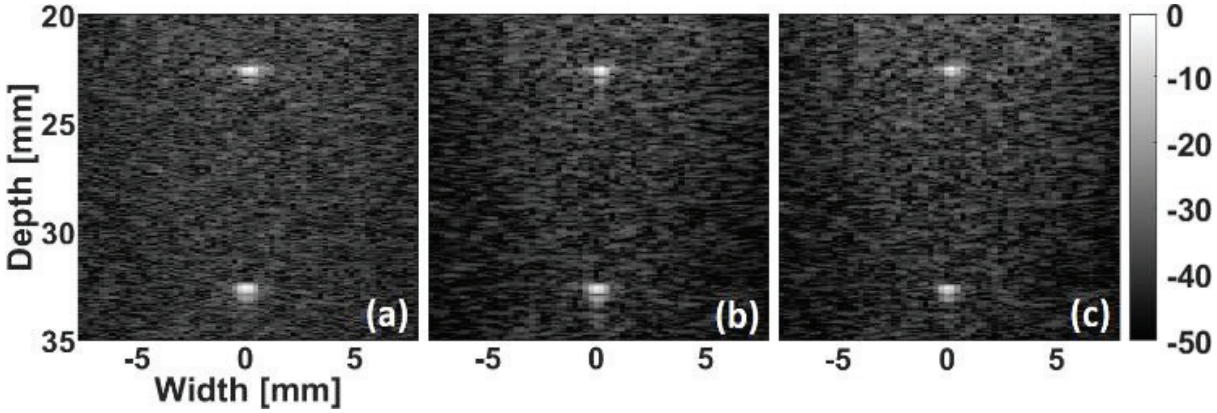

Fig.49. Log-compressed B-mode images of wire phantom obtained with CP (a), REC (b) and REC-Opt (c) using 9 plane waves.

One can observe that REC-Opt provided the best image quality among the three techniques. This is particularly noticeable by the lower thickness of the points corresponding to the two wire targets. This effect is confirmed by studying the axial resolution and the spectrum derived from the radiofrequency data of the wire placed at 32.5mm (Fig.50). The MTF values were 14.4, 14.85 and 18.71 mm^{-1} (which corresponds to a resolution of respectively 218.2, 211.6 and 167.9 µm) for CP, REC and REC-Opt, respectively. Therefore, the axial resolution was improved by 30% between REC-Opt and CP and by 26% between REC-Opt and REC. In accordance with the improvements in the MTF, the -6 dB bandwidths were estimated to be 2.54, 2.61 and 3.57 MHz for CP, REC and REC-Opt, respectively. Because of the attenuation in the medium (0.5dB/MHz/cm) at this depth (3.25 cm), REC is no longer effective and gives almost the same performance in axial resolution and bandwidth as CP.

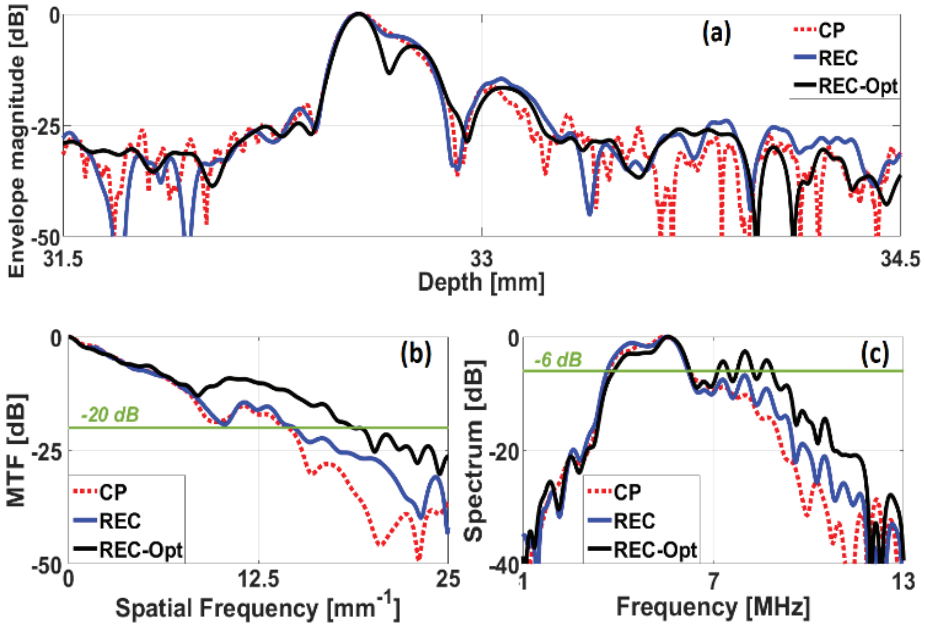

Fig.50. Comparison of performance between REC-Opt (solid black line), REC (solid blue line) and CP (dashed red line). (a) Envelope of the radiofrequency data of the scatterer placed at 3.25 cm. (b) MTF derived from the envelope. (c) Normalized spectrum derived from the radiofrequency data.

5.4.2 Cyst phantom acquisitions

The proposed method was also evaluated experimentally by imaging hypoechoic cyst placed at 4cm depth from the same phantom. Fig.51 shows the obtained B-mode images.

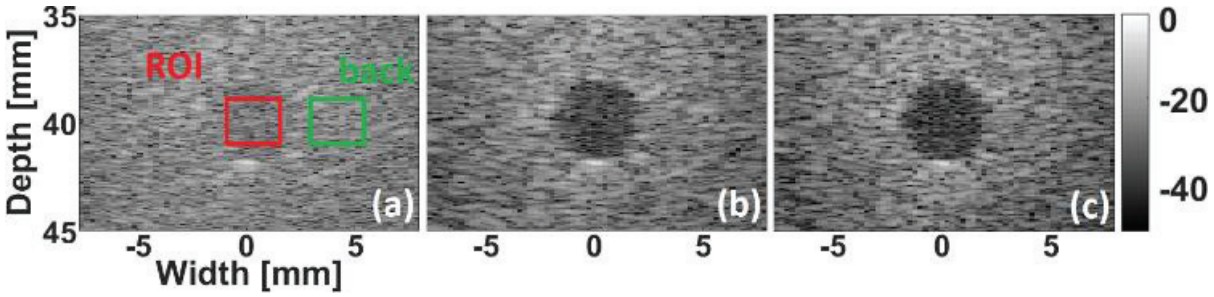

Fig.51. Log-compressed B-mode images of hypoechoic cyst at 4cm depth obtained with CP (a), REC (b) and REC-Opt (c) using 9 plane waves. The red and green zones are the regions used for the computation of the CNR and SNR.

The results clearly show an improvement in terms of image quality between CP and REC/REC-Opt. A slight improvement is also noted between REC and REC-Opt, especially concerning the contrast and the speckle size. To quantify the image quality, the speckle signal-to-noise ratio (SNR) and the contrast-to-noise ratio (CNR) were computed. The obtained values of CNR and SNR calculated using the square areas (Fig.51a) are depicted in Table III. By compensating the attenuation, the new approach improves the CNR and SNR by respectively 1.17 and 2.1 dB in comparison with REC.

Table III: Image quality metrics comparison

	CP	REC	**REC-Opt**
CNR *(dB)*	-4.31	4.32	**5.49**
SNR *(dB)*	14.8	16.1	**18.2**

5.5 Discussion and conclusion

The results obtained from wire phantoms showed clearly the limits of REC in presence of attenuation. Only 6.7% / 2.8% improvements respectively in axial resolution / bandwidth were observed experimentally between REC and CP. The same behaviour was observed in simulation with only 6% / 3.1% enhancements. These problems were solved when the attenuation of the medium was taken into account. Indeed, the results obtained with both simulations and experiments led in bandwidth improvements (i.e., 40.5% and 40.6%, respectively) of REC-Opt in comparison to CP, consistent with the intended bandwidth boost of 42%. The improvement in the spatial resolution of the wire profiles (i.e., 29 and 30% for simulation and experiment as quantified with the k_{-20}dB value derived from the MTF curves) was also consistent with the intended bandwidth improvement. By adapting the compression filter, the proposed approach (REC-Opt) was also capable to improve the CNR by 27% and SNR by 13% compared to REC. Here, the pre-enhanced chirp excitation was designed to achieve only a modest increase in bandwidth. This was due to the aspect of the transducer impulse response spectrum, which decreases sharply at high frequencies (at around 13 MHz). The experimental results suggest that the REC technique adapted to the medium attenuation (REC-Opt) provides a better image quality than the classical REC technique for ultrasonic imaging.

Chapter VI

ENHANCED SECOND HARMONIC IMAGING USING A PULSE COMPRESSION TECHNIQUE COMBINED WITH ULTRASOUND PULSE INVERSION

Contenu

6.1 Theoretical background

As previously shown in Section 2.2, Pulse Inversion (PI) is an emission technique used for harmonic imaging. The PI concept applied to plane wave imaging consists in transmitting a plane wave twice in the same direction, the second time carrying a phase inverted version of the excitation signal used for the first transmission. Both resulting signals are summed to obtain the final signal. In this section, we propose to combine the PI concept with the principle of REC. The main idea being to compensate the excitation signal in such a way that the less efficient frequency bands of the probe receive more energy. In order to better understand the added value of the proposed technique, it will appropriate to first understand the principle of the classical PI. Suppose a successive transmission of two plane waves, where the first one was generated using an excitation signal $a^k(t)$ and the second one was generated using $-a^k(t)$ with:

$$a^k(t) = w^k(t)cos(2\pi f^k t) \tag{137}$$

In (137), it can be seen that the excitation signal is a cosine function centred at the frequency f^k and weighted with a window $w^k(t)$. As it was shown in Section 2.2, the nonlinear propagation of the ultrasound wave can be roughly seen as a superposition of two waves: one that is centered at f^k (the fundamental) and a second one centered at $2f^k$ (the first harmonic). Thus, classically the backscattered echoes generated by any scatterer of the medium are written as follows [**Park (2013)**]:

$$\begin{aligned} {}^{+}e^k(t) &= w^k(t)cos(2\pi f^k t) + \eta(w^k(t))^2 cos(2\pi(2f^k)t) \\ {}^{-}e^k(t) &= -w^k(t)cos(2\pi f^k t) + \eta(w^k(t))^2 cos(2\pi(2f^k)t) \end{aligned} \tag{138}$$

where ${}^{+}e^k(t)$ and ${}^{-}e^k(t)$ are the typical waveforms received after the transmission of the positive and negative excitations respectively. η represents a scaling factor and that will set the amplitude of the harmonic echo and depends on the nonlinear properties of the medium and on the propagation distance. It can be seen that by adding ${}^{+}e^k(t)$ and ${}^{-}e^k(t)$ the impact of the second harmonic can be highlighted:

$${}^{+}e^k(t) + {}^{-}e^k(t) = 2\eta(w^k(t))^2 cos(2\pi(2f^k)t) \tag{139}$$

However the model generated in (138) and (139) makes a very important assumption that is the complete neglecting of the acousto-electrical impulse response of the ultrasound probe. The issue here is that, the wave that propagates inside the medium does not carry the waveform $a^k(t)$ but the signal ${}_{1/2}a^k(t)$ where:

$${}_{1/2}a^k(t) = {}_{1/2}h_I(t) * \left(w^k(t)\, cos(2\pi f^k t)\right) \tag{140}$$

with ${}_{1/2}h_1(t)$ being the acousto-electrical impulse response of the ultrasound probe in transmission.
In Fig.52a, is shown a representation of the second harmonic wave computation where the acousto electrical impulse response of the probe is completely neglected. On the other hand, in Fig.52b is shown the same result where the effect of the bandlimited probe is compensated (for the same excitation signal $a^k(t)$).

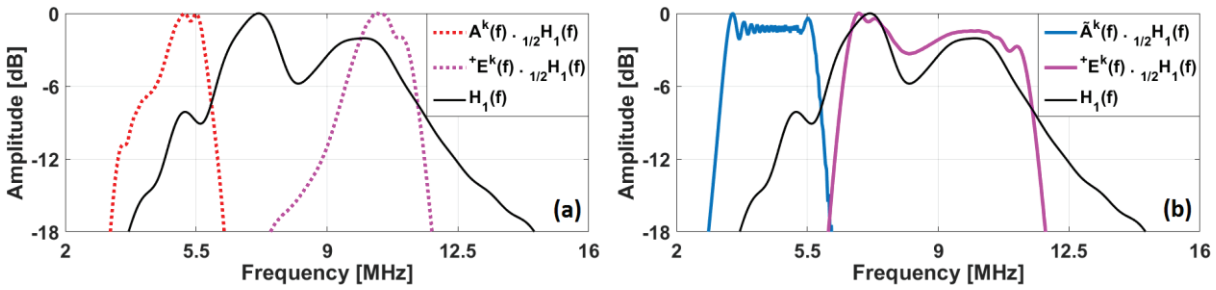

Fig.52. Spectra of the transmitted signals (in both approaches) and of the chirp signal used to compress the received echoes for REC-PI.

As one can see between Fig.52a and Fig.52b, the pulse echo impulse response of the ultrasound probe has an impact on the bandwidth of the second harmonic waveform which results image resolution alteration. This effect may not be that important in the case where the excitation signal is a simple sinusoid and where is no post processing adapted filtering on the received data. However this impact may be overwhelming when the excitation signals is a chirp and after the echo reception phase a pulse compression layer needs to be applied. The problem here would be that the compression filter, computed directly from $a^k(t)$ would not be optimal, the best practice being to compute this filter using ${}_{1/2}a^k(t)$.

In order to overcome this effect, here we propose the following processing pipeline:

1- choose a chirp central frequency f^k which is approximatively half of the central frequency of the probe f_0:

$$f^k = \frac{f_0}{2}; \tag{141}$$

2- generate a linear modulated chirp ${}_{1/2}a^k(t)$ of bandwidth equal to the half of the bandwidth of the ultrasound probe:

$${}_{1/2}a^k(t) = w^k(t)\cos\left(2\pi\left(f^k - \frac{B^k}{2} + \frac{B^k}{T^k}t\right)t\right); \tag{142}$$

where $B^k = B_0/2$ and T^k represent the bandwidth and the duration of the chirp respectively (B_0 is the bandwidth of the ultrasound probe).

3- apply the REC principle in order to calculate the excitation signal needed in order to obtain a wave that carries the waveform ${}_{1/2}a^k(t)$:

$$a^k(t) * {}_{1/2}h_1(t) = {}_{1/2}a^k(t) * {}_{1/2}h_2(t); \tag{143}$$

in the previous relation ${}_{1/2}h_1(t)$ and ${}_{1/2}h_2(t)$ are the acousto electrical impulse responses in emission of the real and hypothetical probe respectively. For this case we will suppose that ${}_{1/2}h_2(t) = \delta(t)$ to have the maximum bandwidth boost of ${}_{1/2}h_1(t)$. This means that from (143) the excitation signal in the frequency domain can be deduced as follows:

$$A^k(f) = {}_{1/2}A^k(f)\frac{{}_{1/2}H_1^*(f)}{\left|{}_{1/2}H_1(f)\right|^2 + \left|{}_{1/2}H_1(f)\right|^{-2}}\ ; \tag{144}$$

4- add the received echoes generated by the successive emissions of $a^k(t)$ and $-a^k(t)$;

5- generate ${}_{2/2}a^k(t)$ as a linear chirp that has twice the bandwidth of ${}_{1/2}a^k(t)$ (in (142)):

$${}_{2/2}a^k(t) = \left(w^k(t)\right)^2 cos\left(2\pi(2f^k - B^k + \frac{2B^k}{T^k}t)t\right)\ ; \tag{145}$$

6- for each time sample τ_i of the resulted echoes (after the summation due to PI)

a. compute the impulse response of the attenuation using the following relation:

$$H_{att}(f,\tau_i c_0) = e^{-\alpha\tau_i c_0|f|}\ e^{-j2\pi f\tau\tau_i c_0}\ e^{j\frac{2f\alpha\tau_i c_0}{\pi}ln(2\pi f)} \tag{146}$$

b. compute the compression filter $\beta_{REC}(f,\tau_i)$ by using (146):

$$\beta_{REC}(f,\tau_i) = \frac{{}_{2/2}A^k(f) * H_{att}(f,\tau_i)}{\left|{}_{2/2}A^k(f) * H_{att}(f,\tau_i)\right|^2 + \gamma\overline{eSNR}(f)^{-1}} \tag{147}$$

c. apply the compression filter for the sample τ_i

7- Repeat the step 6 for the received signals at each element $i \in [1..N_{el}]$ of the probe

In Fig.53 are shown the different signals involved in the proposed method. As one can see, the fact that the proposed excitation signal $a^k(t)$ carries more energy in the frequency bands where the impulse response ${}_{1/2}h_1(t)$ attenuates more the signal frequencies makes that the signal ${}_{1/2}a^k(t)$ that propagates inside the medium is a linear chirp with constant amplitude (thus a maximal bandwidth B^k). Thereby the second harmonic generated form ${}_{1/2}a^k(t)$ (which is ${}_{2/2}a^k(t)$) will have also constant amplitude thus a maximal bandwidth ($2B^k$).

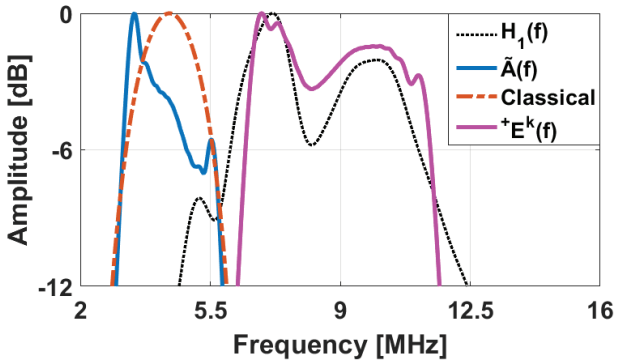

Fig.53. Spectra of the transmitted signals (in both approaches) and of the chirp signal used to compress the received echoes for REC-PI.

6.2 Experimental results

In order to validate the theory described in Section 6.1, an experimental acquisition was made using coherent plane wave compounding. The combination between REC and PI was compared to classical PI. The open ultrasound platform UlaOp-256 (Microelectronics System Design Lab, Florence, Italy) equipped with a LA523E linear array probe was used. An area containing four wires and a hypoechoic cyst from the phantom (model 410SCG HE 0.5 Gammex Sun nuclear, Neu-Isenburg, Germany) was studied. The phantom is characterised with a nonlinear coefficient B/A = 6.7. The obtained B-mode images for both approaches are shown in Fig.54.

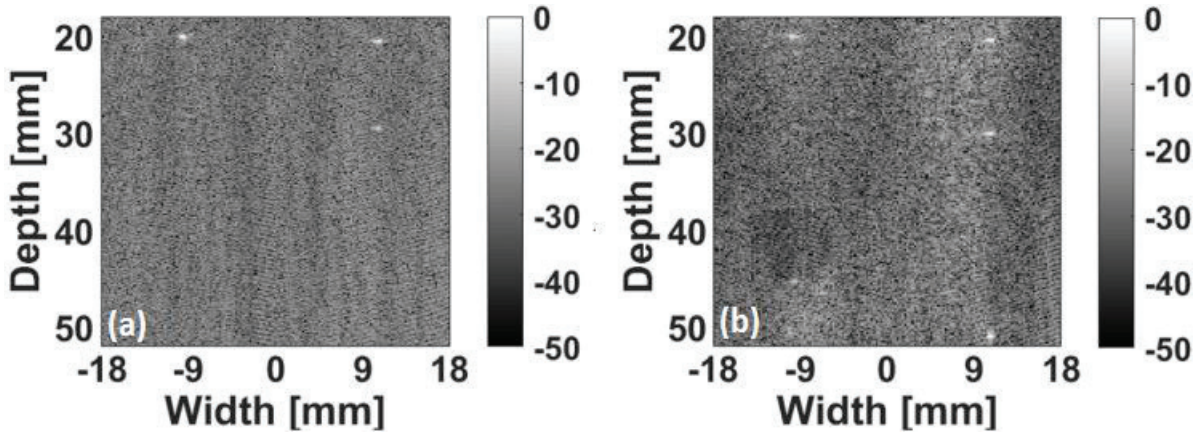

Fig.54. Log-compressed B-mode images obtained using UlaOp-256 for conventional PI (a) and for REC-PI (b).

An improvement of image quality is observed when using REC-PI (Fig.54b) in comparison to classical PI (Fig.54a). An enhancement of 25.4% of the axial resolution was noticed for the scatterer placed at (x = -0.9 cm, z = 2 cm). A better speckle size was also obtained, confirmed by the calculation of the radiofrequency auto correlation length in the axial direction. Indeed, REC-PI provides 20.1% improvement in comparison to classical PI consistent with the previous resolution enhancement. A better penetration depth of REC-PI compared to conventional PI can be observed, in its ability to reconstruct the deeper scatterer which is not visible in the conventional PI. The cyst, which appears in the REC-PI case and not in the classical PI, reveals a gain of 18.2 dB in CNR for the proposed approach.

PART III: CONTRIBUTION 2

Chapter VII

A ROBUST CHIRP COMPRESSION TECHNIQUE COMBINED TO ULTRASOUND MULTI-LINE TRANSMISSION TO ENHANCE SPATIAL RESOLUTION AND IMAGE CONTRAST

Contenu

7.1 Theoretical background

As it was shown in Section 3.4.2, Multi-Mine Transmission (MLT) consists in simultaneous emission of focused beams, which in conventional ultrasound imaging are emitted successively. Simultaneous emission of focused beams (Fig.55b) which enable the reconstruction of multiple image lines implies that a full image of the medium will be reconstructed faster than in conventional ultrasound (Fig.55a) and represents the main advantage of MLT over focused ultrasound imaging. However, where is a gain in frame acquisition rate there is a loss in image quality, simultaneous emission of ultrasound beams generating crosstalk artifacts, reduces slightly the overall quality of the image. Here, to the concept of MLT is applied the principle of REC, the objective being to improve the provided images.

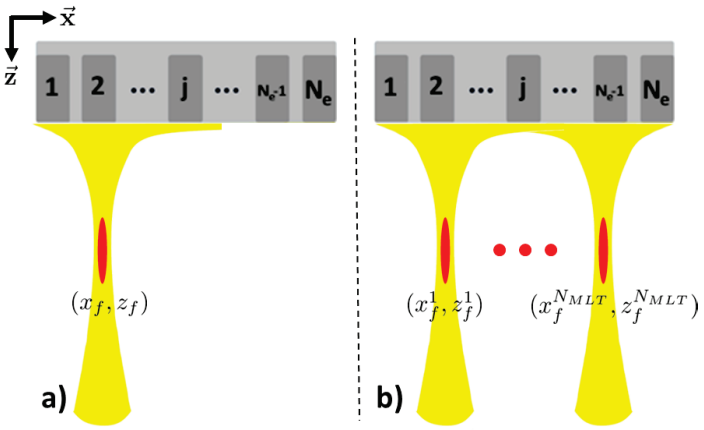

Fig.55: Ultrasound transducer, aligned along $z=0$, with N_e elements in two different emission schemes (a) Single-line transmit (SLT), (b) Multi-line transmit (MLT).

In order to better understand how this improvement is made, let us resume the reasoning shown in Section 3.4.2. Between (76) and (79) it was shown the MLT excitation signal at each element j of the probe can be written as:

$$a_j^{MLT}(t) = w_j \sum_{k=1}^{N_{MLT}} a^k(t) * \delta(t - {}^{MLT}t_j^k) \tag{148}$$

where $a^k(t)$ represents the excitation waveform (which is constant for all the focused beams k) and ${}^{MLT}t_j^k$ represents the emission delays needed in order to focus the beam k in the point (x_f^k, z_f^k). Furthermore, it was shown, that with the hypothesis that there is no frequency dependent tissue attenuation effect, the received backscattered echoes can be written as:

$$y_i^{MLT}(t) = w_i \sum_{k=1}^{N_{MLT}} e^k(t) * g_i^k(t) + b(t) \tag{149}$$

where $e^k(t) = a^k(t) * h_1(t)$ represents the typical waveform generated by an arbitrary scatterer in the medium. In (149), $g_i^k(t) = \sum_{j=1}^{N_e} w_j \delta(t - {}^{MLT}t_j^k) * g_{ji}(t)$ is the pulse echo impulse response of the medium when insonified with the focused ultrasound beam k, seen by the element i (computed using the relation (74)). In (149), $e^k(t) = a^k(t) * h_1(t)$ represents the typical waveform generated by an

arbitrary scatterer in the medium. Since each element focused beam carries the same excitation signal $(a(t) = a^k(t),\ \forall k)$, then (149) becomes:

$$y_i^{MLT}(t) = e(t) w_i * \sum_{k=1}^{N_{MLT}} g_i^k(t) + b(t) \tag{150}$$

In presence of frequency dependent tissue attenuation effect, as seen in Chapter V, the waveform of an echo generated at distinct distances from the surface of the ultrasound probe, changes. Combining (70) with (150) and (132) it can be deduced that:

$$y_i^{MLT}(t) = w_i \sum_{j=1}^{N_e} w_j \sum_{l=1}^{N_s} TRF_l \frac{e^k\left(t - {}^{MLT}t_j^k - \frac{d_{lS_j} + d_{lS_i}}{c_0}\right)}{4\pi^2 d_{lS_j} d_{lS_i}} * h_{att}\left(t - {}^{MLT}t_j^k - \frac{d_{lS_j} + d_{lS_i}}{c_0}, d_{lS_j} + d_{lS_i}\right) \tag{151}$$

where $d_{lS_j} = \left\| \vec{r_l} - \overrightarrow{r_{S_j}^0} \right\|_2$ and $d_{lS_i} = \left\| \vec{r_l} - \overrightarrow{r_{S_i}^0} \right\|_2$ represent the distance from the scatterer to the element j and i of the probe respectively. In (151), the signal $h_{att}(t,d)$ represents the impulse response generated by the attenuation effect on an echo that propagates to a distance d and can be calculated using (131). It can be seen in (151) that the received signal, in presence of attenuation, is similar to the one obtained in (70) only the attenuation impulse response being added. At this point, one can rewrite (151) as follows:

$$\begin{aligned} y_i^{MLT}(t) &= w_i \sum_{j=1}^{N_e} w_j \sum_{l=1}^{N_s} TRF_l \frac{e_{att}^k\left(t - {}^{MLT}t_j^k - \frac{d_{lS_j} + d_{lS_i}}{c_0}, d_{lS_j} + d_{lS_i}\right)}{4\pi^2 d_{lS_j} d_{lS_i}} \\ y_i^{MLT}(t) &= w_i \sum_{j=1}^{N_e} w_j \sum_{l=1}^{N_s} TRF_l \frac{e^k\left(t - {}^{MLT}t_j^k - \frac{d_{lS_j} + d_{lS_i}}{c_0}\right) * h_{att}\left(t - {}^{MLT}t_j^k - \frac{d_{lS_j} + d_{lS_i}}{c_0}, d_{lS_j} + d_{lS_i}\right)}{4\pi^2 d_{lS_j} d_{lS_i}} \end{aligned} \tag{152}$$

As for (131), (152) can be interpreted as follows: the tissue attenuation effect modifies the echoes in such way, so that an reflexion generated by a scatterer l will have a waveform $e_{att}^k\left(t - {}^{MLT}t_j^k - \frac{d_{lS_j} + d_{lS_i}}{c_0}, d_{lS_j} + d_{lS_i}\right)$ that is different for scatterers placed at different positions.

Now applying the core equivalence of REC yields:

$$e_{att}^k(t,d) = \tilde{e}^k(t) \quad \Leftrightarrow \quad a^k(t) * h_1(t) * h_{att}(t,d) = \tilde{a}^k(t) * \mathrm{h}_2(t) \tag{153}$$

where $\tilde{a}^k(t) * \mathrm{h}_2(t)$ is the typical waveform of an echo, that a purely hypothetical ultrasound probe of acousto-electrical pulse echo impulse response $h_2(t)$ would receive when excited with a waveform $\tilde{a}^k(t)$. Of course, if one choses carefully $h_2(t)$ and $\tilde{a}^k(t)$ (as seen in the previous Chapters), the provided image quality will be boosted. Thus, equation (153) allows to compute the excitation signal of the real transducer $a^k(t)$ that needs to be used in order to obtain the same resolution as the fictive

transducer, of wider bandwidth, excited with $h_1(t)$. This relation also shows that in order to receive echoes $\tilde{e}^k(t)$ when emitting with the probe (of impulse response $h_1(t)$) one should adapt the emission signal for each scattering point (since the attenuation effect depends on the wave propagation distance). This requirement could be feasible if one wants to adapt the emission only for one point in the medium (focal point for instance). However, in order to take into account all the scattering points (in a medium with dense distribution of scatterers), we propose to proceed as:

1) Apply the following relation in order to find the excitation signal $a^k(t)$:

$$a^k(t) * h_1(t) = \tilde{a}^k(t) * h_2(t) \tag{154}$$

which implies that the attenuation effect is not compensated by the excitation signal. By solving (20) in the frequency domain, we can compute the excitation signal using:

$$A^k(f) = \tilde{A}^k(f)\frac{H_2(f)}{H_1(f)} \tag{155}$$

where capital letters represent the respective spectrums of the entities present in equation (154). To avoid dividing by zero (due to the presence of $H_1(f)$ at the denominator) and in order to obtain a good approximation of $A^k(f)$, **[Oelze (2007)]** proposed to use, instead of (155), the following filter:

$$A^k(f) = \tilde{A}^k(f)\frac{H_2(f)H_1^*(f)}{\left|H_1(f)\right|^2 + \left|H_1(f)\right|^{-2}} \tag{156}$$

Multiplying the chirp $a^k(t)$ with a 20% apodization Tukey-cosine window was also proposed in order to reduce side-lobe levels **[Chiao (2005)]**.

2) Adapt the pulse compression filter as a function of the echo propagation distance in order to compensate the effect of attenuation. We propose to include the attenuation effect as a modification of the excitation $\tilde{a}^k(t)$, of the hypothetical probe. By combining (153) and (156), we obtain:

$$\tilde{A}^k(f, d(l,j,i)) = A^k(f)\frac{H_1(f)H_{att}(f, d(l,j,i))}{H_2(f)} \tag{157}$$

Since (157) is entirely analytical and does not imply modifying the excitation signal of the real probe (of impulse response $h_1(t)$), adapting $h_1(t)$ as a function of $d(l,i,j)$ is much more convenient than adapting $a^k(t)$. Knowing $\tilde{a}^k(t, d(l,i,j))$ and relying on the echo equivalence (153), we can design an optimal Wiener filter that will allow to compress the echo waveforms $e^k(t)$. We propose the following compression filter:

$$\beta_{REC}\left(f, d(l,j,i)\right) = \frac{(\tilde{A}^k)^*(f, d(l,j,i))}{\left|\tilde{A}^k(f, d(l,j,i))\right|^2 + \gamma\overline{eSNR}^{-1}(f)} \tag{158}$$

where $eSNR(f)$ is the mean signal-to-noise ratio per frequency channel of the received signals $y_i^{MLT}(t)$. γ is a smoothing parameter that controls the tradeoff between bandwidth enhancement (better axial resolution), *eSNR* gain and sidelobe levels **[Oelze (2007); Benane (2018a)]**. Low γ values, for which $\beta_{REC}\left(f, d(l,j,i)\right)$ becomes an inverse filter, improve axial resolution but increase sidelobe levels and degrade *eSNR*. While high values of γ, for which $\beta_{REC}\left(f, d(l,j,i)\right)$ becomes a matched filter, have the opposite effect. In this work, γ was adjusted manually by keeping the best

axial resolution that can be achieved in the image while the acquisition noise level does not exceed the one of classical MLT.

7.2 Simulations

In this section, the performance of the MLT-REC method using 1, 2, 4, 6 and 8 MLT is studied using the Field II software **[Jensen (1992); Jensen (1996)]**. The B-mode images obtained with the proposed approach were compared to the ones given by classical MLT and MLT using classical pulse compression (MLT-PC) techniques.

7.2.1 Simulation setup

A 192-element linear array transducer with a pitch of 0.245 mm was simulated. The center frequency and sampling frequency were 8.5 MHz and 61.6 MHz, respectively. The pulse-echo impulse response $h_1(t)$ was obtained experimentally from a reflection of a planar surface immersed in water after emission and reception with the central element of the LA523E probe (Esaote, Florence, Italy). Three different excitations were used: classical excitation composed of a sinusoid cycle (classical MLT), the pre-enhanced chirp $a(t)$ (MLT-REC) and the linear chirp $\tilde{a}(t)$ (MLT-PC). These excitation signals, all centered at 8.5 MHz (the center frequency of $h_1(t)$), are shown in Fig.56. The chirp $a(t)$ was designed to provide a 35% increase in bandwidth.

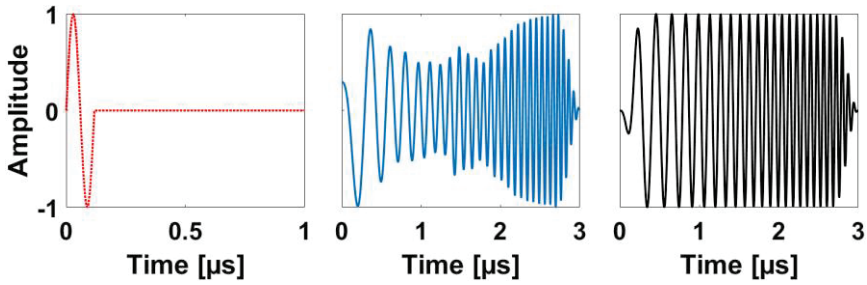

Fig. 56: Excitations used for the different techniques. Classical excitation (left), *a(t)* (middle) and *ã(t)* (right).

Two phantoms from the Plane-wave Imaging Challenge in Medical UltraSound (PICMUS) dataset **[Liebgott (2016)]** with a coefficient attenuation slope of 0.5 dB/MHz/cm were simulated (Fig.57).

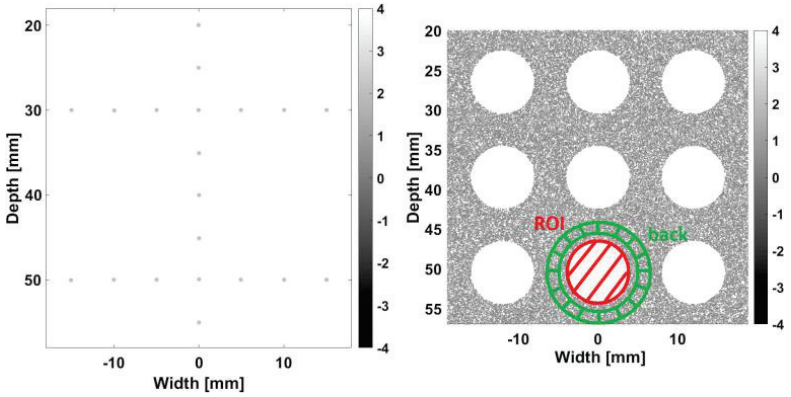

Fig.57: Wire phantom (left) and cyst phantom (right) used for simulations. The cyst on which the *CNR* evolution was studied is highlighted together with its background (green) and ROI (red).

The focal point in transmission was set at $z_f = 50mm$. A white Gaussian noise (AWGN, SNR ≈ 20 dB) was added to the RF data prior to beamforming in order to evaluate the performance of the Wiener filter used for compression in presence of observation noise.

7.2.2 Simulation results

7.2.2.1 Wire phantom

Fig.58 shows the log-compressed B-mode images obtained using the three approaches.

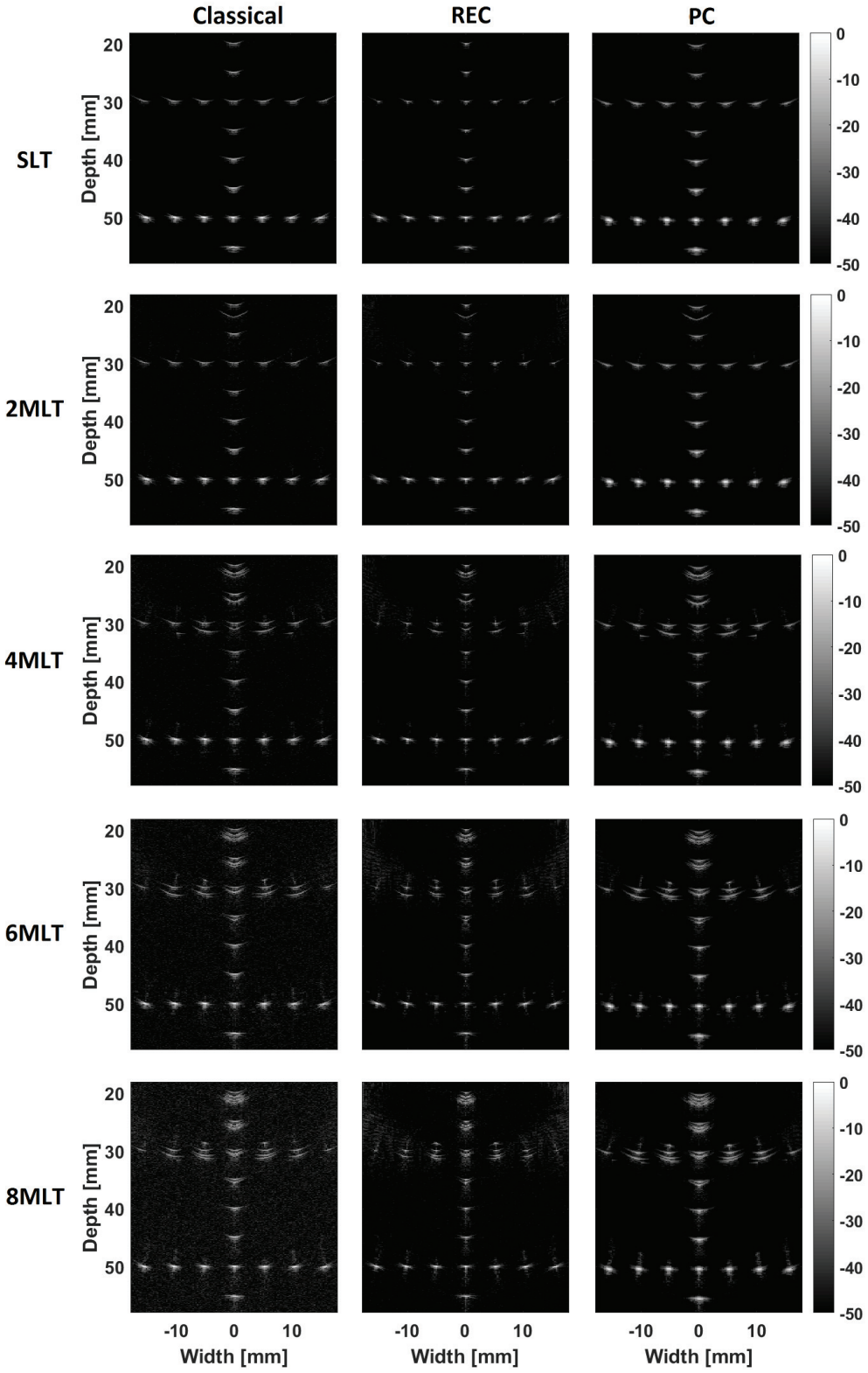

Fig.58: Log-compressed B-mode images obtained using the different techniques with SLT, 2MLT, 4MLT, 6MLT and 8MLT.

It can be visually assessed that MLT-REC allowed obtaining a better spatial resolution than classical MLT and MLT-PC, regardless of the number of MLT used. As shown in Fig.59a, the improvement concerning the axial resolution (for the 4MLT obtained results) was quantified through the envelope of the beamformed radiofrequency signals (at -6dB). The measured values are 124.2 µm, 163.8 µm and 186.2 µm for 4MLT-REC, classical 4MLT and 4MLT-PC respectively. The power spectra of the reflected echoes for the studied wire are shown in Fig.59b. In accordance with the improvement in axial resolution, the -6dB bandwidths were 5.79MHz, 4.39MHz and 3.86MHz for 4MLT-REC, classical 4MLT and 4MLT-PC respectively. Tables IV contain all the measured values for axial resolution and bandwidth, where the same tendency is observed.

The lateral resolution of the images obtained using the different techniques for 4MLT are shown in Fig.60a-b. As it can be seen in Fig.60b, 4MLT-REC improves the lateral resolution by 23.7% and 24.4% in comparison to classical 4MLT and 4MLT-PC respectively. All the numerical values of this metric for each number of MLT are summarized in Table IV.

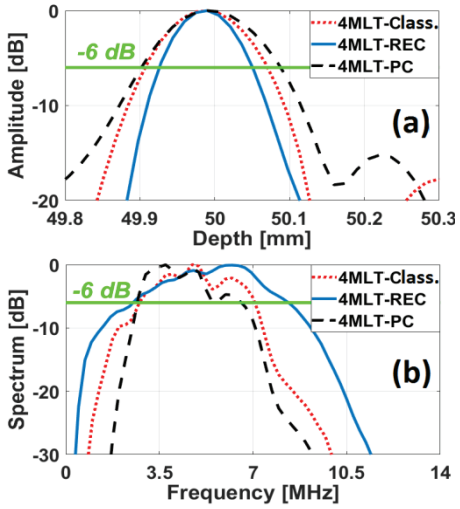

Fig.59: Comparison of performance between 4MLT-REC (solid blue line), classical 4MLT (dotted red line) and 4MLT-PC (dashed black line) using the A-line corresponding to the wire placed at (x = 0 cm, z = 5 cm): (a) Envelope of the RF data. (b) Normalized spectrum derived from the RF data.

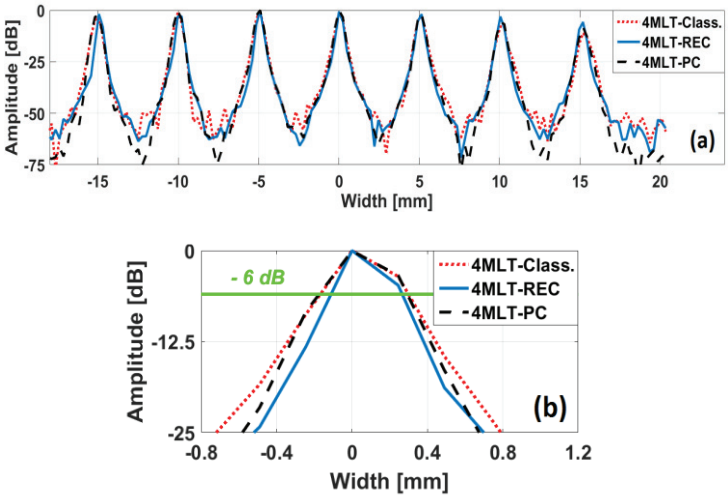

Fig.60: Comparison of performance between 4MLT-REC (solid blue line), classical 4MLT (dotted red line) and 4MLT-PC (dashed black line) using the lateral line corresponding to the wire placed at (x = 0 cm, z = 5 cm): (a) Lateral envelope of the B-mode line at the focal depth, (b) Zoom on the central scatterer placed at x=0 of (a).

The choice of γ (γ = 50) for 4MLT-REC was made with the aim of obtaining the best axial resolution possible while preserving a background noise level below the one of classical MLT. A difference of about 12 dB can be observed between noise levels of classical MLT regarding to MLT-REC (Fig.61a). Concerning the *eSNR,* calculated on the pre-beamformed data (Fig.61b), a higher value is obtained for 4MLT-PC (36.3 dB) followed by 4MLT-REC (28.4 dB). Classical 4MLT provides the lowest value with 19.7 dB. The obtained results are consistent with the expected ones, the difference of 7.9 dB between 4MLT-REC and 4MLT-PC being explained by the modulated shape of the excitation in 4MLT-REC ($a^k(t)$) that carries approximatively 1.8 times less energy than the chirp used for 4MLT-PC emission ($\tilde{a}^k(t)$). The *eSNR* was evaluated for each number of MLT and the obtained results are depicted in Table IV.

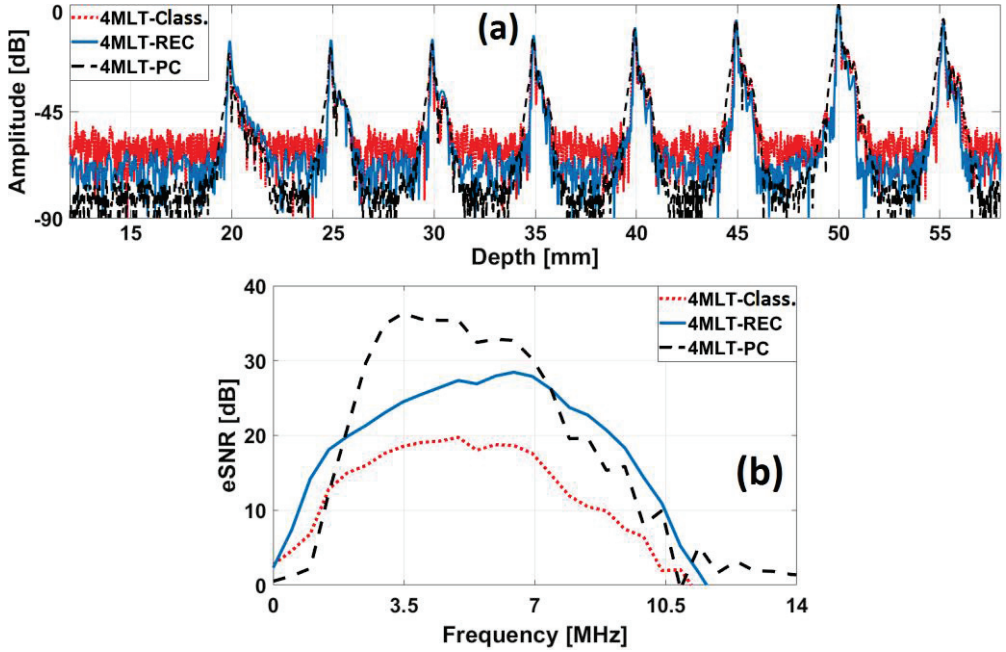

Fig.61: (a) The complete A-line corresponding to all the wires placed at x = 0 mm, (b) the obtained *eSNR* for the wire target placed at 50 mm depth using the different techniques.

Table IV: Summarized metric results for all the different number of MLT (simulated wire phantom).

Axial resolution (Simulation on wire phantom)

n° MLT	Axial resolutions (*µm*)			Enhancements / Degradations	
	Class.	**REC**	PC	*REC vs* Class.	*REC vs PC*
SLT	163.4	**123.7**	186.1	*+32.1%*	*+ 50.4%*
2 MLT	163.7	**124.0**	186.4	*+32.0%*	*+ 50.3%*
4 MLT	163.8	**124.2**	186.2	*+ 31.9%*	*+ 49.9%*
6 MLT	162.9	**123.8**	185.1	*+31.6%*	*+ 49.5%*
8 MLT	162.8	**123.9**	185.0	*+31.4%*	*+ 49.3%*
Average enhancements/degradations				***+31.8%***	***+49.9%***

Bandwidth (Simulation on wire phantom)

n° MLT	Bandwidths (*MHz*)			Enhancements / Degradations	
	Class.	**REC**	PC	*REC vs* Class.	*REC vs PC*
SLT	4.41	**5.85**	3.89	*+32.7%*	*+50.4%*
2 MLT	4.4	**5.82**	3.87	*+32.3%*	*+50.4%*
4 MLT	4.39	**5.79**	3.86	*+31.9%*	*+50%*
6 MLT	4.4	**5.84**	3.90	*+32.7%*	*+49.7%*
8 MLT	4.42	**5.84**	3.90	*+32.1%*	*+49.7%*
Average enhancements/degradations				***+32.3%***	***+49.9%***

Lateral resolution (Simulation on wire phantom)

n° MLT	Lateral resolution (*µm*)			Enhancements / Degradations	
	Class.	**REC**	PC	*REC vs* Class.	*REC vs PC*
SLT	467.2	**377.3**	470.1	*+23.8%*	*+24.6%*
2 MLT	467.1	**377.3**	470	*+23.8%*	*+24.6%*
4 MLT	467.4	**377.7**	469.9	*+23.7%*	*+24.4%*
6 MLT	467.5	**377.5**	469.9	*+23.8%*	*+24.5%*
8 MLT	467	**377.5**	469.7	*+23.7%*	*+24.4%*
Average enhancements/degradations				***+ 23.8%***	***+24.5%***

eSNR (Simulation on wire phantom)

n° MLT	eSNR (*dB*)			Enhancements / Degradations	
	Class.	**REC**	PC	*REC vs* Class.	*REC vs PC*
SLT	19.9	**27.7**	35.1	*+7.9 dB*	*-7.4 dB*
2 MLT	19.4	**28.1**	35.9	*+8.7 dB*	*-7.8 dB*
4 MLT	19.7	**28.4**	36.3	*+8.7 dB*	*-7.9 dB*
6 MLT	20.1	**28.9**	36.7	*+8.8 dB*	*-7.8 dB*
8 MLT	20.3	**29.3**	37.4	*+9.0 dB*	*-8.1 dB*
Average enhancements/degradations				***+ 8.6 dB***	***- 7.8 dB***

7.2.2.2 Cyst phantom

Fig.62 shows the log-compressed B-mode images obtained using the three approaches with SLT and 2, 4, 6, 8 MLT.

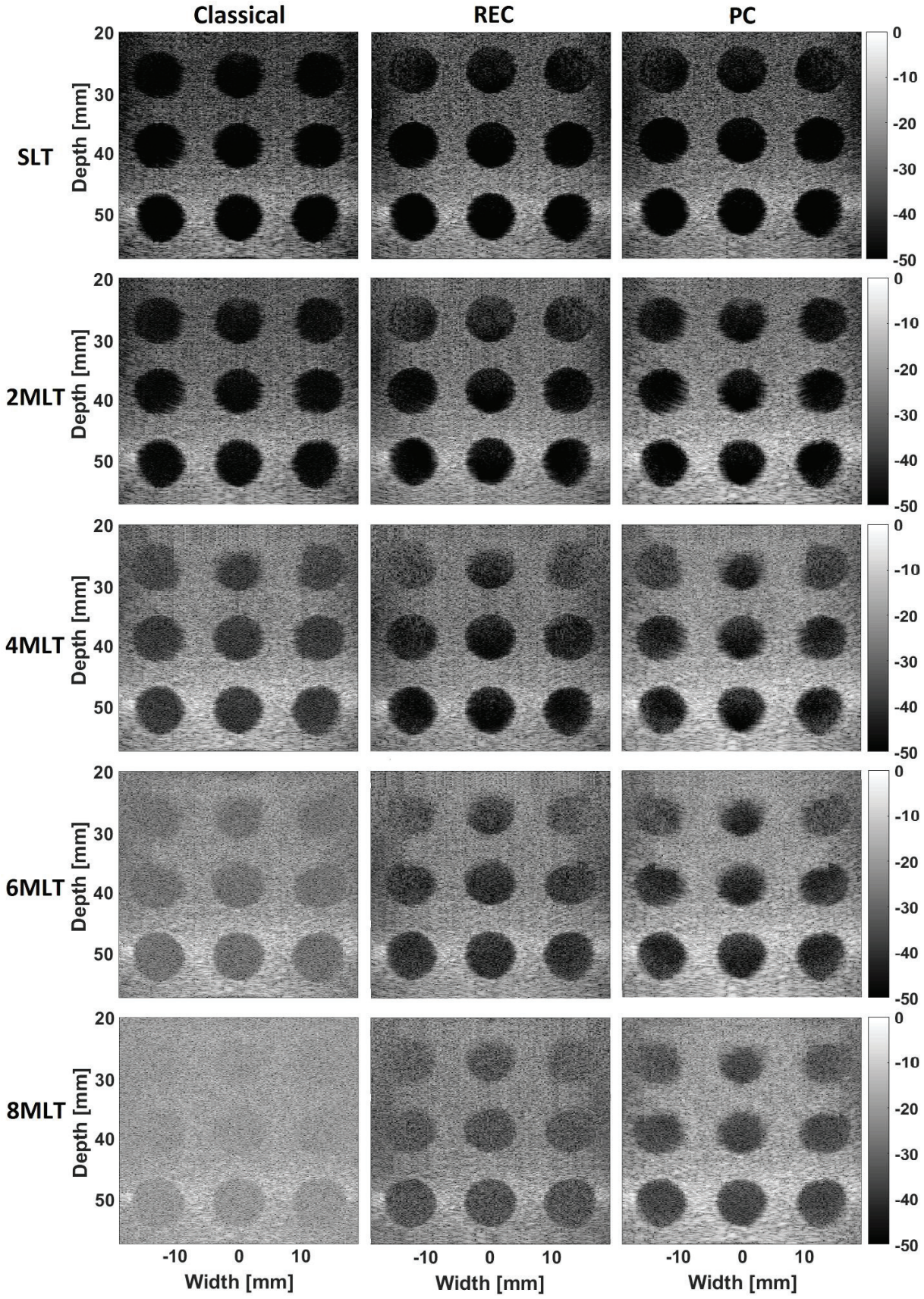

Fig.62: Log-compressed B-mode images obtained using the different techniques with SLT, 2MLT, 4MLT, 6MLT and 8MLT.

As it can be observed in Fig.62, the image quality degrades (even around the focal region: ~ 50 mm) by increasing the number of MLT for the three techniques. It can also be noticed that the MLT-REC approach yields a better compromise between the *CNR* and the definition of the cysts' contours (which is a direct consequence of the improvement of the spatial resolution seen in the previous section). The AACL results for 4MLT in Fig.63a (classical: 510.1 µm, REC: 389.2 µm, PC: 593.4µm) show an improvement of 31.1% between 4MLT-REC / classical 4MLT and of 52.5% between 4MLT-REC / 4MLT-PC. The proposed approach for 4 MLT provides also a boost of 14.7% and of 18.2% in comparison to classical 4MLT and 4MLT-PC respectively. The rest of the AACL and LACL (Fig.63b) measurements are summarized in Table V. The improved speckle size provided by MLT-REC is in accordance with the enhancement in axial / lateral resolution demonstrated in the previous section on the wire phantom.

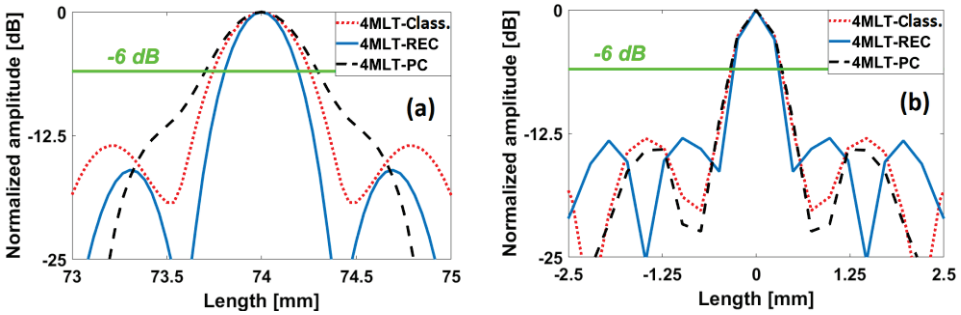

Fig.63: (a) Autocorrelation plot, in the axial direction, performed on the vertical line at 7mm in the cyst B-mode image, (b) Autocorrelation plot, in the lateral direction, performed on the horizontal line at 45 mm depth in the cyst B-mode image.

Table V: Summarized metric results for all the different number of MLT (simulated cyst phantom).

AACL (Simulation on cyst phantom)

n° MLT	AACL *(µm)*			Enhancements / Degradations	
	Class.	**REC**	PC	*REC vs* Class.	*REC vs PC*
SLT	511.7	**387.4**	592.4	*+32.1%*	*+52.9%*
2 MLT	512.1	**388.3**	592.9	*+31.9%*	*+52.7%*
4 MLT	510.1	**389.2**	593.4	*+31.1%*	*+52.5%*
6 MLT	510.6	**389.9**	594.2	*+31.0%*	*+52.5%*
8 MLT	509.8	**389.5**	594.0	*+30.9%*	*+52.5%*
Average enhancements/degradations				***+31.4%***	***+52.6%***

LACL (Simulation on cyst phantom)

n° MLT	LACL *(µm)*			Enhancements / Degradations	
	Class.	**REC**	PC	*REC vs* Class.	*REC vs PC*
SLT	666.4	**581.1**	688.1	*+14.7%*	*+18.4%*
2 MLT	665.9	**580.8**	687.2	*+14.7%*	*+18.3%*
4 MLT	666.6	**581**	686.8	*+14.7%*	*+18.2%*
6 MLT	666.2	**581.3**	687.2	*+14.6%*	*+18.2%*
8 MLT	666.8	**581.7**	687.9	*+14.6%*	*+18.3%*
Average enhancements/degradations				***+14.7%***	***+18.3%***

CNR (Simulation on cyst phantom)

n° MLT	CNR *(dB)*			Enhancements / Degradations	
	Class.	**REC**	PC	*REC vs* Class.	*REC vs PC*
SLT	15.28	**17.21**	18.65	*+1.93 dB*	*-1.44 dB*
2 MLT	12.58	**14.05**	15.08	*+1.47 dB*	*-1.03 dB*
4 MLT	10.72	**13.22**	14.55	*+2.50 dB*	*-1.33 dB*
6 MLT	6.48	**11.08**	12.85	*+ 4.60 dB*	*-1.77 dB*
8 MLT	-0.79	**7.17**	9.55	*+ 7.96 dB*	*-2.38 dB*
Average enhancements/degradations				***+3.69 dB***	***-1.59 dB***

The *CNR* provided by the cyst placed at (x = 0 mm, z = 50 mm) was calculated, by applying equation (62) to the regions shown in Fig.57, on the log-compressed B-mode images. For 4MLT, the REC approach provides a boost of 2.5 dB compared to the classical technique while a 1.33 dB loss is measured in comparison to the PC method. To be noted that a maximum of 7.96 dB improvement

(compared to classical 8MLT) is achieved using 8MLT-REC. In the same time, 8MLT-REC yields a loss of only 2.38 dB compared to 8MLT-PC. The rest of the *CNR* results are shown in Table V.

7.3 Experimental implementation

In order to validate the simulated results, the proposed approach was implemented experimentally. The same comparison between the obtained B-mode images was done (MLT-REC vs classical MLT vs MLT-PC).

7.3.1 Experimental setup

For the data acquisition, the open ultrasound platform UlaOp 256 (Microelectronics System Design Lab, Florence, Italy) equipped with a LA523E linear array probe (Esaote, Genova, Italy) was used. The UlaOp-256 can be tuned to transmit arbitrary waveforms and can be adapted to customized transmissions and reception strategies **[Boni (2016)]**. The probe has 192 elements with a pitch of 0.245 mm, a kerf of 0.03 mm and a center frequency of 8.5 MHz. The pulse-echo impulse response at the focus of the probe was measured from the reflection of a planar surface immersed in water. The experimental excitation signals are the same as the ones shown in Fig.56. The maximum source voltage for each acquisition was set to 24 V. Two different areas from the phantom (model 410SCG HE 0.5 Gammex Sun nuclear, Neu-Isenburg, Germany) were studied. As shown in Fig.64, the first area contains 3 wires of 100 µm diameter placed vertically in the center of the medium and the second one contains a wire and two hypoechoic cysts of -12 dB and of -6 dB. The two phantoms have an attenuation coefficient slope of 0.5 dB/MHz/cm. The focal point was placed at 50 mm.

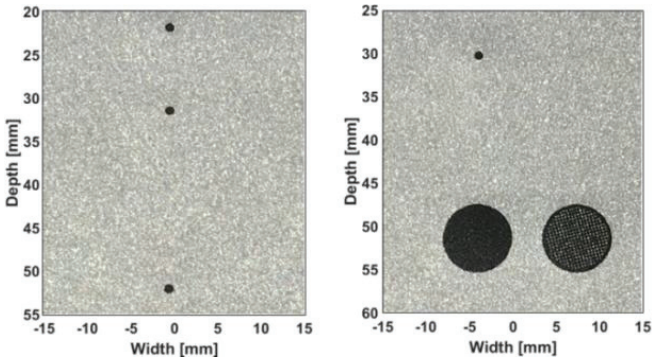

Fig.64: Wire (left) and cyst (right) phantoms used for experimental setups.

7.3.2 Experimental results

7.3.2.1 Wire phantom

Fig.65 shows the log-compressed B-mode images obtained using the three approaches with SLT and 4MLT. Two observations can be made by visualising the obtained results. First, a deterioration of the image quality (for the three techniques) as the number of MLT increases. This phenomenon is logical because of the interferences (crosstalk) generated in emission and reception which increases with the number of MLT. Second, the (SLT/4MLT)-REC presents a better axial and lateral resolution of the points present in the medium and less important artefacts than the two other techniques. The obtained results were measured for the reflector located around 50 mm (which corresponds to the focal region). Enhancements of 29.3% and of 15.5% in axial and lateral resolution respectively are provided by 4MLT-REC in comparison to classical MLT. These two metrics were also improved by the proposed

approach, when compared to 4MLT-PC, by 48.8% and by 24.3% respectively. The detailed results for all the in-vitro wire acquisitions are shown in (Appendix A).

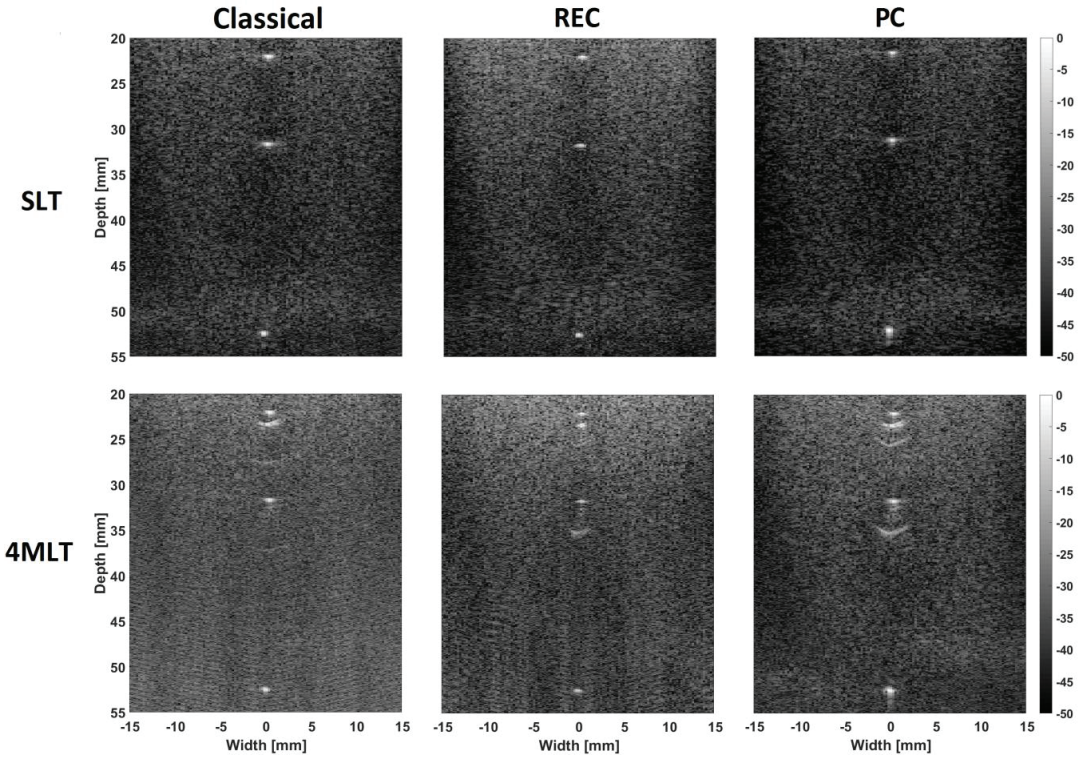

Fig.65: Log-compressed B-mode images obtained using the different techniques with SLT and 4MLT.

7.3.2.2 Cyst phantom

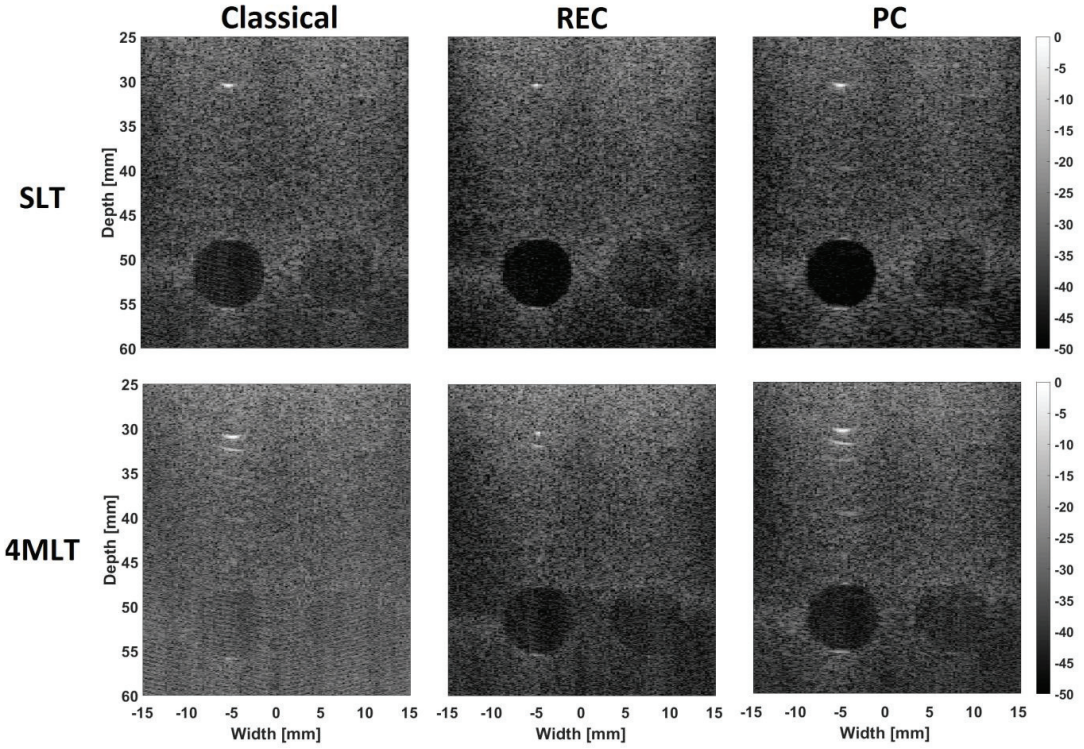

Fig.66: Log-compressed Bmode images obtained using the different techniques with SLT and 4MLT.

Fig.66 shows the log-compressed B-mode images obtained using the three approaches with SLT and 4MLT. One can observe that REC provides a better trade-off between: (spatial resolution and low artefacts / *CNR* and penetration depth) when the number of MLT increases. This trade-off is revealed firstly by a gain in AACL (+30.1%) and LACL (+18.9%) and secondly by an improvement in *CNR* of 9.97 dB in comparison to classical 4MLT. In the same time, the proposed approach enhances AACL (+46.9%) and LACL (+24.9%) when compared to 4MLT-PC while only a loss of 1.58 dB in *CNR* is measured. The rest of the results concerning the speckle size (in the axial and lateral directions) and the *CNR* are summarised in (Appendix B).

7.3.2.3 Ex-vivo phantom

In order to evaluate the performance of the proposed method, ex-vivo experiments were performed on a rabbit liver (the attenuation coefficient was supposed to be 0.5 dB/MHz/cm). The obtained B-mode images for the three methods are displayed in Fig.67. Again for 4MLT, the best results for the AACL and LACL metrics are provided by the REC approach. Indeed, respective improvements of 33.6% (22%) and of 54.5% (23%) in comparison to classical 4MLT (4MLT-PC) are measured. Less gain in *CNR* (+2.88 dB) is achieved between 4MLT-REC and classical 4MLT, in comparison to the previous in-vitro cyst phantom results. However, nearly the same *CNR* values (as 4MLT-REC) are obtained with 4MLT-PC, with a slight advantage of 0.23 dB. Appendix C show the obtained values for AACL, LACL and *CNR* with all the ex-vivo acquisitions.

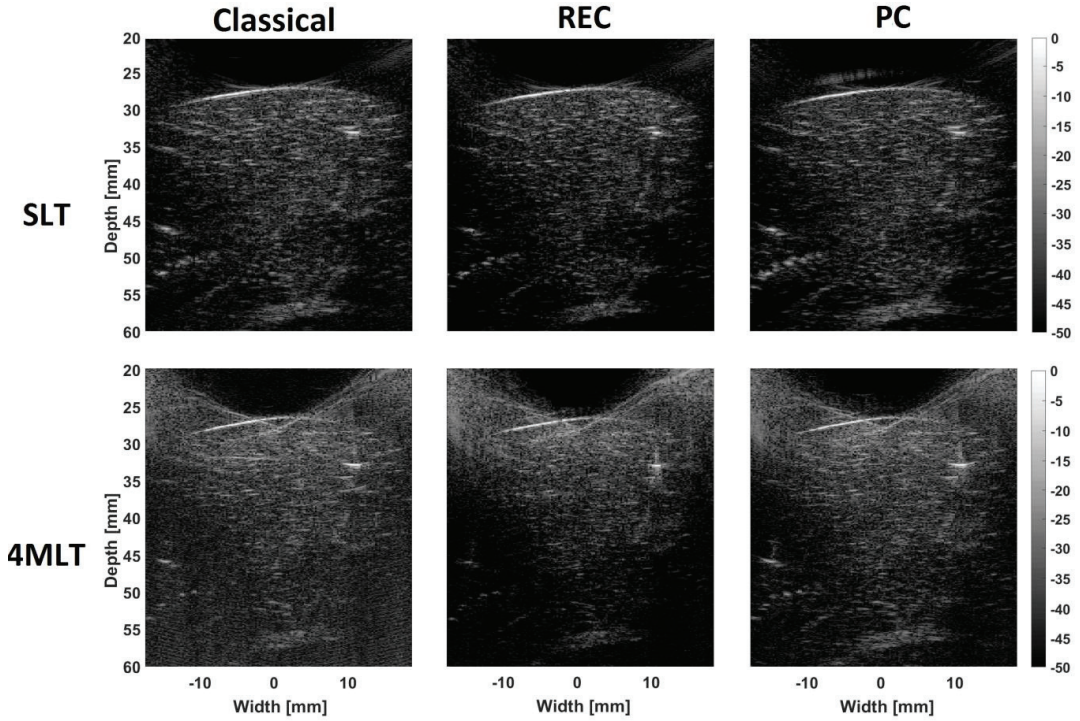

Fig.67: Log-compressed B-mode images obtained using the different techniques with SLT and 4MLT.

7.4 Discussion

A chirp compression technique which compensates the effect of attenuation propagation combined with MLT was implemented on an array based ultrasonic imaging system to enhance its bandwidth and consequently the image resolution, while providing a significant boost in both *eSNR* and *CNR*.

The proposed technique is based on the use of pre-enhanced frequency modulated chirps to excite more energy in frequency bands having decreasing spectral power in the bandwidth (in comparison to the centre frequency). In reception, a modified Wiener filter adapted to the attenuation coefficient slope (which was supposed to be known) of the tissue is used in order to adjust the trade-off between the image resolution and noise level. Simulation and experiments (in-vitro/ex-vivo) results were used to assess the performance of the MLT-REC technique in enhancing the image quality in terms of axial resolution, received echoes bandwidths, *eSNR* and *CNR*. The excitation signal used in the proposed method was designed to provide a theoretical bandwidth boost of 35 % in comparison to a classical MLT in both simulation and experimental setups. The enhancement of the less effective frequency bands of the transducer provided a chirp (MLT-REC excitation) that carries 1.8 times less energy than a linear chirp (MLT-PC excitation).

The results obtained with both simulations and experiments led to an average bandwidth improvements (i.e., 32.3% and 30.4%, respectively) of MLT-REC in comparison to classical MLT, consistent with the intended bandwidth boost of 35%. The improvement in the spatial resolution of the wire profiles (i.e., 31.8% and 29.6% for simulation and experiment as measured on the corresponding B-mode image line at -6 dB) was also consistent with the intended bandwidth improvement. The observed bandwidth enhancements between MLT-REC and MLT-PC (i.e., 49.9% and 48.2% in simulation and experiments respectively) can be explained by the fact that while the MLT- PC excitation is limited by the probe bandwidth, the MLT-REC excitation improves it. Moreover, the MLT-REC compression filter is optimized in a way that the frequency dependent tissue attenuation effect is compensated as compared to MLT-PC, for which a classical matched filter was used for compression. Same trends are observed for axial resolution (i.e., 49.9% and 47.4% for simulations and experiments respectively).

MLT-REC was also capable to improve the lateral resolution in both simulation and experimental setups. Indeed, 15.4% and 24.1% enhancements are measured experimentally for the proposed approach in comparison to classical MLT and MLT-PC respectively. Knowing that echoes with higher bandwidths are less coherent, beamforming image points (closely placed on a lateral line) that yield similar time signatures (inside the radio-frequency data) generates a smaller point spread function on the lateral dimension of the image. Thus, since MLT-REC increases the bandwidth of the backscattered echoes (compared to classical MLT and MLT-PC), its point spread function will be laterally thinner.

The obtained results on the AACL and LACL, for both simulations/experimental setups, show a thinner speckle for the MLT-REC approach compared to the other techniques. This improvement is directly linked to the axial and lateral resolution enhancements previously announced. 33.3% (22%) and 54.2% (23%) AACL (LACL) improvement for MLT-REC compared to classical MLT and MLT-PC respectively, is measured in the ex-vivo experiments. These values are coherent with the AACL (LACL) values obtained in simulations and in-vitro experiments.

The *eSNR* values measured for the classical MLT approach vary between 19.9 dB and 20.3 dB (depending on the number of MLT). Given that the time bandwidth product of the MLT-PC excitation chirp is 36.3, an improvement of 15.6 dB in *eSNR* is expected between MLT-PC and classical MLT. We measure *eSNR* values between 35.1 dB and 37.4 dB for MLT-PC which are coherent with the MLT-PC TBP. Since MLT-REC excitation signal carries 1.8 times less energy and a Wiener filter was used for compression (which allows increasing the axial resolution by amplifying the noise) the expected *eSNR* values for MLT-REC are somewhere between the classical MLT and MLT-PC values. We measure a low limit of 27.7 dB and a high limit of 29.3 dB for MLT-REC.

The proposed approach (MLT-REC) was also capable to improve the *CNR* up to 7.96 dB, 14.53 dB and 3.32 dB in simulations, in-vitro and ex-vivo setups respectively compared to classical MLT. A slight *CNR* loss was observed for MLT-REC when compared to MLT-PC, which can be explained by the loss in the *eSNR*. Indeed a maximal discrepancy of 2.38 dB, 2.47 dB and 0.57 dB in simulations, in-vitro and ex-vivo setups respectively was measured. We observe an overall decrease of the *CNR* for the three methods when the number of MLT increases (see Appendix B and Appendix C) which is related to the increase of crosstalk.

In the presented results, it can be observed that MLT-REC does not provide the same image quality improvement in the ex-vivo experiments as in the simulation and in-vitro setups. This can be explained by the fact that, in simulation and in-vitro experiments, we know the exact value of the tissue attenuation coefficient, thus we can better adapt the compression filters. In ex-vivo experiments however, we make an assumption on the value of the attenuation coefficient which implies that the compression filters are not optimal.

Since for MLT-REC technique the compression filter is adapted for each depth of the received radio-frequency data, the compression filtering is more time consuming than for MLT-PC (which has only an additional matched filtering step compared to classical MLT). However, it is possible to decrease the MLT-REC filtering time by reducing the number of optimized compression filters, the drawback being the degradation of the image quality at the depth where the compression filters are not optimal.

In this chapter, we showed the experimental feasibility of MLT-REC using a linear array probe centred at 8.5 MHz. The transmitted beams were focused perpendicularly to the surface of the probe which generates more inter-beam crosstalk when the number of MLT increases. Thus, we observe an image quality decrease at higher MLTs for the three studied methods. This effect can be reduced by using a convex probe which naturally will spread the simultaneously transmitted beams (which results in less crosstalk noise) or by focusing the beams with different incident angles (between the focused beam and the surface of the linear probe).

Finally, in our theoretical study, we showed that the performance of the proposed approach is directly linked to the impulse response of the ultrasound probe and to the tissue attenuation coefficient. However, by adapting these two entities to a specific probe and imaged medium, the proposed method can be applied to different applications with the condition that the employed scanner can generate arbitrary waveforms.

7.5 Conclusion

In this chapter, the performance of a pulse compression technique adapted to tissue attenuation effects, for multi-line transmit ultrasound, was evaluated. The results achieved both in simulations and on phantom/ex-vivo experiments (using UlaOp-256) show that the proposed method provides a better image quality than conventional multi-line transmit in term of spatial resolution, echoes bandwidth, *eSNR*, *CNR* and speckle size. This study has shown that the proposed technique combines the advantages of a better (than conventional multi-line transmit) image resolution with a higher *CNR*.

The obtained results demonstrates that the proposed method makes it possible to achieve an up to 8-fold improvement of the frame rate in phantom/ex vivo scans while still providing a better image quality than conventional MLT.

7.6 Appendix

APPENDIX A (In-vitro results on wire phantom)

Axial resolution

n° MLT	Axial resolutions *(μm)*			Enhancements / Degradations	
	Class.	**REC**	PC	*REC vs* Class.	*REC vs PC*
SLT	313.9	**241.7**	353.7	*+29.9%*	*+46.3%*
2 MLT	314.3	**243.6**	355.2	*+29.0%*	*+45.8%*
4 MLT	295.9	**228.8**	340.5	*+29.3%*	*+48.8%*
6 MLT	293.2	**225.4**	334.3	*+30.1%*	*+48.3%*
8 MLT	288.9	**223.1**	329.3	*+29.5%*	*+47.6%*
Average enhancements/degradations				***+29.6%***	***+47.4***

Bandwidth

n° MLT	Bandwidths *(MHz)*			Enhancements / Degradations	
	Class.	**REC**	PC	*REC vs* Class.	*REC vs PC*
SLT	2.45	**3.19**	2.18	*+30.2%*	*+46.3%*
2 MLT	2.44	**3.16**	2.17	*+29.5%*	*+45.6%*
4 MLT	2.60	**3.39**	2.26	*+30.4%*	*+50.0%*
6 MLT	2.63	**3.45**	2.30	*+31.2%*	*+50.0%*
8 MLT	2.67	**3.49**	2.34	*+30.7%*	*+49.2%*
Average enhancements/degradations				***+30.4%***	***+48.2%***

Lateral resolution

n° MLT	Lateral resolutions *(μm)*			Enhancements / Degradations	
	Class.	**REC**	PC	*REC vs* Class.	*REC vs PC*
SLT	685.1	**594.2**	736.6	*+15.3%*	*+23.9%*
2 MLT	685.8	**594.1**	737.1	*+15.4%*	*+24.1%*
4 MLT	687.1	**595.1**	739.5	*+15.5%*	*+24.3%*
6 MLT	688.5	**596.6**	740.1	*+15.4%*	*+24.1%*
8 MLT	690.1	**598.8**	742.4	*+15.3%*	*+24%*
Average enhancements/degradations				***+15.4%***	***+24.1***

APPENDIX B (In-vitro results on cyst phantom)

AACL

n° MLT	AACL *(μm)*			Enhancements / Degradations	
	Class.	**REC**	PC	*REC vs* Class.	*REC vs PC*
SLT	628.6	**483.4**	709.2	*+30.0%*	*+46.7%*
2 MLT	628.4	**482.9**	708.9	*+30.1%*	*+46.8%*
4 MLT	627.1	**482.2**	708.1	*+30.1%*	*+46.9%*
6 MLT	627.0	**481.7**	707.6	*+30.2%*	*+46.9%*
8 MLT	626.5	**481.5**	706.7	*+30.1%*	*+46.8%*
Average enhancements/degradations				***+30.1%***	***+46.8%***

LACL

n° MLT	LACL *(μm)*			Enhancements / Degradations	
	Class.	**REC**	PC	*REC vs* Class.	*REC vs PC*
SLT	976.4	**820**	1025.2	*+19.1%*	*+25%*
2 MLT	976.8	**820.6**	1026.1	*+19%*	*+25%*
4 MLT	977.9	**821.8**	1027.2	*+18.9%*	*+24.9%*
6 MLT	979.1	**822.4**	1028.6	*+19.1%*	*+25.1%*
8 MLT	980.2	**823.1**	1030.1	*+19.1%*	*+25.2%*
Average enhancements/degradations				***+19%***	***+25%***

CNR

n° MLT	CNR *(dB)*			Enhancements / Degradations	
	Class.	**REC**	PC	*REC vs* Class.	*REC vs PC*
SLT	3.93	**8.64**	9.15	*+4.71 dB*	*-0.51 dB*
2 MLT	-1.02	**7.81**	8.52	*+8.83 dB*	*-0.71 dB*
4 MLT	-8.08	**1.89**	3.47	*+9.97 dB*	*-1.58 dB*
6 MLT	-17.87	**-5.62**	-3.15	*+12.25 dB*	*-2.47 dB*
8 MLT	-24.18	**-9.65**	-8.83	*+14.53 dB*	*-1.50 dB*
Average enhancements/degradations				***+10.06 dB***	***-1.35 dB***

APPENDIX C (Ex-vivo results on rabbit liver)

AACL

n° MLT	AACL *(µm)*			Enhancements / Degradations	
	Class.	**REC**	PC	*REC vs* Class.	*REC vs PC*
SLT	749.1	**563.2**	867.6	*+33.0%*	*+54.1%*
2 MLT	748.4	**562.1**	866.1	*+33.1%*	*+54.1%*
4 MLT	748.0	**560.0**	865.4	*+33.6%*	*+54.5%*
6 MLT	746.2	**561.1**	864.7	*+33.0%*	*+54.1%*
8 MLT	747.1	**559.4**	863.1	*+33.6%*	*+54.4%*
Average enhancements/degradations				***+33.3%***	***54.2%***

LACL

n° MLT	LACL *(µm)*			Enhancements / Degradations	
	Class.	**REC**	PC	*REC vs* Class.	*REC vs PC*
SLT	1154.2	**945.3**	1163.2	*+22.1%*	*+23.1%*
2 MLT	1155.1	**945.1**	1164.2	*+22.2%*	*+23.2%*
4 MLT	1155.9	**947.2**	1165.1	*+22%*	*+23%*
6 MLT	1157.2	**948.1**	1166.4	*+22.1%*	*+23%*
8 MLT	1156.3	**949.2**	1166.8	*+21.8%*	*+22.9%*
Average enhancements/degradations				***+22%***	***23%***

CNR

n° MLT	CNR *(dB)*			Enhancements / Degradations()	
	Class.	**REC**	PC	*REC vs* Class.	*REC vs PC*
SLT	5.31	**7.89**	7.32	*+2.58 dB*	*+0.57 dB*
2 MLT	4.85	**7.05**	6.93	*+2.20 dB*	*+0.12 dB*
4 MLT	3.34	**6.22**	6.45	*+2.88 dB*	*-0.23 dB*
6 MLT	2.12	**5.44**	5.74	*+3.32 dB*	*-0.30 dB*
8 MLT	1.42	**4.37**	4.63	*+ 2.95 dB*	*-0.26 dB*
Average enhancements/degradations				***+ 2.79 dB***	***-0.02 dB***

Chapter VIII

ULTRASOUND PROBE BANDWIDTH ENHANCEMENT COMBINED WITH NON-STATIONARY COMPRESSION FILTERS TO IMPROVE IMAGE QUALITY

Contenu

8.1 Theoretical background

In the previous chapters, a very important hypothesis had to be made in order to simplify the propagation model that links the received backscattered echoes to the excitation signals, propagation phenomenon and tissue interaction. Indeed, in (35) was shown that for two vibrating acousto-electrical transducers immersed in soft tissues (one that emits j a spherical wave and the other one i that receives the echoes) the signal received at the second transducer can be written as:

$$y_{ji}(t) = h_e(t) *_t a(t) *_t h_r(t) *_t TRF(\vec{r}) *_{\vec{r}} h_{ji}(\vec{r},t) \tag{159}$$

where $h_e(t)$ and $h_r(t)$ are the acousto-electrical impulse responses of j in emission and i in reception respectively. In (159) we have also that:

$$h_{ji}(\vec{r},t) = h_j(\vec{r},t) *_t h_i(\vec{r},t) \qquad \text{with}: \begin{cases} h_j(\vec{r},t) = \int_{S_j} \dfrac{\delta\left(t - t_j - \dfrac{\left\|\vec{r} - \overrightarrow{r_{S_j}} - \overrightarrow{r^0_{S_j}}\right\|_2}{c_0}\right)}{2\pi\left\|\vec{r} - \overrightarrow{r_{S_j}} - \overrightarrow{r^0_{S_j}}\right\|_2} d^2\overrightarrow{r_{S_j}} \\ h_i(\vec{r},t) = \int_{S_i} \dfrac{\delta\left(t - \dfrac{\left\|\vec{r} - \overrightarrow{r_{S_i}} - \overrightarrow{r^0_{S_i}}\right\|_2}{c_0}\right)}{2\pi\left\|\vec{r} - \overrightarrow{r_{S_i}} - \overrightarrow{r^0_{S_i}}\right\|_2} d^2\overrightarrow{r_{S_i}} \end{cases} \tag{160}$$

The hypothesis, that was made in order to derive a general propagation model for all the ultrasound imaging techniques, consists in stating that the waves emitted by the elements / probe propagates / interacts with the imaged media in the far field conditions. Under such conditions, $\left\|\overrightarrow{r_{S_e}}\right\|_2 \ll \left\|\overrightarrow{r^0_{S_e}}\right\|_2$ and $\left\|\overrightarrow{r_{S_r}}\right\|_2 \ll \left\|\overrightarrow{r^0_{S_r}}\right\|_2$ thus (160) becomes:

$$h_{ji}(\vec{r},t) \approx \frac{\delta\left(t - t_j - \dfrac{\left\|\vec{r} - \overrightarrow{r^0_{S_j}}\right\|_2 + \left\|\vec{r} - \overrightarrow{r^0_{S_i}}\right\|_2}{c_0}\right)}{4\pi^2\left\|\vec{r} - \overrightarrow{r^0_{S_j}}\right\|_2\left\|\vec{r} - \overrightarrow{r^0_{S_i}}\right\|_2} \tag{161}$$

In other words, (161) implies that at any point $\vec{r}$, when the emitter j transmits a short impulsion (Dirac), the signal received at the receiver i will be also an impulsion, that will be received with a delay equals to the propagation time that separates emission / scattering / reception. Let us consider a purely hypothetical case where an element of the LA523E probe (Table II) is used both in emission and reception. Suppose that its pulse echo acousto-electrical impulse response is given by: $h_1(t) = h_e(t) *_t h_r(t) = \delta(t)$. Now let us consider three acquisitions made using this element (Fig.68): first acquisition the medium contains only the scatterer l, second acquisition the medium contains only the scatterer 2 and third acquisition the medium contains only the scatterer 3.

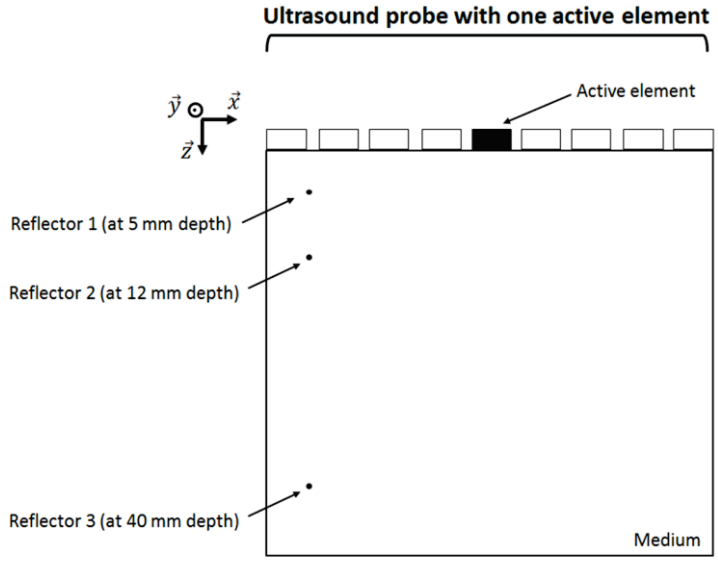

Fig.68: Configuration illustrating the difference, due to the spatial response, of the signals received by the probe from reflectors located at different depths.

The simulated (using Field II) signals $y_{ji}(t)$ are shown with their envelopes respectively in Fig.69a and Fig.69b.

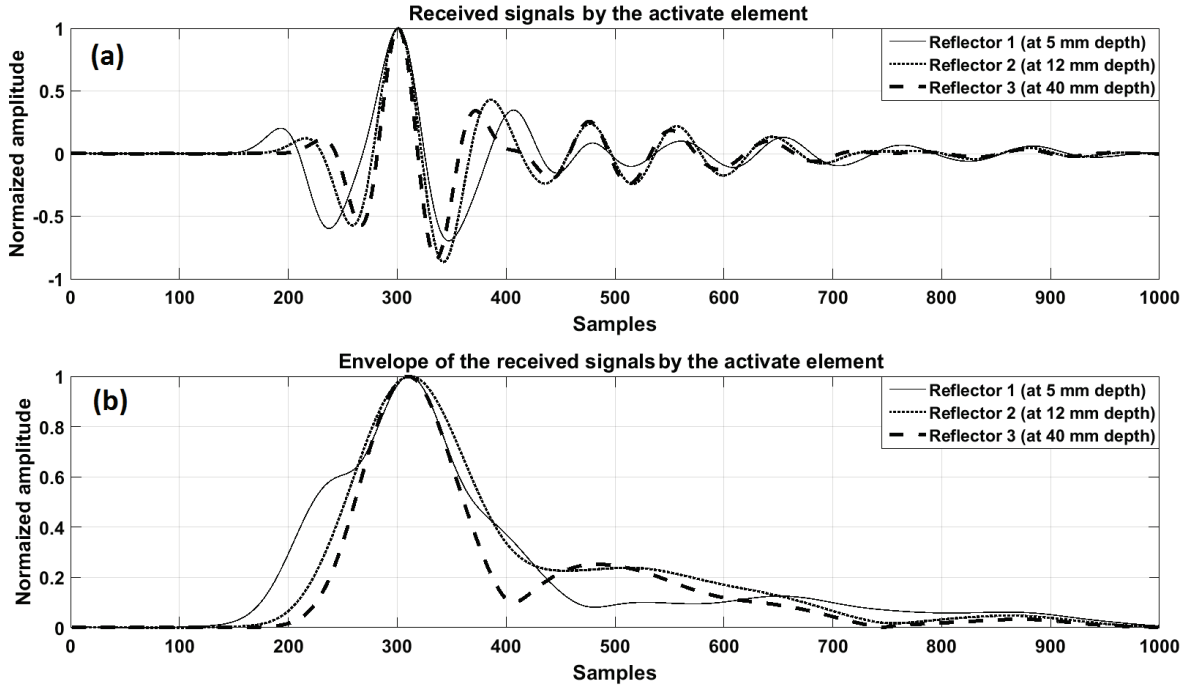

Fig.69: The simulated obtained signals for reflectors placed at different depths.

As it can be seen in this figure, the closest to a Dirac impulsion is the signal $y_{ji}(t)$ obtained when the scatterer was placed at the furthest position from the probe element. What happens here is that $\left\|\overrightarrow{r_{S_e}}\right\|_2 \approx \left\|\overrightarrow{r^0_{S_e}}\right\|_2$ and $\left\|\overrightarrow{r_{S_r}}\right\|_2 \approx \left\|\overrightarrow{r^0_{S_r}}\right\|_2$ thus the far field conditions are satisfied. However as one can observe, when the scatterers are closer to the element, $y_{ji}(t)$ widens. This is the result of the Huygens principle applied on the emission / reception surface of the probe element, where each point of the

surface behaves like a source/receiver, the total recorded signal being thus a sum of slightly delayed (as a function of the position on the surface) Dirac impulsions. Since the employed excitation signal and the acousto-electrical impulse response were short impulsion, these $y_{ji}(t)$ signals can be seen directly as the pulse –echo spatial impulse response of the probe element at the position r of the medium. It can be thus concluded, that during an emission / reception using the full array of probe elements, each element has a different spatial impulse response at each position r of the element. Now, in classical acquisition schemes this effect is completely neglected. However, similar to the implementation of the frequency dependent tissue attenuation effect (Chapter V), this effect could be compensated in a pulse compression scheme. Nonetheless, whereas the impulse response that models the tissue attenuation effect depends only on the Euclidian distance between the source/ scatterer / receiver, as seen in Fig.69, the spatial impulse response of the elements depends also on the relative position of the source / scatterer / receiver. This makes the implementation of a pulse compression scheme, that would compensate the effect of spatial impulse response, compatible only with a certain number of ultrasound acquisition schemes that allow for each received echo, to determine the exact path that this echo followed during its propagation. Such acquisition schemes are the classical focused emission and MLT. In this chapter, the application of a pulse compression technique that compensates the spatial impulse response of the probe in a focused acquisition scheme is presented.

In order to better understand how the proposed method works, let us resume the reasoning shown in Section 3.4.1. Consider the relation (74), here it can be seen that the received signals at each element i of the probe, when a focused beam was emitted inside the medium, can be written as:

$$y_i(t) = e(t) * g_i(t) + b(t) \quad \text{with} : \begin{cases} g_i(t) = \sum_{j=1}^{N_e} \delta(t - t_j) * g_{ji}(t) \\ g_{ji}(t) = \sum_{l=1}^{N_s} TRF_l \, h_j(\vec{r}_l, t) * h_i(\vec{r}_l, t) \\ e(t) = a(t) * h_1(t) \end{cases} \tag{162}$$

where $h_j(t)$ and $h_i(t)$ are the spatial impulse responses of the probe elements in emission and reception respectively. At this point, using (162), one can see that for any single scatterer l, located at the position $\vec{r}_l$, the received echo can be written as follows:

$$\begin{aligned} & e_{li}(t) = TRF_l \, a(t) * h_1(t) * g_p(\vec{r}_l, t) * h_i(\vec{r}_l, t) \\ & \text{with} : \; g_p(\vec{r}_l, t) = \sum_{j=1}^{N_{el}} h_j(\vec{r}_l, t) \end{aligned} \tag{163}$$

In (163), one can observe that the received echo $e_{li}(t)$ by i^{th} element of the probe (generated by the scatterer l) depends on the excitation signal $a(t)$, on the acousto electrical pulse echo impulse response of the probe $h_1(t)$, on the spatial impulse response of the element i at the position of the scatterer and on a signal $g_p(\vec{r}_l, t)$. This signal $g_p(\vec{r}_l, t)$, is the superposition of all the spatial impulse response of the emission elements of the probe at the scatterer position and can be seen as the probe spatial impulse response in emission at the point $\vec{r}_l$.

At this point, one can apply the core equivalence of REC in order to find the optimal excitation signal / compression filters:

$$e_{li}(t) = \tilde{e}(t)$$
$$\Leftrightarrow \quad a(t) * h_1(t) * g_p(\vec{r}_l, t) * h_i(\vec{r}_l, t) = \tilde{a}(t) * h_2(t) \tag{164}$$

where $\tilde{a}(t) * h_2(t)$ is the typical waveform of an echo, that a purely hypothetical ultrasound probe of acousto-electrical pulse echo impulse response $h_2(t)$ and a perfect (Dirac like) spatial impulse response would receive when excited with a waveform $\tilde{a}(t)$. Of course if one chooses carefully $h_2(t)$ and $\tilde{a}(t)$ (as seen in the previous Chapters) the provided image quality will be boosted. Thus, equation (164) allows to compute the excitation signal of the real transducer $a(t)$ (Fig.28b) that needs to be used in order to obtain the same resolution as the fictive transducer, of wider bandwidth, excited with $h_1(t)$. This relation also shows that in order to receive echoes $\tilde{e}(t)$ when emitting with the probe (of impulse response $h_1(t)$) one should adapt the emission signal for each scattering point (since the attenuation effect depends on the wave propagation distance). This requirement could be feasible if one wants to adapt the emission only for one point in the medium (focal point for instance). However, in order to take into account all the scattering points (in a medium with dense distribution of scatterers), we propose to proceed as follows:

1) Apply the following relation in order to find the excitation signal $a(t)$:

$$a(t) * h_1(t) = \tilde{a}(t) * h_2(t) \tag{165}$$

which implies that the spatial impulse response is not compensated by the excitation signal. By solving (165) in the frequency domain, we can compute the excitation signal using:

$$A(f) = \tilde{A}(f) \frac{H_2(f) H_1^*(f)}{\left|H_1(f)\right|^2 + \left|H_1(f)\right|^{-2}} \tag{166}$$

2) Adapt the pulse compression filter as a function of the echo propagation distance in order to compensate the effect of the spatial impulse response. We propose to include the spatial impulse response as a modification of the excitation $\tilde{a}(t)$, of the hypothetical probe. By combining (164) and (165), we obtain:

$$\tilde{A}(\vec{r}_l, f) = A(f) \frac{H_1(f) G_p(\vec{r}_l, f)}{H_2(f)} \tag{167}$$

Since (167) is entirely analytical and does not imply modifying the excitation signal of the real probe (of impulse response $h_1(t)$), adapting $h_1(t)$ as a function of $\vec{r}_l$ is much more convenient than adapting $a(t)$. Knowing $\tilde{a}(\vec{r}_l, f)$ and relying on the echo equivalence (164), we can design an optimal Wiener filter that will allow to compress the echo waveforms $e(t)$. We propose the following compression filter:

$$\beta_{REC}\left(\vec{r}_l, f\right) = \frac{\tilde{A}^*(\vec{r}_l, f)}{\left|\tilde{A}(\vec{r}_l, f)\right|^2 + \gamma \overline{eSNR}^{-1}\left(f\right)} \tag{168}$$

where $eSNR(f)$ is the mean signal-to-noise ratio per frequency channel of the received signals $y_i(t)$. γ is a smoothing parameter that controls the tradeoff between bandwidth enhancement (better axial resolution), *eSNR* gain and sidelobe levels **[Oelze (2007); Benane (2018a)].** Low γ values, for which $\beta_{REC}\left(\vec{r}_l, f\right)$ becomes an inverse filter, improve axial resolution but increase sidelobe levels and

degrade *eSNR*. While high values of γ, for which $\beta_{REC}\left(\vec{r}_l, f\right)$ becomes a matched filter, have the opposite effect. In this work, γ was adjusted manually by keeping the best axial resolution that can be achieved in the image while the acquisition noise level does not exceed the one of classical MLT.

8.2 Simulation results

Three different configurations are considered in simulation. The first one ($\text{Conventional}_{sim}$) is the conventional case where a period of a sinusoidal signal is transmitted and after the reception of the echoes, the beamforming (DAS) is performed. The second case (REC_{sim}) is the classical REC described previously which consists in transmitting a pre-enhanced chirp signal and compressing the obtained echoes before beamforming them using DAS. The third one (I-REC_{sim}) is an improvement of the second method by taking into account the spatial impulse response of the medium in reception during the compression step (just before the beamforming). Fig.70 shows the different log-compressed B-mode images obtained for three different configurations.

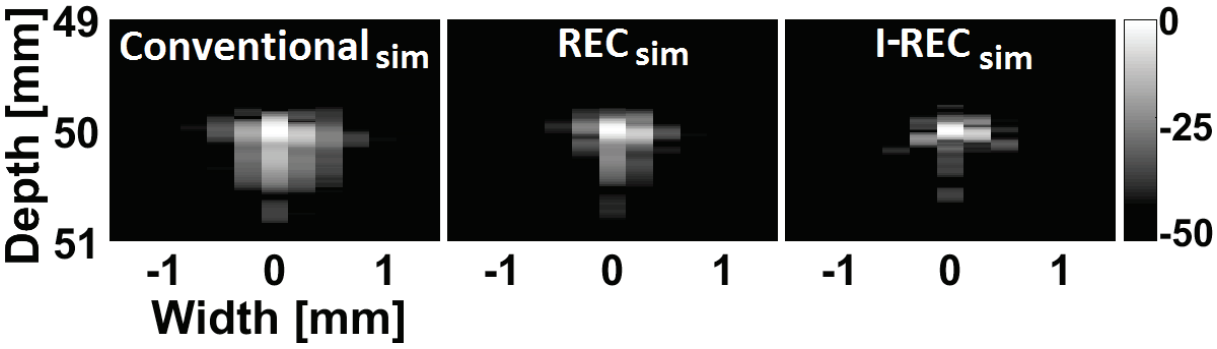

Fig. 70: Log-compressed B-mode images obtained from a single simulated wire using the three different techniques.

It can be visually noticed that the proposed method (I-REC_{sim}) offers a better image quality than the two other techniques. Indeed, the scaterrer is more resolved axially in the I-REC_{sim} image. By studying the axial profile of the PSF, it can be noticed that the axial resolution at -6dB is enhanced by 17% for I-REC_{sim} in comparison to REC_{sim} which in its turn improves it by 38% compared to $\text{Conventional}_{sim}$. Moreover it can be seen that the axial sidelobes have the lower levels on the I-REC_{sim} image. One can measure a 8 dB improvement in comparison to REC_{sim}, knowing that REC_{sim} already improves the axial sidelobe level by 5 dB when compared to $\text{Convenitonal}_{sim}$. As it can be seen for the theoretical formulation previously developed, the improvement achieved by I-REC_{sim} over REC_{sim} comes purely from the fact that the spatial impulse response of the medium is compensated in the Wiener filter used for the RF data compression.

8.3 Experimental results

The same configurations tested in simulation (showed in the previous section) were also implemented in an experimental acquisition using Ula-Op 256 scanner equipped with the LA523E probe. The obtained results on a wire and a cyst phantom (model 410SCG HE 0.5 Gammex Sun nuclear, Neu-Isenburg, Germany) are presented in the following sub-sections.

8.3.1 Wire phantom

In Fig.71 are displayed the results obtained on the wire phantom acquisitions.

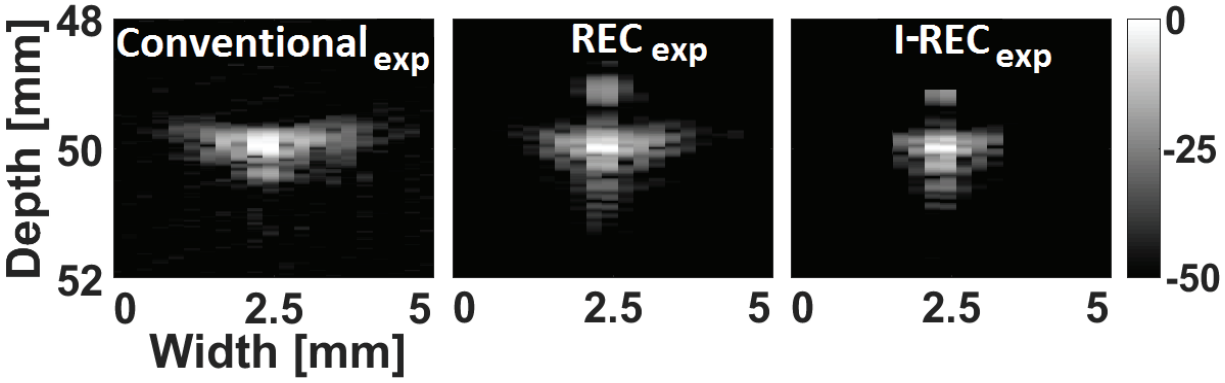

Fig. 71: Log-compressed B-mode images obtained from a wire phantom using the three different techniques.

The obtained results show that I-REC$_{exp}$ provides the better image quality. Indeed, experiments reveal a bandwidth improvement 51% for I-REC$_{exp}$ in comparison to the conventional technique, consistent with the intended bandwidth boost of 54%. When the REC$_{exp}$ approach is used (without compensating the spatial impulse response), only 36% bandwidth enhancement is observed in comparison with the conventional technique. Axial resolution (Fig.72) follows the same trend (i.e. I-REC$_{exp}$: 87.4 µm, REC$_{exp}$: 99.1 µm, conventional$_{exp}$: 132.8 µm).

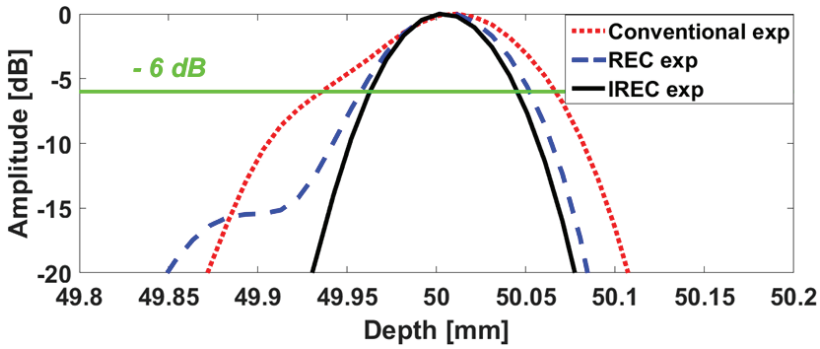

Fig. 72: Envelope of the radio frequency data corresponding to the wire phantom.

8.3.2 Cyst phantom

In Fig.73 are displayed the results obtained on the cyst phantom acquisitions.

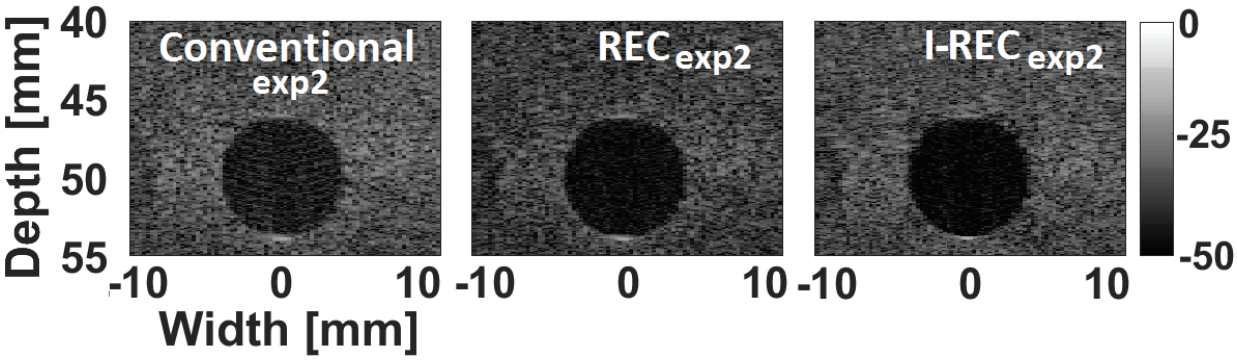

Fig. 73: Log-compressed B-mode images obtained from a cyst phantom using the three different techniques.

The obtained cyst images demonstrate that I-REC$_{exp2}$ improves also CNR by 3.4 dB when compared to the Conventional$_{exp2}$ technique while REC increase it by only 2.2 dB, (i.e. I-REC$_{exp2}$: 7.3 dB, REC$_{exp2}$:

6.1 dB, Conventional$_{exp2}$: 3.9 dB). These results prove again the ability of I-REC to provide better image qualities than the two other techniques. Further measurements on the axial autocorrelation lengths consolidated the observations made on the wire phantom acquisitions, and showed again a thinner speckle as a result of an improved spatial resolution.

Chapter IX

AN ENHANCED CHIRP MODULATED GOLAY CODE FOR ULTRASOUND DIVERGING WAVE COMPOUNDING

Contenu

9.1 Introduction

As shown in Section 3.4.4, diverging wave ultrasound imaging, as other ultrafast emission schemes that lack beam focusing (plane wave and synthetic aperture imaging), provides RF data with a decreased eSNR (compared to conventional, focused ultrasound) which limits considerably its penetration depth compared to classical focused ultrasound. This can be a serious drawback in diverging wave applications such as cardiac imaging **[Papadacci (2014)**; **Zhang (2016)]**. Increasing the excitation length could be a solution, however in order to preserve the image resolution one should search for long excitation signals with good pulse compression properties. Thus different types of long excitation signals, with good autocorrelation products (narrow main-lobe, low side-lobes), have already been implemented in ultrasound acquisition schemes. Large number of binary codes **[Gran (2008); Lashkari (2016); Tiran (2015); Bujoreanu (2017b)]** were tested however for now, the signals that yields the best compression (in terms of temporal resolution, signal to noise ratio and side-lobes) are linear frequency modulated signals **[Lashkari (2016)]**. In **[Oelze (2007)**; **Benane (2018a)],** it has been shown that chirps can be further improved in terms of the provided image quality.
The main idea is to compensate the effect of the narrow-band ultrasound probe on the chirp during the transmission and echo reception. Recently, binary Golay codes also gained a vast interest, since these sequences can be compressed without generation of side-lobes **[Trots (2015)]**. Moreover, groups of mutual orthogonal Golay sequences can be built and transmitted simultaneously. In this chapter, we propose to combine the advantages of enhanced chirp signals with the orthogonality properties of the Golay sequences. Furthermore, we apply thereby designed signals to a Diverging Wave Compounding (DWC) imaging technique and evaluate its performances by comparing the obtained image quality metrics to the classical way of acquiring diverging waves.

9.2 Theoretical background

Let us suppose a linear ultrasound probe, placed at $z = 0$ with a total of N_{el} elements (Fig.74).

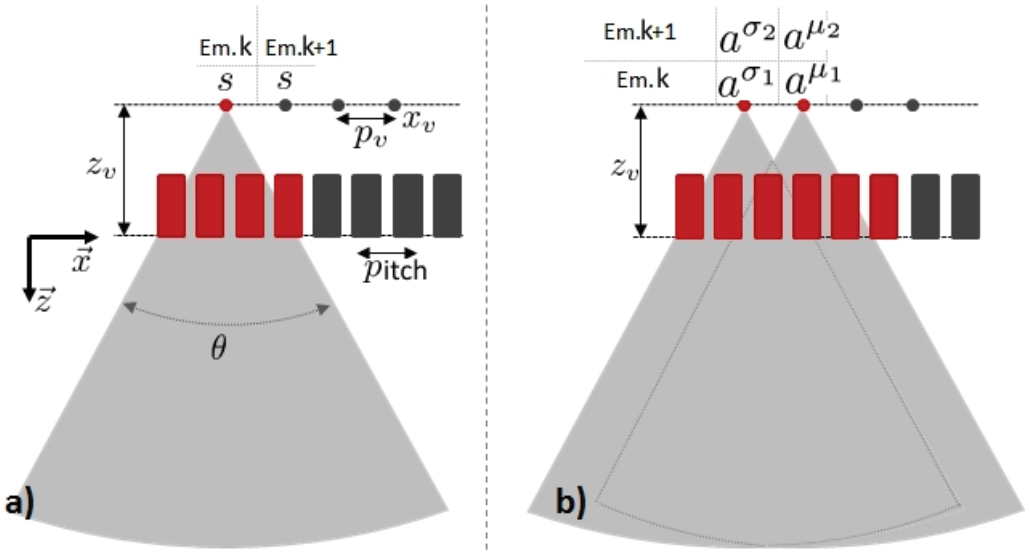

Fig.74. Transmission schemes used for diverging wave compounding: (a) Classical approach, where the transmitted signal represents a cycle of a sinusoid, (b) Orthogonal Golay coded approach.

In Section 3.4.4 was shown that, in order to transmit a diverging wave using this probe one should consider a punctual virtual source located at the point (x_v, z_v) with $z_v < 0$. Depending on the region of interest in the medium, which imposes certain angular aperture θ, n elements of the probe are excited with the same excitation $a^k(t)$ slightly delayed depending on the position of each active element. The number of active elements n and the delay in transmission t_j (for the j^{th} element of the transducer) are determined by **[Papadacci (2014)**; **Zhang (2016)]**:

$$n = \frac{2 \mid z_v \mid \tan\left(\frac{\theta}{2}\right)}{pitch} \tag{169}$$

$$t_j = \frac{1}{c}\left[\sqrt{z_v^2 + \left(\frac{\mathrm{j}.pitch}{2}\right)^2} - z_v\right] \tag{170}$$

where $j \in \{-n/2, ..., n/2\text{-}1\}$, $pitch$ is the pitch of the ultrasound probe, c is the propagation speed of sound in soft tissues and θ is the considered angle aperture.

After one diverging wave transmission, the received echoes are recorded and beamformed in either time or frequency domain **[Zhang (2016)]**. Envelope extraction and log-compression is performed on the resulting radio frequency image. In order to increase the signal to noise ratio and to further widen the region of interest, it was proposed in **[Papadacci (2014)]** to do Diverging Wave Compounding. The main idea is to consider that N_{dw} virtual sources are located behind the real ultrasound probe. Each virtual source k has a position defined by (x_{kv}, z_v) where $x_{kv} = kp_v$, p_v being the pitch of the virtual transducer.

The reconstruction pipeline for the final compounded image can be divided in the following steps:

(a) Activate virtual source k;

(b) Compute, using (169), the corresponding n elements of the ultrasound probe to be activated;

(c) Compute the transmission delays for each j^{th} active element of the probe by adapting (170) to:

$$t_j^k = \frac{1}{c}\left[\sqrt{z_v^2 + \left(x_{jv}\frac{j.pitch}{2}\right)^2} - z_v\right]; \tag{171}$$

(d) Transmit the diverging wave (Em. k on Fig.74a);

(e) Receive the backscattered echoes and do the beamforming to obtain a low resolution image;

(f) Repeat steps a to e for $k \in \{1, ..., N_{dw}\}$;

(g) Add all the low resolution images to obtain the final image.

9.2.1 Orthogonal Golay Coded Diverging Wave Compounding

Complementary Golay coded transmission signals are already used in a large number of imaging techniques **[Nowicki (2007)**; **Liu (2005)]** however their orthogonality properties seem to be explored only in a few papers **[Trots (2015)**; **Kim (2004)]**. In this section, we present the first implementation of the mutually orthogonal Golay codes sets to diverging wave compounding.

Let us suppose a set of two Golay complementary sequences of length $n=8$, (σ_1,σ_2), with $\sigma_i(k)\in\{-1,+1\}$. The complementarity property of σ_1 and σ_2 implies that:

$$R_{\sigma_1\sigma_1}(k)+R_{\sigma_2\sigma_2}(k)=2n\delta(k) \tag{172}$$

where $\delta(k)$ is the Kronecker delta function and $R_{\sigma_1\sigma_1}(k)$ ($R_{\sigma_2\sigma_2}(k)$) represents the autocorrelation products of the sequence σ_1 (σ_2) respectively. As it was shown in **[Tseng (1972)]** it is possible to build from (σ_1,σ_2) a mate set (μ_1,μ_2) that has the following three properties:

i) μ_1 and μ_2 are of the same length (n) as σ_1 and σ_2 respectively;

ii) the set (μ_1,μ_2) is complementary, thus follows (172);

iii) the sets (σ_1,σ_2) and (μ_1,μ_2) are mutually orthogonal meaning that :

$$\sum_{j=1}^{2}R_{\sigma_j\mu_j}(k)=0,\ \forall k \tag{173}$$

where $R_{\sigma_j\mu_j}(k)$ represents the inter-correlation product between the sequences σ_j and μ_j.

Now, in order to transmit a diverging wave that carry a binary sequence σ_j (or μ_j) one should modulate them with a signal $r(t)$ whose frequency content falls inside the bandwidth of the ultrasound probe. Different carriers $r(t)$ were proposed **[Lashkari (2016); Nowicki (2007)]** such as half or full period of a sinusoid, square wave or chirps. The choice of the carrier is very complex since there is an inherent trade-off between the echo signal to noise ratio and the resolution of the reconstructed image [**Nowicki (2007)**]. The resulting modulated signals $a^{\sigma_j}(t)$ and $a^{\mu_j}(t)$ can be written as:

$$\begin{aligned} a^{\sigma_j}(t)&=\sum_{k=0}^{n-1}\sigma_j(k)\delta(t-kT)*r(t)\\ a^{\mu_j}(t)&=\sum_{k=0}^{n-1}\mu_j(k)\delta(t-kT)*r(t)\end{aligned} \tag{174}$$

where $\delta(t)$ is the Dirac delta function and T is the time duration of the carrier $r(t)$. Assuming that the backscattered echoes are exact copies of $a^{\sigma_j}(t)$ and respectively $a^{\mu_j}(t)$ (with less amplitude due to the geometrical spreading of the wave), from (172) and (174) is obtained the expression of the pulse compressed waveforms:

$$\begin{aligned} R_{a^{\sigma_1}a^{\sigma_1}}(t)+R_{a^{\sigma_2}a^{\sigma_2}}(t)&=2n[r(t)*r(-t)]\\ R_{a^{\mu_1}a^{\mu_1}}(t)+R_{a^{\mu_2}a^{\mu_2}}(t)&=2n[r(t)*r(-t)]\end{aligned} \tag{175}$$

In (175), it can be seen that the quality of the compressed waveforms depends on the autocorrelation product of the carrier signal $r(t)$. Furthermore, using (173) and (174) it can be also deduced that:

$$\sum_{j=1}^{2}R_{a^{\sigma_j}a^{\mu_j}}(t)=0,\ \forall t \tag{176}$$

which in other words means that the modulated sets $(a^{\sigma_1},a^{\sigma_2})$ and (a^{μ_1},a^{μ_2}) are also mutually orthogonal.

In order to use the above described properties of $(a^{\sigma_1}, a^{\sigma_2})$ and (a^{μ_1}, a^{μ_2}) in DWC we propose the following pipeline:

(a) Consider virtual source j and $j+1$;

(b) Compute, using (169), the corresponding n elements of the ultrasound probe to be activated for j and $j+1$;

(c) Compute, using (171), the transmission delays for the i^{th} active element of the probe for j and $j+1$;

(d) Transmit simultaneously with the source j: $a^{\sigma_1}(t)$ and with the source $j+1$: $a^{\mu_1}(t)$ (Em. j in Fig.74b);

(e) Receive the backscattered echoes at each i element of the probe: $y_{1i}(t)$;

(f) Transmit simultaneously with the source j: $a^{\sigma_2}(t)$ and with the source $j+1$: $a^{\mu_2}(t)$ (Em. $j+1$ in Fig.74b);

(g) Receive the backscattered echoes at each i element of the probe: $y_{2i}(t)$;

(h) Compress the backscattered echoes received at the steps (e) and (g) as in (175) by applying the corresponding matched filters:

$$\begin{aligned} \hat{g}_j(t) &= y_{1i}(t) * a^{\sigma_1}(-t) + y_{2i}(t) * a^{\sigma_2}(-t) \\ \hat{g}_{j+1}(t) &= y_{1i}(t) * a^{\mu_1}(-t) + y_{2i}(t) * a^{\mu_2}(-t) \end{aligned}; \tag{177}$$

(i) Beamform the compressed signals $\hat{g}_j(t)$ and $\hat{g}_{j+1}(t)$ in order to obtain simultaneously the low resolution images (corresponding to a successive transmission with the virtual source j and $j+1$);

(j) Repeat steps (a) to (i) $N_{dw}/2$ times, increasing j with a step of 2;

(k) Sum all the low resolution images to obtain the final image.

9.2.2 Chirp modulated orthogonal coded diverging wave

As mentioned in Section 9.2.1, depending on the modulation signal $r(t)$ in (174), for the same lengh n of the Golay sequences, the resulting compressed echoes have either a good temporal resolution (T decreases) or a good echo signal to noise ratio (T increases). Nevertheless, recent work **[Lashkari (2016)]** has shown that it is possible to combine complementary Golay sequences with chirp signals (Fig.73b) in order to increase the eSNR for a small loss of temporal resolution (Fig.74b). However, as it was shown in **[Oelze (2007)]**, a narrow band ultrasound probe can downgrade the quality of the autocorrelation of a chirp signal, by increasing the compression side-lobes and decreasing the temporal resolution.

In this work, we propose to improve the above described chirp modulation technique, by compensating the effects of the narrow band ultrasound probe using the REC technique **[Oelze (2007)]**; **Benane (2018a)]**. REC can improve the temporal resolution even with a narrow band probe. One of the central aspects of REC is the generation of an excitation signal referred to as pre-enhanced

chirp. This chirp can artificially enlarge the bandwidth of the transducer, thereby providing higher axial resolution. The core principle on which REC relies in the following convolution equivalence:

$$\tilde{a}(t) * h_1(t) = a(t) * h_2(t) \tag{178}$$

where, as shown in Fig.75, $h_1(t)$ is the pulse-echo impulse response of a probe element at its focal length, $h_2(t)$ describes the designed pulse-echo impulse response with such desired properties as larger spectral support and $\tilde{a}(t)$ is a chirp that covers the bandwidth of $h_2(t)$.

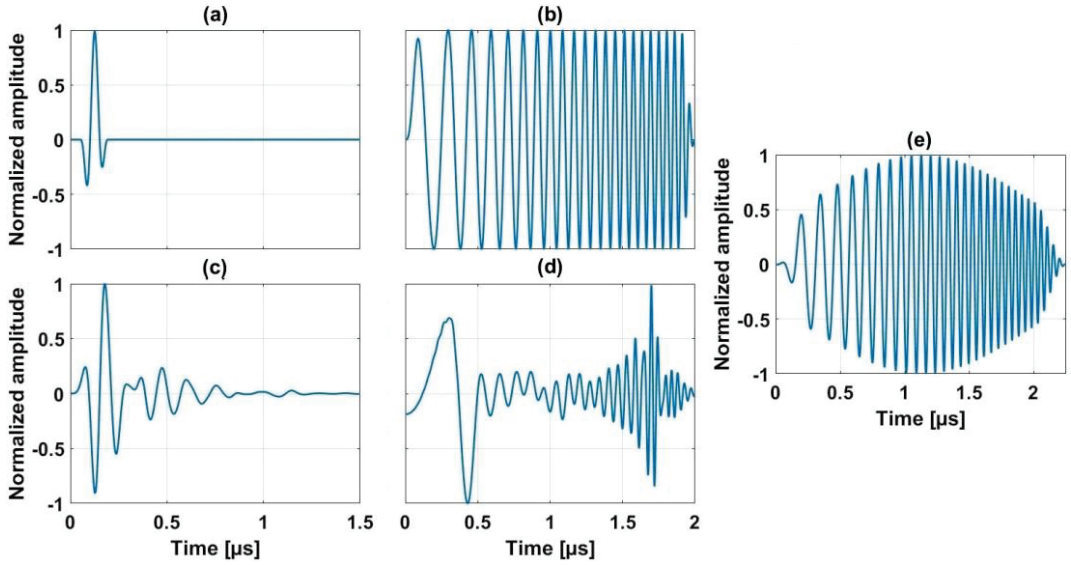

Fig.75. (a) Desired pulse-echo impulse response $h_2(t)$, (b) chirp $\tilde{a}(t)$ used for the modulation of the Golay codes in **[Lashkari (2016)]**, (c) Real pulse-echo impulse response of the probe $h_1(t)$, (d) chirp $a(t)$ used for modulation of the Golay codes in our approach, (e) Result of the convolution expression (178).

The probe elements are excited with a frequency and amplitude modulated waveform $a(t)$ called pre-enhanced chirp. Equation (178) suggests that by exciting the probe that has a narrow bandwidth with the pre-enhanced chirp, this transducer can yield the same axial resolution as a probe with a larger bandwidth when it is excited by a simple linear chirp, thereby resulting into a higher axial resolution. By solving (178) in the frequency domain, the pre-enhanced chirp is obtained:

$$A(f) = \tilde{A}(f)\frac{H_2(f)}{H_1(f)} \tag{179}$$

where the capital letters represent the Fourier transforms of the corresponding temporal signals. In order to obtain a good approximation of $a(t)$, **[Oelze 2007]** proposed to replace $H_2(f)/H_1(f)$ by a filter that avoids division by zero due to the bandlimited aspect of the $h_1(t)$ response. $A(f)$ becomes:

$$A(f) = \tilde{A}(f)\frac{H_1^*(f)H_2(f)}{|H_1(f)|^2 + |H_1(f)|^{-2}} \tag{180}$$

where $()^*$ denotes complex conjugation. $a(t)$ is multiplied with a Tukey-cosine window with a 20% taper in order to reduce side-lobe levels. The full generation process of the signal $a(t)$ is presented in the Fig.75.

Where in the classical chirp modulation of the Golay codes **[Lashkari (2016)]**, the signal illustrated in Fig.76b is used, we propose to use for modulation $a(t)$ (Fig.75d). This modulation can be achieved by replacing in (174) $r(t)$ with $a(t)$. In Fig.76 is presented the process of modulating the Golay code $(n=8)$ $a_1(k)=\{-1,-1,-1,1,-1,-1,1,-1\}$ (Fig.76a).

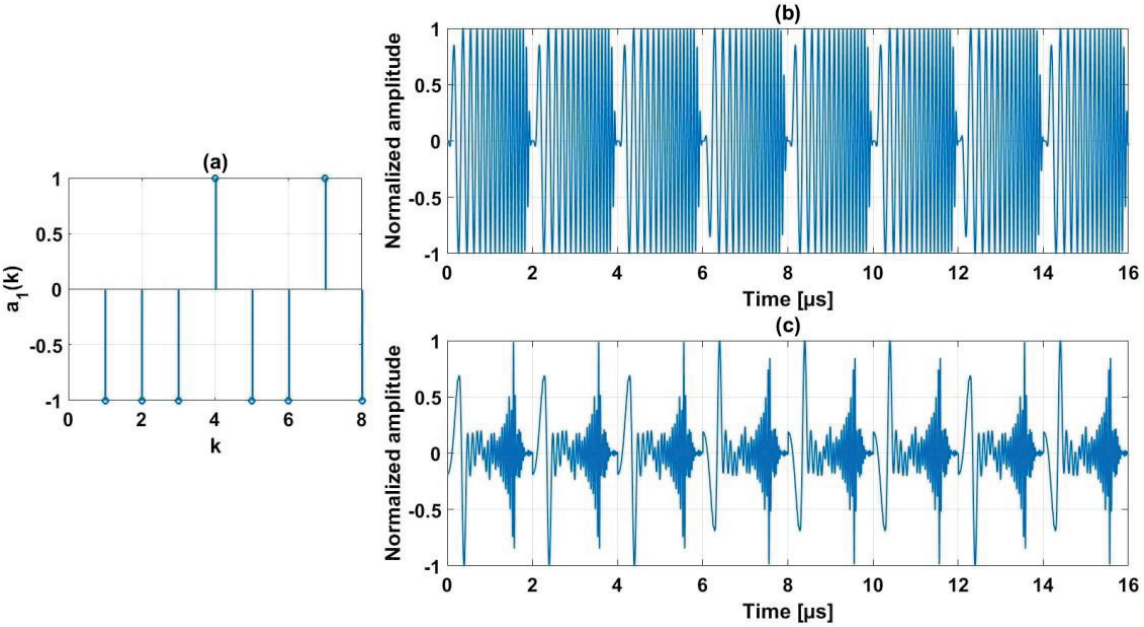

Fig.76. Example of a chirp modulation of a Golay code using (174): (a) Golay code $a_1(k)$, (b) Modulated Golay code using $\tilde{a}(t)$, (c) Modulated Golay code using $a(t)$.

An illustration of the compressed waveforms of the chirp modulated signals (Fig.76b and 76c) is displayed in Fig.77a.

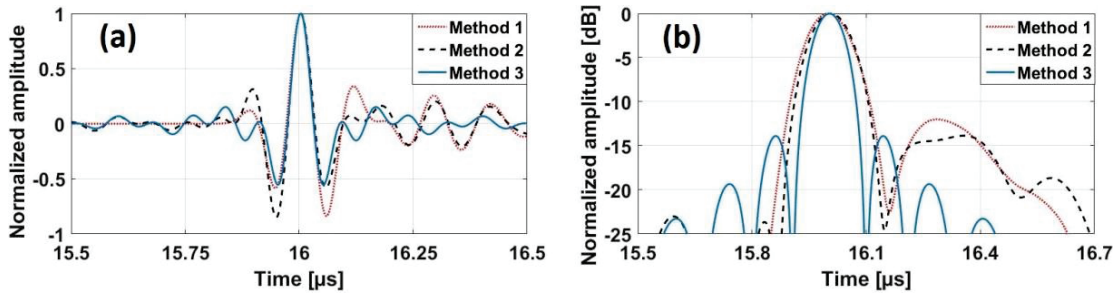

Fig.77. (a) Signal obtained after echo compression using (9), (b) Envelope of the beamformed radiofrequency data.

Fig.77b shows that the designed chirp $a(t)$, used for Golay code modulation yields 37% better temporal resolution than $\tilde{a}(t)$. Moreover, Fig.77b shows that the proposed method increases also the temporal resolution (after compression) even compared to classical approach, where the probe excitation signal $cp(t)$ is a cycle of a sinusoid at the center frequency of the probe bandwidth: 39% boost is achieved.

9.3 Simulation results

A linear probe with 192 elements and a pitch of 0.245mm was used for simulations. The center frequency and sampling frequency were 8.5MHz and 61.6MHz, respectively. To assess the perfomance of the studied methods (in terms of axial resolution, bandwidth and eSNR)) a resolution phantom from the Plane-wave Imaging Challenge in Medical UltraSound (PICMUS) dataset **[Liebgott (2016)]** was simulated using Field II **[Jensen (1992); Jensen (1996)]**. The CNR and the speckle size were measured on B-mode images obtained from simulations on a cyst phantom from the Field II database. A white Gaussian noise (SNR = 20dB) was added into the channel data before pulse compression and beamforming were performed. Three acquisition methods using diverging wave compounding $(N_{dw} = 40,\ z_v = -1cm,\ x_v \in [-2...2]cm)$ were compared:

Method I: Conventional approach, where the excitation signal is a period of a sinusoid;
Method II: Orthogonal Golay coded, where the codes are modulated with $\tilde{a}(t)$;
Method III (proposed approach): Orthogonal Golay coded, where the codes are modulated with $a(t)$.

9.3.1 Resolution phantom results

The obtained B-mode images for the different techniques are shown in Fig.78. It can be visually observed that Method III shows a better axial resolution and lower background noise.

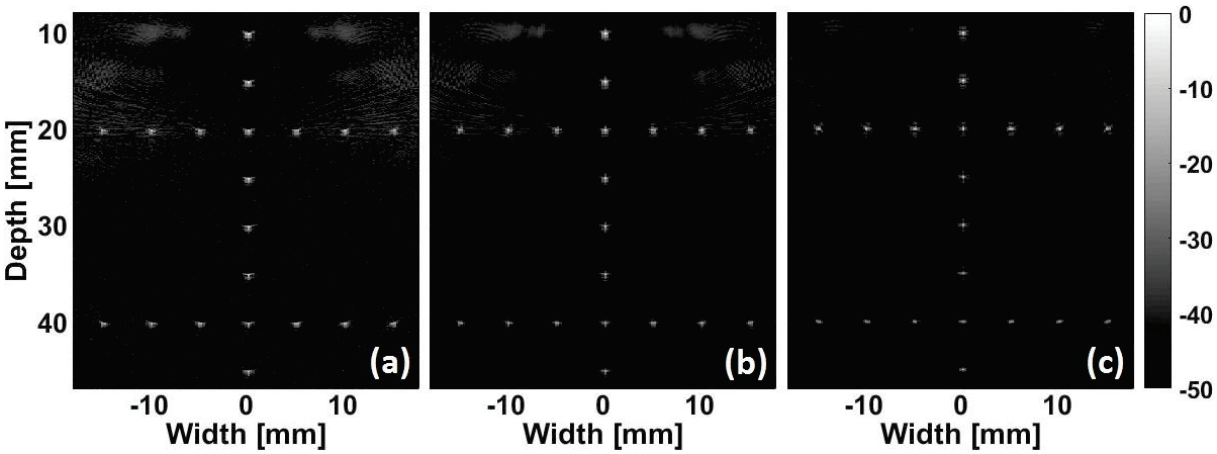

Fig.78. Log-compressed B-mode images obtained using Field II simulation program for: (a) Method I, (b) Method II, (c) Method III.

As shown in Fig.79a the improvement concerning the axial resolution is quantified through the envelope of the beamformed radiofrequency signals (at -6dB). The measured values are 133.1µm, 130.9µm and 96µm for Method I, Method II and Method III respectively. The power spectra of the reflection from the wire at 4cm depth is shown in Fig.79b. In accordance with the improvement in axial resolution, the -6dB bandwidths were 5.14MHz, 5.22MHz and 7.16MHz for Method I, Method II and Method III respectively. Concerning the eSNR calculated on the pre-beamformed data, a higher value is obtained in Method II (48.7dB) than Method III (40.1dB), Method I providing the lowest value (21.4dB). The obtained values are consistent with the expected ones, the difference of 8.6dB between Method II and III being explained by the modulated shape of the excitation in Method III (Fig.75d) that carries approximatively 2.8 times less energy than the transmitted chirp used in Method II (Fig.75b).

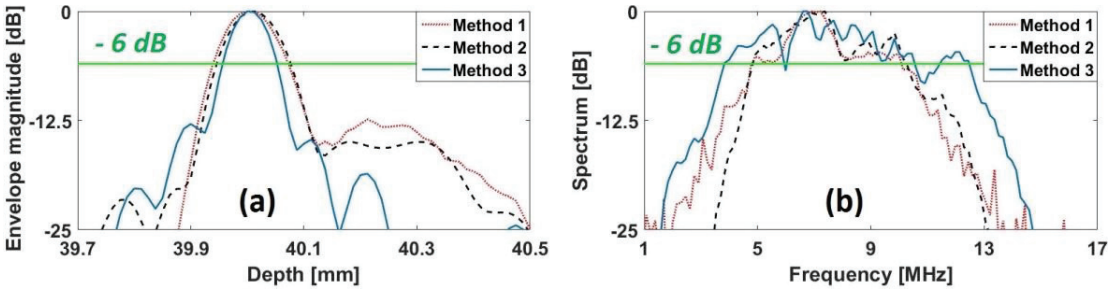

Fig.79. (a) Envelope of the beamformed radiofrequency data, (b) Normalized spectrum from the beamformed radiofrequency data.

9.3.2 Cyst phantom results

The obtained B-mode images are shown in Fig.80. These results show an improvement in terms of image quality between Method III (Fig.80c) compared to Method I and Method II (Fig.80a and Fig.80b).

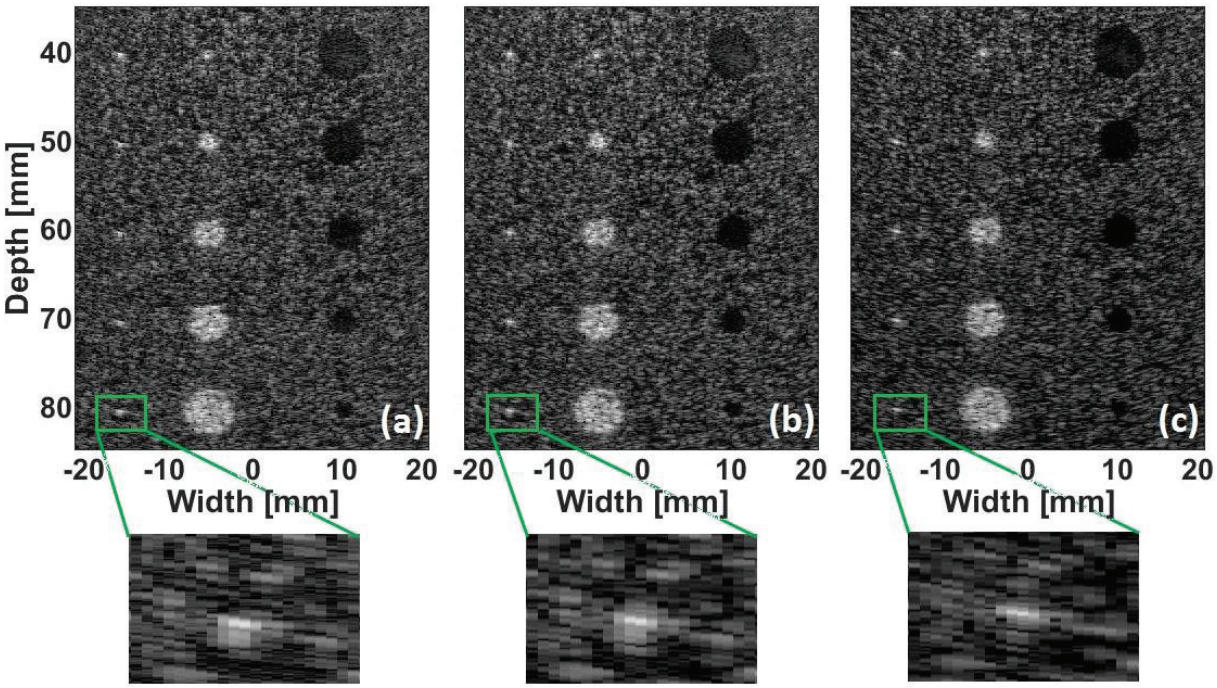

Fig.80. Log-compressed B-mode images obtained using Field II simulation program for: (a) Method I, (b) Method II, (c) Method III.

The obtained CNR values for the hypo-echoic (hyper-echoic) were -4.11dB, -2.48dB, 1.51dB (-8.21dB, -8.23dB, 9.46dB) for Method I, Method II and Method III respectively.

The speckle axial size was also evaluated through autocorrelation length (ACL) which consists in calculating the autocorrelation product of a vertical beamformed radio-frequency line. The ACL results in Fig.81 (Method I 474.4µm, Method II 505.9µm, Method III 364.6µm) show an improvement of 30% between Method III/Method I and 39% between Method III/Method II. The improved speckle size, provided by Method III, is in accordance with the boost of axial resolution observed on the scatterer placed at $(x,z)=(-15,80)$ mm (see zoomed zone in Fig.80). We measure a boost of 29.2% and 37.5% for Method III/Method I and Method III/Method II respectively.

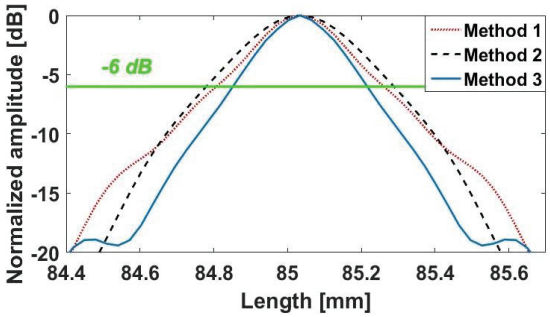

Fig.81. Axial autocorrelation length performed on the vertical line at 3mm in the cyst B-mode image.

9.4 Experimental results

For the data acquisition, the open ultrasound platform UlaOp-256 (Microelectronics System Design Lab, Florence, Italy) **[Boni (2016)]** equipped with a LA523E-array probe (Esaote, Genova, Italy) was used. The UlaOp-256 is able to transmit arbitrary waveforms and defined specific transmission/reception strategies. The probe has 192 elements (pitch = 245µm) and is centered at 8.5MHz. The phantom studied (model 410SCG HE 0.5 Gammex Sun nuclear, Neu-Isenburg, Germany) has an attenuation coefficient slope of 0.5dB/MHz/cm. The obtained log compressed B-mode images for the three studied methods are displayed in Fig.82.

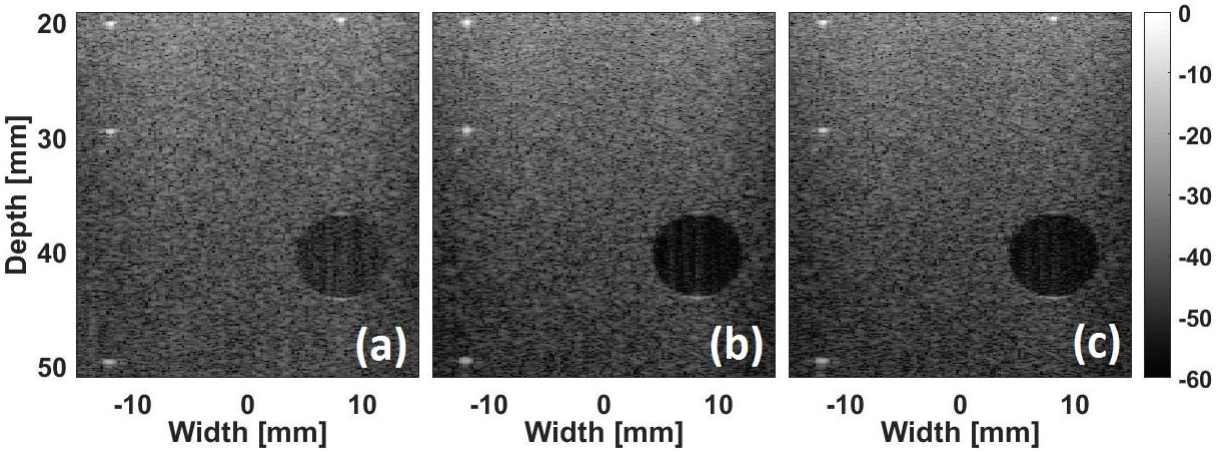

Fig.82. Log-compressed B-mode images obtained using the UlaOp-256 scanner for: (a) Method I, (b) Method II, (c) Method III.

The results clearly show an improvement in term of CNR between Method III (Fig.82c) and Method I (Fig.82a). Indeed the obtained values are 7.4dB and 3.9dB respectively. The difference of CNR between Method III and Method II (Fig.80b) is only of 0.2dB. The discrepancy, in comparison to the simulation results in CNR, is due to the effect of attenuation that alters the received echoes more for Method III than Method II since the Method III excitation signals content more high frequency (due to enhancement of the bandwidth).

As it can be seen in Fig.83a, a better axial resolution is obtained using Method III than Method I and II. 14% and 29.4% of enhancement is achieved between Method III/Method I (228.2µm/260.1µm) and Method III/Method II (228.2µm/295.2µm) respectively. The axial autocorrelation length measurement (Fig.83b) is consistent with the obtained axial resolution values and show a 15% and 34,4% boost for Method III/Method I and Method III/Method II respectively.

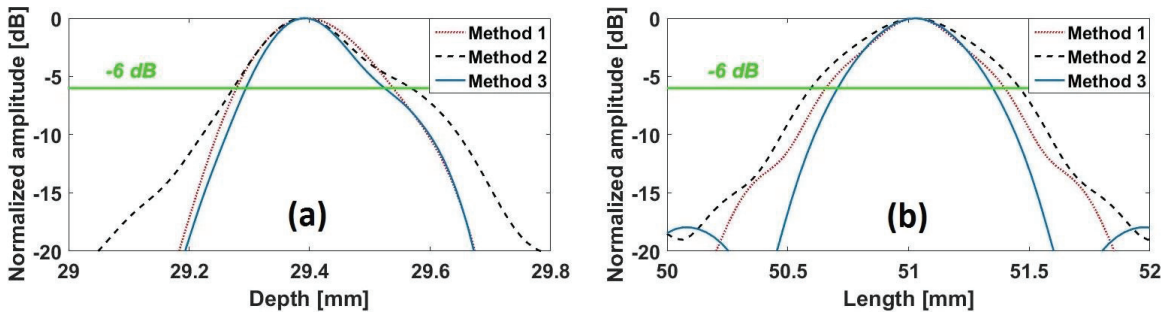

Fig.83. (a) Envelope of the beamformed radiofrequency data, (b) Autocorrelation length in the axial direction performed on the vertical line at 3mm in the cyst B-mode image.

9.5 Conclusion

In this study, the first experimental implementation of enhanced chirp modulation of orthogonal Golay codes (Method III) is presented. In comparison with conventional imaging technique (Method I) and classical chirp modulation of orthogonal Golay codes (Method II), the results show improvements in terms of image quality as quantified by the CNR, axial resolution, bandwidth and speckle size. The experimental results suggest that the combination between binary Golay codes and pre-enhanced modulated chirps is feasible and provide advantages for imaging when implemented on narrow-band ultrasound probes.

CONCLUSION AND PERSPECTIVES

Chapter X

CONCLUSION AND PERSPECTIVES

Contenu

10.1 General conclusion

In the ultrasound imaging literature exists a large number of acquisition schemes such as: focused, diverging, plane wave imaging etc. The image quality provided by these methods depends heavily on the excitation signal, wave / tissue interaction but also on the properties of the hardware used for the ultrasound imaging. In a first part of this manuscript the principles of ultrasound wave propagation and tissue interaction were explained and on this theoretical background the concepts of classical ultrasound imaging were detailed. Then, relying on these principles it was shown that classical acquisition schemes provide image qualities that depend on the acquisition noise, bandwidth of the employed ultrasound probe and tissue attenuation frequency effect. Furthermore, it was shown that the performance of the classical acquisition scheme can be greatly improved by employing phase / frequency / amplitude modulated signals in transmission and pulse compression filters in reception. A very promising method called Resolution Enhancement Compression (REC) was identified, that in addition of using frequency modulated signals that increase the echo signal to noise ratio, is able to overcome the effect of band limited ultrasound probe by boosting the energy of the emitted signals in the frequency bands where the probe is less efficient. The objective of this work was to extend the concept of REC and to combine it with an ultrafast acquisition scheme in order to achieve a higher image quality at ultrafast acquisition rates.

In the first contribution of this work, REC was combined with the concept of Coherent Plane Wave Compounding (CPWC), the objective being to achieve a better image quality at frame rates far larger than the ones provided by the conventional (focused) imaging. Firstly, a theoretical study was detailed which proved that REC can be adapted to CPWC and that important gains in terms of the recorded signals bandwidth and spatial resolution of the reconstructed image can be achieved. Then, the proposed method (CPWC-REC) was tested in simulation on wire and cyst phantoms and it was observed that it outperforms, as expected, the classical CPWC (that employs sinusoidal pulses as excitation signals). CPWC-REC was also implemented on a research scanner, acquisitions on in-vitro phantoms and in-vivo / ex-vivo organs being done. Here again, the ability of CPWC-REC to provide better image quality than CPWC was noticed. As such, it was observed that CPWC-REC can achieve better image qualities than classical CPWC from a less number of plane waves used for compounding. In the context of the inherent image quality / frame acquisition rate present in the ultrasound imaging field, such property implies that CPWC-REC can achieve similar to classical CPWC image qualities at faster frame rates.

In the CPWC-REC results was observed a certain difference between the expected / simulation performance and the achieved in the in-vitro / ex-vivo / in-vivo results. A further investigation allowed finding to conclude that this discrepancy was generated by the frequency dependent tissue attenuation effect. Thus, the objective of the second contribution of this thesis was to overcome the effect of tissue attenuation. Firstly, it was decided to model the tissue attenuation by its impulse response. Then, this response was used in order to modify REC in such way so the excitation signals remain the same but the compression filters evolve as a function of the depth where the echoes that are being compressed are generated. In this way, the theoretical background of the second contribution was settled. Simulation implementation of the improved CPWC-REC proved its ability to overcome the attenuation effect and provided us with the motivation to implement it in in-vitro experiments. Here again, was observed a better performance of improved CPWC-REC.

Another phenomenon that was impairing the REC performance in the in-vitro / ex-vivo / in-vivo experiments was the non-linear propagation of the acoustic waves. Thus the objective of the third contribution of this work was to somehow adapt REC to the non-linear behaviour of ultrasound in soft tissues. It was decided to combine improved (to overcome the tissue attenuation effect) CPWC-REC with the concept of pulse inversion that consists in successive emission of acoustic waves carrying signals of opposite polarity. In-vitro acquisition showed promising results, the proposed method being able to outperform the classical method of pulse inversion.

In order to check the REC ability to adapt to other ultrafast acquisitions schemes, it was decided to combine REC with the technique of Multi Line Transmit (MLT) which consists in the simultaneous transmission / reception / reconstruction of several focused lines inside the ultrasound image. Firstly, the theoretical and simulation studies were conducted. Then, following the promising obtained results, MLT-REC was implemented on the Ula-Op 256 scanner equipped with a linear array probe. It was concluded that REC-MLT was able to enhance the bandwidth of the backscattered echoes thus providing a better spatial resolution in the provided B-mode images. Moreover, thanks to the frequency modulated signals, the echo signal to noise ratio was also increased when compared to the conventional MLT which resulted in an increased signal / contrast to noise ratio in the obtained B-mode images. The obtained results demonstrated that the MLT-REC makes it possible to achieve an up to 8-fold improvement of the frame rate in phantom / ex vivo scans while still providing a better image quality than conventional MLT.
Since, at the core of REC stands the principle of boosting the excitation energy in the frequency bands where the ultrasound probe is less efficient, what it was observed in all the practical implementations of ultrafast methods based on REC was that, despite the better spatial resolution and contrast to noise ratio, the echo signal to noise ratio of REC based methods was lower than the one provided by the methods employing non-enhanced chirps. Thus, in the next contribution of this work, we decided to merge REC with another coding technique that will allow us to boost further the echo signal to noise ratio. The proposed techniques combines the advantages of REC with the ones of temporal Golay encoding, and was applied to Diverging Wave Compounding (DWC), thus proving again the ability of REC to adapt to different acquisition schemes. The experiments on real phantoms showed that DWC employing pre-enhanced modulated Golay codes is able to provide better results in terms of CNR, axial resolution, bandwidth and speckle size when compared to DWC based on chirp / phase modulated Golay codes. Thus, experimental results proved that the combination between binary Golay codes and pre-enhanced modulated chirps is feasible and provide advantages for imaging when implemented on narrow-band ultrasound probes.

In a final contribution of this work, another effect of the ultrasound acquisitions that was damaging the performance of the REC based methods was considered. The object of study of this project was the spatial impulse response of the ultrasound probe. Firstly, the theoretical study proposed showed that the REC can be adapted to overcome the spatial impulse response of the probe only in the acquisition schemes that employ focused transmission. Thus, in the context of ultrafast acquisitions, it was decided to apply this REC optimisation on the MLT-REC technique. Simulation and experimental results showed improvements of the proposed amelioration over the classical MLT-REC.

The different combinations of techniques performed in this thesis are summarized in the following table:

	REC	REC + Attenuation compensation	REC + Pulse inversion	REC + Spatial impulse response compensation	REC + Attenuation compensation + Spatial impulse response compensation	Golay codes + REC
Plane wave imaging	X	X	X			
Conventional ultrasound (focused imaging)				X		
Multi-line transmit imaging					X	
Diverging wave imaging						X

10.2 Perspectives

The work that I have done so far during my PhD is greatly due to the REC ability to adapt to any emission scheme and to its theoretical framework that allows accounting for different acoustic wave propagation phenomena that damage the provided image quality. However, despite all this amount of work done, there are still some improvements that we overlooked during these three years mostly because of the time that we allocated for the exploring. For me, the next step of this work would be to implement all the computation pipeline of the REC-based techniques directly on the ultrasound scanners. Since the only computational heavy part of REC is the Wiener filtering in post-processing which can be vectorized in the frequency domain, a "real time" demeanor of REC filtering can be achieved. Such technique will not require raw RF to be retrieved from the scanner for the REC filtering, which could lead to the implementation of REC based methods on clinical echographs.

Another improvement of REC in a short run would be to combine REC with a technique that allows determining the frequency dependent tissue attenuation coefficient. In fact, in the second contribution of this work, we showed how REC can be adapted in order to overcome the frequency dependent tissue attenuation effect. However, an important assumption had to be made in order for this framework to operate: the assumption that the attenuation coefficient is known and constant for the entire imaged medium. In reality however, the tissue attenuation is different for different types of tissues (muscles, fat, organ tissues etc.) which means that this coefficient either is unknown or is a function that depends on each position inside the imaged medium. Thus, an interesting idea would be to combine REC with a method that allows estimating the attenuation coefficient, the novel method relying on two steps: on the RF data obtained after REC emission estimate the attenuation coefficient and then inject this coefficient in the REC filtering blocks.

Possible improvements can be also brought to the MLT-REC technique. In fact, in this work we showed an implementation of MLT-REC on a linear array probe with a central frequency adapted for shallow tissue imaging. However, MLT as imaging tool is used mostly for imaging deep tissues such as the cardiac muscles, which implies that the required employed ultrasound probe should be of a very small footprint (to allow inter-ribs insonification) and of a lower central frequency. This will benefit greatly MLT-REC, since REC can be adapted to overcome the attenuation effect that is omnipresent when imaging deep-tissues.

RESUME ETENDUE EN FRANAIS

I- Introduction

1. Ultrasons médicaux

L'échographie est devenue l'une des principales modalités d'imagerie médicale et est actuellement le premier outil d'examen diagnostique pour la plupart des organes, à l'exception du cerveau et des poumons. Ceci est lié aux nombreux avantages de l'imagerie par ultrasons, tels que: le coût relativement faible d'un échographe (comparé au prix d'autres modalités telles que la tomographie par rayons X, la tomographie par émission de positrons et l'imagerie par résonance magnétique), la portabilité de l'équipement, la sécurité de l'examen échographique (pas de rayonnement) pour le patient et pour le praticien, le fait que l'échographie est non invasive et l'excellente résolution temporelle. Cela fait de l'imagerie par ultrasons la seule modalité d'imagerie non invasive capable d'acquérir des images en temps réel et donc de permettre la visualisation et l'évaluation des tissus statiques et en mouvement.

L'imagerie par ultrasons repose sur l'interaction entre une onde acoustique et le milieu dans lequel elle se propage. Les principales formes d'interactions avec le milieu sont la réfraction, la réflexion et l'absorption, qui peuvent être soit spéculaires, soit diffuses. Lorsque l'onde atteint une interface entre deux milieux ayant des propriétés acoustiques différentes, une partie de celle-ci est renvoyée à la source. De plus, l'onde ultrasonore transfère de l'énergie au milieu insonifié, qui est ensuite converti en chaleur. Il est donc évident qu'en transmettant une impulsion ultrasonore dans le tissu imagé, les échos obtenus contiennent des informations importantes à la fois sur les propriétés acoustiques des milieux insonifiés et sur la position spatiale des interfaces les séparant.

Le processus d'imagerie par ultrasons peut être divisé en trois phases principales: une phase de transmission, une phase de réception et une phase de reconstruction d'image. Tout d'abord, une onde acoustique est générée par un transducteur piézoélectrique excité par un signal électrique. L'onde se propage à l'intérieur du milieu et la présence d'hétérogénéités dans le champ de densité moyenne entraîne la formation d'échos qui se propagent dans toutes les directions et donc dans la direction de la sonde à ultrasons. La même sonde de transmission est utilisée pour collecter les échos rétrodiffusés et les transformer en signal électrique. Ce signal contient des informations sur la géométrie du support et est appelé signal radiofréquence (RF). Par conséquent, ces signaux peuvent être filtrés (pour réduire le bruit) et formés par faisceau afin de reconstruire l'image finale du tissu.

Malgré les nombreux avantages qu'elle présente, l'imagerie par ultrasons présente certains inconvénients, notamment la qualité d'image fournie qui ne peut rivaliser avec celles de la plupart des autres modalités d'imagerie (tomographie à rayons X et imagerie par résonance magnétique). Ainsi, l'imagerie par ultrasons n'est pas capable de fournir les détails de structures biologiques avec le même niveau de précision.

La qualité de l'image peut être quantifiée à l'aide de différentes mesures. L'une des plus importantes est la résolution spatiale, généralement exprimée en millimètres. De nombreuses approches peuvent être utilisées pour évaluer cette métrique fondamentale, mais l'idée générale est de considérer que la résolution d'un système d'imagerie est sa capacité à distinguer clairement les détails les plus fins d'une image. Pour améliorer la résolution spatiale en imagerie par ultrasons, il est nécessaire d'exciter la sonde ultrasonore avec des signaux courts temporellement. Cependant, les signaux les plus courts transportent plus de hautes fréquences qui s'accompagnent inévitablement d'une limitation de la profondeur de pénétration due à l'effet d'atténuation. Ce phénomène limite fortement le champ d'application de l'imagerie par ultrasons à haute fréquence aux tissus de surface tels que les couches superficielles de l'épiderme et des tissus sous-cutanés.

2. Objectifs de la thèse

L'objectif principal de cette thèse est de fournir une méthode d'imagerie par ultrasons qui améliore la qualité de l'image tout en conservant une bonne profondeur de pénétration dans le tissu et un taux d'acquisition d'images élevé. Le deuxième objectif est de mettre en œuvre la méthode proposée sur différents scanners de recherche par ultrasons, en utilisant différentes technologies de sonde.

II- Etat de l'art

1. Propagation linéaire

Pour bien comprendre d'où provient l'équation de propagation de l'onde ultrasonore et comment l'obtenir, certaines variables ainsi que des hypothèses doivent être définies. Si un objet se déplace lentement dans un fluide, le fluide circule autour de lui. Si l'objet se déplace rapidement, cela produit un déplacement local du fluide, ce qui entraîne une variation de la densité locale. La variation de densité correspond également à un changement de pression. Considérons l'exemple d'un diaphragme de haut-parleur dont le déplacement produit une compression de la couche d'air adjacente (VF_Fig.1). Dans cette situation, l'air ambiant, ayant une pression P_0 (pression atmosphérique) et une densité ρ_0, est soumis à une perturbation acoustique. Cette expérience génère une pression locale et une densité locale. Pour calculer l'équation des ondes linéaires, les trois lois suivantes doivent être prises en compte:

- L'équation de conservation de la masse;
- L'équation d'état;
- L'équation d'Euler.

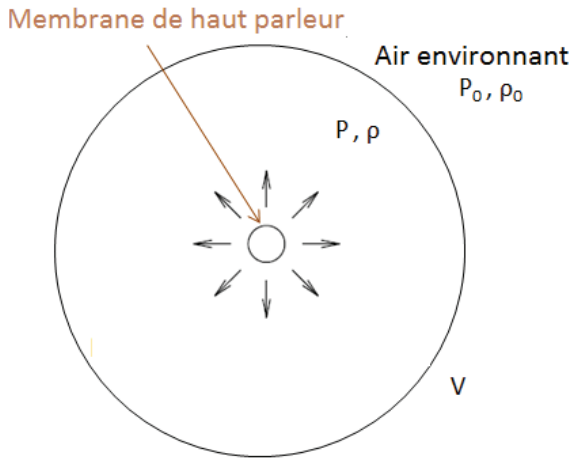

VF_Fig.1: Le volume d'air (V) soumis à une perturbation acoustique (dû à une membrane de haut-parleur) génère la pression P et la densité ρ. La pression ambiante de l'air ambiant est notée P_0 et sa densité ρ_0.

➢ L'équation d'onde

Ici, l'hypothèse suivante est faite: le passage de l'onde acoustique crée de petites différences de pression, de densité et de vitesse par rapport aux valeurs d'équilibre. Par conséquent, seuls les termes d'ordre 1 dans les trois équations précédentes sont conservés.

- En notant $\rho_a = \rho - \rho_0$ l'excès de densité, l'équation de masse de conservation peut être écrite comme **[Hamilton (1988)]**:

$$\rho_0 \vec{\nabla} \cdot \left[\vec{v}\left(\vec{r},t\right) \right] + \frac{\partial \rho_a \left(\vec{r},t\right)}{\partial t} = 0 \qquad \text{(VF\_1)}$$

- L'équation d'état du premier ordre est donnée par $p = c^2 \rho_a$. Ainsi, l'équation de conservation de la masse est déduite comme suit:

$$\rho_0 \vec{\nabla} \cdot \left[\vec{v}\left(\vec{r},t\right) \right] + \frac{1}{c^2} \frac{\partial p\left(\vec{r},t\right)}{\partial t} = 0 \qquad \text{(VF\_2)}$$

- Enfin, l'équation d'Euler linéarisée devient **[Hamilton (1988)]**:

$$\rho_0 \frac{\partial \vec{v}}{\partial t} + \vec{\nabla} p = 0 \qquad \text{(VF\_3)}$$

Tous les éléments sont rassemblés maintenant pour obtenir l'équation d'onde linéaire. Cette dernière est déduite en soustrayant la dérivée temporelle de l'équation de conservation de la masse de la divergence de l'équation d'Euler. Le résultat de cette opération donne:

$$\Delta p\left(\vec{r},t\right) - \frac{1}{c^2} \frac{\partial^2 p\left(\vec{r},t\right)}{\partial t^2} = 0 \qquad \text{(VF\_4)}$$

- **Solution de l'équation d'onde**

La solution générale de l'équation précédente s'écrit comme:

$$p\left(\vec{r},t\right) = \frac{1}{r} g\left(t - \frac{r}{c}\right) + \frac{1}{r} h\left(t - \frac{r}{c}\right) \qquad \text{(VF\_5)}$$

où r est la distance (radiale) entre l'origine et le point considéré. g et h sont des fonctions arbitraires. En développant (VF_5), on peut avoir accès à l'expression du champ de pression en chaque point $\vec{r}$:

$$p(\vec{r},t) = P_0 e^{j(\omega t - \vec{k}\vec{r})} + P_0^{'} e^{j(\omega t + \vec{k}\vec{r})} \qquad \text{(VF\_6)}$$

où P_0 est l'amplitude de l'onde de propagation dans la direction z et $P_0^{'}$ l'amplitude de l'onde de retour (dans la direction - z). Considérons que le terme de phase peut aussi être exprimé comme dans VF_7, dans lequel apparaît une fraction représentant le temps de parcours à la vitesse de l'onde ultrasonore

$$\omega t - \vec{k}\vec{r} = \omega\left(t - \frac{r}{c}\right) \qquad \text{(VF\_7)}$$

En pratique, il est courant de modéliser la pression en tant que partie réelle (noté Re ()) de l'onde progressive:

$$p(\vec{r},t) = P_0 \times \mathrm{Re}\left(e^{j(\omega t - \vec{k}\vec{r})}\right) = P_0 \cos(\omega t - \vec{k}\vec{r}) \qquad \text{(VF\_8)}$$

2. Transmission et réflexion d'une onde ultrasonore

Chaque milieu est caractérisé par son impédance acoustique Z (exprimée en $kg^{-2}.s^{-1}$) qui est fonction de la vitesse de propagation de l'onde c et de la densité moyenne ρ :

$$Z = \rho c \qquad \text{(VF\_9)}$$

Lorsqu'une onde ultrasonore arrive à l'interface entre deux milieux différents, caractérisée par deux impédances acoustiques différentes Z_1 et Z_2, elle génère une onde réfléchie et une onde transmise (VF_Fig.2). La relation entre les angles d'incidence et de réflexion est donnée par la loi de Snell Descartes:

$$Z_1 \sin(\theta_i) = Z_2 \sin(\theta_t), \qquad \text{(VF\_10)}$$

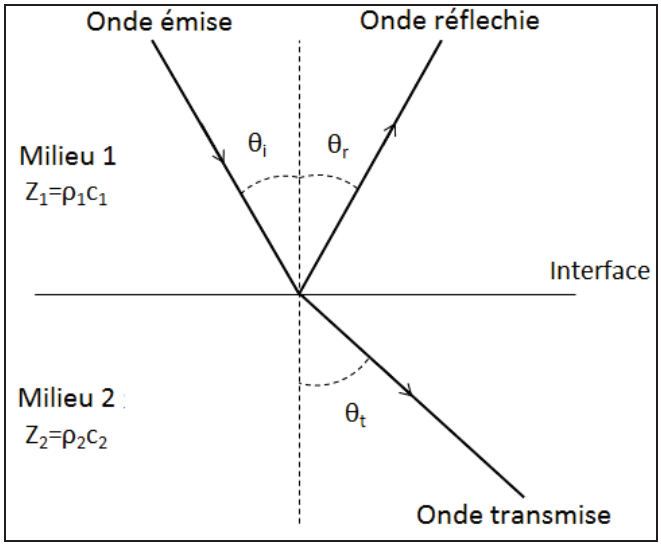

VF_Fig. 2: Illustration de la réflexion et transmission d'une onde de pression incidente à l'interface entre deux milieux d'impédances différentes.

3. Diffusion d'ondes ultrasonores

Dans le cas de l'imagerie médicale par ultrasons, les tissus biologiques ne sont pas des milieux homogènes parfaits. En effet, ils sont composés d'inhomogénéités multiples, inférieures à la longueur d'onde ultrasonore, distribuées aléatoirement **[Meunier (1995)]**. Chacune de ces petites inhomogénéités, lorsqu'elle est insonifiée par l'onde acoustique incidente, devient une source ponctuelle qui renvoie une onde sphérique dans toutes les directions de l'espace (VF_Fig.3). Une partie des échos générés par l'ensemble des réflecteurs est donc rétro-diffusée vers la sonde et leur analyse permet de caractériser la structure des tissus internes. L'amplitude du signal reçu est déterminée par l'échogénicité du milieu imagé.

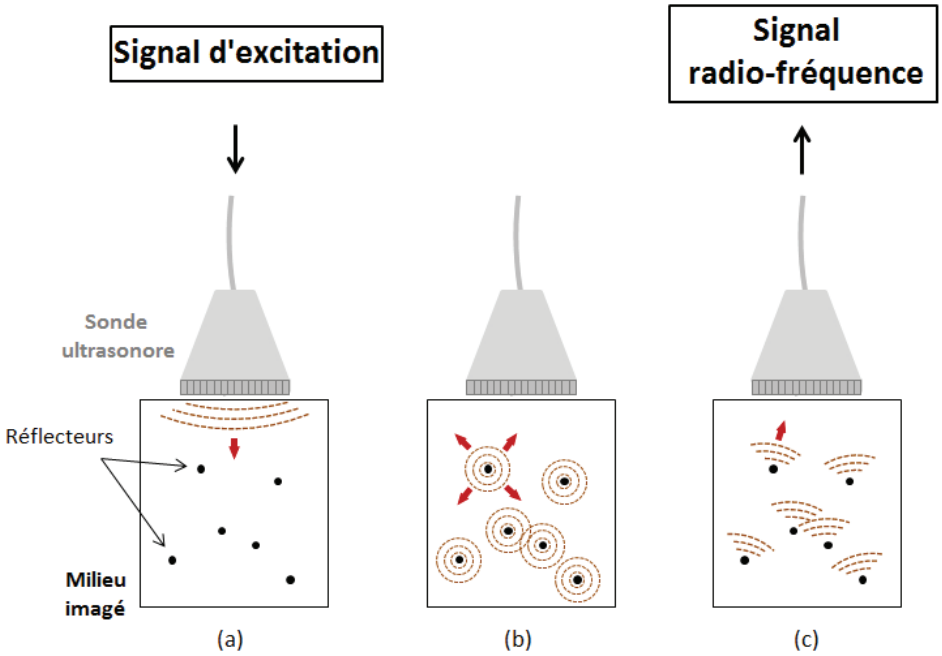

VF_Fig.3: Transmission et réflexion diffuse de l'onde ultrasonore. (a) Un signal électrique pulsé excite la sonde à ultrasons et provoque la création d'une onde incidente se propageant dans le milieu. (b) En contact avec l'onde incidente, les réflecteurs multiples rétrodiffusent une onde sphérique. (c) Les échos rétrodiffusés sont reçus par la sonde et convertis en un signal électrique appelé radiofréquence.

4. Materiel echographique

- Echographe

Les images échographiques sont acquises à l'aide d'un échographe. Il est généralement composé d'une sonde d'émission et de réception des ondes acoustiques, d'une console de sélection des paramètres, d'un système informatique de construction des images, d'une carte d'acquisition des signaux de conversion analogique-numérique et d'un écran de visualisation des images et des paramètres (VF_Fig.4).

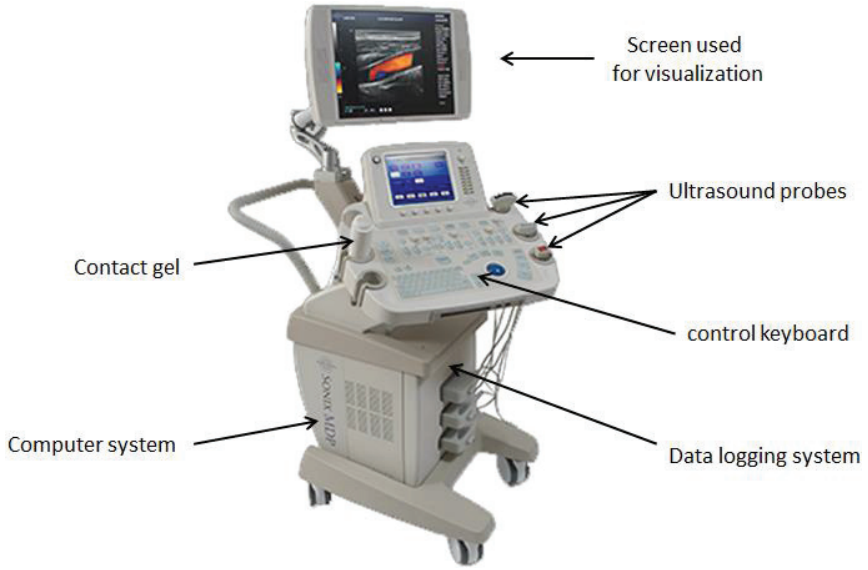

VF_Fig.4: Echographe, SonixMDP (Ultrasonix Medical Corporation).

- Sonde ultrasonore

Il existe plusieurs catégories de sondes avec des géométries et des caractéristiques différentes. Uniquement les sondes de types linéaires seront considérées dans cette thèse, bien adaptée aux principaux types d'examens cliniques. Cette sonde consiste en une seule rangée de petits capteurs, alignés longitudinalement (VF_Fig.5). La longueur d'une sonde linéaire est de l'ordre de 5 cm et le nombre N de capteurs élémentaires est généralement compris entre 64 et 256.

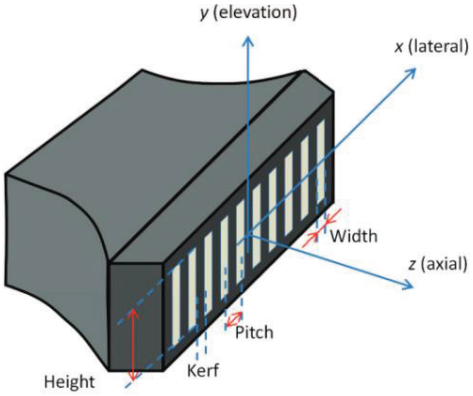

VF_Fig.5: Description géométrique d'une sonde ultrasonore linéaire.

La géométrie de la sonde, illustrée à la VF_Fig.5, est caractérisée par la largeur et la hauteur de chaque élément de capteur. Il se caractérise également par l'espace séparant deux éléments voisins (appelés kerf, généralement entre 20 et 40 µm) ainsi que l'espace entre les centres de deux éléments voisins (appelé pitch, généralement compris entre 250 et 500 µm). Grâce à la disposition rectiligne des éléments de la sonde linéaire, l'image acquise correspond à une coupe bidimensionnelle selon les directions radiale et longitudinale de l'espace. La hauteur des éléments dans la direction azimutale (environ 3 mm) est faible par rapport aux deux autres dimensions de l'image reconstruite (environ 30 mm), et permet de considérer que l'épaisseur est négligeable dans cette direction. C'est pourquoi, dans notre contexte, une représentation bidimensionnelle (dans les directions radiale et longitudinale) est utilisée pour décrire l'imagerie par ultrasons.

5. Formation d'image

En échographie, la propagation des échos est basée sur le modèle décrit précédemment. À partir de l'onde ultrasonore transmise initiale, les différents diffuseurs du milieu scanné réémettent des échos vers la sonde. En utilisant la sonde ultrasonore en mode réception (ce qui signifie que la sonde enregistre la pression qui arrive à sa surface et la convertit en un signal électrique), une image est ainsi créée. En effet, tous les diffuseurs réémettent des ondes qui arrivent à des moments différents sur la surface de la sonde en fonction de la position du diffuseur. La somme de ces différents échos donne cet aspect bruyant visible dans l'image résultante (également appelée «speckle»).

L'image échographique conventionnelle (focalisée) est obtenue en appliquant les étapes suivantes. Tout d'abord, une sous-partie de la sonde à ultrasons est sélectionnée et seule cette partie du transducteur transmet l'onde ultrasonore dans le milieu. À partir des ondes de pression globales rétrodiffusées par le milieu, chaque capteur actif de la sonde enregistre les échos et crée ce que l'on appelle un signal RF. En juxtaposant ces signaux ensemble, l'image RF est obtenue. En utilisant une stratégie de formation de faisceau en réception, l'image RF élémentaire est combinée en un seul signal appelé: ligne RF post-formée. Ensuite, en changeant la sous-partie de la sonde utilisée, différentes

lignes RF post-formées sont créées et correspondent à différentes parties du support. L'image RF finale est obtenue en utilisant toutes ces lignes ensemble.

Cependant, l'image RF, malgré la quantité d'informations qu'elle contient, est difficile à visualiser car les échos rétrodiffusés sont des oscillations sinusoïdales à la fréquence transmise (VF_Fig.6a).

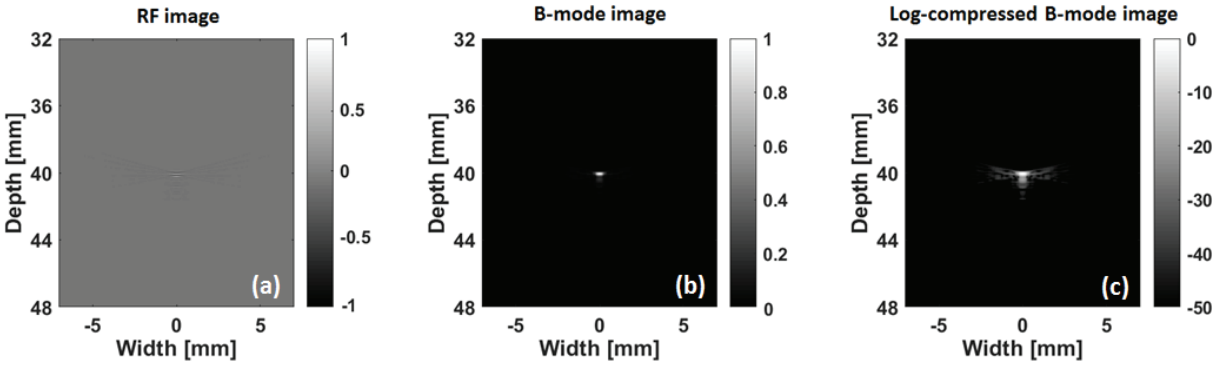

VF_Fig.6: Illustration des différentes images ultrasonores simulées obtenues à partir d'une cible ponctuelle: (a) l'image RF post-formée, (b) l'image en B-mode avant la compression logarithmique et (c) l'image en mode B log-compressée.

Pour visualiser l'image, il est nécessaire de démoduler le signal autour d'une fréquence inférieure contenant moins d'informations par rapport au signal RF. Cette démodulation est généralement réalisée en deux étapes, en premier lieu une multiplication par une sinusoïde centrée sur la fréquence de l'onde transmise. Un filtre passe-bas est ensuite appliqué au résultat intermédiaire. La valeur absolue d'une transformation de Hilbert peut également être utilisée. L'image résultante, appelée image en B-mode, propose une image interprétable (VF_Fig.6b). Pour réduire la dynamique de l'image et mettre en évidence les différentes régions, une compression logarithmique est utilisée. Dans l'image résultante, où l'amplitude est exprimée en dB, toutes les structures sont finalement visibles et l'utilisateur a la possibilité de choisir la dynamique pour l'affichage (VF_Fig.6c).

Pour compenser l'effet d'atténuation présent dans les tissus, une fonction TGC (Time Gain Compensation) est utilisée. Le TGC augmente synthétiquement l'amplitude des échos rétrodiffusés en fonction de la profondeur afin de compenser la perte due à l'atténuation. Par exemple, un TGC de 1 dB.cm-1 augmente la dynamique de 1 dB tous les centimètres.

6. Méthodes d'imagerie

La transmission / réception d'ondes acoustiques qui se propagent à l'intérieur du tissu est réalisée par la sonde ultrasonore, permettant la conversion réciproque des ondes ultrasonores en signaux électriques. Pour une paire de transducteurs d'émission / réception, le signal reçu contient des informations sur le support balayé par l'intermédiaire de sa Fonction de Réflectivité Tissulaire (TRF). Cela signifie que pour plusieurs centaines de transducteurs en émission / réception (que contient la sonde à ultrasons), non seulement plus d'informations sur le TRF sont acquises (dues aux multiples récepteurs), mais cette information est également moins bruyante (due aux émetteurs multiples). Le fait que chaque sonde à ultrasons comporte de multiples éléments en émission / réception permet également de générer différentes stratégies de formation de faisceau d'émission / réception qui offrent une large gamme de qualités d'image et de fréquences d'acquisition de trames. Ces techniques sont les

suivantes: l'imagerie ultrasonore conventionnelle (appelée également imagerie focalisée), la transmission multi-lignes (MLT), l'imagerie par ondes planes et l'imagerie par ondes divergentes.

Dans cette section, ces méthodes d'imagerie ont été examinées en détaillant succinctement le processus de formation de l'image. On définit alors trois différents processus :

- Transmission: les signaux émis sont générés et les délais de transmission correspondants pour chaque élément de la sonde sont calculés pour effectuer la formation de faisceau de transmission;
- Réception: les échos rétrodiffusés du support sont reçus;
- Post-traitement: en fonction de la méthode d'imagerie, différentes approches de formation de voies sont appliquées afin de reconstruire une estimation de la TRF.

6.1. Imagerie conventionnelle

Le principe de l'imagerie conventionnelle par ultrasons est présenté par la VF_Fig.7. Ici, on peut voir qu'une image ultrasonore complète du milieu est obtenue après N_f évenements de transmission / réception / post-traitement. Comme on peut le voir sur la VF_Fig.7, après chaque événement de transmission / réception / post-traitement, une ligne de l'image est formée **[Shattuck (1984)]**. N_f est le nombre exact d'événements de transmission / réception / post-traitement nécessaires pour reconstruire une image complète du milieu.

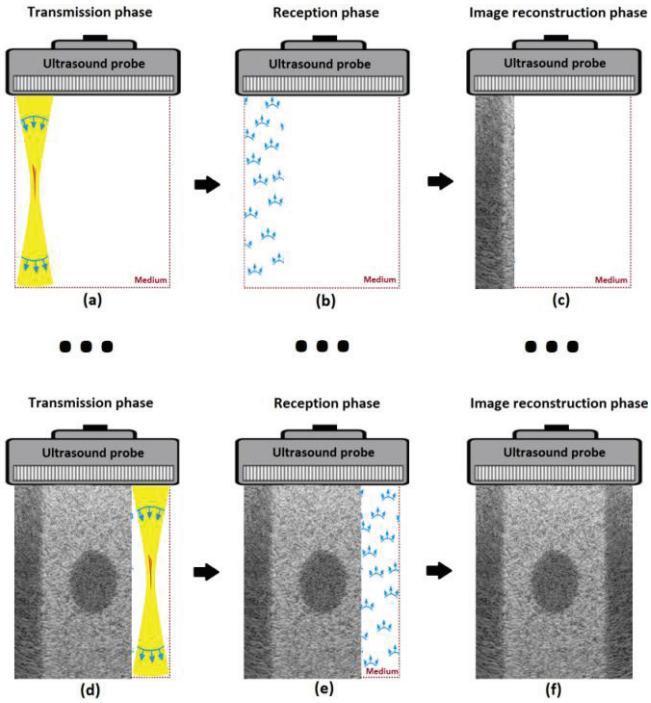

VF_Fig.7: Principe de l'imagerie conventionnelle. (a) Transmission du faisceau focalisé, (b) réception des échos rétrodiffusés, (c) reconstruction de la première ligne de l'image. (d), (e) et (f) sont respectivement la phase de transmission, de réception et de reconstruction pour la dernière ligne de l'image.

6.2. L'imagerie en Transmission Multi-Lines

Le schéma d'acquisition MLT représente une variation de la transmission focalisée qui augmente la cadence d'acquisition en utilisant la transmission simultanée de faisceaux d'ultrasons focalisés à l'intérieur du milieu insonifié. Le principe du MLT est résumé dans la VF_Fig.8. Comme les N_{MLT} faisceaux sont transmis simultanément (les N_{MLT} lignes de l'image peuvent ainsi être reconstituées simultanément), la fréquence des images est multipliée par un facteur N_{MLT} (dans la VF_Fig.8, $N_{MLT} = 2$).

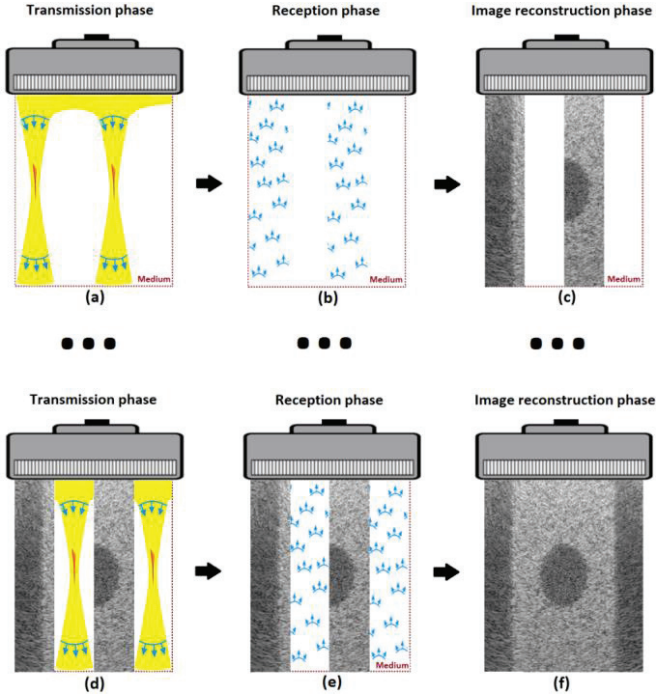

VF_Fig.8: Principe de l'imagerie MLT. (a) Transmission des faisceaux focalisés, (b) réception des échos rétrodiffusés, (c) reconstruction simultanée de deux lignes de l'image. (d), (e) et (f) sont respectivement la phase de transmission, de réception et de reconstruction pour les deux dernières lignes de l'image.

6.3. Imagerie en ondes planes

Comme le montre la VF_Fig.9, en imagerie à onde plane, le milieu entier est insonifié en utilisant une seule onde plane. Après chaque événement de transmission, tous les échos rétrodiffusés sont reçus et utilisés pour reconstruire l'image en utilisant une variante de l'algorithme DAS détaillée plus loin dans cette section **[Sandrin & Fink (1999)]**. L'absence de focalisation du faisceau dans la transmission implique que les échos rétrodiffusés ont un rapport signal sur bruit plus faible, de sorte que l'image radiofréquence reconstruite est de très faible qualité par rapport au CU (et même au MLT). Afin de remédier à ce problème, **[Montaldo (2009)]** a proposé une approche qui repose sur la somme cohérente d'images de faible qualité obtenues à partir de l'insonification du milieu avec des ondes planes inclinées (selon un angle d'émission) dans différentes directions. Cette technique s'appelle: *Coherent Plane Wave Compounding (CPWC)*.

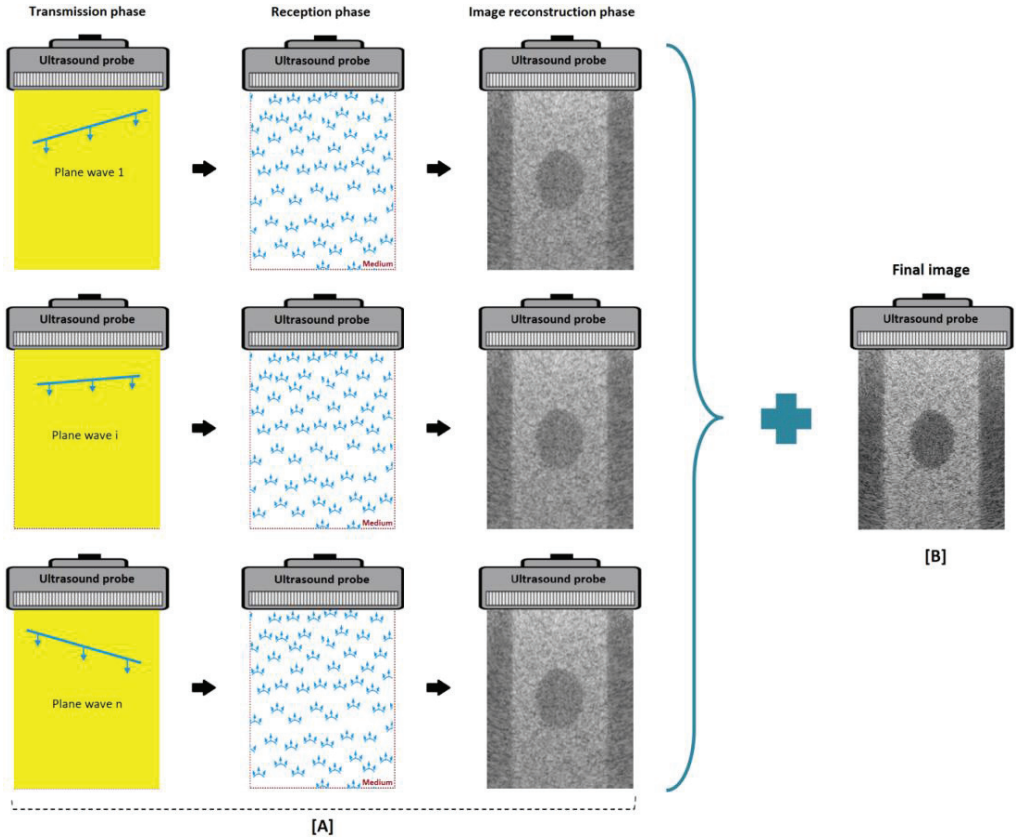

VF_Fig.9: Principe de l'imagerie en ondes planes. [A]: (à gauche) Transmission des différentes ondes planes, (au milieu) réception des différents échos rétrodiffusés (à droite) reconstruction des différentes images de faible qualité. [B]: Image finale obtenue après le CPWC.

- La phase de transmission

Dans **[Montaldo (2009)]**, il a été démontré que pour obtenir la même qualité à la profondeur z_f que celle fournie par l'imagerie conventionnelle, il faut utiliser N_{pw} insonifications d'ondes planes dans CPWC. N_{pw} est donné par:

$$N_{pw} = \frac{N_e\, pitch}{\lambda F^{\#}} \tag{VF_16}$$

où $N_e\, pitch$ est la largeur totale couverte par les éléments de transmission actifs généralement appelée taille d'ouverture latérale, λ est la longueur d'onde d'impulsion transmise et $F^{\#}$ est le F-number défini comme:

$$F^{\#} = \frac{z_f}{N_e pitch} \tag{VF_17}$$

La direction de transmission d'une onde plane peut être calculée en utilisant la relation suivante:

$$\theta_k = \arcsin\left(\frac{k\lambda}{N_e pitch}\right) \tag{VF_18}$$

avec $k = -(N_{pw} - 1) / 2,\ldots,+(N_{pw} - 1) / 2$

Dans ces conditions, pour la $k^{ème}$ transmission par onde plane, les délais de transmission pour chaque élément de la sonde peuvent être obtenus en utilisant le modèle géométrique présenté à la VF_Fig.10.

Ainsi:

$$t_j^k = \frac{(j-1)\cdot pitch \cdot \tan(\theta_k)}{c_0} \qquad \text{(VF\_19)}$$

En prenant en compte les délais de transmission, les signaux d'excitation de chaque élément de la sonde peuvent être écrits comme:

$$a_j^k(t) = w_j \sum_{k=1}^{N_{MLT}} a^k(t) * \delta(t - t_j^k) \qquad \text{(VF\_20)}$$

Il est à noter que chaque élément de la sonde transmet une onde sphérique avec un retard t_j^k. La transmission en onde plane repose sur l'approximation selon laquelle la superposition des N_e ondes sphériques (transmises avec un retard calculé en conséquence) génère une onde plane à l'intérieur du support.

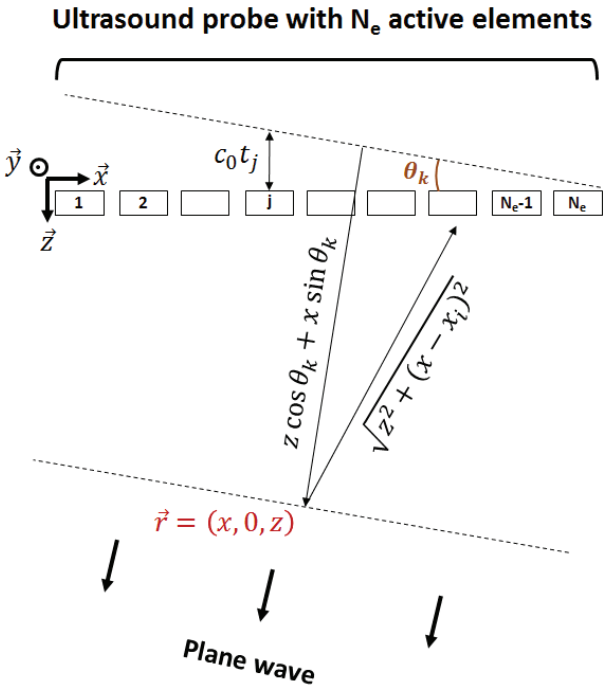

VF_Fig.10: Représentation géométrique de la sonde ultrasonore utilisée pour le calcul du retard pendant la phase de transmission.

- La phase de réception

Comme montré pour l'imagerie conventionnelle, l'imagerie MLT et comme expliqué précédemment pour les ondes planes, le front d'onde focalisé (ou plan, selon le mode d'imagerie) est obtenu grâce à la

superposition d'ondes sphériques. Cela signifie que le signal reçu par chaque élément de la sonde peut être écrit comme:

$$y_i^{PW}(t) = w_i\, e^k(t) * {}^{PW}g_i^k(t) + b(t) \quad \text{(VF\_21)}$$

où ${}^{PW}g_i^k(t) = \sum_{j=1}^{N_e} w_j \delta(t - t_j^k) * g_{ji}(t)$ représente la réponse impulsionnelle du milieu lorsque l'onde plane k est transmise et que les échos sont reçus par le $i^{ème}$ élément de la sonde. Dans VF_21, $e^k(t) = a^k(t) * h_l(t)$ représente la forme d'onde typique générée par un diffuseur arbitraire dans le milieu.

- La phase de post traitement

Après la réception simultanée de tous (N_e) les signaux radiofréquence $y_i^{PW}(t)$, une image de mauvaise qualité est obtenue en utilisant l'équation DAS suivante:

$$A^{PW}(x,z) = \sum_{i=1}^{N_e} y_i^{MLT}(\tau_i(x\ ,z)) \quad \text{(VF\_22)}$$

où $\tau_i(x\ ,z)$ représente le temps de vol nécessaire pour que l'onde plane (l'écho) se propage entre la transmission (la diffusion) au point $(x\ ,z)$ du milieu. $\tau_i(x\ ,z)$ peut être calculé en utilisant la relation suivante:

$$\tau_i(x,z) = \frac{z\cos(\theta_k) + x\sin(\theta_k)}{c_0} + \frac{\sqrt{z^2 + (x - x_i)^2}}{c_0} \quad \text{(VF\_23)}$$

Une fois toutes les N_{pw} images A^{PW} de mauvaise qualité reconstruites, suivant le principe du CPWC, l'image finale est obtenue en utilisant:

$$A^{CPWC} = \sum_{k=1}^{N_{pw}} A^{PW} \quad \text{(VF\_24)}$$

Des études récentes **[Toulemonde (2015)]** ont montré que pour le CPWC, la qualité de l'image s'améliorait très peu à partir de 9 ondes planes.

6.4. Imagerie en ondes divergentes

Le principe de l'imagerie par ondes divergentes est représenté par la VF_Fig.11. Semblable à l'imagerie par ondes planes, l'imagerie en ondes divergentes repose sur une insonification large du milieu afin de reconstruire des images ultrasonores complètes à partir d'un événement de transmission / réception. Cependant, comme dans l'imagerie en ondes planes, l'absence de focalisation du faisceau lors de la transmission diminue la qualité de l'image fournie. Ainsi, la sommation cohérente de plusieurs images obtenues en ondes divergentes est appliquée également afin d'améliorer la qualité de l'image finale.

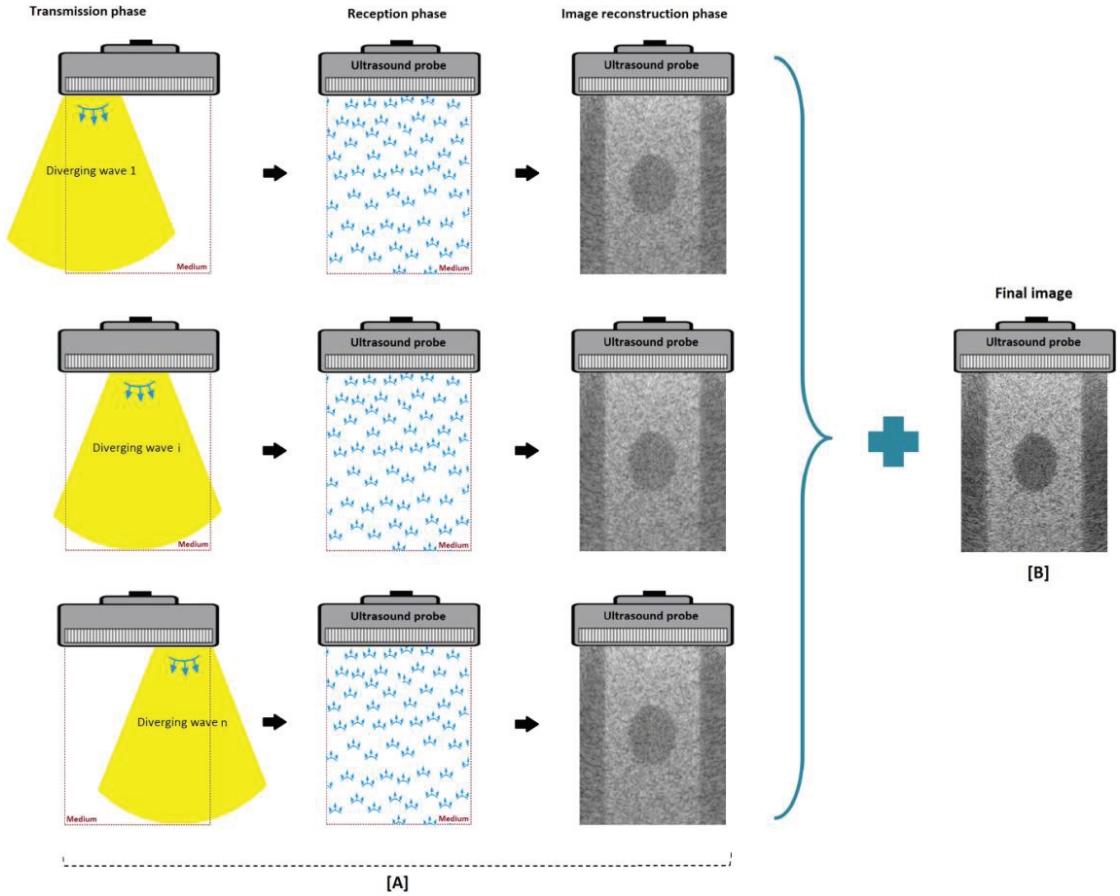

VF_Fig.11: Principe de l'imagerie en onde divergente, les étapes de formations de l'image, sont semblables à ceux de de la VF_Fig.10.

7. Compression d'impulsion utilisant des chirps

En transmettant des impulsions courtes en imagerie médicale, une résolution élevée peut être obtenue aux dépens d'une faible profondeur de pénétration. Afin d'améliorer la profondeur de pénétration, l'énergie du signal d'excitation doit être augmentée en élargissant la durée de l'impulsion transmise ou en augmentant son amplitude. Cependant, prolonger la durée de l'impulsion implique une diminution de la résolution axiale de l'image et l'augmentation de l'amplitude de l'impulsion (ou du niveau de pression maximal) peut potentiellement entraîner des effets biologiques néfastes. Ainsi, la Food and Drug Administration (FDA) a établi une limite à l'indice mécanique (MI) et à l'indice thermique (TI), où des valeurs élevées de MI et TI peuvent provoquer une cavitation inertielle et donc des dommages tissulaires **[Szabo (2004)]**. Un grand défi se pose donc et il consiste à atteindre une bonne profondeur de pénétration sans dépasser les limites de sécurité.

Les techniques de compression d'impulsions ont été initialement introduites dans le domaine du radar **[Cook & Bernfeld (1967); Skolnik (1981)]** et ont été adaptés avec succès aux systèmes d'imagerie par ultrasons quelques années plus tard **[Chiao (2005); Misaridis (2000); O'Donnell (1992)]**. Leur principale objectif, jusqu'à ces dernières années, était d'augmenter la profondeur de pénétration en augmentant l'énergie totale transmise tout en maintenant le même niveau d'intensité maximale en utilisant des durées d'impulsions plus longues **[O'Donnell (1992)]**. De nos jours, ces signaux sont également utilisés pour augmenter la cadence d'acquisition des systèmes d'imagerie

ultrasonores en s'appuyant sur les propriétés d'orthogonalité des signaux modulés en fréquence **[Lashkari (2016); Bujoreanu (2017); Benane (2018b); Benane (2018c)]**.
Bien que les excitations chirp présentent de nombreux avantages par rapport aux impulsions sinusoïdales courtes, il n'est pas facile d'utiliser et de concevoir un signal de chirp. Tout d'abord, il n'est pas facile de concevoir les bons signaux d'excitation, en choisissant les largeurs de bande adaptées, les longueurs d'excitation, etc. Deuxièmement, les échos rétrodiffusés après la transmission d'un chirp doivent être filtrés. L'étape de filtrage est effectuée en post-traitement en appliquant une technique de compression d'impulsion. Cette étape permet de rassembler toute l'énergie transportée par la chirp dans une très courte impulsion, fournissant ainsi une bonne résolution axiale tout en gardant un bon ratio signal sur bruit. La largeur de bande du signal d'excitation est la clé pour obtenir une compression substantielle, pour des largeurs de bande comparables à la bande passante de la sonde à ultrasons employée, la résolution axiale obtenue étant comparable à celle fournie par les systèmes à impulsions classiques. Cependant, si l'excitation par impulsions et la compression des impulsions ne sont pas bien conçues, les niveaux élevés de lobes secondaires ainsi générés peuvent fortement diminuer la résolution de l'image, le rapport contraste / bruit et d'autres paramètres quantifiant sa qualité **[Borsboom (2005)]**.

- **Définition d'un chirp**

La formulation analytique d'un signal chirp est:

$$a(t) = C(t)e^{j2\pi\phi(t)} \tag{VF_25}$$

où $C(t)$ et $\phi(t)$ sont respectivement les fonctions de modulation d'amplitude et de phase. $\phi(t)$ est défini comme:

$$\phi(t) = \left(f_c + \frac{B}{2T} t \right) t \quad \text{avec: } -\frac{T}{2} \le t \le \frac{T}{2} \tag{VF_26}$$

où f_c est la fréquence centrale, B est la largeur de bande, T est la durée du signal et $f_c - (B/2)$ est la fréquence de départ. La fréquence instantanée est donnée par:

$$f_i(t) = \frac{d\phi(t)}{dt} = \frac{d\left[\left(f_c + \frac{B}{2T} t \right) t \right]}{dt} = f_c + \frac{B}{T} t \tag{VF_27}$$

On peut remarquer dans VF_27 que la fréquence instantanée est une fonction linéaire du temps. Bien qu'une contradiction puisse exister entre la notion de fréquence instantanée et la théorie de Fourier (qui considère qu'un signal doit être infini dans le temps pour être limité en bande), le terme f_i indique en pratique la bande spectrale dans laquelle se concentre l'énergie du signal à l'instant t. Le paramètre $\kappa = B/T$ est le taux de modulation en fréquence. Ainsi, le signal balaye linéairement les fréquences dans l'intervalle $[f_c - \frac{B}{2}, f_c + \frac{B}{2}]$.
Pour générer numériquement ce type de signaux, on considère une autre expression sans temps négatif qui peut s'écrire comme:

$$a(t) = C(t)e^{\left(j2\pi \left[\left(f_c - \frac{B}{2} \right) t + \frac{B}{2T} t^2 \right] \right)}, \quad 0 \le t \le T \tag{VF_28}$$

Un exemple de chirp linéaire apodisé avec une fenêtre de Tukey à 20% est illustré à la VF_Fig.12. Les paramètres de ce signal sont d étaillés dans la VF_Table1.

VF_Table 1: Paramètres su signal

Paramètre	Valeur
Freq. d'echantillonage	100 MHz
Freq. centrale	8.5 MHz
Bande passante (frac.)	100 %
Durée	10 µs

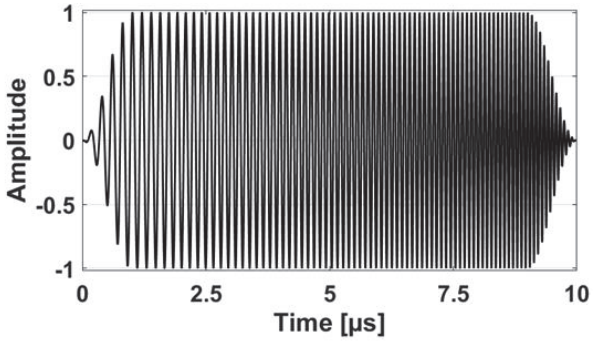

VF_Fig.12: Illustration d'un chirp apodisé

- **Compression d'impulsion**

Après avoir transmis un chirp linéaire à l'intérieur d'un tissu, les échos reçus doivent être compressés pour rétablir une bonne résolution dans l'image finale. Cette étape de filtrage (également appelée compression d'impulsion) est réalisée en corrélant les signaux reçus avec les signaux transmis. Plusieurs techniques de compression d'impulsion présentant des avantages / inconvénients différents existent et les plus utilisées sont:

- Le filtre inverse : $H_{INVERSE}(f) = 1 / A(f)$;
- Le macthed filter : $H_{MATCHED}(f) = e^{-j2\pi f \tau_d} \ A^*(f)$;
- Le filtre de Wiener : $H_{WIENER}(f) = \dfrac{A^*(f)}{|A(f)|^2 + SNR(f)^{-1}}$;

où $SNR(f)$ est le rapport signal sur bruit.

III- « Resolution enhancement compression » combiné à la sommation coherente d'images ultrasonores obtenue par ondes planes

1. Théorie

Les échos rétrodiffusés reçus après une insonification complète du milieu à l'aide d'une onde plane k peuvent s'écrire comme suit:

$$y_i^{PW}(t) = w_i e^k(t) * \sum_{j=1}^{N_e} w_j \sum_{l=1}^{N_s} TRF_l \frac{\delta\left(t - t_j^k - \dfrac{\left\| \vec{r_l} - \vec{r_{S_j}^0} \right\|_2 + \left\| \vec{r_l} - \vec{r_{S_i}^0} \right\|_2}{c_0} \right)}{4\pi^2 \left\| \vec{r_l} - \vec{r_{S_j}^0} \right\|_2 \left\| \vec{r_l} - \vec{r_{S_i}^0} \right\|_2} \qquad \text{(VF\_29)}$$

où N_s représente le nombre de diffuseurs à l'intérieur du milieu, $\overrightarrow{r_{S_j}^0}$ et $\overrightarrow{r_{S_i}^0}$ correspondent aux positions de l'élément j et i respectivement. Supposons maintenant un écho généré par un seul diffuseur l, le signal reçu correspondant peut s'écrire comme suit:

$$y_i^{PW}(t) = w_i \sum_{j=1}^{N_e} w_j TRF_l \frac{e^k\left(t - t_j^k - \frac{\left\|\vec{r_l} - \overrightarrow{r_{S_j}^0}\right\|_2 + \left\|\vec{r_l} - \overrightarrow{r_{S_i}^0}\right\|_2}{c_0}\right)}{4\pi^2 \left\|\vec{r_l} - \overrightarrow{r_{S_j}^0}\right\|_2 \left\|\vec{r_l} - \overrightarrow{r_{S_i}^0}\right\|_2} \qquad \text{(VF\_30)}$$

On peut remarquer dans (VF_30), que le signal reçu est une pondération (par w_j, w_i, $1/4\pi^2 \left\|\vec{r_l} - \overrightarrow{r_{S_j}^0}\right\|_2 \left\|\vec{r_l} - \overrightarrow{r_{S_i}^0}\right\|_2$) de versions superposées légèrement retardées (par $t_j^k - \left[\left\|\vec{r_l} - \overrightarrow{r_{S_j}^0}\right\|_2 + \left\|\vec{r_l} - \overrightarrow{r_{S_i}^0}\right\|_2\right] / c_0$) de la forme d'onde transmise $e^k(t) = a^k(t) * h_1(t)$. Ainsi, on peut voir que, si un filtre de compression (matched ou Wiener) adapté uniquement à la forme d'onde transmise $a^k(t)$ est appliqué au signal $y_i^{PW}(t)$, la résolution obtenue est celle définie par la réponse impulsionnelle de la sonde $h_1(t)$. En d'autres termes, pour les sondes ultrasonores avec des largeurs de bande inférieures, la résolution de l'image fournie est dégradée.

Considérons maintenant un cas hypothétique idéal, dans lequel un transducteur de réponse impulsionnelle $h_2(t)$ (VF_Fig.13d), de largeur de bande supérieure à celle de $h_1(t)$ (VF_Fig.13a), et dans lequel aucun effet d'atténuation n'est présent dans le milieu. Dans ces conditions, la relation (VF_30) devient:

$$\tilde{y}_i^{PW}(t) = w_i \sum_{j=1}^{N_e} w_j TRF_l \frac{\tilde{e}^k\left(t - t_j^k - \frac{\left\|\vec{r_l} - \overrightarrow{r_{S_j}^0}\right\|_2 + \left\|\vec{r_l} - \overrightarrow{r_{S_i}^0}\right\|_2}{c_0}\right)}{4\pi^2 \left\|\vec{r_l} - \overrightarrow{r_{S_j}^0}\right\|_2 \left\|\vec{r_l} - \overrightarrow{r_{S_i}^0}\right\|_2} \qquad \text{(VF\_31)}$$

avec $\tilde{e}^k(t) = \tilde{a}^k(t) * h_2(t)$ (VF_Fig.13f). Dans la relation précédente, $\tilde{a}^k(t)$ (VF_Fig.13e) est un chirp qui couvre toute la bande passante de $h_2(t)$. Incontestablement, la résolution axiale fournie par $\tilde{e}^k(t)$ est meilleure que celle de $e^k(t)$, car $h_2(t)$ a une bande passante plus large que $h_1(t)$.

Le principe de base de notre méthode repose sur l'équivalence entre $e^k(t)$ et $\tilde{e}^k(t)$ qui implique:

$$a^k(t) * h_1(t) = \tilde{a}^k(t) * h_2(t) \qquad \text{(VF\_32)}$$

En exprimant l'équation (VF_32) dans le domaine fréquentiel, on peut calculer le signal d'excitation du transducteur réel $a^k(t)$ (VF_Fig.13b). En utilisant ce signal ($a^k(t)$), on peut obtenir la même résolution que le transducteur fictif, de bande passante plus large, excité avec $a^k(t)$. Le signal d'excitation peut être généré en utilisant:

$$A^k(f) = \tilde{A}^k(f)\frac{H_1^*(f)H_2(f)}{|H_1(f)|^2 + |H_1(f)|^{-2}} \qquad \text{(VF\_33)}$$

Pour compresser les échos $e^k(t)$, on utilise le filtre de Wiener suivant:

$$\beta_{REC}(f) = \frac{(\tilde{A}'^k)^*(f)}{|\tilde{A}'^k(f)|^2 + \gamma\overline{eSNR}(f)^{-1}} \qquad \left(\text{avec: } \tilde{A}'^k = \tilde{A}^k\frac{H_1(f)}{H_2(f)}\right) \qquad \text{(VF\_34)}$$

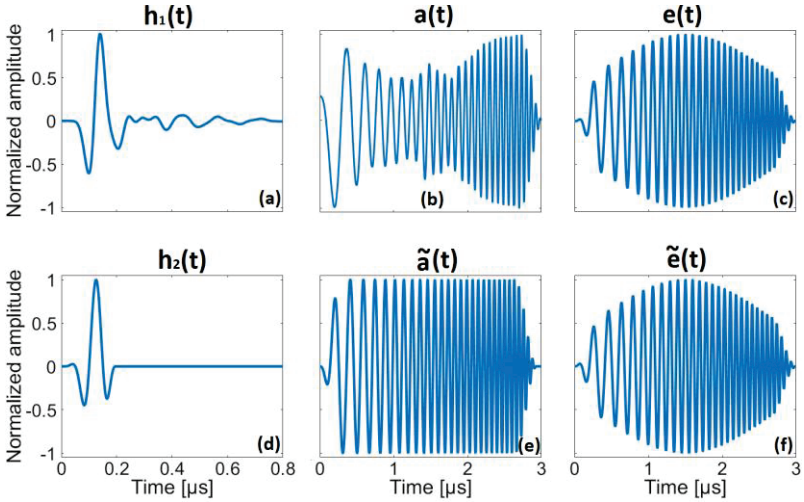

VF_Fig.13. Réponses impulsionnelles, chirps et produits de convolution résultants impliqués dans le schéma REC. (a) est la réponse impulsionnelle réelle de la sonde d'environ 92% de bande passante fractionnelle à -6 dB. (d) est la réponse impulsionnelle fictive avec une largeur de bande d'environ 125% à -6 dB. (b) est un chirp modifié utilisé pour exciter (a). (e) est un chirp linéaire utilisé pour exciter (d). (c) et (f) sont les produits de convolution des réponses impulsionnelles avec leurs séquences de chirp respectives.

2. Résultats expérimentaux

Pour la mise en œuvre expérimentale, la plateforme ultrasonore UlaOp-64 (Microelectronics System Design Lab, Florence, Italy) équipée d'une sonde linéaire LA523E a été utilisée. Le UlaOp-64 peut transmettre des formes d'onde arbitraires définies par des stratégies de transmission et de réception personnalisées **[Tortoli (2009)]**. Les signaux d'excitation sont illustrés en VF_Fig.14.

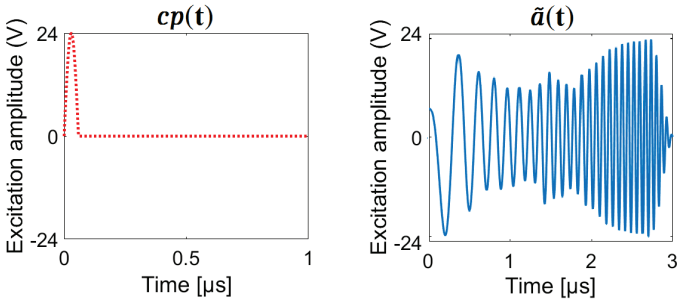

VF_Fig.14. Les signaux d'excitation CPWC-CP (à gauche) et CPWC-REC (à droite) utilisés pour des acquisitions expérimentales.

- **Acquisition sur un diffuseur ponctuel**

Il s'agit, ici, d'une acquisition des signaux rétrodiffusés enregistrés à partir d'un fil de 50 µm de diamètre immergé à 22 mm de profondeur dans l'eau. La VF_Fig.15 montre les images B-mode obtenues pour les deux types de signaux d'excitation.

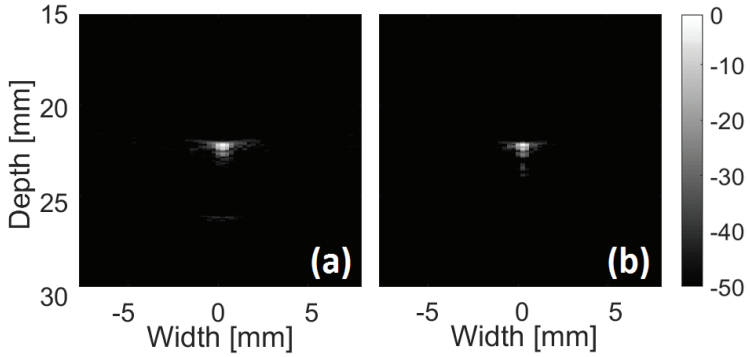

VF_Fig.15. Images B-mode obtenues à partir d'un fil imergé dans l'eau en utilisant le UlaOp-64: CPWC-CP (a) and CPWC-REC (b).

Un graphique du profil axiale de l'enveloppe obtenue, d'une part par la technique conventionnelle (CPWC-CP) et d'autre part avec la technique proposée (CPWC-REC), est représenté sur les VF_Fig.16a et VF_Fig.16b.

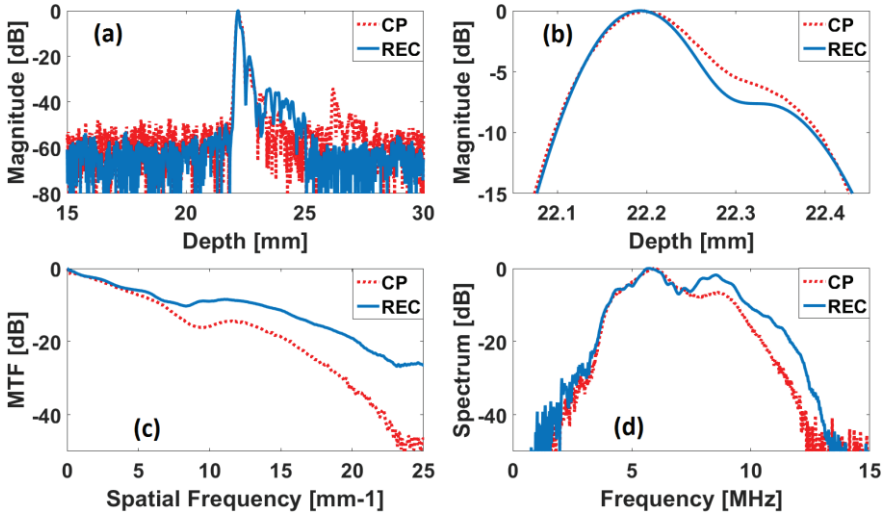

VF_Fig.16. Comparaison des performances entre CPWC-REC (ligne continue) et CPWC-CP (ligne pointillée). (a) Enveloppe des données radiofréquences. (b) Zoom de l'enveloppe représentée en (a). (c) MTF dérivé de l'enveloppe. (d) Spectre normalisé dérivé des données radiofréquences.

L'approche CPWC-REC montre que l'étape de compression des données RF se fait correctement. L'approche proposée offre également un bruit de fond plus faible par rapport à celui obtenu par CPWC-CP (différence d'environ 7 dB, voir VF_Fig.16a). Les lobes secondaires créés, de 0 dB à -40 dB, sont légèrement inférieurs à ceux de CPWC -CP (VF_Fig.16a). De plus, la résolution axiale qui dérive de la MTF a été améliorée de 29% grâce à la technique CPWC-REC. Les valeurs correspondantes sont 201,7 µm / 156,3 µm pour CPWC- (CP / REC) (VF_Fig.16c).

Les spectres de puissance des formes d'onde comprimées utilisant la technique REC et l'impulsion conventionnelle sont représentés sur VF_Fig.16d. L'examen du spectre de puissance CPWC-REC révèle que plus d'énergie est portée par les hautes fréquences. Cela s'explique par le fait que, comme les fréquences situées sur les bords de la bande passante sont excitées avec une énergie plus grande, la

forme d'onde comprimée a une largeur de bande élargie. La largeur de bande à -6 dB de la réponse impulsionnelle du transducteur ($h_1(t)$) est de 7,8 MHz (92% de la fréquence centrale). Par ailleurs, la largeur de bande améliorée du transducteur ($h_2(t)$) est de 12,1 MHz (142% de la fréquence centrale). La VF_Fig.16d montre que l'approche CPWC-REC augmente la largeur de bande à -6 dB de 49%. Les largeurs de bande mesurées à -6 dB sont respectivement de 4,7 MHz pour CPWC-REC et de 3,1 MHz pour CPWC -CP. À noter que la différence entre la largeur de bande des signaux émis et des signaux reçus est due aux phénomènes de propagation et à l'algorithme utilisé pour reconstruire l'image finale. Le eSNR résultant pour CPWC-CP et CPWC-REC est respectivement de 26,6 dB et 32,1 dB, ce qui correspond à une amélioration de 5,5 dB.

- **Acquisition in-vivo**

Une dernière expérience a été réalisée in vivo sur un lapin soumis à une anesthésie gazeuse (Aerrane, Baxter, Deerfield, IL).

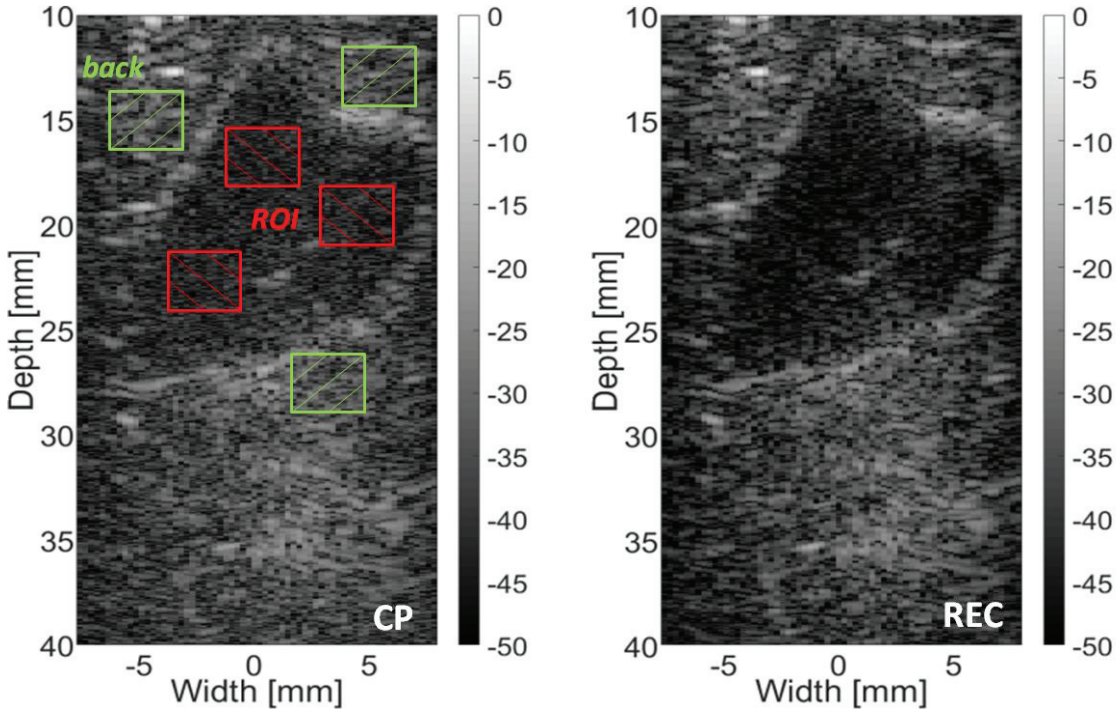

VF_Fig.17. Images B-mode de la vésicule biliaire d'un lapin obtenues en utilisant le UlaOp-64: CPWC-CP (à gauche) et CPWC-REC (à droite). ROI et back sont les zones utilisées pour calculer le SNR et le CNR.

Les images CPWC-CP et CPWC-REC ont été acquises sur la vésicule biliaire de l'animal. Dans ce cas, les tissus intermédiaires (c'est-à-dire la peau, la graisse sous-cutanée et les muscles) n'ont pas été enlevés, de sorte que les propriétés d'atténuation de ces tissus et la présence d'artefacts d'aberration ont directement affecté les résultats des acquisitions.

On peut constater sur la VF_Fig.17 que CPWC-REC offre une meilleure qualité d'image globale conformément aux métriques obtenues montrées à la VF_Fig.18. Une amélioration de 2,2 dB pour le CNR et de 0,6 pour le SNR est obtenue, ainsi qu'une amélioration de la mesure de la longueur d'autocorrélation à -6 dB de 9,5% et 7,0% respectivement dans les directions axiale et latérale (VF_Fig.18c et VF_Fig.18d)). L'évolution du CNR en fonction du nombre d'ondes planes (VF_Fig.18a) confirme que le contraste entre la partie interne du corps de la vésicule biliaire

(anéchoïque) et le foie, à l'extérieur de la vésicule biliaire (échogène), est meilleur dans l'image obtenue en utilisant CPWC-REC que dans l'image obtenue en utilisant CPWC-CP.

On peut remarquer que le CNR obtenu avec une seule onde plane avec CPWC-REC est supérieur au CNR obtenu par neuf ondes planes avec CPWC-CP. Les courbes SNR présentées à la VF_Fig.18b vérifient l'observation visuelle que les zones anéchoïques de l'image CPWC-REC sont plus sombres que celles de l'image CPWC-CP. Un rapport signal sur bruit équivalent est obtenu avec CPWC-REC lorsque quelques ondes planes sont impliquées dans la construction de l'image par rapport à CPWC-CP utilisant plusieurs ondes planes.

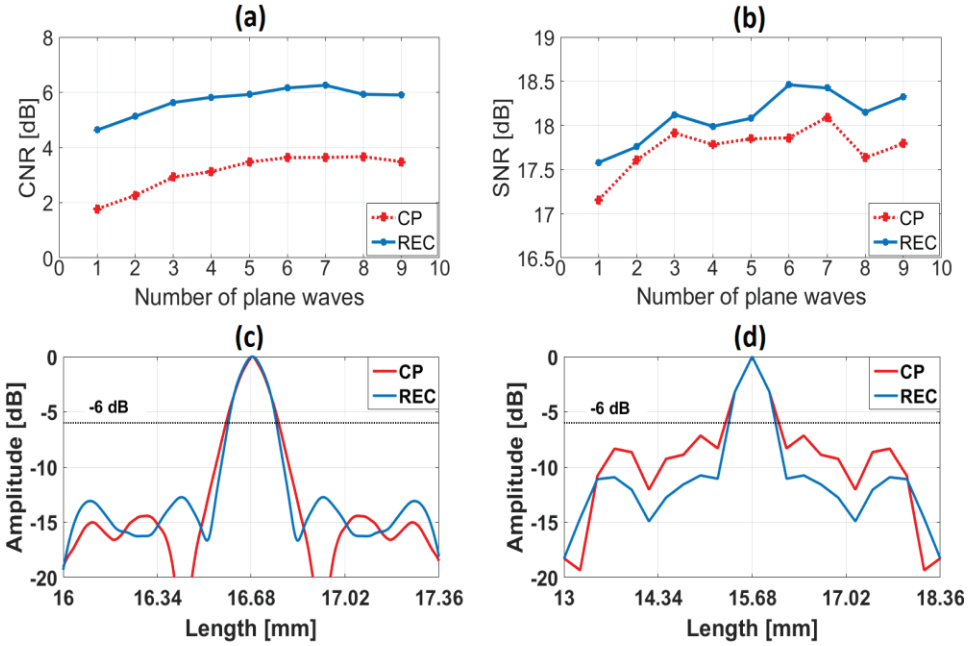

VF_Fig.18. Evolution du CNR (a) et du SNR (b) avec CPWC-REC et CPWC-CP en fonction du nombre d'ondes planes. Longueur d'autocorrélation dans les directions axiale (c) et latérale (d) CPWC-REC et CPWC-CP.

IV- Technique de compression d'impulsion adaptée à l'atténuation du tissue combinée à l'imagerie ultrasonore ultra-rapide pour élargir la bande passante et améliorer la résolution de l'image

1. Théorie

Dans la partie précédente, il a été conclu que la présence d'atténuation dans les tissues altère les performances de la technique CPWC-REC. Ici, cet effet est étudié et la méthode a été optimisée (REC-Opt) afin de compenser cet effet. Comme il a été montré dans **[Gurumurthy (1982)]**, l'effet de l'atténuation peut être modélisé par sa réponse impulsionnelle. Cette dernière modélise l'évolution de l'onde ultrasonore au cours de la propagation entre deux points dans le milieu séparés par une distance d . Dans **[Gurumurthy (1982)]**, l'expression suivante s'est avérée être une bonne approximation de la transformée de Fourier de $h_{att}(t,d)$:

$$H_{att}(f,d) = e^{-\alpha d|f|}\; e^{-j2\pi f\tau d}\; e^{j\frac{2f\alpha d}{\pi}\ln(2\pi f)} \quad (\text{avec: } \tau = \tau_b + \frac{\alpha}{\pi^2}\tau_m) \qquad \text{(VF\_35)}$$

où α est la pente du coefficient d'atténuation (supposée être connue), τ_b est le retard global et τ_m est le facteur de retard minimum de phase. Dans **[Gurumurhy (1982)]**, les auteurs ont proposé d'utiliser $\tau_m = 20$ et $\tau_b = 6.67 \mu m / s$ afin d'adapter la dispersion dans les tissus mous. Dans (VF_35):

- $e^{-\alpha d|f|}$ correspond à l'évolution de l'amplitude de chaque fréquence dans le spectre de la forme d'onde qui se propage à l'intérieur du milieu.
- $e^{-j2\pi f \tau d}$ représente la réponse de phase du tissu en supposant que la vitesse de phase est constante.
- $e^{j\frac{2f\alpha d}{\pi} ln(2\pi f)}$ représente un terme dispersif de Hilbert qui rend $h_{att}(t,d)$ causal.

La VF_Fig.19a montre comment un écho généré par un diffuseur, lorsqu'un seul élément de la sonde émet une impulsion courte, évolue en fonction de la profondeur.

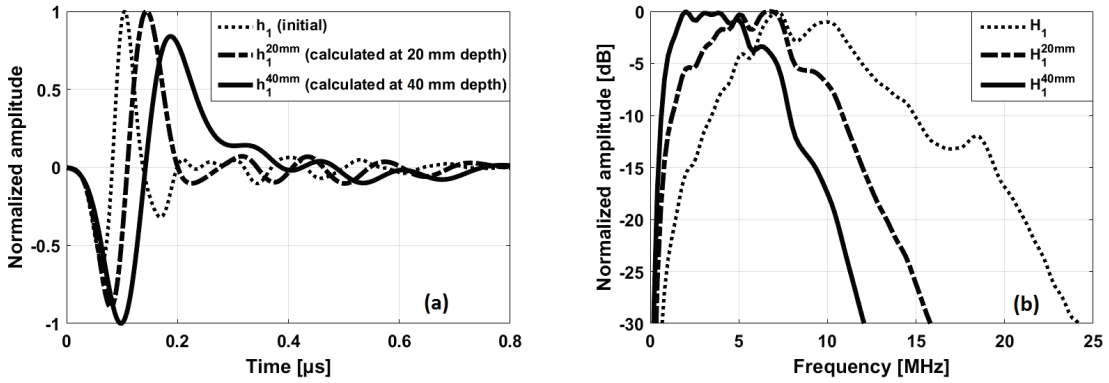

VF_Fig.19. Evolution d'un écho généré par un diffuseur placé à différentes profondeurs (20 mm et 40 mm) lorsqu'un seul élément de la sonde émet une impulsion courte (impulsion de Dirac). (a) - représentation temporelle, (b) - représentation fréquentielle. La ligne pointillée représente l'écho reçu si aucune atténuation n'était présente, la ligne en tirets représente l'écho généré à une profondeur de 20 mm et la ligne continue représente l'écho généré à 40 mm.

Si aucun effet d'atténuation n'est présent dans milieu, les échos reçus seraient une version légèrement pondérée de la réponse impulsionnelle électroacoustique de la sonde (VF_30). Cependant, la présence de l'atténuation réduit l'amplitude des hautes fréquences du signal transmis en fonction de la distance de propagation, ce qui donne un signal reçu avec une bande passante plus étroite. Ceci est visible à la VF_Fig.19b, où entre un écho généré à 20 mm et un autre généré à 40 mm, on peut voir qu'une réduction de la largeur de bande fractionnelle (à -6dB) de 10% a été générée. Dans de telles conditions, l'expression des signaux reçus pour une insonification utilisant une onde plane k (VF_29) devient:

$$y_i^{PW}(t) = w_i \sum_{j=1}^{N_e} w_j \sum_{l=1}^{N_s} TRF_l \frac{e^k\left(t - t_j^k - \frac{d_{IS_j} + d_{IS_i}}{c_0}\right)}{4\pi^2 d_{IS_j} d_{IS_i}} * h_{att}\left(t - t_j^k - \frac{d_{IS_j} + d_{IS_i}}{c_0}, d_{IS_j} + d_{IS_i}\right) \quad \text{(VF\_36)}$$

où $d_{IS_j} = \left\| \vec{r_l} - \overrightarrow{r_{S_j}^0} \right\|_2$ and $d_{IS_i} = \left\| \vec{r_l} - \overrightarrow{r_{S_i}^0} \right\|_2$. On peut voir dans (VF_36) que le signal reçu, en présence d'atténuation, est similaire à celui obtenu dans (VF_30), seule la réponse impulsionnelle d'atténuation étant ajoutée. A ce stade, on peut récrire (VF_36) comme:

$$y_i^{PW}(t) = w_i \sum_{j=1}^{N_e} w_j \sum_{l=1}^{N_s} TRF_l \frac{e_{att}^k\left(t - t_j^k - \frac{d_{lS_j} + d_{lS_i}}{c_0}, d_{lS_j} + d_{lS_i}\right)}{4\pi^2 d_{lS_j} d_{lS_i}} \quad \text{(VF\_37)}$$

with: $e_{att}^k\left(t - t_j^k - \frac{d_{lS_j} + d_{lS_i}}{c_0}, d_{lS_j} + d_{lS_i}\right) = e^k\left(t - t_j^k - \frac{d_{lS_j} + d_{lS_i}}{c_0}\right) * h_{att}\left(t - t_j^k - \frac{d_{lS_j} + d_{lS_i}}{c_0}, d_{lS_j} + d_{lS_i}\right)$

L'équation (VF_37) peut être interprété comme suit: l'effet d'atténuation modifie les échos de telle sorte qu'une réflexion générée par un diffuseur l aura une forme d'onde $e_{att}^k\left(t - t_j^k - \frac{d_{lS_j} + d_{lS_i}}{c_0}, d_{lS_j} + d_{lS_i}\right)$ qui sera différente pour des diffuseurs placés à d'autres positions dans le milieu.

Appliquons maintenant le principe du REC :

$$e_{att}^k(t,d) = \tilde{e}^k(t) \quad \Leftrightarrow \quad a^k(t) * h_1(t) * h_{att}(t,d) = \tilde{a}^k(t) * h_2(t) \quad \text{(VF\_38)}$$

L'équation (VF_38) montre que pour recevoir des échos $\tilde{e}^k(t)$ lors de la transmission avec la sonde (de réponse impulsionnelle $h_1(t)$), il convient d'adapter le signal de transmission pour chaque point du milieu (car l'effet d'atténuation dépend de la distance de propagation de l'onde). Cette exigence pourrait être réalisable si l'on voulait adapter la transmission à un seul point du milieu. Cependant, afin de prendre en compte tous les points du milieu (dans un tissu à distribution dense de diffuseurs), nous proposons de n'effectuer la compensation de l'effet d'atténuation qu'en réception. Ainsi, le principe suivant doit être suivi:

5- générer le signal d'excitation $a^k(t)$ comme s'il n'y avait pas d'effet d'atténuation dans le milieu imagé (en utilisant (VF_33))

6- transmettre l'onde plane et recevoir les échos rétrodiffusés $y_i^{PW}(t)$

7- pour chaque échantillon temporel τ_i du signal $y_i^{PW}(t)$

- calculer la réponse impulsionnelle d'atténuation en utilisant la relation suivante:

$$H_{att}(f, \tau_i c_0) = e^{-\alpha \tau_i c_0 |f|} \; e^{-j2\pi f \tau \tau_i c_0} \; e^{j \frac{2 f \alpha \tau_i c_0}{\pi} \ln(2\pi f)} \quad \text{(VF\_39)}$$

- calculer le filtre de compression $\beta_{REC}(f, \tau_i)$ en utilisant (VF_39) et en résolvant (VF_37) dans le domaine fréquentiel

$$\beta_{REC}(f, \tau_i) = \frac{(\tilde{A}'^k)^*(f, \tau_i)}{\left|\tilde{A}'^k(f, \tau_i)\right|^2 + \gamma \overline{eSNR}(f)^{-1}} \quad \text{(VF\_40)}$$

où $(\tilde{A}'^k)^*(f, \tau_i) = A^k(f, \tau_i) H_1(f) H_{att}(f, \tau_i) / H_2(f)$

- appliquer le filtre de compression pour chaque échantillon τ_i

8- Répéter l'étape 3 pour les signaux reçus par tous les éléments $i \in [1..N_{el}]$ de la sonde.

2. Résultas

Afin de valider la théorie, des simulations ont été effectuées à l'aide de CPWC. Les mêmes signaux d'excitation que dans la partie II ont été utilisés. Pour l'excitation de type REC, les signaux reçus ont été compressés en utilisant $\beta_{REC}(f)$ pour REC et en utilisant $\beta_{REC}(f,d)$ pour REC-Opt. Le milieu simulé a un coefficient d'atténuation de 0,5 dB / MHz / cm, ce qui est comparable à la valeur présente dans le foie humain. Les images B-mode obtenues pour les différentes techniques sont illustrées à la VF_Fig.20.

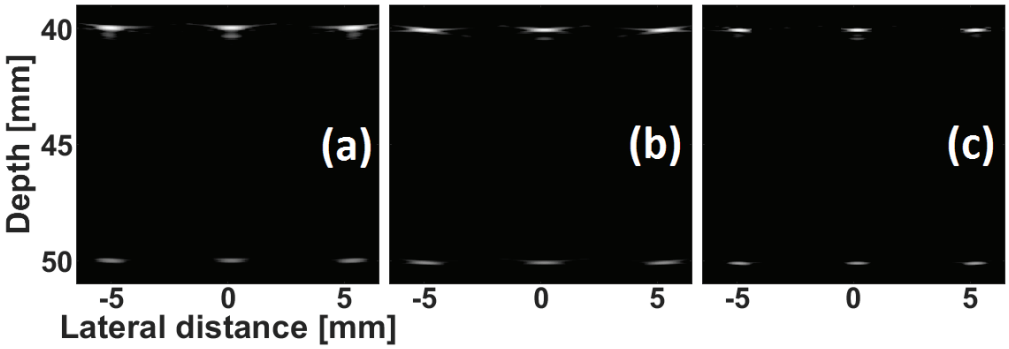

VF_Fig.20. Images B-mode obtenue pour les trois différentes methodes: CP (a), REC (b) and REC-Opt (c). Toutes les images ont une dynamique de 55 dB.

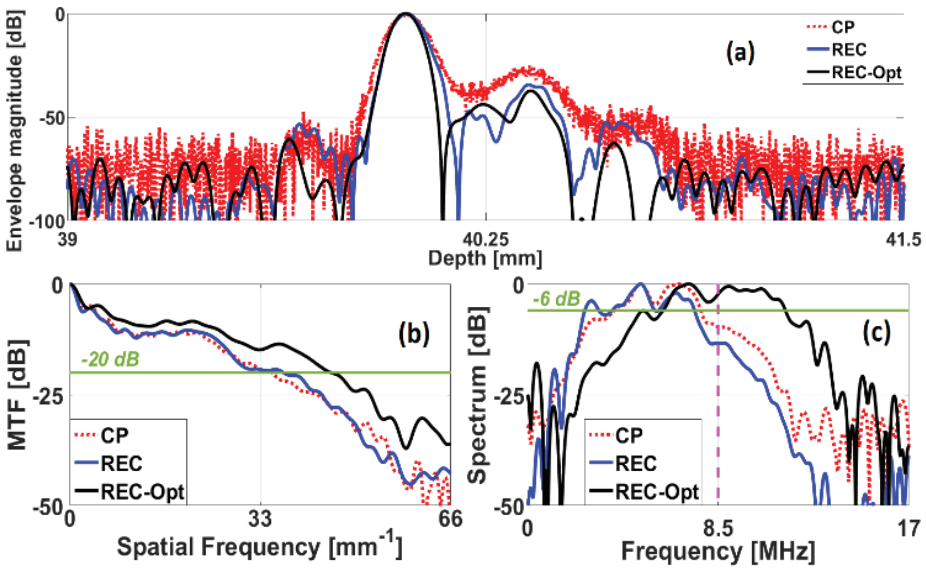

VF_Fig.21. Comparaison des performances entre REC-Opt (ligne noire continue), REC (ligne bleue continue) et CP (ligne rouge en pointillé). (a) Enveloppe des données radiofréquences du diffuseur placé à 4 cm de profondeur au centre de l'image. (b) MTF dérivé de (a). (c) Spectre normalisé dérivé des données radiofréquences du même diffuseur.

On peut observer visuellement que REC-Opt (VF_Fig.20c) permet d'obtenir une meilleure résolution spatiale que REC (VF_Fig.20b) et CP (VF_Fig.20a). Le choix de γ (γ = 50) pour REC et REC-Opt a été effectué dans le but d'obtenir la meilleure résolution axiale possible tout en préservant un niveau de bruit inférieur à celui de CP. Une différence d'environ 15 dB peut être observée entre le niveau de bruit de CP par rapport à REC et REC-Opt (VF_Fig.21a). Comme le montre la VF_Fig.21b, l'amélioration de la résolution axiale a été quantifiée par le calcul de la fonction de transfert de

modulation (MTF) dérivée des données d'enveloppe. En particulier, les nombres d'onde k_{-20} dB auxquels les MTF sont tombées en dessous de -20 dB étaient respectivement 35, 37,1 et 45,2 mm^{-1} pour CP, REC et REC-Opt. Les spectres de puissance de la réflexion du fil à une profondeur de 4 cm sont illustrés à la VF_Fig.21c. Conformément aux améliorations apportées au MTF, les largeurs de bande de -6 dB étaient respectivement de 3,9, 4,1 et 5,5 MHz. Ces résultats correspondent à des améliorations de la résolution axiale et de la bande passante entre 30% et 40,5%, respectivement, entre REC-Opt et CP.

V- Amélioration de la qualité de l'imagerie du second harmonique en utilisant une technique de compression d'impulsion combine à l'inversion d'impulsion ultrasonore

1. Théorie

L'inversion d'impulsion (PI) est une technique d'émission utilisée pour l'imagerie harmonique. Le concept de PI appliqué à l'imagerie par onde plane consiste à transmettre une onde plane deux fois dans la même direction, la seconde fois comportant une version inversée en phase du signal d'excitation utilisé pour la première transmission. Les deux signaux résultants sont additionnés pour obtenir le signal final. Dans cette section, nous proposons de combiner le concept du PI avec le principe de REC. L'idée principale étant de compenser le signal d'excitation de manière à ce que les bandes de fréquences les moins efficaces de la sonde reçoivent plus d'énergie. Afin de mieux comprendre la valeur ajoutée de la technique proposée, il convient d'abord de comprendre le principe du PI classique. Supposons une transmission successive de deux ondes planes, où la première a été générée à l'aide d'un signal d'excitation $a^k(t)$ et la deuxième à l'aide de $-a^k(t)$, suivant:

$$a^k(t) = w^k(t)cos(2\pi f^k t) \tag{VF_41}$$

L'équation (VF_41) montre que le signal d'excitation est une fonction cosinus centrée sur la fréquence f^k et pondérée par une fenêtre $w^k(t)$. La propagation non linéaire de l'onde ultrasonore peut être vue grossièrement comme une superposition de deux ondes: une centrée en f^k (la fondamentale) et une seconde centrée en $2f^k$ (le second harmonique). Ainsi, classiquement, les échos rétrodiffusés générés par un diffuseur quelconque du milieu sont écrits comme suit **[Park (2013)]**:

$$\begin{aligned} {}^{+}e^k(t) &= w^k(t)cos(2\pi f^k t) + \eta(\mathrm{w}^k(t))^2 cos(2\pi(2f^k)t) \\ {}^{-}e^k(t) &= -w^k(t)cos(2\pi f^k t) + \eta(\mathrm{w}^k(t))^2 cos(2\pi(2f^k)t) \end{aligned} \tag{VF_42}$$

où ${}^{+}e^k(t)$ et ${}^{-}e^k(t)$ sont les formes d'onde typiques reçues après la transmission des excitations positives et négatives respectivement. η représente un facteur d'échelle qui déterminera l'amplitude de l'écho harmonique et dépend des propriétés non linéaires du milieu et de la distance de propagation. On peut remarquer, qu'en sommant ${}^{+}e^k(t)$ et ${}^{-}e^k(t)$, l'impact du second harmonique peut être mis en évidence:

$${}^{+}e^k(t) + {}^{-}e^k(t) = 2\eta(w^k(t))^2 cos(2\pi(2f^k)t) \tag{VF_43}$$

Cependant, le modèle généré dans (VF_42) et (VF_43) repose sur une hypothèse très importante, à savoir la négligence totale de la réponse impulsionnelle acousto-électrique de la sonde ultrasonore. Le problème ici est que, l'onde qui se propage à l'intérieur du milieu ne porte pas la forme d'onde $a^k(t)$ mais le signal ${}_{1/2}a^k(t)$ où:

$$ {}_{1/2}a^k(t) = {}_{1/2}h_I(t) * \left(w^k(t) cos(2\pi f^k t) \right) \qquad \text{(VF\_44)} $$

avec ${}_{1/2}h_1(t)$ la réponse impulsionnelle acousto-électrique de la sonde en transmission.

La VF_Fig.22a montre une représentation du calcul de l'onde du second harmonique dans laquelle la réponse impulsionnelle acousto-électrique de la sonde est complètement négligée. D'autre part, la VF_Fig.22b montre le même résultat où l'effet de la sonde à bande limitée est compensé (pour le même signal d'excitation $a^k(t)$).

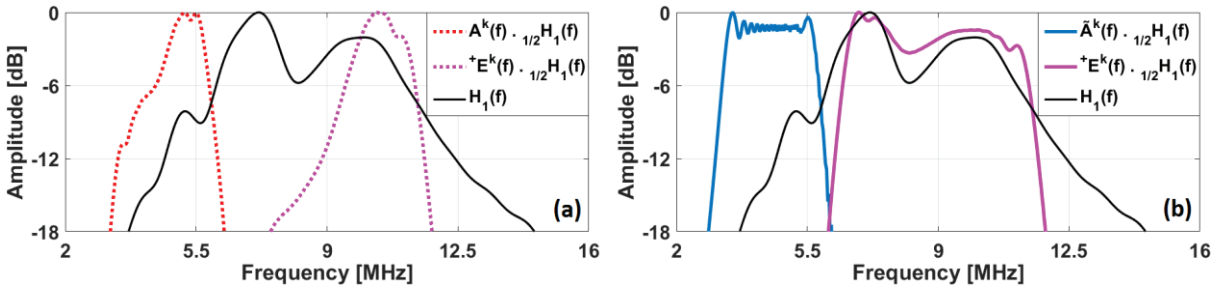

VF_Fig.22. Spectres des signaux transmis (après convolution avec la réponse impulsionnelle) et du signal utilisé pour compresser les échos reçus en utilisant un chirp linéaire plat comme excitation (a) et en utilisant un chirp modulé de type REC (b).

Comme on peut le voir entre les Fig.52a et Fig.52b, la réponse impulsionnelle de la sonde a un impact sur la largeur de bande de la forme d'onde du second harmonique, ce qui entraîne une modification de la résolution de l'image. Cet effet peut ne pas être aussi important dans le cas où le signal d'excitation est une simple sinusoïde et où aucun filtrage adapté en post-traitement n'est effectué sur les données reçues. Cependant, cet impact peut être important lorsque le signal d'excitation est un chirp qui nécessite une phase de compression après réception des échos. Le problème, ici, est que le filtre de compression, calculé directement à partir de $a^k(t)$ ne serait pas optimal, la meilleure façon de faire serait de calculer ce filtre en utilisant ${}_{1/2}a^k(t)$. Nous proposons, ainsi, de procéder comme suit:

1- choisir une fréquence centrale de chirp qui est approximativement la moitié de la fréquence centrale de la sonde (f_0):

$$ f^k = \frac{f_0}{2} \qquad \text{(VF\_45)} $$

2- générer un chirp linéaire ${}_{1/2}a^k(t)$ de bande passante égale à la moitié de la bande passante de la sonde:

$$ {}_{1/2}a^k(t) = w^k(t) cos\left(2\pi \left(f^k - \frac{B^k}{2} + \frac{B^k}{T^k} t \right) t \right) \qquad \text{(VF\_46)} $$

où $B^k = B_0 / 2$ et T^k représentent respectivement la largeur de bande et la durée du chirp (B_0 correspond à la largeur de bande de la sonde).

3- appliquer le principe REC afin de calculer le signal d'excitation nécessaire pour obtenir la forme d'onde ${}_{1/2}a^k(t)$:

$$a^k(t) * {}_{1/2}h_1(t) = {}_{1/2}a^k(t) * {}_{1/2}h_2(t) \quad \text{(VF\_47)}$$

où ${}_{1/2}h_1(t)$ et ${}_{1/2}h_2(t)$ sont respectivement les réponses impulsionnelles en émission de la sonde réelle et de la sonde fictive. Ici nous supposerons que ${}_{1/2}h_2(t) = \delta(t)$ pour élargir au maximum la bande passante de ${}_{1/2}h_1(t)$. Ainsi, on peut en déduire le signal d'excitation dans le domaine fréquentiel comme suit:

$$A^k(f) = {}_{1/2}A^k(f)\frac{{}_{1/2}H_1^*(f)}{\left|{}_{1/2}H_1(f)\right|^2 + \left|{}_{1/2}H_1(f)\right|^{-2}} \quad \text{(VF\_48)}$$

4- sommer les échos reçus après la transmission successive de $a^k(t)$ et $-a^k(t)$;

5- générer ${}_{2/2}a^k(t)$ qui est un chirp linéaire possédant une bande passante deux fois plus large que ${}_{1/2}a^k(t)$ (dans (VF_46)): ${}_{2/2}a^k(t) = \left(w^k(t)\right)^2 cos\left(2\pi(2f^k - B^k + \frac{2B^k}{T^k}t)t\right)$

6- pour chaque échantillon temporal τ_i du signal $y_i^{PW}(t)$

a. calculer la réponse impulsionnelle d'atténuation avec:

$$H_{att}(f, \tau_i c_0) = e^{-\alpha\tau_i c_0 |f|}\ e^{-j2\pi f \tau\tau_i c_0}\ e^{j\frac{2f\alpha\tau_i c_0}{\pi} ln(2\pi f)} \quad \text{(VF\_49)}$$

b. calculer le filtre de compression $\beta_{REC}(f, \tau_i)$ en utilisant:

$$\beta_{REC}(f, \tau_i) = \frac{\left[{}_{2/2}A^k(f) * H_{att}(f, \tau_i)\right]^*}{\left|{}_{2/2}A^k(f) * H_{att}(f, \tau_i)\right|^2 + \gamma\overline{eSNR}^{-1}(f)} \quad \text{(VF\_50)}$$

c. appliquer le filtre de compression pour chaque échantillon τ_i

7- répéter l'étape 6 pour les signaux reçus par tous les éléments $i \in [1..N_{el}]$ de la sonde

La VF_Fig.23 montre les différents signaux impliqués dans le procédé proposé. Comme on peut le constater, le signal d'excitation proposé $a^k(t)$ transporte plus d'énergie dans les bandes de fréquences où la réponse impulsionnelle ${}_{1/2}h_1(t)$ atténue davantage les fréquences du signal, ce qui fait que le signal ${}_{1/2}a^k(t)$ qui se propage à l'intérieur du support est un chirp linéaire à amplitude constante (donc une bande passante maximale B^k). Ainsi, la forme d'onde ${}_{1/2}a^k(t)$ générée par le deuxième harmonique aura également une amplitude constante, donc une largeur de bande maximale ($2B^k$).

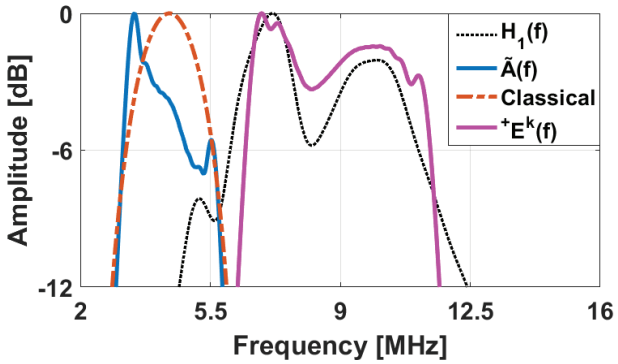

VF_Fig.23. Spectres des signaux transmis (pour les deux approches) et du signal chirp utilisé pour compresser les échos reçus pour REC-PI.

2. Résultats expérimentaux

Afin de valider la théorie, une acquisition expérimentale a été réalisée à l'aide plate-forme ultrasonore UlaOp-256 équipée d'une sonde à réseau linéaire LA523E. La combinaison entre REC et PI a été comparée au PI classique. Une zone contenant quatre fils et un cyst hypoéchogène du fantôme (modèle 410SCG HE 0.5 Gammex Sun nuclear, Neu-Isenburg, Allemagne) a été étudiée. Le fantôme est caractérisé par un coefficient non linéaire B / A = 6,7. Les images B-mode obtenues pour les deux approches sont illustrées à la VF_Fig.24.

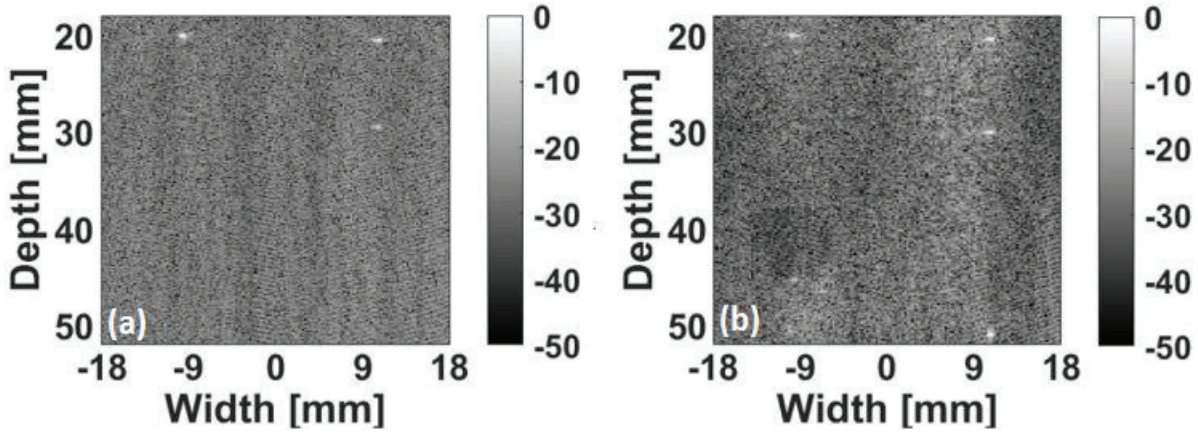

VF_Fig.24. Images B-mode obtenues en utilisant UlaOp-256 pour la méthode PI conventionnelle (a) and for REC-PI (b).

Une amélioration de la qualité de l'image est observée lors de l'utilisation de REC-PI (VF_Fig.24b) par rapport au PI classique (VF_Fig.24a). Une augmentation de 25,4% de la résolution axiale a été constatée pour le diffuseur placé à (x = -0,9 cm, z = 2 cm). Une meilleure taille de speckle a également été obtenue, confirmée par le calcul de la longueur d'auto corrélation des lignes RF dans la direction axiale. En effet, REC-PI fournit une amélioration de 20,1% par rapport à un PI classique compatible avec l'amélioration de la résolution axiale. On peut observer une meilleure profondeur de pénétration du REC-PI par rapport au PI conventionnel, dans sa capacité à reconstruire le diffuseur plus profond qui n'est pas visible dans le PI conventionnel. Le cyst, qui apparaît dans le cas REC-PI et non dans l'IP classique, révèle un gain de 18,2 dB en CNR pour l'approche proposée.

VI- Amélioration de la bande passante et de la qualité d'image en utilisant des filtres de compression non stationnaires

1. Théorie

Considérons une onde acoustique transmise par un transducteur piézoélectrique de surface S_j et les échos diffusés reçus par un transducteur de surface S_i. Comme il a été montré dans **[Jensen(1992)]**, l'expression du signal électrique reçu par S_i (vérifiant l'équation de propagation), lorsque S_j est excité à l'aide d'un signal $a(t)$, peut s'écrire comme suit:

$$y_{ji}(t) = h_i(t) *_t a(t) *_t h_j(t) *_t TRF(\vec{r}) *_{\vec{r}} h_{ji}(\vec{r},t) \qquad \text{(VF\_51)}$$

où $h_j(t)$ et $h_i(t)$ sont respectivement les réponses impulsionnelles électroacoustiques des transducteurs S_j et S_i. $TRF(\vec{r})$ représente la fonction de réflectivité tissulaire du milieu et représente la distribution de l'amplitude des diffuseurs en fonction de leur position $\vec{r}$. $h_{ji}(\vec{r})$ est la réponse impulsionnelle spatiale (en émission et réception) des deux transducteurs en un point $\vec{r}$ et est définie comme suit **[Jensen(1992)]**:

$$h_{ji}(\vec{r},t) = h_j(\vec{r},t) *_t h_i(\vec{r},t) \qquad \text{avec :} \begin{cases} h_j(\vec{r},t) = \int_{S_j} \dfrac{\delta\left(t - t_j - \dfrac{\left\|\vec{r} - \vec{r}_{S_j} - \vec{r}^{\,0}_{S_j}\right\|_2}{c_0}\right)}{2\pi\left\|\vec{r} - \vec{r}_{S_j} - \vec{r}^{\,0}_{S_j}\right\|_2} d^2\vec{r}_{S_j} \\ h_i(\vec{r},t) = \int_{S_i} \dfrac{\delta\left(t - \dfrac{\left\|\vec{r} - \vec{r}_{S_i} - \vec{r}^{\,0}_{S_i}\right\|_2}{c_0}\right)}{2\pi\left\|\vec{r} - \vec{r}_{S_i} - \vec{r}^{\,0}_{S_i}\right\|_2} d^2\vec{r}_{S_i} \end{cases} \qquad \text{(VF\_52)}$$

où $\vec{r}^{\,0}_{S_j}$ et $\vec{r}^{\,0}_{S_i}$ sont respectivement les positions vectorielles des origines des surfaces S_j et S_i. t_j est le délai de transmission de la source. Dans (VF_52), $h_j(\vec{r},t)$ et $h_i(\vec{r},t)$ peuvent respectivement être appelées réponses impulsionnelles spatiales des transducteurs en émission et en réception.
L'hypothèse, qui a été faite afin d'en déduire un modèle de propagation général pour toutes les techniques d'imagerie par ultrasons, consiste à indiquer que les ondes transmises par les éléments interagissent avec le support imagé dans des conditions de champ éloigné. Dans de telles conditions, $\left\|\vec{r}_{S_e}\right\|_2 \approx \left\|\vec{r}^{\,0}_{S_e}\right\|_2$ et $\left\|\vec{r}_{S_r}\right\|_2 \approx \left\|\vec{r}^{\,0}_{S_r}\right\|_2$. Ainsi, (VF_52) devient:

$$h_{ji}(\vec{r},t) \approx \frac{\delta\left(t - t_j - \dfrac{\left\|\vec{r} - \vec{r}^{\,0}_{S_j}\right\|_2 + \left\|\vec{r} - \vec{r}^{\,0}_{S_i}\right\|_2}{c_0}\right)}{4\pi^2\left\|\vec{r} - \vec{r}^{\,0}_{S_j}\right\|_2\left\|\vec{r} - \vec{r}^{\,0}_{S_i}\right\|_2} \qquad \text{(VF\_53)}$$

En d'autres termes, (VF_53) implique que, en tout point $\vec{r}$, lorsque l'élément j émet une impulsion courte (Dirac), le signal reçu par le récepteur i est également une impulsion reçue avec un retard égal au temps de propagation qui sépare la transmission / diffusion / réception. Considérons un cas purement hypothétique dans lequel un élément de sonde est utilisé à la fois en émission et en réception. Sa réponse impulsionnelle en émission/réception est donnée par:

$$h_1(t) = h_e(t) *_t h_r(t) = \delta(t) \qquad \text{(VF\_54)}$$

Considérons maintenant trois simulations réalisées à l'aide de cet élément (VF_Fig.25): premièrement: le milieu ne contient que le diffuseur 1; deuxièmement: le milieu ne contient que le diffuseur 2; troisième: le milieu ne contient que le diffuseur 3.

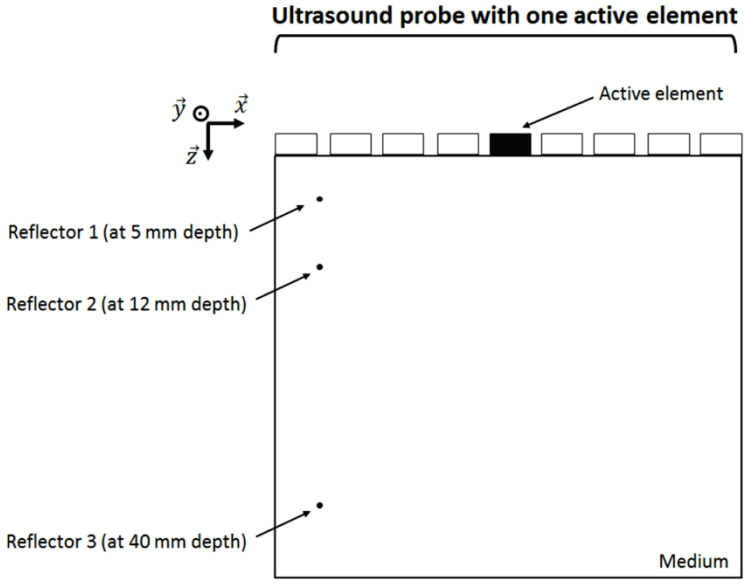

VF_Fig.25: Configuration illustrant la différence, due à la réponse spatiale, des signaux reçus par la sonde provenant de réflecteurs situés à différentes profondeurs.

Les signaux simulés (en utilisant Field II) sont représentés avec leurs enveloppes respectives sur les VF_Fig.26a et VF_Fig.26b. Comme on peut le voir, le signal $y_{ji}(t)$ le plus proche de l'impulsion de Dirac est celui obtenu lorsque le diffuseur a été placé à la position la plus éloignée de la sonde. Ici, $\left\|\vec{r}_{S_e}\right\|_2 \approx \left\|\vec{r}^{\,0}_{S_e}\right\|_2$ et $\left\|\vec{r}_{S_r}\right\|_2 \approx \left\|\vec{r}^{\,0}_{S_r}\right\|_2$. Ainsi, les conditions de champ éloigné ne sont pas satisfaites. Cependant, comme on peut le constater, lorsque les diffuseurs sont plus proches de l'élément, les signaux $y_{ji}(t)$ s'élargissent. C'est le résultat du principe de Huygens appliqué sur la surface d'émission / réception de l'élément de sonde, où chaque point de la surface se comporte comme une source / récepteur, le signal total enregistré étant donc une somme d'impulsions de Dirac légèrement retardées (en fonction de la position considérée sur la surface) **[Jensen (2012)]**. Le signal d'excitation utilisé et la réponse impulsionnelle acousto-électrique étant une impulsion courte, ces $y_{ji}(t)$ signaux peuvent être vus directement comme la réponse impulsionnelle spatiale en émission / réception de l'élément de sonde à la position $\vec{r}$ du milieu. On peut donc en conclure que lors d'une émission / réception utilisant l'ensemble des éléments de sonde, chaque élément a une réponse impulsionnelle spatiale différente à chaque position $\vec{r}$ du support. Or, dans les schémas d'acquisition classiques, cet

effet est complètement négligé. Cependant, comme pour la mise en œuvre de l'effet d'atténuation tissulaire **[Benane (2018b)]**, cet effet pourrait être compensé dans un schéma de compression d'impulsion. Néanmoins, alors que la réponse impulsionnelle qui modélise l'effet d'atténuation des tissus ne dépend que de la distance euclidienne entre la source / le diffuseur / le récepteur, comme le montre la VF_Fig.26, la réponse impulsionnelle spatiale des éléments dépend également de la position relative de la source / diffuseur / récepteur. Cela rend la mise en oeuvre d'un schéma de compression d'impulsion, qui compenserait l'effet de la réponse impulsionnelle spatiale, compatible uniquement avec un certain nombre de schémas d'acquisition ultrasonores permettant à chaque écho reçu, de déterminer le chemin exact suivi par cet écho lors de sa propagation. Ces schémas d'acquisition sont la transmission classique focalisée et le MLT.

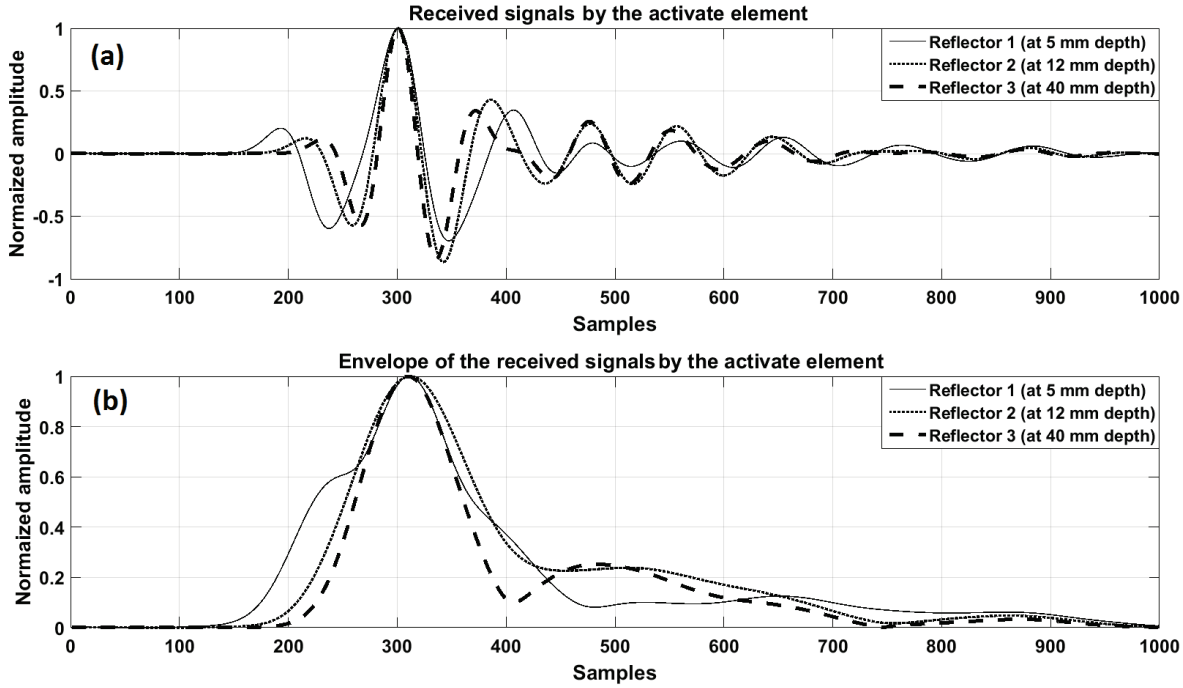

VF_Fig.26: Les signaux obtenus simulés pour des réflecteurs placés à différentes profondeurs.

Lorsqu'un faisceau focalisé est transmis à l'intérieur du support, les signaux reçus sur chaque élément de la sonde peuvent être écrits ainsi:

$$y_i(t) = e(t) * g_i(t) + b(t) \quad \text{avec:} \begin{cases} g_i(t) = \sum_{j=1}^{N_e} \delta(t - t_j) * g_{ji}(t) \\ g_{ji}(t) = \sum_{l=1}^{N_s} TRF_l \, h_j(\vec{r}_l, t) * h_i(\vec{r}_l, t) \\ e(t) = a(t) * h_1(t) \end{cases} \qquad \text{(VF\_55)}$$

où $h_j(t)$ et $h_i(t)$ sont les réponses impulsionnelles spatiales des éléments de sonde en émission et en réception, respectivement. À ce stade, en utilisant (VF_55), on peut voir que pour tout diffuseur l, situé à la position $\vec{r}_l$, l'écho reçu peut être écrit ainsi:

$$e_{li}(t) = TRF_l\, a(t) * h_1(t) * g_p(\vec{r}_l,t) * h_i(\vec{r}_l,t) \qquad \left(\text{avec :} \quad g_p(\vec{r}_l,t) = \sum_{j=1}^{N_{el}} h_j(\vec{r}_l,t) \right) \qquad \text{(VF\_56)}$$

En (VF_56), on peut observer que l'écho $e_{li}(t)$ reçu par le $i^{ème}$ élément de la sonde (généré par le diffuseur l) dépend du signal d'excitation $a(t)$, de la réponse impulsionnelle d'impulsion acousto-électrique de la sonde $h_1(t)$, de la réponse impulsionnelle spatiale de l'élément à la position du diffuseur et d'un signal $g_p(\vec{r}_l,t)$. Le terme $g_p(\vec{r}_l,t)$ représente la superposition de toute la réponse impulsionnelle spatiale des éléments d'émission de la sonde à la position du diffuseur et peut être vu comme la réponse impulsionnelle spatiale de la sonde en émission au point $\vec{r}_l$.

À ce stade, le principe du REC peut être appliquée (de la même manière que pour la partie III) afin de le bon signal d'excitation et le filtre correspondant.

2. Résultats expérimentaux

Trois configurations différentes sont considérées. Le premier ($Conventional_{exp}$) est le cas classique dans lequel une période d'un signal sinusoïdal est transmise et après la réception des échos, la formation de faisceau (Delay and Sum) est effectuée. Le deuxième cas (REC_{exp}) est le REC classique décrit précédemment, qui consiste à transmettre un chirp pré-amélioré et à comprimer les échos obtenus avant de reconstruire l'image à l'aide de DAS. La troisième ($I\text{-}REC_{exp}$) est une amélioration de la seconde méthode en prenant en compte la réponse impulsionnelle spatiale de la sonde en réception lors de l'étape de compression (juste avant la formation de l'image). La VF_Fig27 montre les différentes images B-mode (log-compressées) obtenues pour les trois configurations différentes.

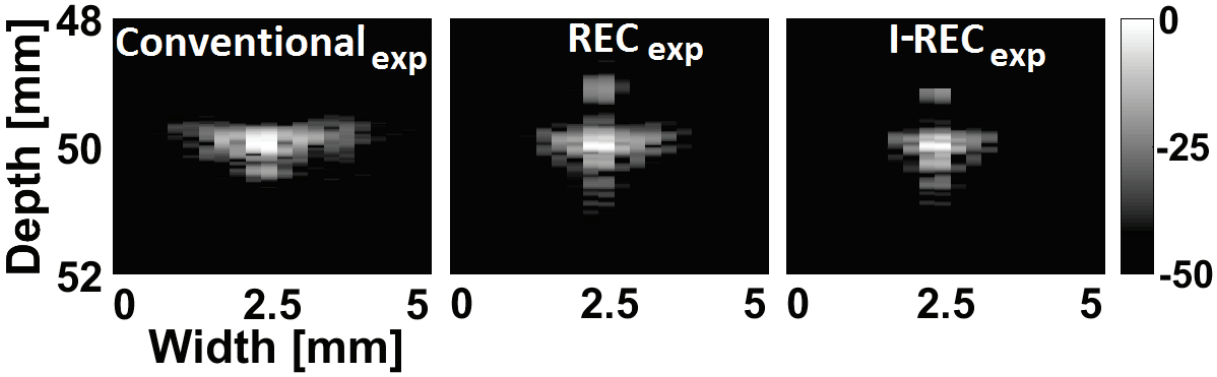

VF_Fig.27: Images B-mode log-compressées obtenues à partir d'un fil immergé dans l'eau, en utilisant les trois méthodes

Les résultats obtenus (VF_Fig.27) montrent que $I\text{-}REC_{exp}$ fournit la meilleure qualité d'image. En effet, les expériences révèlent une amélioration de la bande passante de 51% pour $I\text{-}REC_{exp}$ par rapport à la technique classique, ce qui est cohérent avec l'augmentation de bande passante prévue de 54%. Lorsque l'approche REC_{exp} est utilisée (sans compenser la réponse impulsionnelle spatiale), seule une amélioration de la largeur de bande de 36% est observée par rapport à la technique conventionnelle. La résolution axiale (VF_Fig 5) suit la même tendance (à savoir $I\text{-}REC_{exp}$: 87 µm, REC_{exp}: 99 µm, $Conbentional_{exp}$: 133 µm).

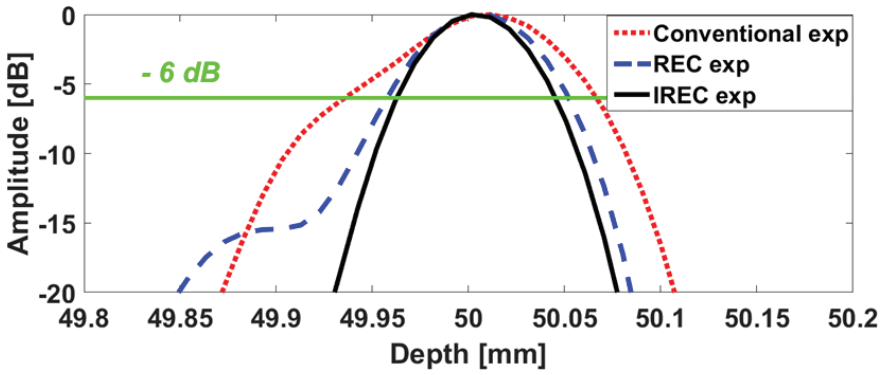

VF_Fig.28: Enveloppe axiale des données radiofréquences correspondant au fil.

VII- Conclusion générale

Dans la littérature de l'imagerie ultrasonore, il existe un grand nombre de schémas d'acquisition tels que: l'imagerie focalisée, l'imagerie par ondes planes (ondes divergentes), etc. La qualité d'image fournie par ces méthodes dépend fortement du signal d'excitation, de l'interaction onde / tissu mais aussi des propriétés du matériel utilisé. Dans une première partie de ce manuscrit, les principes de la propagation des ondes ultrasonores et de l'interaction tissulaire ont été expliqués. Ensuite, en s'appuyant sur ces principes, il a été montré que les schémas d'acquisition classiques fournissent des qualités d'image qui dépendent du bruit d'acquisition, de la largeur de bande de la sonde ultrasonore utilisée et de l'effet d'atténuation présente dans les tissus. En outre, il a été montré que les performances du schéma d'acquisition classique peuvent être grandement améliorées en employant des signaux modulés phase / fréquence / amplitude dans les filtres de transmission et de compression d'impulsions en réception. Une méthode très prometteuse appelée « Resolution Enhancement Compression (REC) » a été identifiée, qui, en plus d'utiliser des signaux modulés en fréquence qui augmentent le rapport signal / bruit de l'écho, est capable de surmonter l'effet bande limitée de la sonde ultrasonore en augmentant l'énergie des signaux émis dans les bandes de fréquences où la sonde est moins efficace. L'objectif de ce travail était d'étendre le concept de REC et de l'associer à un schéma d'acquisition ultrarapide afin d'obtenir une qualité d'image supérieure à des vitesses d'acquisition ultra-rapides.

Dans la première contribution de ce travail, REC a été combiné avec le concept de la sommation cohérente d'images obtenues par ondes planes (CPWC), l'objectif étant d'obtenir une meilleure qualité d'image à des fréquences d'images bien supérieures à celles fournies par l'imagerie conventionnelle (focalisée). Tout d'abord, une étude théorique a été détaillée, qui a prouvé que REC peut être adapté au CPWC et que des gains importants en termes de largeur de bande des signaux enregistrés et de résolution spatiale de l'image reconstruite peuvent être obtenus. Ensuite, la méthode proposée (CPWC-REC) a été testée en simulation sur les fantômes de fils et à kystes et on a observé qu'elle surpassait, comme on pouvait s'y attendre, le CPWC classique (qui utilise des impulsions sinusoïdales comme signaux d'excitation). CPWC-REC a également été mis en œuvre sur un scanner de recherche, des acquisitions sur des fantômes in vitro et des organes in vivo / ex-vivo ont été réalisés. Là encore, la capacité de CPWC-REC à fournir une meilleure qualité d'image que CPWC a été remarquée. En tant que tel, il a été observé que CPWC-REC peut obtenir de meilleures qualités d'image que le CPWC classique à partir d'un nombre moindre d'ondes planes. Dans le contexte de la qualité inhérente de l'image / du taux d'acquisition d'images présent dans le domaine de l'imagerie par ultrasons, cette

propriété implique que CPWC-REC peut atteindre des qualités d'image CPWC classiques à des fréquences d'images plus rapides.

Dans le CPWC-REC, les résultats ont montré une certaine différence entre les performances attendues / simulées et les résultats obtenus dans les résultats in vitro / ex vivo / in vivo. Une enquête plus poussée a permis de conclure que cet écart était dû à l'effet d'atténuation tissulaire. Ainsi, l'objectif de la deuxième contribution de cette thèse était de surmonter l'effet de l'atténuation tissulaire. Tout d'abord, il a été décidé de modéliser l'atténuation tissulaire par sa réponse impulsionnelle. Ensuite, cette réponse a été utilisée afin de modifier REC de telle manière que les signaux d'excitation restent les mêmes mais que les filtres de compression évoluent en fonction de la profondeur à laquelle sont générés les échos compressés. De cette manière, le contexte théorique de la deuxième contribution a été réglé. La mise en œuvre de la simulation du CPWC-REC amélioré a prouvé sa capacité à surmonter l'effet d'atténuation et à nous inciter à l'appliquer dans des expériences in vitro. Là encore, on a observé une meilleure performance du CPWC-REC amélioré.

Un autre phénomène qui altérait les performances du REC dans les expériences in vitro / ex vivo / in vivo était la propagation non linéaire des ondes acoustiques. L'objectif de la troisième contribution de ce travail était donc d'adapter REC à un comportement non linéaire des ultrasons dans les tissus mous. Il a été décidé d'associer l'amélioration (pour surmonter l'effet de l'atténuation tissulaire) CPWC-REC au concept d'inversion d'impulsion qui consiste en l'émission successive d'ondes acoustiques portant des signaux de polarité opposée. L'acquisition in vitro a montré des résultats prometteurs, la méthode proposée pouvant surpasser la méthode classique d'inversion des impulsions.

Afin de vérifier la capacité du REC à s'adapter à d'autres schémas d'acquisition ultrarapides, il a été décidé de combiner REC avec la technique MLT (Multi Line Transmit) qui consiste à transmettre / recevoir / reconstruire simultanément plusieurs lignes focalisées à l'intérieur de l'image ultrasonore. Tout d'abord, les études théoriques et de simulation ont été menées. Ensuite, suite aux résultats prometteurs obtenus, MLT-REC a été implémenté sur le scanner Ula-Op 256 équipé d'une sonde linéaire. Il a été conclu que REC-MLT était ab le a augmenter la bande passante des échos rétrodiffusés fournissant ainsi une meilleure résolution spatiale dans les images fournies en mode B. De plus, grâce aux signaux modulés en fréquence, le rapport signal sur bruit de l'écho a également été augmenté par rapport à la MLT conventionnelle, ce qui s'est traduit par un rapport signal / contraste / bruit accru dans les images obtenues en mode B. Les résultats obtenus ont montré que le MLT-REC permettait d'améliorer jusqu'à 8 fois la fréquence d'images dans les analyses fantômes / ex vivo tout en offrant une meilleure qualité d'image que les MLT classiques.

Comme le cœur de REC repose sur le principe de l'élévation de l'énergie d'excitation dans les bandes de fréquences où la sonde à ultrasons est moins efficace, ce qui a été observé dans toutes les applications pratiques des méthodes ultrarapides et le rapport contraste sur bruit, le rapport signal sur bruit de l'écho des méthodes basées sur REC était inférieur à celui fourni par les méthodes employant des effets non améliorés. Ainsi, dans la prochaine contribution de ce travail, nous avons décidé de fusionner REC avec une autre technique de codage qui nous permettra de renforcer davantage le rapport signal sur bruit de l'écho. Les techniques proposées combinent les avantages de REC avec ceux du codage Golay temporel et ont été appliquées à la DWC (Diverging Wave Compounding), prouvant ainsi à nouveau la capacité de REC à s'adapter à différents schémas d'acquisition. Les expériences sur des fantômes réels ont montré que DWC employant des codes de Golay modulés pré-améliorés est capable de fournir de meilleurs résultats en termes de CNR, résolution axiale, largeur de

bande et taille de speckle par rapport aux DWC basés sur les codes Golay Ainsi, les résultats expérimentaux ont prouvé que la combinaison entre les codes de Golay binaires et les chirps modulés pré-améliorés est réalisable et offre des avantages pour l'imagerie lorsqu'elle est mise en œuvre sur des sondes à ultrasons à bande étroite.

Dans une contribution finale de ce travail, un autre effet des acquisitions échographiques qui nuisait à la performance des méthodes basées sur le REC a été considéré. L'objet de l'étude de ce projet était la réponse impulsionnelle spatiale de la sonde à ultrasons. Tout d'abord, l'étude théorique proposée a montré que le REC ne peut être adapté pour surmonter la réponse impulsionnelle spatiale de la sonde que dans les schémas d'acquisition utilisant une transmission focalisée. Ainsi, dans le cadre d'acquisitions ultrarapides, il a été décidé d'appliquer cette optimisation REC à la technique MLT-REC. La simulation et les résultats expérimentaux ont montré des améliorations de l'amélioration proposée par rapport au système MLT-REC classique.

PERSONAL BIBLIOGRAPHY

Award (1)

Prize for the best student paper from the ICASSP conference received on April 17, 2018:

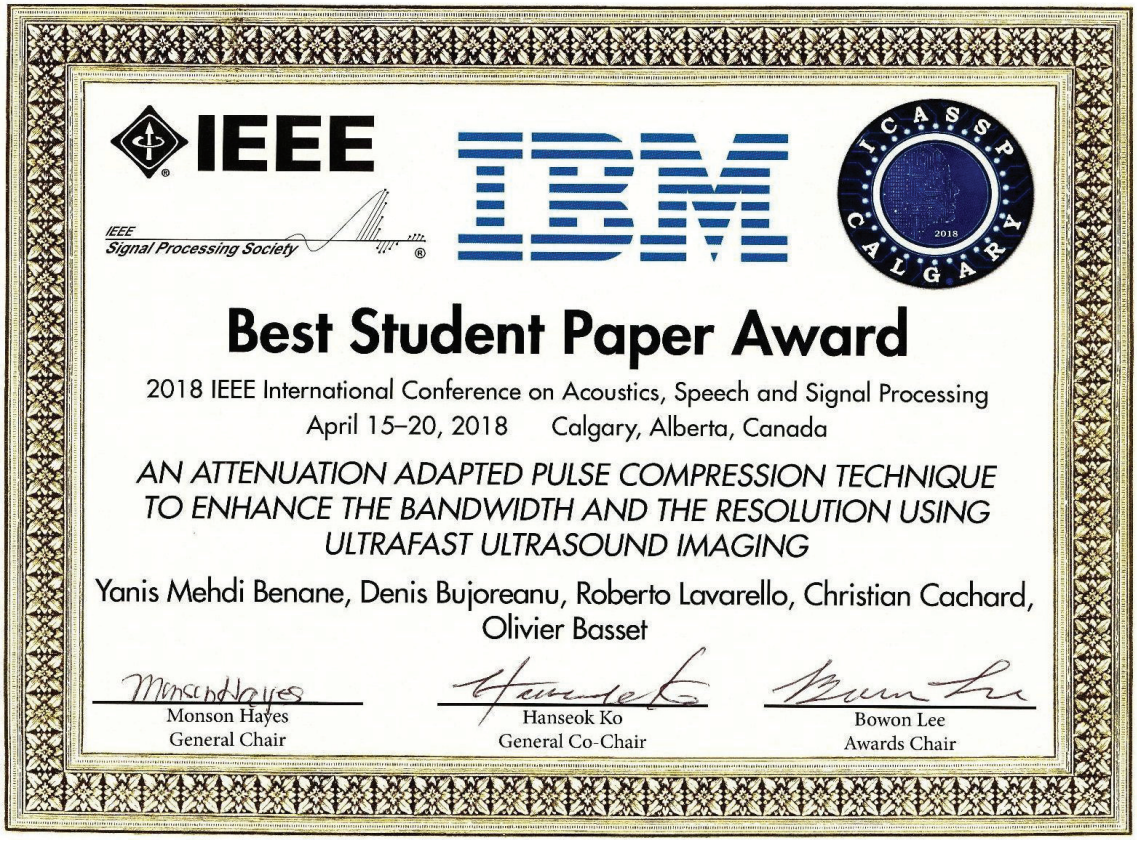

Journal articles (1)

1- **Benane, Y. M.**, Bujoreanu, D., Lavarello, R., Cachard, C., Varray, F., Escoffre, J. M., ... & Basset, O. (2018, March). Experimental implementation of a pulse compression technique using coherent plane wave compounding. In Transactions on Ultrasonics Ferroelectrics and Frequency Control (TUFFC). IEEE.

Journal articles submitted (4)

1- **Benane, Y. M.**, Bujoreanu, D., Badescu, .E, Nicolas, B., Cachard, C., Liebgott, H., Basset, O. (2018, October). A Robust Chirp Compression Technique Combined to Multi-line Transmission to Enhance the Bandwidth and Spatial Resolution. In Transactions on Ultrasonics Ferroelectrics and Frequency Control (TUFFC). IEEE.

2- Bujoreanu, D., Nicolas, B., **Benane, Y. M**., Liebgott, H., Friboulet, D. An Advanced Direct Model for Coded Ultrasound Imaging. In Transactions on Ultrasonics Ferroelectrics and Frequency Control (TUFFC). IEEE.

3- Sekimoto, K., **Benane, Y. M**., Alloubia, K., Arteil, R. and Fruleux, A., "A Macroscopic Rigid-body Behavior as Classical Mössbauer Effect". In Physical Review Letters (PRL).

4- Franceschini, E., Escoffre, J. M., Novell, A., Auboire, L., Mendes, V., **Benane, Y. M**., Bouakaz, A. and Basset, O. Quantitative ultrasound in ex vivo fibrotic rabbit livers. In Ultrasound in Medicine and Biology (UMB).

International conference papers (12)

1- **Benane, Y. M.**, Bujoreanu, D., Lavarello, R., Bernard, A., Cachard, C. & Basset, O. (2018, October). Enhanced second harmonic imaging using a pulse compression technique combined with ultrasound pulse inversion. In *Ultrasonics Symposium (IUS), 2018 IEEE International*. IEEE.

2- **Benane, Y. M.**, Bujoreanu, D., Liebgott, H., Cachard, C. & Basset, O. (2018, October). Ultrasound probe bandwidth enhancement combined with non-stationary compression filters to improve image quality. In *Ultrasonics Symposium (IUS), 2018 IEEE International*. IEEE.

3- **Benane, Y. M.**, Bujoreanu, D., Badescu, .E, Lavarello, R., Liebgott, H., Cachard, C. & Basset, O. (2018, October). Experimental implementation of resolution enhancement compression for ultrasound diverging wave compounding using a tri-state voltage drive. In *Ultrasonics Symposium (IUS), 2018 IEEE International*. IEEE.

4- Perrot, V., **Benane, Y. M.**, Badescu, E., Liebgott, H. & Garcia, D. (2018, October). Dual-frequency alias-free color Doppler using chirping and pulse compression. In *Ultrasonics Symposium (IUS), 2018 IEEE International*. IEEE.

5- Bujoreanu, D., **Benane, Y. M.**, Nicolas, B., Liebgott, H. & Friboulet, D. (2018, October). Jointly optimized modulation/filtering technique for pseudo-orthogonal binary sequences. In *Ultrasonics Symposium (IUS), 2018 IEEE International*. IEEE.

6- **Benane, Y. M**., Bujoreanu, D., Cachard, C, Nicolas, B. & Basset, O. (2018, September). An enhanced chirp modulated Golay code for ultrasound diverging wave compounding. In *Signal Processing Conference (EUSIPCO), 2018 26th European*. IEEE.

7- Bujoreanu, D., **Benane, Y. M**., Liebgott H., Nicolas, B., Basset, O & Friboulet, D. (2018, September). A resolution enhancement technique for ultrafast coded medical ultrasound. In *Signal Processing Conference (EUSIPCO), 2018 26th European*. IEEE.

8- **Benane, Y. M**., Bujoreanu, D., Lavarello, R., Cachard, C & Basset, O. (2018, April). An attenuation adapted pulse compression technique to enhance the bandwidth and the resolution using ultrafast ultrasound imaging. In *Acoustics, Speech and Signal Processing (ICASSP), 2018 IEEE International Conference*. IEEE.

9- **Benane, Y. M.**, Lavarello, R., Bujoreanu, D., Cachard, C., Varray, F., Savoia, A. S., ... & Basset, O. (2017, September). Ultrasound bandwidth enhancement through pulse compression using a CMUT probe. In *Ultrasonics Symposium (IUS), 2017 IEEE International* (pp. 1-4). IEEE.

10- **Benane, Y. M.**, Lavarello, R., Bujoreanu, D., Cachard, C., Varray, F., Escoffre, J. M., ... & Basset, O. (2017, September). Ultrafast ultrasound imaging using a resolution and bandwidth enhancement technique. In *Ultrasonics Symposium (IUS), 2017 IEEE International* (pp. 1-4). IEEE.

11- Escoffre, J. M., Novell, A., Bouakaz, A., **Benane, Y. M.**, Basset, O., & Franceschini, E. (2017, September). Quantitative ultrasound parameters in ex-vivo fibrotic rabbit livers: Liver stiffness and tissue microstructure estimation. In Ultrasonics Symposium (IUS), 2017 IEEE International (pp. 1-4). IEEE.

12- Salles, S., Varray, F., **Benane, Y. M.**, & Basset, O. (2016, September). Optimization of resolution enhancement compression technique with plane wave imaging. In *Ultrasonics Symposium (IUS), 2016 IEEE International* (pp. 1-4). IEEE.

BIBLIOGRAPHIES

[Szabo, 2004] Szabo, T. L. (2004). Diagnostic ultrasound imaging: inside out. Academic Press.

[Hamilton (1988)] Hamilton, M. F., & Blackstock, D. T. (1988). On the coefficient of nonlinearity β in nonlinear acoustics. The Journal of the Acoustical Society of America, 83(1), 74-77.

[Ziomek (1994)] Ziomek, L. (1994). Fundamentals of acoustic field theory and space-time signal processing. CRC press.

[Meunier (1995)] Meunier, J., & Bertrand, M. (1995). Ultrasonic texture motion analysis: theory and simulation. IEEE transactions on medical imaging, 14(2), 293-300.

[Jensen (1991)] Jensen, J. R. A. (1991). A model for the propagation and scattering of ultrasound in tissue. The Journal of the Acoustical Society of America, 89(1), 182-190.

[Jensen (1991)]Jensen, J. A., & Svendsen, N. B. (1992). Calculation of pressure fields from arbitrarily shaped, apodized, and excited ultrasound transducers. IEEE transactions on ultrasonics, ferroelectrics, and frequency control, 39(2), 262-267.

[Beyer (1960)] Beyer, R. T. (1960). Parameter of nonlinearity in fluids. The Journal of the Acoustical Society of America, 32(6), 719-721.

[Beyer (1974)] Beyer, R. T. (1974).Nonlinear Acoustics. Naval Ship Systems Command.

[Fubini (1935)] Fubini, E. (1935). Anomalie nella propagazione di onde acustiche di grande ampiezza. Alta Frequenza 4, 530–581.

[Kuznetsov (1970)] Kuznetsov, V. (1970). Equation of nonlinear acoustics. Sov. Phys. Acoustics, 16, 749–768.

[Zabolotskaya (1969)] Zabolotskaya, E. and Khokhlov, R. (1969). Quasi-plane waves in the nonlinear acoustics of confined beams. Sov. Phys. Acoustics, 15, 35–40.

[Frinking (2000)] Frinking, P. J., Bouakaz, A., Kirkhorn, J., Ten Cate, F. J., & De Jong, N. (2000). Ultrasound contrast imaging: current and new potential methods. Ultrasound in medicine & biology, 26(6), 965-975.

[Chiao (2003)] Chiao, R. Y., & Hao, X. (2003, October). Coded excitation for diagnostic ultrasound: A system developer's perspective. In Ultrasonics, 2003 IEEE Symposium on (Vol. 1, pp. 437-448). IEEE.

[Haider (2001)] Haider, B., & Chiao, R. Y. (2001). Higher order nonlinear ultrasonic imaging. The Journal of the Acoustical Society of America, 109(5), 2360-2360.

[Eckersley (2005)] Eckersley, R. J., Chin, C. T., & Burns, P. N. (2005). Optimising phase and amplitude modulation schemes for imaging microbubble contrast agents at low acoustic power. Ultrasound in medicine & biology, 31(2), 213-219.

[Hwang, (1999)] Hwang, J. J., & Simpson, D. H. (1999). Two Pulse Technique for Ultrasonic Harmonic Imaging. U.S. Patent No. 5,951,478. Washington, DC: U.S. Patent and Trademark Office.

[Simpson (1999)] Simpson, C. T. (1999). Pulse Inversion Doppler: a New Method for Detecting Nonlinear Echoes from Microbubble Contrast Agents. IEEE transactions on ultrasonics, ferroelectrics, and frequency control, 1999, 46 (2), 372–382.

[Lin (2015)] Lin, F., Cachard, C., Varray, F., & Basset, O. (2015). Generalization of multipulse transmission techniques for ultrasound imaging. Ultrasonic imaging, 37(4), 294-311.

[Van Wijk (2002)] Van Wijk, M. C., & Thijssen, J. M. (2002). Performance testing of medical ultrasound equipment: fundamental vs. harmonic mode. Ultrasonics, 40(1-8), 585-591.

[Beutel (2000)] J. Beutel, H. L. Kundel, and R. L. Van Metter, Handbook of Medical Imaging. Bellingham, WA: SPIE Press, 2000.

[Chartuvedi (1996)] Chaturvedi, P., & Insana, M. F. (1996). Error bounds on ultrasonic scatterer size estimates. The Journal of the Acoustical Society of America, 100(1), 392-399.

[Rouyer (2015)] Rouyer, J., Varray, F., Pozo, E., Basset, O., Cachard, C., & Lavarello, R. (2015, August). Evaluation of a frequency-domain ultrasonic imaging attenuation compensation technique. In Engineering in Medicine and Biology Society (EMBC), 2015 37th Annual International Conference of the IEEE (pp. 1560-1563). IEEE.

[Benane (2018a)] Benane, Y. M., Bujoreanu, D., Lavarello, R. J., Varray, F., Escoffre, J. M., Novell, A., ... & Basset, O. (2018). Experimental Implementation of a Pulse Compression Technique Using Coherent Plane-Wave Compounding. *IEEE transactions on ultrasonics, ferroelectrics, and frequency control*, *65*(6), 1025-1036.

[Thijssen (2003)] Thijssen, J. M. (2003). Ultrasonic speckle formation, analysis and processing applied to tissue characterization. Pattern Recognition Letters, 24(4-5), 659-675.

[Stetson (1997)] Stetson, P. F., Sommer, F. G., & Macovski, A. (1997). Lesion contrast enhancement in medical ultrasound imaging. IEEE transactions on medical imaging, 16(4), 416-425.

[Jensen A.C (2012)] Jensen, A. C., Nasholm, S. P., Nilsen, C. I. C., Austeng, A., & Holm, S. (2012). Applying Thomson's multitaper approach to reduce speckle in medical ultrasound imaging. *IEEE transactions on ultrasonics, ferroelectrics, and frequency control*, *59*(10).

[Wagner (1983)] Wagner, R. F. (1983). Statistics of speckle in ultrasound B-scans. IEEE Trans. Sonics & Ultrason., 30(3), 156-163.

[Liu (2005)] Liu, J., & Insana, M. F. (2005). Coded pulse excitation for ultrasonic strain imaging. IEEE transactions on ultrasonics, ferroelectrics, and frequency control, 52(2), 231-240.

[Tanter (2014)] Tanter, M., & Fink, M. (2014). Ultrafast imaging in biomedical ultrasound. IEEE transactions on ultrasonics, ferroelectrics, and frequency control, 61(1), 102-119.

[Shattuck (1984)] Shattuck, D. P, Weinshenker, M. D., Smith, S. W., & von Ramm, O. T. "Explososcan: A parallel processing technique for high speed ultrasound imaging with linear phased arrays," J. Acoust. Soc. Am., vol. 75, no. 4, pp. 1273–1282, Apr. 1984.

[Bujoreanu (2017a)] Bujoreanu, D., Liebgott, H., & Nicolas, B. (2017, March). Simultaneous coded plane wave imaging in ultrasound: Problem formulation and constraints. In *Acoustics, Speech and Signal Processing (ICASSP), 2017 IEEE International Conference on* (pp. 6254-6258). IEEE.

[Tong (2014)] Tong, L., Ramalli, A., Jasaityte, R., Tortoli, P., & D'hooge, J. (2014). Multi-transmit beam forming for fast cardiac imaging—Experimental validation and in vivo application. *IEEE transactions on medical imaging*, *33*(6), 1205-1219.

[Sandrin & Fink (1999)] Sandrin, L., Catheline, S., Tanter, M., Hennequin, X., & Fink, M. (1999). Time-resolved pulsed elastography with ultrafast ultrasonic imaging. Ultrasonic imaging, 21(4), 259-272.

[Montaldo (2009)] Montaldo, G., Tanter, M., Bercoff, J., Benech, N., & Fink, M. (2009). Coherent plane-wave compounding for very high frame rate ultrasonography and transient elastography. IEEE transactions on ultrasonics, ferroelectrics, and frequency control, 56(3), 489-506.

[Toulemonde (2015)] Toulemonde, M., Basset, O., Tortoli, P., & Cachard, C. (2015). Thomson's multitaper approach combined with coherent plane-wave compounding to reduce speckle in ultrasound imaging. *Ultrasonics*, *56*, 390-398.

[Cook (1967)] Cook, C. E. & Bernfeld, M. (1967). Radar signals: An introduction to theory and application. New York: Academic Press.

[Skolnik (1981)] Skolnik, M.I. (1981). Introduction to Radar Systems. McGraw-Hill.

[Chiao (2005)] Chiao, R. Y., & Xiaohui, H., (2005). Coded excitation for diagnostic ultrasound: A system developer's perspective. EEE Trans. Ultrason. Ferroelectr. Freq. Control, 52, 160-170.

[Misaridis (2000)] Misaridis, T. X., Gammelmark, K., Jørgensen, C. H., Lindberg, N., Thomsen, A. H., Pedersen, M. H., & Jensen, J. A. (2000). Potential of coded excitation in medical ultrasound imaging. Ultrasonics, 38(1-8), 183-189.

[O'Donnell (1992)] O'Donnell, M. (1992). Coded excitation system for improving the penetration of real-time phased-array imaging systems. IEEE transactions on ultrasonics, ferroelectrics, and frequency control, 39(3), 341-351.

[Lashkari (2016)] Lashkari, B., Zhang, K., & Mandelis, A. (2016). High-frame-rate synthetic aperture ultrasound imaging using mismatched coded excitation waveform engineering: A feasibility study. IEEE transactions on ultrasonics, ferroelectrics, and frequency control, 63(6), 828-841.

[Benane (2018b)] Benane, Y. M., Bujoreanu, D., Benane, Y. M., Lavarello, R., Cachard, C., & Basset, O. (2018). An attenuation adapted pulse compression technique to enhance the bandwidth and the resolution using ultrafast ultrasound imaging. In Acoustics, Speech and Signal Processing (ICASSP), 2018 IEEE International Conference. IEEE.

[Benane (2018c)] Benane, Y. M., Bujoreanu, D., Nicolas, B., Cachard, C., Basset, O., (2018). An enhanced chirp modulated Golay code for ultrasound diverging wave Compounding. In Signal Processing Conference (EUSIPCO), 2018 26th European. IEEE.

[Borsboom (2005)] Borsboom, J. M., Chin, C. T., Bouakaz, A., Versluis, M., & de Jong, N. (2005). Harmonic chirp imaging method for ultrasound contrast agent. IEEE transactions on ultrasonics, ferroelectrics, and frequency control, 52(2), 241-249.

[Cook (1993)] Cook C. E. & Bernfeld. (1993). M. Radar signals. Artech House, Inc.

[Misaridis (1999)] Misaridis, T. X., & Jensen, J. A. (1999). An effective coded excitation scheme based on a predistorted FM signal and an optimized digital filter. In Ultrasonics Symposium, 1999. Proceedings. 1999 IEEE (Vol. 2, pp. 1589-1593). IEEE.

[Gordon (1987)] Gordon S. Kino. (1987) Acoustic Waves, Devices, Imaging, & Analog Signal Processing. Prentice-Hall, Englewood Cliffs, N.J.

[Oppenheim (1989)] Oppenheim A. V. & Schafer. R. W. (1989) Discrete-Time Signal Processing. Prentice-Hall, Engle-wood Cliffs, N.J.

[Oelze (2007)] Oelze, M. L. (2007). Bandwidth and resolution enhancement through pulse compression. IEEE transactions on ultrasonics, ferroelectrics, and frequency control, 54(4).

[Nowicki (2007)] Nowicki, A., Trots, I., Lewin, P. A., Secomski, W., & Tymkiewicz, R. (2007). Influence of the ultrasound transducer bandwidth on selection of the complementary Golay bit code length. Ultrasonics, 47(1-4), 64-73.

[Jensen (1992)] Jensen, J. A., & Svendsen, N. B. (1992). Calculation of pressure fields from arbitrarily shaped, apodized, and excited ultrasound transducers. IEEE transactions on ultrasonics, ferroelectrics, and frequency control, 39(2), 262-267.

[Jensen (1996)] Jensen, J. A. (1996). Field: A program for simulating ultrasound systems. In 10th Nordicbaltic conference on biomedical imaging, 4, Supplement 1, Part 1: 351-353.

[Garcia (2013)] Garcia, D., Le Tarnec, L., Muth, S., Montagnon, E., Porée, J., & Cloutier, G. (2013). Stolt's fk migration for plane wave ultrasound imaging. IEEE transactions on ultrasonics, ferroelectrics, and frequency control, 60(9), 1853-1867.

[Tortoli (2009)] Tortoli, P., Bassi, L., Boni, E., Dallai, A., Guidi, F., & Ricci, S. (2009). ULA-OP: An advanced open platform for ultrasound research. IEEE transactions on ultrasonics, ferroelectrics, and frequency control, 56(10), 2207-2216.

[Pan (1998)] Pan, L., Zan, L., & Foster, F. S. (1998). Ultrasonic and viscoelastic properties of skin under transverse mechanical stress in vitro. Ultrasound in medicine & biology, 24(7), 995-1007.

[Hinkelman (1998)] Hinkelman, L. M., Mast, T. D., Metlay, L. A., & Waag, R. C. (1998). The effect of abdominal wall morphology on ultrasonic pulse distortion. Part I. Measurements. The Journal of the Acoustical Society of America, 104(6), 3635-3649.

[Gurumurthy (1982)] Gurumurthy, K. V., & Arthur, R. M. (1982). A dispersive model for the propagation of ultrasound in soft tissue. Ultrasonic Imaging, 4(4), 355-377.

[Park (2013)] Park, J., Huang, Y., Chen, R., Lee, J., Cummins, T. M., Zhou, Q., ... & Shung, K. K. (2013). Pulse inversion chirp coded tissue harmonic imaging (PI-CTHI) of zebrafish heart using high frame rate ultrasound biomicroscopy. Annals of biomedical engineering, 41(1), 41-52.

[Liebgott (2016)] Liebgott, H., Rodriguez-Molares, A., Cervenansky, F., Jensen, J. A., & Bernard, O. (2016). Plane-wave imaging challenge in medical ultrasound. In Ultrasonics Symposium (IUS), 2016 IEEE International (pp. 1-4). IEEE.

[Boni (2016)] Boni, E., Bassi, L., Dallai, A., Guidi, F., Meacci, V., Ramalli, A., ... & Tortoli, P. (2016). ULA-OP 256: A 256-channel open scanner for development and real-time implementation of new ultrasound methods. IEEE transactions on ultrasonics, ferroelectrics, and frequency control, 63(10), 1488-1495.

[Papadacci (2014)] Papadacci, C., Pernot, M., Couade, M., Fink, M., & Tanter, M. (2014). High-contrast ultrafast imaging of the heart. IEEE transactions on ultrasonics, ferroelectrics, and frequency control, 61(2), 288-301.

[Gran (2008)] Gran, F., & Jensen, J. A. (2008). Spatial encoding using a code division technique for fast ultrasound imaging. ieee transactions on ultrasonics, ferroelectrics, and frequency control, 55(1), 12-23.

[Tiran (2015)] Tiran, E., Deffieux, T., Correia, M., Maresca, D., Osmanski, B. F., Sieu, L. A., ... & Tanter, M. (2015). Multiplane wave imaging increases signal-to-noise ratio in ultrafast ultrasound imaging. Physics in Medicine & Biology, 60(21), 8549.

[Bujoreanu (2017b)] Bujoreanu, D., Bernard, A., Nicolas, B., Liebgott, H., & Friboulet, D. (2017, September). Simultaneous coded plane wave imaging: Implementation on a research echograph. In Ultrasonics Symposium (IUS), 2017 IEEE International (pp. 1-4). IEEE.

[Trots (2015)] Trots, I. (2015). Mutually Orthogonal Golay Complementary Sequences in Synthetic Aperture Imaging Systems. Archives of Acoustics, 40(2), 283-289.

[Kim (2004)] Kim, B. H., & Song, T. K. (2004, April). Multibeam Simultaneous Transmit Multizone (MB-STMZ) focusing method using modulated orthogonal codes for ultrasound imaging. In Medical Imaging 2004: Ultrasonic Imaging and Signal Processing (Vol. 5373, pp. 315-324). International Society for Optics and Photonics.

[Tseng (1972)] Tseng, C. C., & Liu, C. (1972). Complementary sets of sequences. IEEE Transactions on Information theory, 18(5), 644-652.